Spring 2021

Designing transition metal chalcogenides electrocatalyst surfaces for high-efficiency water oxidation

Umanga De Silva

Department: Chemistry

DESIGNING TRANSITION METAL CHALCOGENIDES ELECTROCATALYST SURFACES FOR HIGH-EFFICIENCY WATER OXIDATION

by

SAMMU HANDI UMANGA IROSHINI DE SILVA

A DISSERTATION

Presented to the Graduate Faculty of the

MISSOURI UNIVERSITY OF SCIENCE AND TECHNOLOGY

In Partial Fulfillment of the Requirements for the Degree

DOCTOR OF PHILOSOPHY

in

CHEMISTRY

2021

Approved by:

Manashi Nath, Advisor
Amitava Choudhury
Jeffery G. Winiarz
Risheng Wang
Xinhua Liang

PUBLICATION DISSERTATION OPTION

This dissertation consists of the following five articles, formatted in the style used by the Missouri University of Science and Technology:

Paper I, found on pages 32–88, has been published as "Nickel telluride as a bifunctional electrocatalyst for efficient water splitting in alkaline medium", in *Journal of Materials Chemistry A, 6*(17), 7608-7622, 2018.

Paper II, found on pages 89–145, has been submitted as **"**Cobalt Telluride: A Highly Efficient Trifunctional Electrocatalyst for Water Splitting and Oxygen Reduction" , to *Chemistry of Materials Journal.*

Paper III, found on pages 146–200, has been submitted as "Understanding Surface Structural Evolution of Nickel Chalcogenide Electrocatalysts for Water Oxidation", to *ACS Applied Energy Materials*.

Paper IV, found on pages 201–214, has been published as "Magnetic Multifunctional Nanostructures as High-efficiency Catalysts for Oxygen Evolution Reactions", by *MRS Advances Journal,* 1(34), 2401-2407, 2016.

Paper V, found on pages 215–257, has been submitted as "Synthesis and characterization of a series of nickel selenides for high efficient water oxidation catalysis", to *Nano-Micro Letters Journal.*

ABSTRACT

The rising demand for energy security and reducing fossil fuel dependence has prompted researchers to search for a clean, sustainable, and efficient energy generation system with low environmental impact. Water electrolysis has been identified as one of the most important processes satisfying the above needs to generate hydrogen as a clean fuel. Two half-cell reactions of oxygen evolution reaction (OER) at the anode and hydrogen evolution reaction (HER) at the cathode comprise the main process of water electrolysis. However, the oxygen evolution reaction is the most crucial step for efficient water splitting. Traditionally, metal oxides have been utilized as catalysts to enhance OER. Recent developments however have shown that transition metal chalcogenides exhibit better OER electrocatalytic activity surpassing state-of-the-art precious oxides.

In this research, the design principle of these electrocatalysts was explored further and the highly efficient OER catalytic activity of tellurides with various transition metals including Ni and Co was demonstrated. Interestingly it was observed that telluride-based electrocatalysts exhibited some of the lowest overpotentials reported to date along with high current density, surpassing those reported with analogous oxides and selenides. This research thus validated the primary hypothesis that decreasing anion electronegativity is instrumental in improving electrocatalytic activity, by tuning electrochemical response around the active transition metal site. This project also focused on understanding the active surface composition of chalcogenide electrocatalysts by measuring the catalytic activity of tailor-made surfaces and comparing it with constructed surface models. The effect of nanostructuring on the electrocatalytic performance was also investigated.

ACKNOWLEDGMENTS

First I would like to express my sincere gratitude to Missouri University of Science & Technology for letting me fulfil my dream of being a student here. I would like to extend my heartfelt gratitude to my advisor, Dr. Manashi Nath, for her guidance and support through my research endeavor. Without her support and guidance this dissertation would not have been possible. I am also taking this opportunity to extend my sincere gratitude to my committee members, Dr. Amitava Choudhury, Dr. Jeffery G. Winiarz, Dr. Risheng Wang, and Dr. Xinhua Liang, for their continuous support and assistance and accepting to be a part of my committee.

I am extremely thankful to the Department of Chemistry for providing continuous kind support and help as well as providing a teaching assistantship during my graduate studies. My thanks also goes to chairman, faculty and staff at the Department of Chemistry as well for their efforts to create an efficient and friendly working environment in DoC. I also like to thank the Materials Research Center for numerous supports provided through characterization techniques. I am taking this opportunity to thank my lab mates, Dr. Jahangir Masud, friends, and all of those who supported me in numerous ways during my research life.

Finally I am immensely thankful to my loving son, Nejan Liyanage, and husband, Rasika Liyanage, mother, father and two brothers for their kind and continuous love and support. I have no words to express my deepest gratitude to them bearing me, believing in me and always having my back. This journey would have been impossible without them. I like to dedicate this dissertation to them.

TABLE OF CONTENTS

Page

LIST OF ILLUSTRATIONS

SECTION Page

LIST OF TABLES

1. INTRODUCTION

1.1. IDENTIFYING SUSTAINABLE AND RENEWABLE ENERGY SOURCES: OVERVIEW AND SIGNIFICANCE

The global rise in population and the changes in the standards of living are the main reasons for the increase in world's energy consumption during the last decades. [1] Indicatively, the current global energy demand is around 15 terawatts (TW) and the average global power demand is predicted to be approximately 30 TW and 46 TW in 2050 and 2100, respectively. [2] Currently, fossil fuels consisting of coal, oil and natural gas are the primary sources of energy which covers more than 70% of the global energy needs as shown in Figure 1.1.

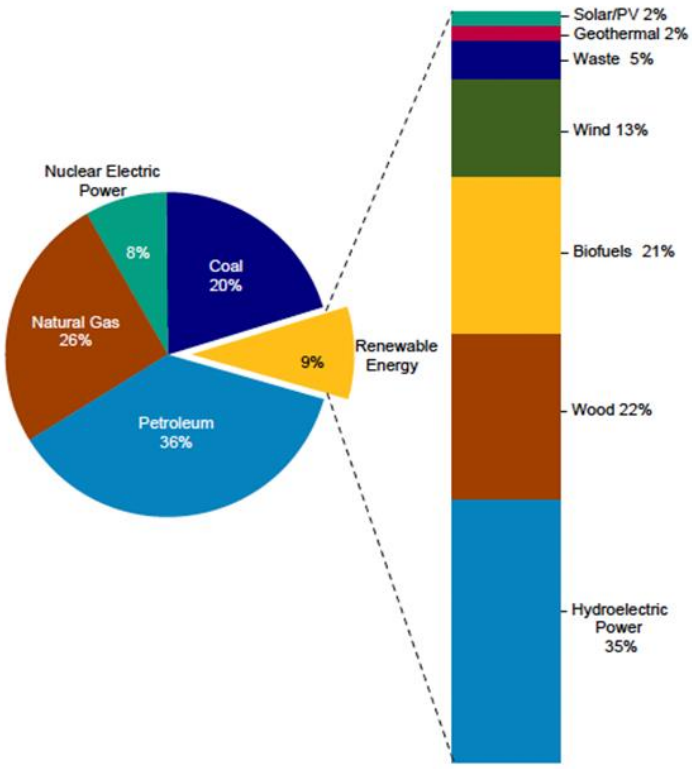

Figure 1.1. Globe primary energy supply in 2017 [3].

However, the fixation rate of carbon emission from fossil fuels through natural photosynthesis is much lower than the consumption rate of fossil fuels. [4] The continuously increasing energy demands and high consumption rate has led to the rapid depletion of fossil fuel resources. This has caused several environmental and societal problems including global warming, acid rain, and local air quality deterioration. In addition, the uneven distribution of fossil fuel reserves around the globe has also led to increasing geopolitical anxieties. These issues have rendered an urgent need for the development of new energy strategies with limited greenhouse gas emissions. In particular, rising threats in climate variation has inspired movements toward identifying renewable, stable, eco-friendly, and benign energy sources. These will include both renewable energy sources, which are more abundant, and cleaner compared to fossil fuels, as well as chemical processes for synthetic fuel production. [5-10]

1.2. RENEWABLE ENERGY SOURCES

Renewable energy is defined as an energy source which provides electricity, heat, and light without adding any pollutant to the environment. The main advantage of renewable energy is that it is generated from sources that are continuously being replenished on earth's atmosphere, and it reduces carbon dioxide emissions which have been identified as a main environmental pollutant. More favorably, scientists have been optimistic that using renewable energy can reduce gas emissions to the environment by 70% in 2050. Earth has numerous renewable energy sources including solar, biomass, hydrogen, wind, tidal, and geothermal energies (Figure 1.1)

1.2.1. Solar Energy. Solar energy is one of the best sources among other renewable energies capable of powering the earth. While other renewable energy resources are limited and fall short of meeting the present and foreseeable future energy requirements, the sun represents the most plentiful source of energy that can provide enough power for 50 TW of energy in the form of light irradiance, which is significantly higher than current societal needs across the globe. [11, 12] There are numerous practical methods to harvest solar energy in the form of solar power plants, seawater desalination, solar collectors, and solar cells.The fundamental problem related to the use of solar energy is its intermittent supply which often mismatches the power demands of the grid. The influx of solar energy is seasonal with the highest sunlight being received during the summer months. Another drawback of solar energy is that it is not a continuous source of energy due to the unavailability of direct sunlight during nighttime. Therefore, the development of systems for efficient collection and storage of solar energy is required. [13, 14] The primary challenge of solar radiation is that it needs to be converted to other forms of energy as electrical, chemical, and heat prior to usage. Consequently, the development and application of efficient energy conversions and storage systems are essentially required. Traditionally, solar energy is stored in solar-powered fuel cells, batteries, and supercapacitors, or in the form of heat in solar-thermal technology. Some semiconductor materials which have a pronounced photovoltaic effect can convert solar energy to electricity through the photovoltaic process. In addition to solar energy conversion efficiency, cost-effectiveness is also an issue for the success of solar energy technology since the conversion of solar energy to electricity should occur at a price that is comparable with the usage of fossil fuels. Solar radiation is an environmentally benign

source and can reduce CO2 emission by approximately 40 million tons of solar grids can generate enough energy to meet about 1% of the world's electricity demand [15].

1.2.2. Wind Energy. Wind power is another renewable energy source on earth. Similar to solar energy, it is also an environmentally friendly power source that does not produce minimal pollution to the atmosphere. Wind turbines can convert the kinetic energy of the wind into electrical energy that can be used for generating electricity. There is no fuel burning on wind turbines in the process of generating electricity [2, 16]. Wind energy has contributed to the world energy demand with more than 23 billion kWh of electricity. Some countries around the world have used wind power to produce electricity such as Germany has produced more than 4400 MW, India has produced an estimated 1000W and Denmark has produced more than a quarter of its electricity production through wind power [16]. In addition, more than 80 countries around the globe also use wind power as a commercial source. Wind energy has been considered an environmentally benign and clean energy production resource. Wind power could be produced at a low cost in the areas where natural weather patterns and geographical location ensures high wind.

However, wind power also has its limitations, major drawbacks being that it is not readily available all the time and in every region. In addition, wind power should have a speed of at least 13-15 m/s to run the wind turbine efficiently. If it is not windy weather, the productivity of the wind power plant is about an average of 30-60% [17]. In addition, wind energy production has faced some major challenges in turbine blades such as erosion of the blades by moisture and sand, ice deposition on the blades, and the adhesion

and insect accretion on the turbine blades which have reduced the efficiency of the electricity production [17, 18].

1.2.3. Bio Energy. Bioenergy produced from biomass can be defined as all plant materials produced from photosynthesis, organic wastes, and land and water-based vegetation. Bioenergy is a form of gaseous, liquid, or solid fuels that store chemical energy in plant-based materials. Biomass has a 10-14% contribution to the world energy demand [19]. Biodegradability and environmentally friendly resources, reduction of greenhouse gasses and waste, along with easily available energy sources that can be applied to both domestic and industrial landscape, has made bioenergy as a very promising, economically feasible sustainable source of energy [20]. There are various types of bioenergy sources such as biofuels, biogas, bio-oils, biodiesel, and vegetable oils [2, 21]. Bioethanol is the main biofuel and that can be produced from several crops including corn, wheat, sugar beet, and sugar cane. Biodiesel can be produced from edible and non-edible vegetable oils, animal fats, and recycled waste vegetable oils. Biogas is similar to natural gas which consists of a gaseous mixture of carbon dioxide and methane. It can be used for cooking and heating. Bio oils are also a mixture of chemical products which consists of hydrocarbons, alcohols, aldehydes, fatty acids, and other aliphatic and aromatic compounds [22]. It can be used as fuels for gas turbines, furnaces, and stationery, and diesel engines.

The drawbacks of bioenergy is that it is expensive technology due to process costs including deforestation, transportation and labor, the requirement of huge space and massive amount of water and land and biomass storage facilities. In addition, biomass

energy is not entirely clear due to the production of some greenhouse gasses which are comparatively lower than that produced from petroleum fuels [23].

1.2.4. Hydrogen Engery. Hydrogen is the simple, colorless, odorless, tasteless, plentiful, and most lightweight gas in the universe. Traditionally Hydrogen has been used as a town gas for street lighting and house energy supply for cooking, heating, and lighting [2]. Hydrogen is also an important chemical resource for ammonia synthesis and crude oil hydrogenation. As a clean atomic energy carrier, it plays a vital role in mobile, stationary, and portable applications as well as transportation [24]. The innovation of fuel cell technology has revived the interest in hydrogen. A fuel cell is a device that combines hydrogen and oxygen gases into the water, generating electricity and heat along with it [25]. With the rapid development of hydrogen fuel cell technology, hydrogen has become a most favorable, potential, and renewable energy source for future energy generation [25-27]. The Hydrogen energy cycle is illustrated in Figure 1.2.

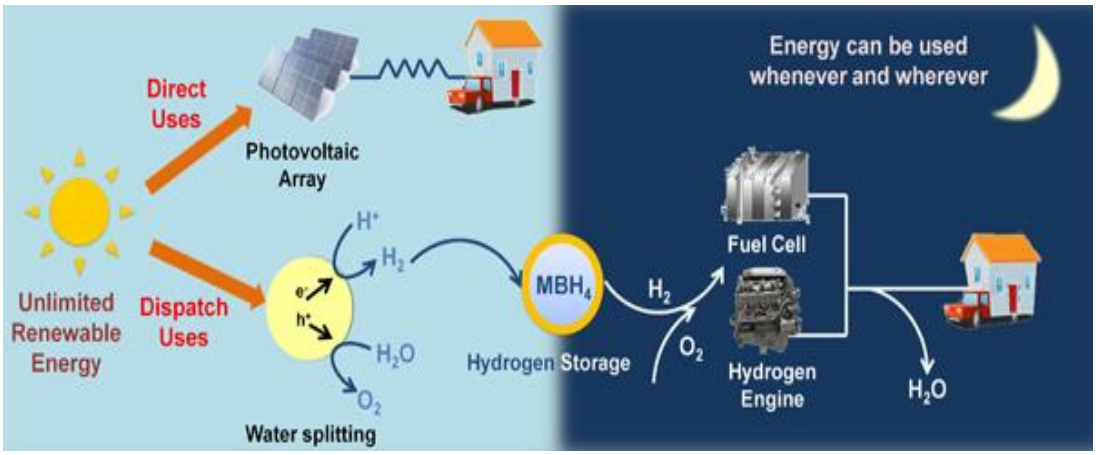

Figure 1.2. The hydrogen energy cycle [28].

However, limitations to large scale hydrogen production has been detrimental to the development of hydrogen fuel economy. Typically, hydrogen is produced from catalytic steam reformation of methane, catalytic decomposition of natural gas, gasification of coal, partial oxidation of crude oil, all of which results in depletion of fossil fuel reserves. Hydrogen can also be produced from nuclear electricity and water electrolysis [27]. The use of hydrogen as an energy carrier has a number of advantages, such as (a) Hydrogen is in water which is abundant in nature [1] and can be produced using either renewable or non-renewable sources [29], (b) can be used as a fuel in both fuel cells and internal combustion engines [10], (c) has high gravimetric energy density i.e. up to three times larger than liquid hydrocarbon-based fuels [6, 30] (d) has a small environmental footprint, since the only product of its oxidation is water [8, 14]. Hydrogen supply and demand is shown in Figure 1.3.

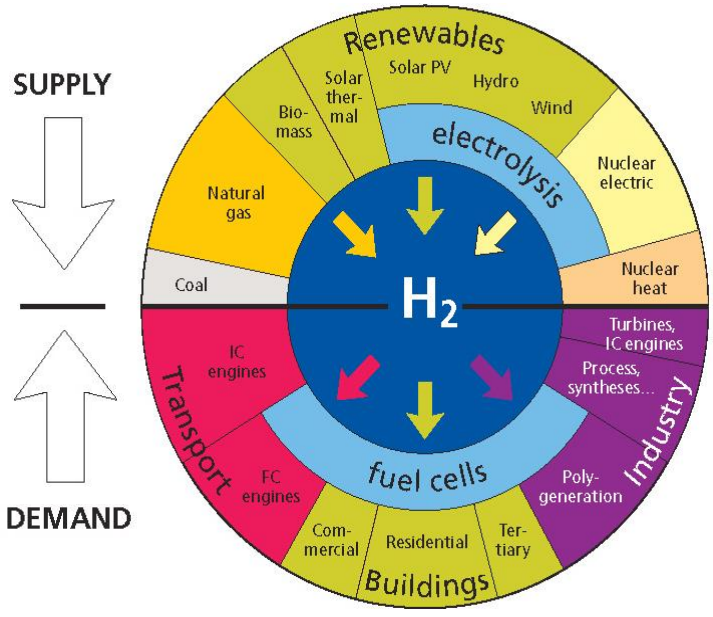

Figure 1.3. Hydrogen supply vs demand [31].

However, using hydrogen as a fuel requires appropriate infrastructures and huge investments. A more feasible scenario for tackling the energy problem concerns the employment of water electrolysis for the production of synthetic fuels that can be used in the current infrastructures. Renewable energy sources will provide the electrons required for water splitting. In a parallel process, CO_2can be captured from large point sources and recycled with the utilization of the renewably produced hydrogen (reverse water– gas shift reaction) for the production of synthetic fuels [32]. Additionally, hydrogen can be also used as a reducing agent in several other catalytic processes in the petroleum and chemical industry, e.g. for the refining and upgrading of crude oil and for ammonia synthesis, respectively [1].

In 2015, the worldwide hydrogen production was around 50 Mt per year [1, 14, 29, 32–35] and was covered by fossil fuels used in the processes of steam reforming of natural gas, coal gasification and partial oxidation of hydrocarbons; however, this includes the concomitant production of CO_2. Within the vision for a sustainable future, several methods for renewable hydrogen production have been developed, other than water electrolysis, , such as biomass gasification, thermochemical water splitting and photoelectrochemical water splitting [29, 34]. Among them, the only mature technology for hydrogen production is through water electrolysis that is currently commercially available [34].

1.3. WATER ELECTROLYSIS

Water electrolysis technologies can play a vital role for the indirect storage of surplus renewable energy via the conversion of electricity to chemical energy [14]. Water

electrolysis is considered to be a promising approach which can resolve the looming energy and environmental crisis because it produces clean hydrogen with zero CO_2 emission [27, 36]. During water electrolysis, renewable energy can be used as the electricity source to split water into hydrogen and oxygen. The produced hydrogen can be either stored and used in the chemical industry or used for electricity generation through fuel cells or internal combustion engines with zero post-combustion pollutants [8]. Water splitting, a combination of two half-cell reactions: the hydrogen evolution reaction (HER) at cathode and oxygen evolution reaction (OER) at the anode can be utilized for on-demand production of hydrogen and oxygen gases. These gases can be stored or recombined and converted into electricity at the point of usage in a fuel cell, providing a promising and environmentally friendly pathway for conversion and storage of these clean renewable energy sources.Water electrolysis schematic has been illustrated in Figure 1.4.

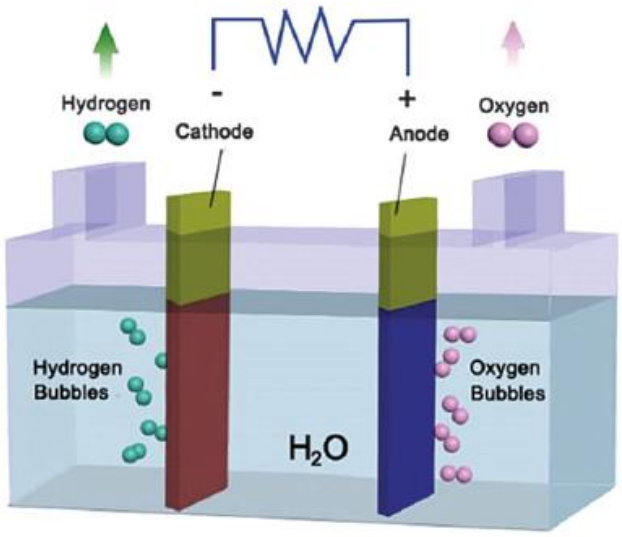

Figure 1.4. Schematics of water electrolysis [37].

Hydrogen production via water electrolysis using renewable energy sources amounts to only 4% of today's hydrogen production, mainly due to economic factors such as lack of widely available renewable energy systems of low cost, high capital cost and high energy input requirement [30]. This picture is going to change in the near future and increase in the use of renewable energy sources is expected, since the European Energy Directive has set the target for covering 14% of the energy needs by renewable energy sources by 2020. Hydrogen production by water electrolysis using renewable energy sources is expected to play a key role in the scenario of a green energy economy [14]. Clear advantages of this method is the high purity of the produced hydrogen, which is of great importance for its subsequent conversion to electricity using low temperature polymer electrolyte fuel cells [38]. Furthermore, high purity oxygen is a valuable by-product of water electrolysis. Its utilization both in medical care and in chemical industries in blast furnaces, electric furnaces, glass melting and gasification could lead to substantial decrease in the nominal cost of water electrolysis [39].

The full water splitting reaction is given below in Equation (1):

$$2H_2O_{(l)} \rightarrow 2H_{2\,(g)} + O_{2\,(g)} \qquad E°_{cell} = -1.23\ V \qquad (1)$$

This overall reaction consists of two half-cell reactions: OER, which is the oxidation reaction that happens at the anode, and the reduction reaction, HER, which occurs at the cathode. These half-cell reactions have different electron transformations during the process. There are 2 electrons involved in HER while 4 electrons are involved in OER. As a result, OER is a kinetically very sluggish reaction. In an alkaline medium, the two reactions can be given below in Equation (2) and (3):

	Low Temperature Electrolysis			High Temperature Electrolysis		
	Alkaline (OH^-) electrolysis		Proton Exchange (H^+) electrolysis	Oxygen ion(O^{2-}) electrolysis		
	Liquid	Polymer Electrolyte Membrane		Solid Oxide Electrolysis (SOE)		
	Conventional	Solid alkaline	H^+ - PEM	H^+ - SOE	O^{2-} - SOE	Co-electrolysis
Operation principles	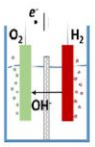	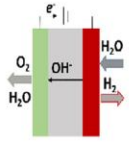	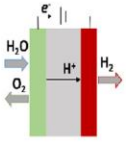	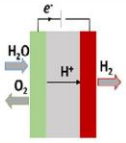	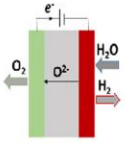	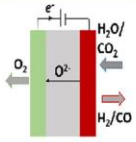
Charge carrier	OH^-	OH^-	H^+	H^+	O^{2-}	O^{2-}
Temperature	20-80°C	20-200°C	20-200°C	500-1000°C	500-1000°C	750-900°C
Electrolyte	liquid	solid (polymeric)	solid (polymeric)	solid (ceramic)	solid (ceramic)	solid (ceramic)
Anodic Reaction (OER)	$4OH^- \rightarrow 2H_2O + O_2 + 4e^-$	$4OH^- \rightarrow 2H_2O + O_2 + 4e^-$	$2H_2O \rightarrow 4H^+ + O_2 + 4e^-$	$2H_2O \rightarrow 4H^+ + 4e^- + O_2$	$O^{2-} \rightarrow {}^1/_2O_2 + 2e^-$	$O^{2-} \rightarrow {}^1/_2O_2 + 2e^-$
Anodes	Ni > Co > Fe (oxides) Perovskites: $Ba_{0.5}Sr_{0.5}Co_{0.8}Fe_{0.2}O_{3-\delta}$, $LaCoO_3$	Ni-based	IrO_2, RuO_2, $Ir_xRu_{1-x}O_2$ Supports: TiO_2, ITO, TiC	Perovskites with protonic-electronic conductivity	$La_xSr_{1-x}MnO_3$ + Y-Stabilized ZrO_2 (LSM-YSZ)	$La_xSr_{1-x}MnO_3$ + Y-Stabilized ZrO_2 (LSM-YSZ)
Cathodic Reaction (HER)	$4H_2O + 4e^- \rightarrow 4OH^- + 2H_2$	$2H_2O + 4e^- \rightarrow 4OH^- + 2H_2$	$4H^+ + 4e^- \rightarrow 2H_2$	$4H^+ + 4e^- \rightarrow 2H_2$	$H_2O + 2e^- \rightarrow H_2 + O^{2-}$	$H_2O + 2e^- \rightarrow H_2 + O^{2-}$ $CO_2 + 2e^- \rightarrow CO + O^{2-}$
Cathodes	Ni alloys	Ni, Ni-Fe, $NiFe_2O_4$	Pt/C MoS_2	Ni-cermets	Ni-YSZ Subst. $LaCrO_3$	Ni-YSZ perovskites
Efficiency	59-70%		65-82%	up to 100%	up to 100%	-
Applicability	commercial	laboratory scale	near-term commercialization	laboratory scale	demonstration	laboratory scale
Advantages	low capital cost, relatively stable, mature technology	combination of alkaline and H^+-PEM electrolysis	compact design, fast response/start-up, high-purity H_2	enhanced kinetics, thermodynamics: lower energy demands, low capital cost		+ direct production of syngas
Disadvantages	corrosive electrolyte, gas permeation, slow dynamics	low OH^- conductivity in polymeric membranes	high cost polymeric membranes; acidic: noble metals	mechanically unstable electrodes (cracking), safety issues: improper sealing		
Challenges	Improve durability/reliability; and Oxygen Evolution	Improve electrolyte	Reduce noble-metal utilization	microstructural changes in the electrodes: delamination, blocking of TPBs, passivation		C deposition, microstructural change electrodes

Figure 1.5. The main electrolysis technologies [40].

$$\text{HER: } 4H_2O_{(l)} + 4e^- \rightarrow 2H_{2(g)} + 4OH^-_{(aq)} \quad E° = 0.00 \text{ V vs RHE} \tag{2}$$

$$\text{OER: } 4OH^-_{(aq)} \rightarrow 2H_2O_{(l)} + O_{2(g)} + 4e^- \quad E° = 1.23 \text{ V vs RHE} \tag{3}$$

where, E° is the standard thermodynamic potential (under standard conditions of 273.15 K and an absolute pressure of 101.325 kPa) and RHE is reversible hydrogen electrode. Water electrolysis has been identified as one of the most utilized industrial processes and it can be classified as several categories depending on electrolyte and the operation temperature [40]. Different types of water electrolysis technologies and their pros and cons are given in Figure 1.5. In alkaline electrolyzers, potassium hydroxide is the most

commonly used liquid electrolyte and anode and cathode are immersed in the electrolyte. Water electolysis requires a larger thermodynamic potential due to some kinetic barriers happening at both HER and OER sides [41]. This higher energy barrier of the water splitting reaction is shown in Figure 1.6.

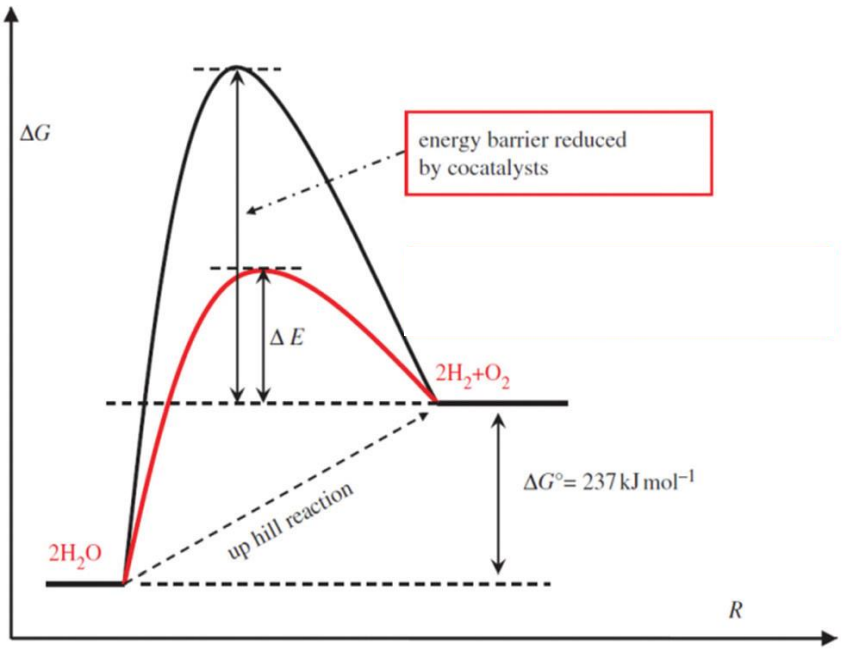

Figure 1.6. Energy diagram for catalytic water splitting [49].

Water electrolysis requires a larger thermodynamic potential due to some kinetic barriers for both HER and OER processes [41]. This higher energy barrier of the water-splitting reaction is shown in Figure 1.6. Water splitting is an uphill reaction and as a result, it is a non-spontaneous process. This large thermodynamic potential can be overcome by decorating the surface of the electrode with some active catalytic materials which reduce the energy barrier of the reaction. Several catalysts are normally used to

expedite this inherently sluggish water oxidation process by reducing the energy barrier at the respective electrode and by increasing the rate of conversion [36, 42-48].

The mechanism of OER is not yet fully understood. Since it has complex reactions which require high overpotentials (usually at least 0.4 V), OER is the most difficult reaction in an electrochemical cell, so that the cell voltage is governed by that of the anodic half-reaction and is typically an electron-intensive energy-demanding step, requiring 4 proton-coupled electron transfers (PCET) and O=O bond formation [50, 51]. In each step, an accumulation of the energy barrier is produced and leads to the sluggish kinetics of OER with large overpotential. The proposed mechanism for OER is given below in Equations (4) to (10):

$$S^* + OH^- \rightarrow S^*(OH^-)_{ads} \quad (4)$$

$$S^*(OH^-)_{ads} \rightarrow S^*(OH^-)_{ads} + e \quad (5)$$

$$S^*(OH^-)_{ads} + OH^- \rightarrow S^*O^-_{ads} + H_2O \quad (6)$$

$$S^*O^-_{ads} \rightarrow S^*O_{ads} + e \quad (7)$$

$$S^*O_{ads} + OH^- \rightarrow S^*OOH_{ads} + e \quad (8)$$

$$S^*OOH_{ads} + OH^- \rightarrow S^*O_{2\,(ads)} + H_2O + e \quad (9)$$

$$S^*O_{2\,(ads)} + OH^- \rightarrow O_2 + S^*(OH^-)_{ads} \quad (10)$$

where *S** refers to the catalytically active site in the anodic catalyst. From the proposed mechanism above, the reaction is initiated by the attachment of the hydroxyl group (-OH) to *S** which can be facilitated by local oxidation of the metal center. Since the hydroxyl and the oxide groups adhere to the surface at the initiation of the process, so the metal oxides, hydroxides and oxyhydroxides could form the most active catalyst. Therefore, any factor that can modify the oxidation potential of the catalytically active surface site,

should affect the catalytic activity. One feasible way to change the oxidation potential of the metal site is by replacing the ligand which adjusts the chemical potential. The primary considerations for designing an efficient OER catalyst includes long term stability under corrosive conditions of oxygen evolution, low cost, and widely available materials together with a low overpotential [36, 47,52].

1.4. CATALYSTS

Catalysts are materials that enhance the rate of the chemical reaction. Catalysts are typically not consumed in the chemical conversion, and only a small amount of material is required which is regenerated and reused during the reaction. The chemical reactions involved with the electrical charge transfer from the molecule to the molecule can occur effectively and efficiently when the chemical reaction and charge transfer rate is high [53]. Using a catalyst can effectively maximize the efficiency of the chemical transformations; generally, catalysts actively involve and facilitate both chemical reaction as well as charge transfer rate. The method of catalyst involvement, utilization, and the form of catalysts that participate in the reaction are dependent on the chemical reaction [53]. Having a catalyst is the key consideration for these systems to get maximum efficiency and productivity of the chemical transformation. Three different types of catalysts: photocatalysts, photoelectrocatalysts, and electrocatalysts are typically utilized in the water electrolysis reaction to generate oxygen and hydrogen gasses from water. Types of catalysts depend on the sort of energy source that is involved in the chemical transformation. This research work is mainly focused on electrocatalysts.

1.4.1. Electrocatalysts. An electrocatalyst is a material that enhances charge transfer in electrochemical reactions which consists of electron transfer oxidation or reduction reactions. Electrocatalysts are also defined as heterogeneous catalysts of electrochemical reactions that happen at the electrode-electrolyte interface and where the electrode plays a crucial role in electron acceptors and donors. In addition, they are specific forms of catalysts which have a function at the electrode surface. These catalysts are specifically used in different industrial and energy-related applications. In industry, electrocatalysts are used for electroplating, electro galvanizing, and electrowinning processes. Electrocatalysts are typically used to increase the efficiency and effectiveness of the electrochemical reactions of OER and HER in water electrolysis processes. Specifically, in water electrolysis, anodic and cathodic catalysts are typically used to reduce the overpotential for OER and HER and increase output current density. Figure 1.7 illustrates the energy conversion applications for earth-abundant inorganic electrocatalysts [53]. Most of these electrocatalysts are synthesized from earth-abundant transition metals which are indicated in red in the periodic table. The green elements in the periodic table belong to the non-metal elements. Both transition metal and main group elements have been utilized for synthesizing earth-abundant inorganic electrocatalysts for energy conversion reactions. To date some of the most efficient and robust OER catalysts in the acidic or alkaline medium are based on precious metal oxides like $IrO_2$and $RuO_2$for OER [46, 54-56] while Pt/C is used for HER[46, 56]. However, these precious metal oxides are not the most economically viable options for these catalytic processes based on cost considerations and scarcity of raw materials [57-59].

Figure 1.8. illustrates the abundance of chemical elements on the earth's crust. [60] It is highly desirable to explore low-cost, efficient, and stable catalysts designed from earth-abundant metals for catalytic water splitting. As a result of an incessant search

for efficient OER catalysts from earth-abundant non-precious metals, researchers have identified several transition metal based oxides as efficient OER catalysts with low η, some of them being comparable with the $IrO_2$and RuO_2catalysts [46, 54-56].

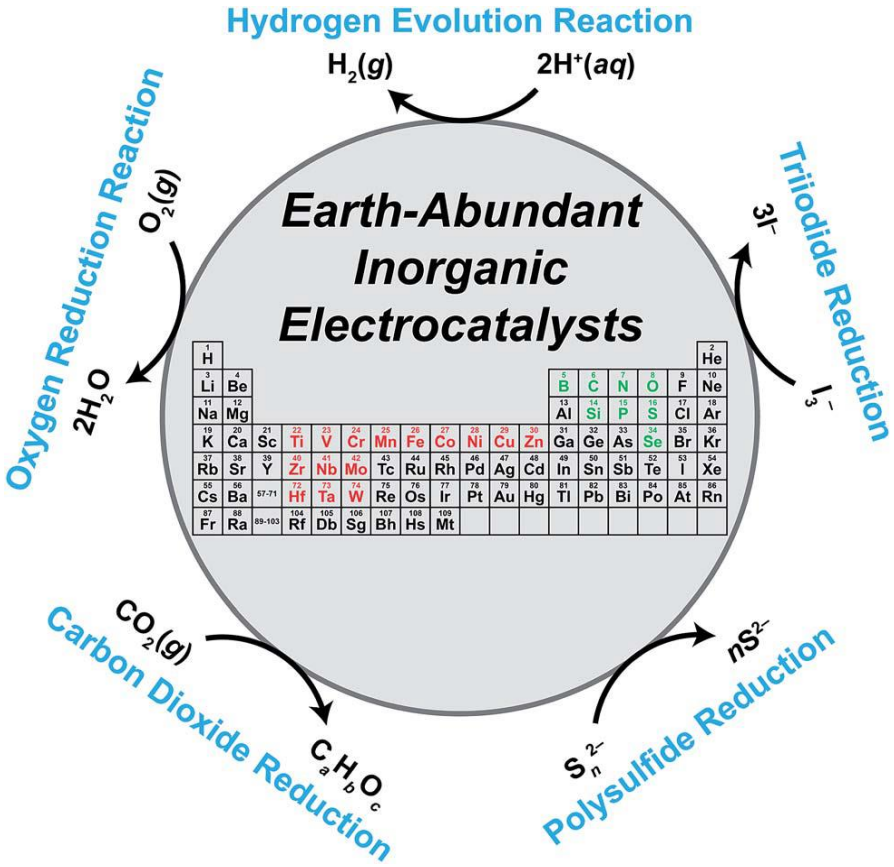

Figure 1.7. The schematic of some earth abundant inorganic electrocatalysts [53].

A closer insight into the mechanism of OER, specifically, adsorption and desorption of intermediates during the reaction revealed that the reaction involved -OH as a primary intermediate and adsorbate and includes bond formation and bond breakage between such reaction intermediates and the electrode surface. Therefore, optimizing the bond strength between active sites and adsorbed -OH intermediate could influence the

activation energy for electrochemical reaction. The adsorption of -OH intermediates on the surface is accompanied by local oxidation of the active site to a higher oxidation state. To mediate the adsorption and desorption of the catalyst surface, the catalyst should be able to change rapidly between lower and higher oxidation states. This can be quantified by the enthalpy of formation (ΔH_{f0}) from a lower to a higher oxidation state in the material [61].

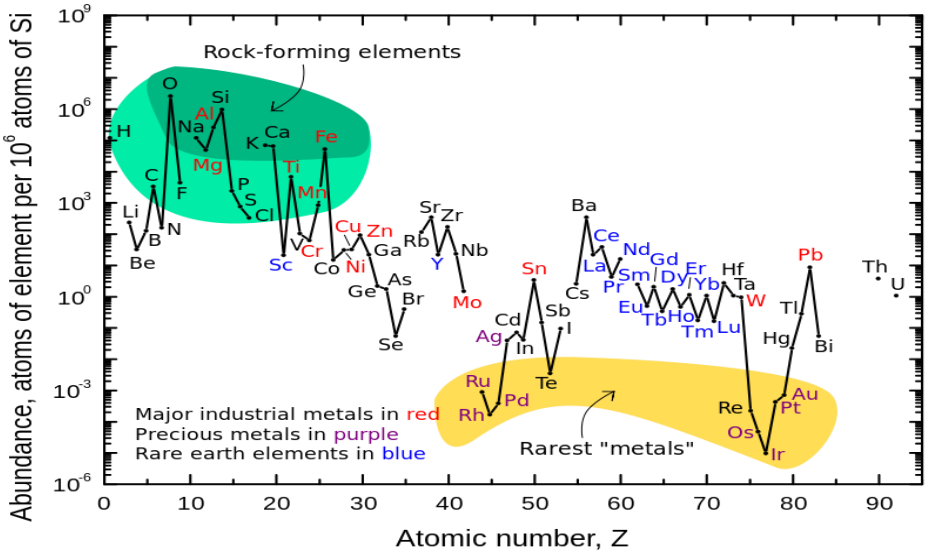

Figure 1.8. Abundance of elements on the earth's crust [60].

Plotting the electrocatalytic activity as a function of ΔH_{f0} for different materials results in a volcano relations plot for different metal oxides is shown in Figure 1.9 [61]. As can be seen from the following plot, materials possessing intermediate enthalpies display the highest catalytic activities. The catalytic activity on the vertical axis is typically represented as negative of the overpotential or the current at a given

overpotential. In Figure 1.9., the left side of the plot are materials with a small tendency to be oxidized to a higher valence state, minimizing the adsorption of the intermediates and thus results in higher overpotentials. Whereas the materials to the right are oxidized easily, binding intermediates too strongly due to very high ΔH_f of formation and hinders desorption of the products, thus becoming catalytically inactive. RuO_2 and IrO_2 are found at the top of the peak which demonstrates the high activity of these materials for the OER in acidic media [62].

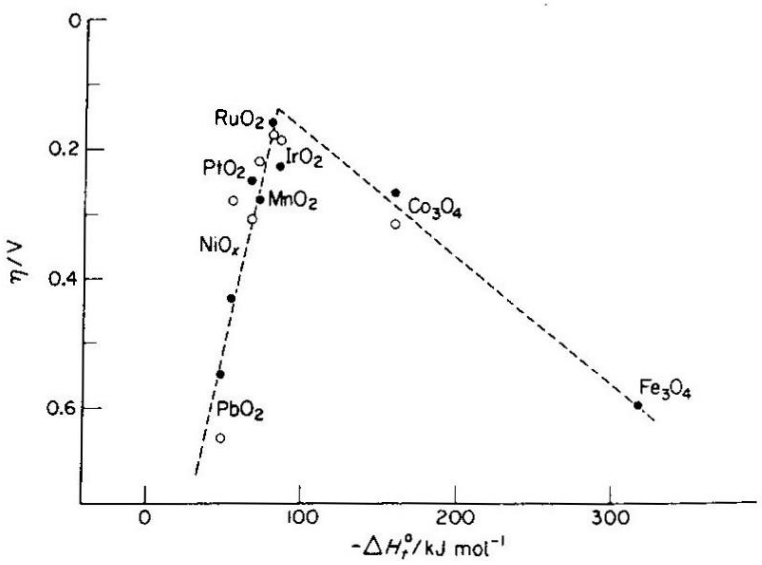

Figure 1.9. Volcano plot of the oxide catalysts for OER electrocatalytic activity [61].

1.4.2. How to Design Efficient Electrocatalysts? Designing an efficient electrocatalyst is a challenging phenomenon since it should be developed from earth-abundant, readily available, cost-effective, environmentally friendly, highly active, and stable materials. The practical concerns for the development of efficient and highly active electrocatalyst also considers their stability and functionality in acidic or alkaline of the

electrolyte environment as well as the operating temperature of the electrolyte.Designing efficient OER catalysts are not a straightforward task for the following reasons [40,63-65]: (1) thermodynamic potential for the oxidation of water should be slightly below the oxidation potential of the designed catalyst,low intrinsic overpotential for the desired reactions of OER and HER; (2) for less-energy intermediates, coupling of the catalyst local site oxidation should simultaneously take place with proton transfer, followed by fast O−O the bond formation, high electrical conductivity; (3) a high rate of catalytic reaction,high the active surface which facilitates both good accessibilities to the reactants and sufficiently fast removal of products of gases, liquids, and ions; (4) the catalyst is not susceptible to oxidative damage at OER potentials (corrosion), better compatibility with the electrolyte and the temperature and (5) the catalyst should operate at extreme conditions of acidity and alkalinity. To date, catalyst compositions meeting all these requirements has been rarely achieved.

1.4.3. Transition Metal Catalysts. Continuous quest over the last few years has led to the replacement of the noble metal catalysts with the transition metal catalysts in energy conversion processes attributed to their higher intrinsic activity and stability. The last few years have witnessed the discovery of several transition metal based OER and HER electrocatalysts, especially those containing Ni, Co, Fe, Mo, W, and Cu transition metals. Transition metals have remarkable catalytic activity toward the energy conversion reactions due to their partially filled d orbitals, different number of accessible oxidation states, ability to form complexes and easily gain electrons from reagents or give electrons to the reagents depending on the nature of the reaction. These metals can rapidly form the transition metal anionic complex during the reaction and that complex remarkably

catalyzes the chemical reaction more effectively than the noble metal catalysts [66]. Replacing noble precious metals using the transition metal is a great achievement in the electrocatalytic field. The transition metal electrocatalysts for HER in alkaline [67] and acidic [68] electrolyte has facilitated the creation of state-of-the-art earth-abundant inorganic electrocatalysts. The electrocatalytic activity of these transition metal electrodes were determined from the overpotential at a standard current density of 10 mA cm^{-2}, exchange current density, the work function of the transition metals, and the onset potential in both alkaline and acidic media [67,68]. Figure 1.10 shows the transition metal elements and the substrates that have been used to synthesize the electrocatalysts for water splitting process [69].

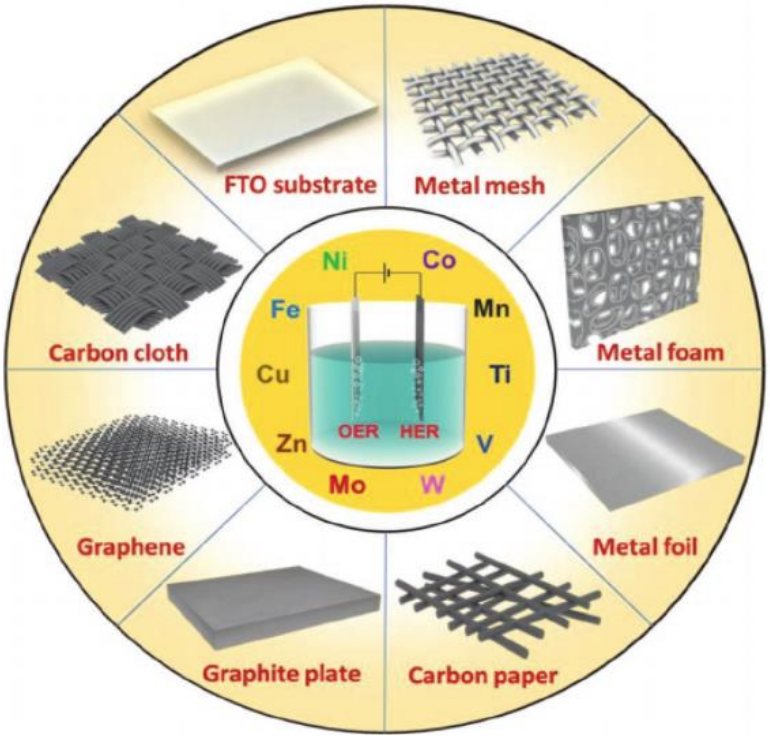

Figure 1.10. Transition metals and substrates used to synthesize electrocatalysts [69].

In addition, the correlation between physical properties of the transition metal electrodes and the rate of HER is also another factor for higher catalytic performance [70]. Electronic properties of the catalytic material also affects the electrocatalytic activity and can in turn be used to predict the trend of the intrinsic catalytic activity of these materials. These trends of electrocatalytic activity in energy conversion processes have been used to design highly active electrocatalysts using transition metals and their alloys.

1.4.4. Transition Metals and Their Alloys. Using a transition metal alloys or multimetallic electrodes could improve the catalytic activity of hydrogen generation through water electrolysis [53]. The synergistic effect of combining transition metals could improve the catalytic performance through the cooperative interactions between the metal sites as well as hydrogen affinity to the surface active sites improves surface activity of these electrocatalysts [71-74]. The aim of alloying of transition metals is to tune the d-band electron filling, Fermi level energy, interatomic spacing and all these could impact the affinity of the alloy electrodes toward the adsorbate species of interests [75]. These are some the transition metal alloys that have higher catalytic activity; Ni-Mo alloys show the outstanding HER activity towards the HER in the alkaline conditions [76,77], the other transition metal alloys of Ni-W, Ni-Fe, Ni-V, Fe-Mo and Co-Mo also shows better activity toward the HER in alkaline medium. Remarkably these catalytic films retain their performance for about a year for continuous HER process in the alkaline medium without decay [78,79]. In addition, to the binary alloys, researchers have also investigated ternary alloys as electrocatalysts for water splitting reactions. Ternary transition metal alloys of Ni-Mo-Cd [80] and different combinations of ternary Ni-Mo

alloys which contain Co, W, Fe, Zn, Cr and Cu have shown better HER electrocatalytic performance in alkaline medium [81]. In addition, bimetallic [82,83] and trimetallic [84] alloys of IrCu based electrocatalysts and Ir-based Co, Ni, W and Fe doped alloys [84-87] also performed well in OER reactions for both acid and alkaline conditions.

1.4.5. Transition Metal Oxides. Even though transition metal oxides are used as industrial catalysts, they are not widely used as electrocatalysts for energy conversion through water splitting process [88]. Transition metal oxides are poor electrical conductors and they have low chemical stability especially in acidic medium [89]. Nevertheless, researchers have been working with several transition metal oxide as electrocatalysts for OER and HER in water splitting due to their high abundance, low cost and substantial anti-corrosion ability in the alkaline medium [90]. Spinel type oxides (AB_2O_4), inverse spinel oxides $B(AB)O_4$, perovskite (ABO_3) and Metal oxides (MO_2) are different forms of transition metal oxides that have been reported as electrocatalysts. In transition metals spinel type oxides of AB_2O_4, *A* and *B* are 3d transition metals of Co, Ni, Cu, Zn, Mn and Fe. They are composite oxides which show better catalytic performance as electrocatalysts [91-93]. 3D porous $CoFe_2O_4$ nanorod arrays grown on Ni-form have shown better catalytic performance for OER [94]. Similarly, spinel type bimetallic oxides of $NiCo_2O_4$/CC nanowall arrays [95] and $NiFe_2O_4$/NF nanosheets [96] also show the higher performance in OER reaction. The metal oxides of MO_2 also have been studied as better OER catalysts. Synthesis of different kinds of porous nanostructures grows on vivid conductive substrates as

Ni- form, carbon fiber paper, foils and sheets, and doping different cations with these metal oxides are different strategies to increase the catalytic performance. MoO_2 transition metal oxides have been extensively studied as OER catalysts [97,98]. MoO_2 shows better catalytic performance due to its intrinsic property of higher conductivity and having most abundant active sites in porous nanostructured morphology [97,98]. MnO_2 is also active catalytic material for OER but it is inundated by its higher overpotential and low conductivity of the materials. These issues were addressed by engineering Mn/O vacancies as well as V, Fe, Ni and Co cations doping [99]. In addition, different kinds of perovskite oxides materials of Sr_2CoIrO_6 [100], $Sr_2Fe_{0.5}Ir_{0.5}O_4$ [100] also found as efficient OER catalysts in acidic medium and $Ba_{0.5}$ $Sr_{0.5}$ $Co_{0.8}Fe_{0.2}O_{3-\delta}$ [101] shows a better OER catalytic performance in alkaline medium.

These perovskite structures have been created combining different transition metals elements and their vivid physical and electronic properties have been engineered together to provide a better catalytic performance for OER in energy conversion applications. In HER applications, $SrNb_{0.1}Co_{0.7}Fe_{0.2}O_{3-\delta}$ perovskite nanorods exhibits higher catalytic performance and stability in basic medium due to the unique structural characteristics and the catalytic features of perovskite materials [102]. Similarly, $Pr_{0.5}(Ba_{0.5}Sr_{0.5})_{0.5}Co_{0.8}Fe_{0.2}O_{3-\delta}$ perovskite nanosized nonprecious electrocatalysts was found with a superior HER activity and stability in basic medium due to modified electronic properties and structures

induced by doping Pr [103]. Ni and Co oxide catalytic materials have been investigated as better catalysts for HER process tuning by attaching an N- doped reduced graphene oxides and their dominant transition metals of Ni and Co. Both of these transition metal oxides catalysts are demonstrated as better electrocatalysts for HER in the energy conversion process in alkaline medium [104]. Also, different phases of oxides, hydroxides and (oxy)hydroxides of 3d transition metals of Ni, Fe, Co and Mn have been studied as electrocatalysts for the energy conversion process of OER and HER [105-107].

1.4.6. Transition Metal Phosphides, Nitrides and Carbides. Transition metal phosphides (TMPs) are another family of electrocatalysts that researchers have been working on for OER and HER in acidic, alkaline and neutral electrolytes. TMPs are better catalysts due to its suitable d-electron configuration, rich chemical states and similar zero-valent metallic characteristics as well as the phosphate centers were investigated as active sites for OER [108-110]. Interestingly, these TMPs active sites have been found in the bulk form. Density functional theory (DFT) of binary TMPs predicted that their catalytic activity is intrinsic property due to the hydrogen adsorption free energy is not too strong or not too weak [111]. TMPs have been identified as bifunctional electrocatalytic performance for water splitting but they have some drawbacks due to less number of active sites, poor conductivity, higher overpotential and less anti corrosion resistance in strong alkaline medium [112]. Consequently, scientists have made

various efforts to solve these shortcomes, such as cation and anion doping into the TMPs optimize the electronic structure as well as improve the catalytic activity and the self-supported TMPs nanostructures grown on conductive 3D substrates have been widely studied. Ni_2P has been studied as an alternative for Pt electrocatalysts in HER due to its higher intrinsic catalytic activity, higher conductivity, higher thermostability and material cost effectiveness [113]. CoP, FeP, Cu_3P, MoP have been found as earth-abundant transition metal Phosphides for HER [114].

Transition metal carbides (TMCs) and nitrides (TMNs) have been widely exploited as an alternative Pt electrocatalysts due to their Pt like electronic behavior, desirable attributes of corrosion resistance, higher electrical conductivity, mechanical strength and significant stability in acidic and basic conditions [111]. As a result, TMCs and TMNs are suggested as long lifetime electrocatalysts. TMCs are synthesized from a carbonization process which consists of agglomeration and sintering of the catalysts in higher temperatures. Researchers have been doing many effective strategies of assembling self-supported electrodes and doping some cations to improve the catalytic performance of TMCs as electrocatalysts for OER and HER. Bulk and nanostructures of Mo_2C, their different phases (MoC & Mo_2C) and various morphologies of Mo_2C [115-117], various phases of tungsten carbides and metal rich carbides (WC, W_2C) [118] and bifunctional hybrid electrocatalyst of

$Ni_3ZnC_{0.7}$ nanodots [119] also shown as higher electrocatalysts for HER and OER in acidic and alkaline medium.

TMNs also showed lower HER catalytic performance compared to TMCs due to their chemical, electronic and physical properties. TMNs have higher metallic conductivity due to the N atoms in nitride which could increase the d-electron density and d-band contraction of the TMNs electronic structure similar to the precious metal catalysts [120]. TMNs are considered better electrocatalysts for water splitting in acidic medium due to its higher intrinsic metallic characteristic and higher corrosion resistance. Researchers have been working on in situ growth on self-supported conductive substrates, producing nano morphologies. Cation doping into TMNs was able to provide better catalytic performance toward the HER in the energy conservation process. Vanadium doped Co_4N (V-Co_4N) nanosheets exhibited greater HER activity [121], 3d porous NiMoN/CC has been identified as effective HER electrocatalysts due to its, synergistic effect of Ni-Mo-N, facile mass transport, fast electron transfer, and high roughness factor of the electrocatalysts [122]. In addition, hydrothermally synthesized Ni_3N-NiMoN heterostructures on carbon cloth exhibit superior performance for HER and OER in overall water splitting [123].

1.4.7. Transition Metal Chalcogenides. The bifunctional electrocatalysts are always limited by the activity, poor conductivity and the stability. As a result, researchers have been working with chalcogenides comprising sulphides, selenides and tellurides which have shown unprecedented high catalytic activity, some of which even surpass that of the corresponding oxides, phosphides, nitrides and carbides. Indeed, the trend in catalytic activity between the oxides and the rest of the chalcogenide series (sulfides,

selenides, and tellurides) can be best explained through the gradual change in their electronic band structure and alignment of the valence and conduction band edges with the water oxidation–reduction levels [124-125] which is illustrated in Figure 1.11. [124].

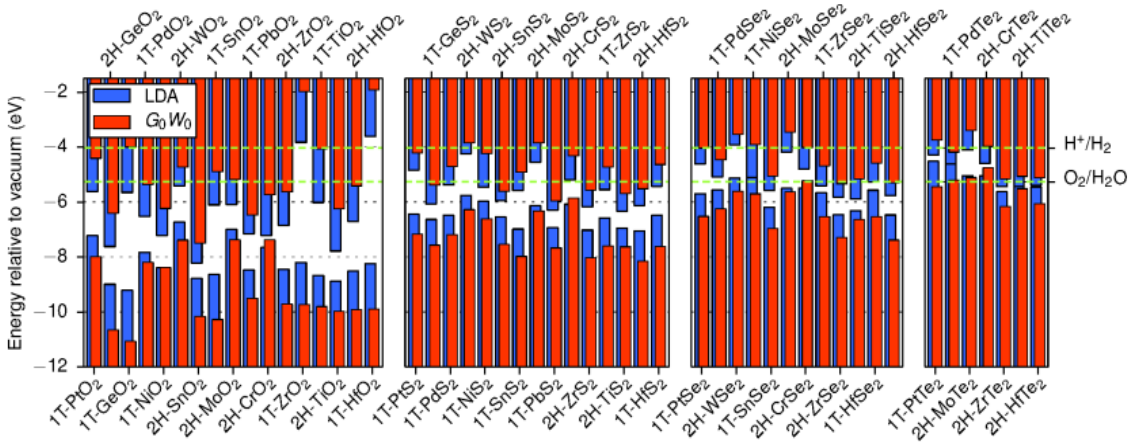

Figure 1.11. Position of the valence band maximum and conduction band minimum relative to the vacuum level in chalcogenides [124].

As the electronegativity of the chalcogen atom decreases down the series, the degree of covalency in the metal–chalcogen bond increases. Based on previous research which has shown that OER catalytic efficiency is enhanced by a higher degree of covalency in the metal–anion bonding, [126] it can be expected that catalytic efficiency will increase in the chalcogenide series from oxide to telluride. In accordance with this hypothesis, it has been observed that among the Ni-based binary chalcogenides, nickel selenides exhibit some of the best catalytic efficiencies [126-130]. Since the electronegativity of Te (2.1) is lower than that of Se (2.55), the degree of covalency in nickel tellurides will be even higher than that in the selenides. In fact, qualitative band structure analysis has confirmed that tellurides indeed have better band alignment with

the water oxidation levels compared to the selenides [124,125]. Hence, we propose that transition metal tellurides will be even better OER electrocatalysts than the transition metal selenides. There are several transition metal tellurides that are claimed as excellent bifunctional electrocatalysts for the water splitting process [131-134].

Apart from band structure considerations, this hypothesis is also based on the change of the chemical potential of the catalytically active metal site as a function of anion composition. For example, in all of these Ni-based OER electrocatalysts, the catalytic Ni site is activated by a pre-oxidation step which converts $Ni^{2+}$to Ni^{3+}. This pre-oxidation step is influenced by the coordination of the environment around the Ni atom, and it has been shown previously in coordination complexes that by changing the coordination from sulfide to selenide, i.e. decreasing the electronegativity, the oxidation peak can be moved to more cathodic potentials [135, 136]. Since metal oxidation plays a pivotal role in the catalytic process, it can be envisioned that lowering the oxidation potential through increasing the covalency in the coordination environment will have a positive influence on lowering the onset potential for the OER, thereby increasing the catalytic efficiency.

The promising water splitting activities of platinum group free metal (PGM-free) based catalysts [42,47] motivated us to investigate a new family of transition metal telluride and selenide-based catalysts for water electrolysis, and several requirements have been considered to enhance the catalytic performance. The major requirements for designing these catalysts were as follows; 1) increasing covalency in the metal-anion bond, 2) high active surface area, 3) attempting directional growth, 4) doping in the metal and anion sites, 5) introduction of layer-by-layer strategies 6) achieving long-term

mechanical and chemical stability, and 7) materials availability and low-cost fabrication methods.

1.5. CHALLENGES FACING ELECTROCATALYSTS

The earth-abundant transition metal electrocatalysts have been found as an alternative solution for the precious metal electrocatalysts for the water electrolysis process. But these transition metal-based electrocatalysts have several challenges that need to be addressed and improved for successful implementation of electrocatalysts in practical devices. The first challenge is the desirable level of intrinsic electrocatalytic activity. The catalytic materials with higher intrinsic activity as a property of material will be favorably chosen for electrocatalysts. In addition, there are many strategies that have been applied to enhance the electrocatalytic performance for water electrolysis. The second challenge is that electrocatalysts should be stable under the operational conditions for a prolonged duration without deterioration of catalyst performance. Generally, electrocatalyst stability has been examined for a long time under a continuous operational environment. In these stability experiments, the constant electrical potential has been applied to drive the catalytic reaction for a long time period. Peripheral processes such as catalyst oxidation, corrosion, and catalyst poisoning or leaching of the catalysts are expected to lead to loss of catalytic performance and degradation of the current response over time. In addition, electrocatalysts should be highly stable in the electrolyte without any applied potential or under the reversible current of the electrolysis condition. The interesting fact about the earth-abundant transition metal electrocatalysts is that they can be easily regenerated and replaced and should be able to operate continuously with

minimal decay of the catalytic performance. Also, ideal transition metal-based electrocatalysts have higher electrical conductivity, and higher current density at a low overpotential, fast charge transportation, and low Ohmic losses under the operating conditions. It is very important that transition metal electrocatalysts should have higher chemical compatibility with the electrolysis operating environment and should not get poisoned, contaminated, or degraded thereby forming other compositions in the electrochemical system. An ideal transition metal electrocatalyst should be also widely and readily available, showing higher catalytic performance towards the water splitting process, have high stability for a long period, and widely applicable as an electrocatalyst for various energy conversion processes.

1.6. STATERGIES FOR ENHANCING ELECTOCATALYTIC PERFORMANCE

The performance metrics that researchers have focused on to increase in electrocatalysts are higher current density, faster kinetics of the reactions, higher charge and mass transfer rates, stability, lower onset potential and lower overpotential at specific current density. Researchers have been applying various strategies to boost the electrocatalytic performance of transition metal electrocatalysts for OER and HER in the water splitting process. The various strategies belong to the different fields of chemical, physical, mechanical and engineering. All these efforts in numerous fields are aimed to improve and increase the catalytic performance of the water electrolysis toward the interest of reduction and oxidation processes or available number of active sites. By optimizing these two factors at the highest possible level, transition metal electrocatalysts can become excellent catalysts for the electrocatalytic water splitting process. Also these

factors can be applied during catalyst synthesis or through post-synthetic processes. Following section describes some of the commonly adapted strategies for increasing electrocatalytic performances.

Catalytic performance can be enhanced in two ways: increasing the number of active sites or increasing intrinsic activity. Synthesizing nano structures can enhance the number of active sites as well as the surface area of catalytic materials which boost the catalytic performance. Also increasing catalyst texture by hybridizing with conductive materials, creating rough surface area of the catalysts using dissolution, the direct growth of the catalytic materials on 3-D conductive substrates, introducing overlayer strategies and increasing catalysts loading are some of the treatments that increase the number of active sites on catalytic surface. The second attempt to enhance the catalytic performance is to increase the intrinsic activity of the catalytic materials. Variety of catalyst compositions, alloying, doping cations and anions and changing anion composition such as replacing oxide with selenides or tellurides are some of the common ways of increasing intrinsic activity of the catalyst.

PAPER

I. NICKEL TELLURIDE AS A BIFUNCTIONAL ELECTROCATALYST FOR EFFICIENT WATER SPLITTING IN ALKALINE MEDIUM

Journal of Materials Chemistry A, 6.17 (2018): 7608-7622

Umanga De Silva [a], Jahangir Masud [a], Ning Zhang [b], Yu Hong [b], Wipula P. R. Liyanage [a], Mohsen Asle Zaeem [b] and Manashi Nath *[a]

[a] Department of Chemistry, Missouri University of Science and Technology, Rolla, MO 65409, USA.

[b] Department of Materials Science & Engineering, Missouri University of Science & Technology, Rolla, MO 65409, USA

*Email: nathm@mst.edu

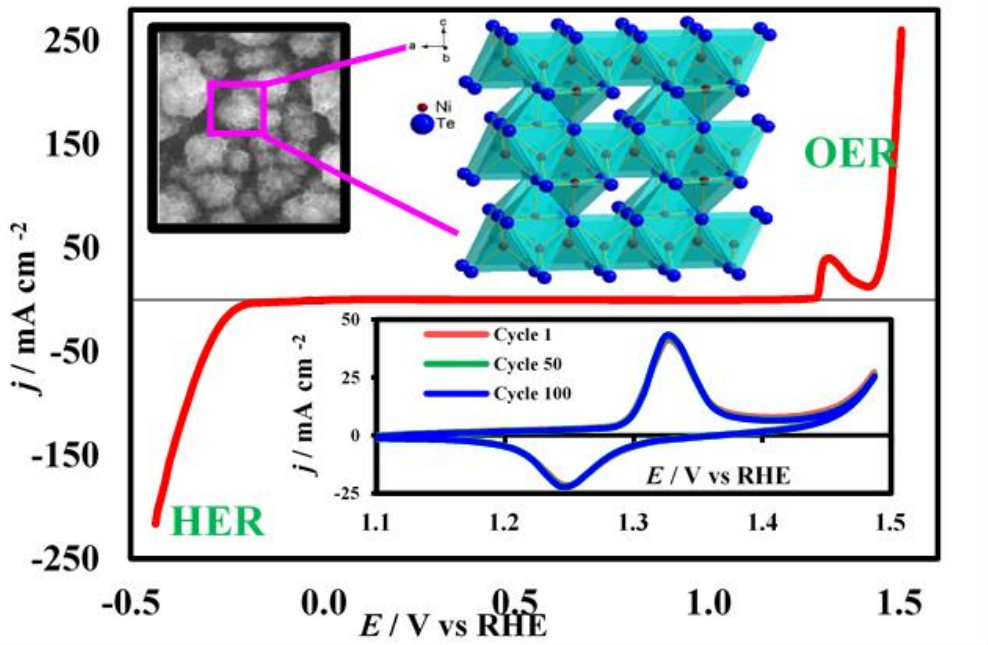

ABSTRACT

Designing efficient electrocatalysts has been one of the primary goals for water electrolysis, which is one of the most promising routes towards sustainable energy generation from renewable sources. In this article, we have tried to expand the family of transition metal chalcogenide based highly efficient OER electrocatalysts by investigating nickel telluride, Ni_3Te_2 as a catalyst for the first time. Interestingly Ni_3Te_2 electrodeposited on a GC electrode showed very low onset potential and overpotential at 10 mA cm^{-2} (180 mV), which is the lowest in the series of chalcogenides with similar stoichiometry, Ni_3E_2 (E = S, Se, Te) as well as Ni-oxides. This observation falls in line with the hypothesis that increasing the covalency around the transition metal center enhances catalytic activity. Such a hypothesis has been previously validated in oxide-based electrocatalysts by creating anion vacancies. However, this is the first instance where this hypothesis has been convincingly validated in the chalcogenide series. The operational stability of the Ni_3Te_2 electrocatalyst surface during the OER for an extended period of time in alkaline medium was confirmed through surface-sensitive analytical techniques such as XPS, as well as electrochemical methods which showed that the telluride surface did not undergo any corrosion, degradation, or compositional change. More importantly we have compared the catalyst activation step (Ni^{2+} / Ni^{3+} oxidation) in the chalcogenide series, through electrochemical cyclic voltammetry studies, and have shown that catalyst activation occurs at lower applied potential as the electronegativity of the anion decreases. From DFT calculations we have also shown that the hydroxyl attachment energy is more favorable on the Ni_3Te_2 surface compared to the Ni-oxide,

confirming the enhanced catalytic activity of the telluride. Ni_3Te_2 also exhibited efficient HER catalytic activity in alkaline medium making it a very effective bifunctional catalyst for full water splitting with a cell voltage of 1.66 V at 10 mA cm^{-2}. It should be noted here that this is the first report of OER and HER activity in the family of Ni-tellurides.

1. INTRODUCTION

The intensive search for sustainable alternative energy and clean fuel has intensified research activities in the energy sector.[1,2] Amongst the various technologies for alternative energy generation and storage, catalytic water splitting has been at the center of attention for decades.[3] Water electrolysis typically involves two half-cell reactions, the oxygen evolution reaction (OER) occurring at the anode and the hydrogen evolution reaction (HER) occurring at the cathode.[4] Among these the OER is a more challenging step involving an uphill complex proton-coupled electron transfer (PCET) reaction which leads to this step being kinetically sluggish and typically requires a high overpotential to get over the energy barrier.[5] Hence, anodic catalysts are typically used to reduce the overpotential for the OER and increase the output current density. Traditionally precious metal oxides such as RuO_2 and IrO_2 exemplify the most active catalysts for the OER in alkaline and acidic medium, respectively.[6,7] However, the scarcity and rising costs of the noble metals have led to the continuous quest for replacing these precious metals with earth abundant, non-precious metals without compromising catalytic efficiency. This quest has been rewarded over the last couple of years by the discovery of several transition metal based OER electrocatalysts, specifically those

containing Ni, Co, and Fe.[4,8–24] Although transition metal based OER electrocatalysts have been over-represented with oxides,[4,20,22,25] during the last couple of years sulfides[26–29] selenides[14,16,17,19,21,24,30–34] and pnictides[35–40] have shown unprecedented high catalytic activity, some of which even surpass that of the corresponding oxides. In fact, the trend in catalytic activity between the oxides and the rest of the chalcogenide series (sulfides, selenides, and tellurides) can be best explained through the gradual change in their electronic band structure and alignment of the valence and conduction band edges with the water oxidation–reduction levels.[41,42] As the electronegativity of the chalcogen atom decreases down the series, the degree of covalency in the metal–chalcogen bond increases. Based on previous research which has shown that OER catalytic efficiency is enhanced by a higher degree of covalency in the metal–anion bonding,[32] it can be expected that catalytic efficiency will increase in the chalcogenide series. In accordance with this hypothesis, it has been observed that among the Ni-based binary chalcogenides, nickel selenides exhibit some of the best catalytic efficiencies.[17,24,30–33] Since the electronegativity of Te (2.1) is lower than that of Se (2.55), the degree of covalency in nickel tellurides will be even higher than that in the selenides. In fact, qualitative band structure analysis has confirmed that tellurides indeed have better band alignment with the water oxidation levels compared to the selenides.[41,42] Hence, we propose that nickel tellurides will be even better OER electrocatalysts than the selenides. Apart from band structure considerations, this hypothesis is also based on the change of chemical potential of the catalytically active Ni site as a function of anion composition. In all of these Ni-based OER electrocatalysts, the catalytic Ni site is activated by a peroxidation step which converts Ni^{2+} to Ni^{3+}. This peroxidation step is influenced by the coordination

environment around the Ni atom and it has been shown previously in coordination complexes that by changing the coordination from sulfide to selenide, i.e. decreasing the electronegativity, the oxidation peak can be moved to more cathodic potentials. [43,44] Since the Ni oxidation plays a pivotal role in the catalytic process, it can be envisioned that lowering of the oxidation potential through increasing the covalency in the coordination environment will have a positive influence on lowering the onset potential for the OER, thereby increasing the catalytic efficiency. In this article, we have provided the first proof of this hypothesis by investigating the OER catalytic activity of Ni_3Te_2 in an alkaline electrolyte. Ni_3Te_2 was synthesized both by a hydrothermal technique as well as direct electrodeposition on the electrodes. Both hydrothermally synthesized as well as electrodeposited Ni_3Te_2 showed OER catalytic activity indicating that it was indeed an intrinsic property of the material. The electrodeposited Ni_3Te_2 exhibited high catalytic efficiency requiring a very low overpotential of only 180 mV to reach 10 mA cm^{-2}, which is one of the lowest overpotentials reported till date. This overpotential is also significantly lower than that required for nanostructured Ni_3Se_2 (190 mV)[31] and Ni_3S_2 (260 mV),[29] which proves the hypothesis that increasing the covalency in the chalcogenide series can indeed lead to better catalytic efficiency. Through DFT calculations we have also shown that the hydroxyl attachment to the Ni sites is energetically more favorable in Ni_3Te_2 than in NiO (NiOOH). The discovery of efficient catalytic activity in Ni tellurides along with the trend of increasing catalytic activity in the chalcogenide series provides valuable insights that will lead us to designing highly efficient electrocatalysts by optimizing the material properties.

2. EXPERIMENTAL SECTION

2.1. MATERIALS

All the chemicals used for the synthesis were of analytical grade and were used without further purification. All solutions were prepared using deionized water (DI: resistivity 18 MU cm). Nickel sulfate ($NiSO_4.6H_2O$) was purchased from Fisher Scientific, tellurium dioxide (TeO_2) and hydrazine hydrate ($N_2H_4.H_2O$, 100%) were purchased from Acros Organics. Au coated glass slides (Au-glass, hereafter) were bought from Deposition Research Lab Incorporated (DRLI), Lebanon, Missouri.

2.2. ELECTRODEPOSITION OF Ni_3Te_2

A conventional three-electrode system was used for the electrodeposition of Ni_3Te_2 films on different conducting substrates (e.g. Au-glass, GC (0.196 cm^2), Ni foam, carbon fiber paper, etc.). Ag|AgCl and Pt mesh were used as the reference and counter electrodes, respectively. Substrates were cleaned using Micro-90 detergent followed by sonication in a mixture of isopropanol, ethanol, and deionized water. The clean and air dried Au-glass substrates were masked with a scotch tape, leaving a circular exposed geometric area of known dimensions for the electrodeposition. Electrodeposition of Ni_3Te_2 films was carried out in an electrolytic bath containing 15 mM $NiSO_4.6H_2O$ and 3 mM TeO_2 maintained at 80 ºC. Dilute HCl was added to adjust the pH at 2.5. After mixing, the solution was purged for 30 minutes with N_2 gas to remove all dissolved O_2 from the electrochemical bath. An IviumStat potentiostat was used to deposit Ni_3Te_2

films at -1.05 V applied potential (vs. Ag|AgCl). After deposition the films were thoroughly washed with DI water to remove any adsorbents from the surface of the film.

2.3. HYDROTHERMAL SYNTHESIS OF Ni_3Te_2

In a typical synthesis, $NiSO_4.6H_2O$ (9.0 mM) was dissolved in 15.0 mL of deionized water under magnetic stirring to form a homogeneous solution. After mixing the solution for 10 min, TeO_2 (6.0 mM) was added and stirred vigorously for 20 min. Finally, $N_2H_4.H_2O$ (3.0 mL) was added to the mixture and stirred continuously for another 10 min. The resulting solution was transferred to a Teflon-lined stainless-steel autoclave. The autoclave was sealed and maintained at 185 ºC for 20 h, then naturally cooled to room temperature. The black product formed was centrifuged, washed several times with DI water and then with a mixture of ethanol and DI water to remove impurities. The product was dried in a vacuum oven at 60 ºC for 24 h.

2.4. CHARACTERIZATION

2.4.1. Powder X-ray Diffraction (PXRD). The electrodeposited Ni_3Te_2 films and hydrothermally synthesized products were characterized by powder X-ray diffraction (PXRD) using a Philips X-Pert X-ray diffractometer (PANalytical, Almelo, The Netherlands) with CuKa (1.5418 °A) radiation. For the electrodeposited film the PXRD pattern was collected from the as-synthesized Ni_3Te_2 layer on the Au-glass substrate. The deposited Ni_3Te_2 layer was very thin on the substrate, therefore, the PXRD pattern was collected at grazing angle incidence in thin film geometry (GI mode with G¨obel mirrors).

2.4.2. Scanning Electron Microscopy (SEM). The SEM image of Ni_3Te_2 was obtained using a FEI Helios NanoLab 600 FIB/FESEM at an accelerating voltage of 10 kV and a working distance of 4.5 mm. Energy dispersive spectroscopy (EDS) spectra along with line scan analysis data were also obtained from the same SEM.

2.4.3. Transmission Electron Microscopy (TEM). High resolution TEM (HRTEM) images and selected area electron diffraction (SAED) patterns of Ni_3Te_2 were obtained using a FEI Tecnai F20. The spot size was less than 2 nm and probe current was 1.2 nA. STEM mode in the TEM was also used for imaging with a camera length of 30 mm and convergence angle of 13 mrad. An Oxford ultra-thin (UTW) window EDS detector was used to detect the elements in TEM mode.

2.4.4. X-ray Photoelectron Spectroscopy (XPS). XPS measurements of the Ni_3Te_2 were carried out using a KRATOS AXIS 165 X-ray photoelectron spectrometer (Kratos Analytical Limited, Manchester, United Kingdom) using a monochromatic Al X-ray source. C 1s signal at 284.5 eV was used as a reference to correct all the XPS binding energies.

2.5. ELECTROCHEMICAL CATALYTIC ACTIVITY

The OER and HER catalytic performances were recorded by linear sweep voltammetry (LSV), cyclic voltammetry (CV) and the stability of the catalyst was obtained from chronoamperometry using a conventional three electrode electrochemical cell with an IviumStat potentiostat. Ag|AgCl, Pt mesh and electrodeposited Ni_3Te_2 films on various substrates were used as the reference, counter and working electrodes,

respectively. All potentials acquired vs. Ag|AgCl were converted to the reversible hydrogen electrode (RHE) by using the following equation (Equation 1).

$$E_{RHE} = E_{Ag|AgCl} + 0.059pH + E^{0}_{Ag|AgCl} \quad (1)$$

where E_{RHE} is the calculated potential vs. RHE, $E_{Ag|AgCl}$ is the experimentally measured potential vs. Ag|AgCl reference electrode, and E^0 Ag|AgCl is the standard thermodynamic potential of Ag|AgCl at 25 °C (0.197 V), which was calibrated following standard procedures as described in the ESI.† Electrochemical data were calculated using 0.08 cm^2 as the measured film deposition area, which was kept constant for all electrodeposition experiments.

The electrochemically active surface area of the catalyst was measured by using electrochemical double layer capacitance at different scan rates (Equation 2) and comparing the electrochemical capacitance with the specific capacitance of given catalysts (Equation 3). Capacitive current (i_{DL}) is the product of double layer capacitance (C_{DL}) and scan rate (υ).

$$i_{DL} = C_{DL} \times \upsilon \quad (2)$$

$$\text{ECSA} = C_{DL}/C_S \quad (3)$$

The ECSA of the catalyst was calculated using Equation 3 where Cs is the specific capacitance and reported to be between 0.022 and 0.130 mF cm^{-2} in alkaline solution. In this study, we assumed the value of Cs to be 0.040 mF cm^{-2} based on previously reported Ni-based OER catalysts.[6] The Tafel slope is an important parameter to explain the electrocatalytic activity and kinetics of a given reaction and can be expressed as follows (Equation 4).

$$\eta = a + \frac{2.3\,RT}{\alpha nF} \log j \quad (4)$$

where η is the overpotential, a is the transfer coefficient, n is the number of electrons involved in the reaction, F is the Faraday constant, j is the current density and the slope is given by 2.3RT/ anF.

Turnover frequency (TOF) is another critical parameter that can be calculated to study the OER performance of a catalyst. The turnover frequency quantifies the specific activity of a catalytic center for the OER reaction under defined reaction conditions by the number of catalytic cycles occurring at the center per unit time (Equation 5).

$$\text{TOF} = (I) / (4 \times F \times m) \quad (5)$$

where I is the current in amperes, F is the Faraday constant and m is the number of moles of the active catalyst.

Faradaic efficiency of the Ni_3Te_2 catalytic film was estimated by combined ORR–OER studies investigated in the bipotentiostat mode of the IviumStat using a Rotating Ring Disk Electrode (RRDE) set-up where Pt and glassy carbon (GC) were used as the ring and disk electrodes, respectively. The faradaic efficiency was calculated using Equation 6.

$$\text{Faradaic efficiency} = \frac{2ir}{id\ N} \quad (6)$$

where i_r and i_d are the measured ring and disk currents, respectively, and N is the collection efficiency of RRDE, 0.17 in this work (see the ESI†).

2.6. ELECTRODE PREPARATION

To analyze the activity of hydrothermally synthesized Ni_3Te_2, a homogeneous catalyst ink was prepared by adding 7.0 mg of catalyst powder in 100.0 mL of Nafion solution (50 mL of 1% Nafion solution in 50 mL of 50% IPA in water) followed by

ultrasonication for 30 min. 20 mL of the dispersion was dropcast on a confined area (0.283 cm2) on Au-coated glass. The dropcast film was then dried at room temperature and finally heated at 130 °C for 30 min in an oven.

3. RESULTS AND DISCUSSION

3.1. STRUCTURAL AND MORPHOLOGICAL CHARACTERIZATION

The powder X-ray diffraction (PXRD) patterns of the hydrothermally synthesized as well as electrodeposited product showed the presence of Ni_3Te_2, where the diffraction peaks matched with those reported for standard Ni_3Te_2 (PDF # 04-014-3418) as shown in Fig. 1. Ni_3Te_2 crystallizes with a monoclinic crystal structure in the *P21/m* space group. Both PXRD patterns showed that the product was very pure with no other noticeable impurity peaks. However, the hydrothermally synthesized product showed better crystallinity compared to the electrodeposited sample as revealed by the higher intensity of the diffraction peaks (Fig. 1a and b). Moreover, it was observed that the diffraction peaks were considerably broadened corresponding to the hydrothermally prepared Ni_3Te_2. From the Scherrer equation, the average particle size was calculated to be approximately 40 nm.[45] It must be mentioned here that from PXRD studies it was apparent that there is no preferred direction of growth for either the electrodeposited or hydrothermally synthesized Ni_3Te_2. Both products contained randomly oriented nanocrystalline grains.

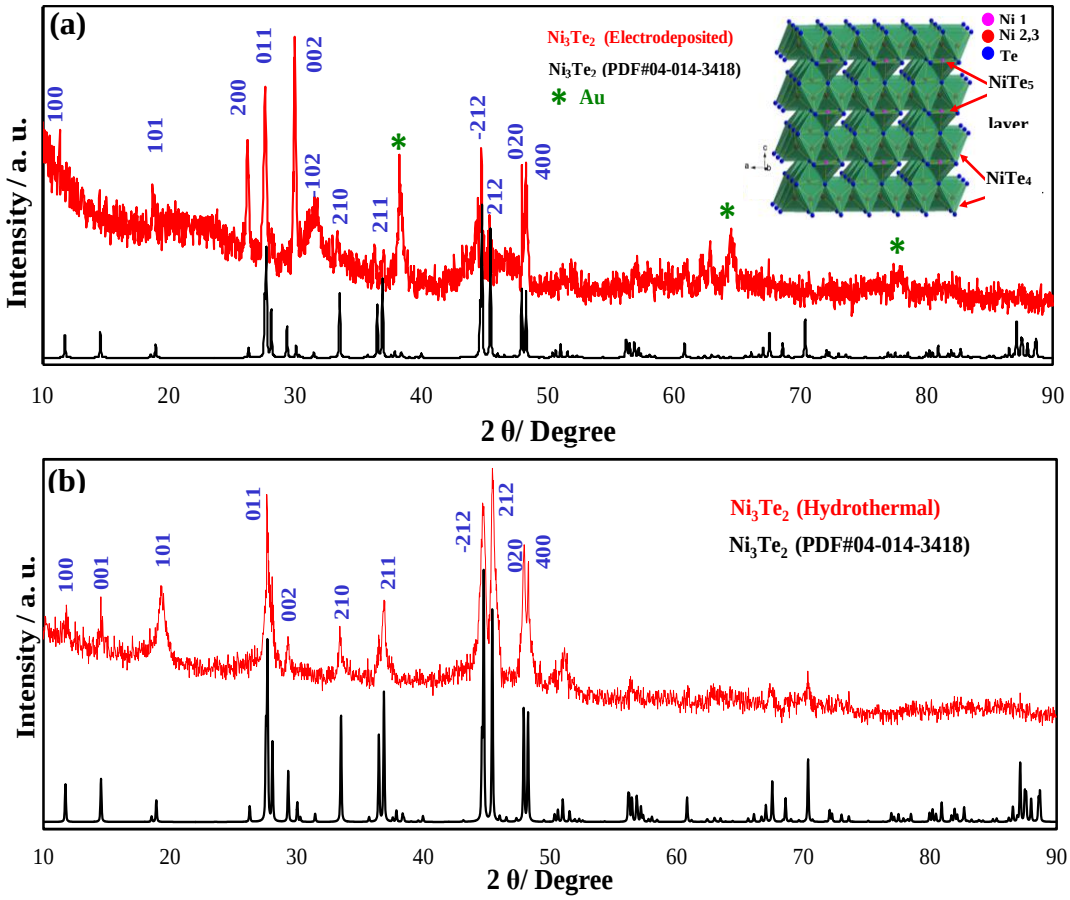

Figure 1. PXRD patterns of (a) electrodeposited on Au and (b) hydrothermally synthesized Ni_3Te_2 catalysts along with the reference (PDF # 04-014-3418) spectrum. Inset in (a) shows the crystal structure of Ni_3Te_2 created from the corresponding cif file.

The crystal structure of Ni_3Te_2 is very interesting. It shows unique coordination for Ni, where two Ni atoms (Ni(2) and Ni(3)) are coordinated to 4 Te atoms in a tetrahedral geometry, while the 3rd one (Ni(1)) has a 5-coordinated square-pyramidal coordination, where Ni sites are at the centre of the square planar base and the 5th Te atom occupies a vertical position atop the Ni atom with a long Ni–Te bond (inset of Figure 1a). The $NiTe_4$ tetrahedra are connected via edge-sharing and form a continuous layer along the ab-plane. The 5-coordinated $NiTe_5$ square-pyramids are also connected through edge-sharing and the chains of such square-pyramidal $NiTe_5$ polyhedra run along

the b-axis, while along the a-axis, the $NiTe_5$ square pyramids are present as edge-shared dimeric units with each unit oriented 180° with respect to its neighbor. The periodic arrangement of the $NiTe_5$ dimeric units along the a-axis gives rise to a rectangular channel within the structure. The layer formed by edges-hared $NiTe_5$ polyhedra propagates along the ab-plane. The $NiTe_4$ layer and the $NiTe_5$ layer are stacked alternately along the c-axis. The Ni(1)–Ni(2) and Ni(1)–Ni(3) distances are also quite short indicating that the structure can have several Ni–Ni metallic bonds. Interestingly due to the unique atomic arrangement and coordination geometry, at least one of the Ni atoms, Ni(1), is coordinatively under-saturated and a vacant site is available in the vertical position, which when occupied by an 3 anion, can give rise to an octahedral geometry. The availability of such a vacant site may be extremely useful for anion (e.g. OH^-) adsorption and subsequent onset of catalytic activities. The importance of NiX_4 (X = Se) polyhedra in enhancing the OER catalytic performance has also been exemplified by investigating a molecular complex containing an $NiSe_4$ core.[32] The tetrahedral NiX_4 unit can possibly undergo a coordination expansion (tetrahedral to octahedral transition) initiated by hydroxyl attachment, as has been observed in coordination complexes.[46,47] It must be noted here that, although Ni_3Se_2 and Ni_3Te_2 have similar stoichiometries, their crystal structures are distinctly different indicating that their properties can also be widely varied from each other.

The SEM image of the as-grown electrodeposited films showed that the surface was mainly composed of randomly oriented nanoflakes (Figure 2a). These nanoflakes can expectedly increase the surface area of the catalytic films thereby increasing the contact area between the catalyst and electrolyte. The average thickness of the flakes was

estimated to be around 8 nm. TEM imaging of the electrodeposited film also showed random distribution of thin flake-like nanostructures as shown in Figure 2c. High resolution TEM imaging revealed lattice fringes corresponding to <110> lattice planes of Ni_3Te_2 (Figure 2d). SAED pattern collected from these nanostructures showed diffraction rings corresponding to <002>, <210>, and <312> lattice planes, which also confirmed the presence of crystalline Ni_3Te_2 in the film. SEM imaging of the hydrothermally prepared sample showed that the product was composed of nanoflakes with an average thickness of 5 nm for the nanoflakes (Figure 3a). TEM images also confirmed the presence of thin nanoflakes in the product (Figure 3c) while HRTEM images revealed that these nanostructures are highly crystalline with lattice fringes corresponding to <212> lattice spacing of Ni_3Te_2 (Figure 3d). The SAED pattern showed diffraction spots corresponding to crystalline Ni_3Te_2 (inset of Figure 3d).

The elemental composition of the electrodeposited film and hydrothermally prepared sample was further confirmed through EDS elemental mapping. While elemental mapping showed the presence of Ni and Te uniformly distributed over the sample 4 surface (Figure 2b and 3b), the average EDS data showed that the relative elemental composition was 62% Ni and 38% Te, revealing a relative atomic ratio of 1.5 : 1, confirming the formation of Ni_3Te_2. It must be noted here that there was no noticeable oxygen peak detected in the EDS spectra of either products indicating the high purity of the film surface.

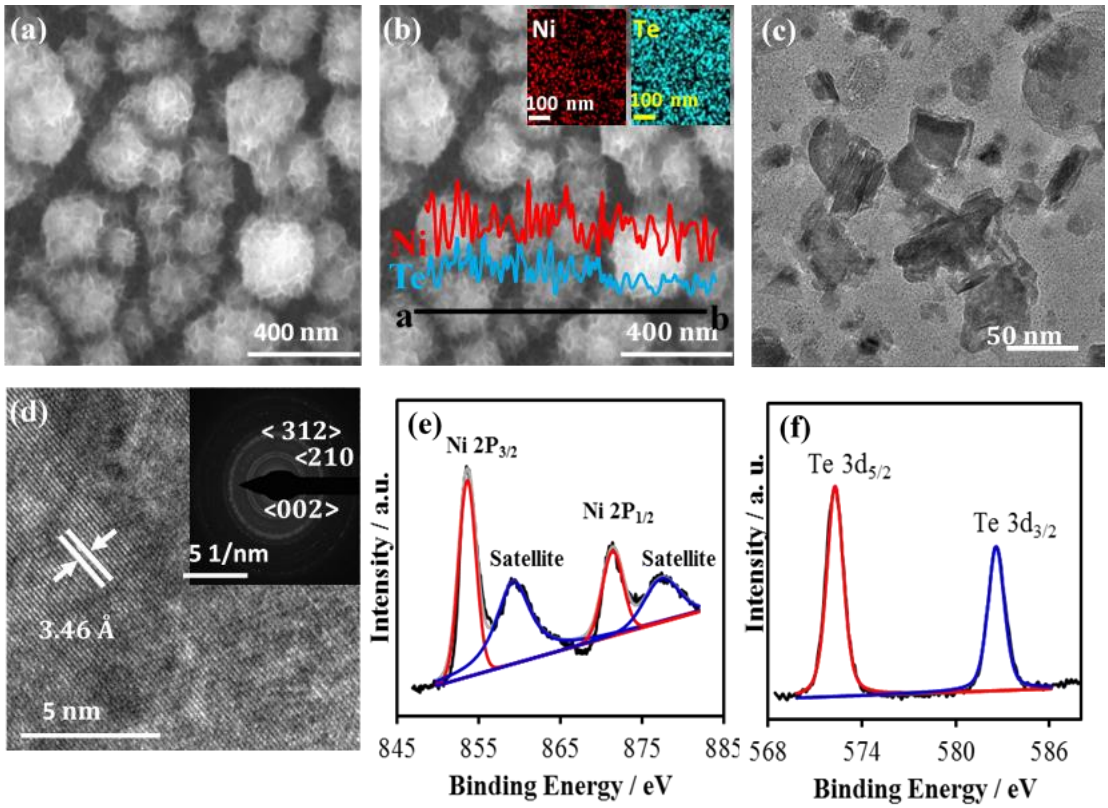

Figure 2. Characterization of electrodeposited Ni_3Te_2 catalyst: (a) SEM image; (b) EDS mapping and line scan analysis; (c) TEM image; (d) HRTEM image. Inset of (d) shows the SAED pattern. (e) Ni 2p and (f) Te 3d XPS spectra.

The surface electronic state of the Ni_3Te_2 catalyst was analyzed by X-ray photoelectron spectroscopy (XPS) and is presented in Figure 2e and f. The first doublet at 853.5 and 871.4 eV in the Ni 2p spectra (Figure 2e) indicated the presence of Ni^{2+} as seen in nickel telluride.[48,49] An obvious satellite peak at the higher binding energies due to the overlapping of the antibonding orbital between the Ni atom and Te atom of Ni 2p can be observed.[48] Figure 2f shows the Te 3d spectra where the peaks at 572.3 and 582.5 eV corresponding to the $3d_{5/2}$ and $3d_{3/2}$ peaks can be assigned to Te^{2-} in nickel telluride.[48,49] It

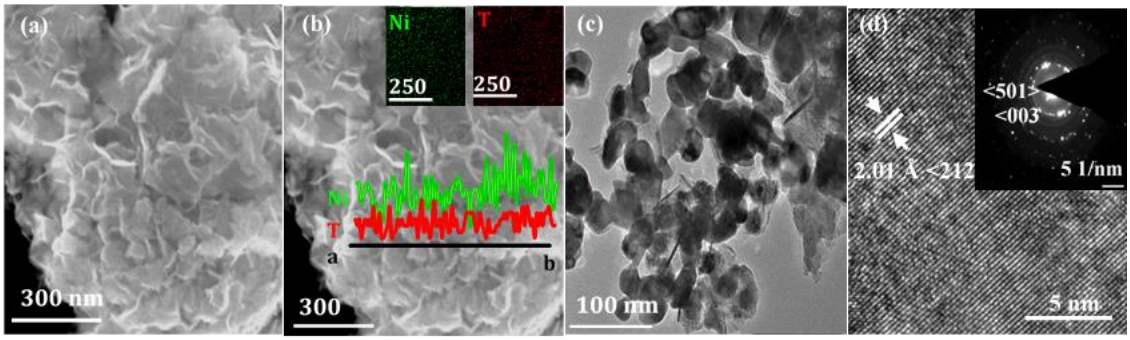

Figure 3. Characterization of hydrothermally synthesized Ni_3Te_2 catalyst: (a) SEM image; (b) EDS mapping and line scan analysis; (c) TEM image (d) HRTEM image. Inset in (d) shows the SAED pattern from individual nanocrystallites.

should be noted that peaks corresponding to Ni-oxides were visibly absent in the XPS spectra, indicating that the film surface was devoid of oxidic impurities. Raman spectra of the as-synthesized catalyst are shown in Figure S1 (ESI†). The peaks at 108, 124 and 143 cm^{-1} can be assigned to Ni_3Te_2. There was no evidence of Ni-oxide or Te-oxide phases indicating that the films were free from any oxidic impurities.

3.2. ELECTROCHEMICAL CHARACTERIZATION

The OER activity of the electrodeposited Ni_3Te_2 films was examined through electrochemical measurements in 1 M KOH. Before measuring the electrocatalytic activity, the electrochemically active surface area (ECSA) was calculated from the double layer capacitance measurement, as has been described previously. [6] Specifically, cyclic voltammograms (CVs) of the electrodeposited Ni_3Te_2 catalyst were measured from -0.35 to -0.25 V vs. Ag|AgCl at scan rates between 2.5 and 20 mV s^{-1} in N_2 saturated 1 M KOH as shown in Figure 4a. The cathodic and anodic current was measured at - 0.305 V vs. Ag|AgCl from Figure 4a and plotted as a function of scan rates (Figure 4b).

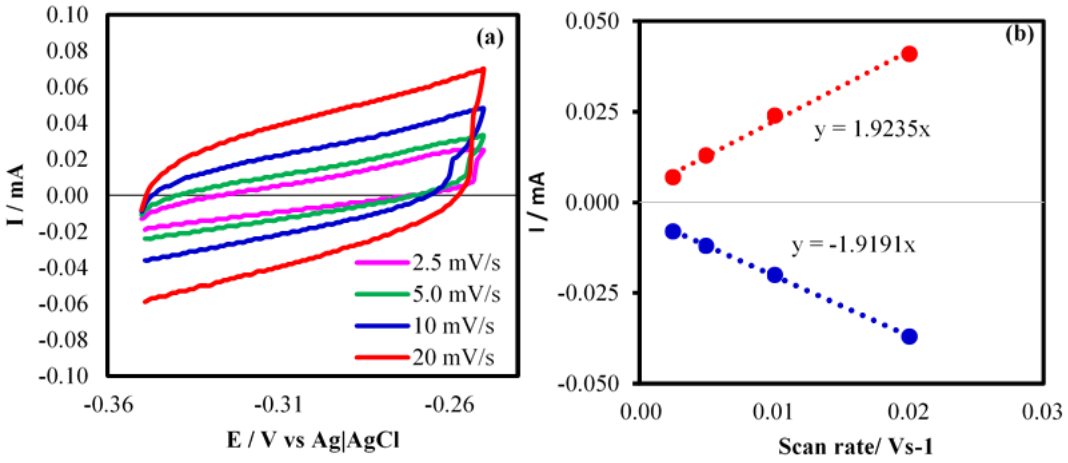

Figure 4. Cyclic voltammograms measured for the electrodeposited Ni_3Te_2 catalyst. (a) on Au in N_2 saturated 1 M KOH solution at different scan rates from 2.5 to 20 mV s^{-1}. (b) Shows a plot of anodic and cathodic currents measured at - 0.305 V as a function of scan rate.

From the average of the cathodic and anodic slopes, C_{DL} can be obtained and ECSA was calculated using eqn (3). It was observed that the electrodeposited Ni_3Te_2 films have a moderately high ECSA, 48.03 cm^2. Comparing ECSA with the geometric area gave the roughness factor. The high roughness factor of the electrodeposited film (608.0) supports the nanoflake-like geometry and might be one of the factors responsible for high catalytic activity.

3.3. OER CATALYTIC ACTIVITY

The electrocatalytic activity of Ni_3Te_2 was measured in N_2 saturated 1 M KOH by performing linear sweep voltammetry (LSV) as well as CVs. For fair comparison of the electrocatalytic activities, RuO_2 was electrodeposited on Au-glass using a reported procedure (details have been provided in the ESI†), and its OER activity was also measured. Figure 5a shows the LSVs of electrodeposited and hydrothermally synthesized

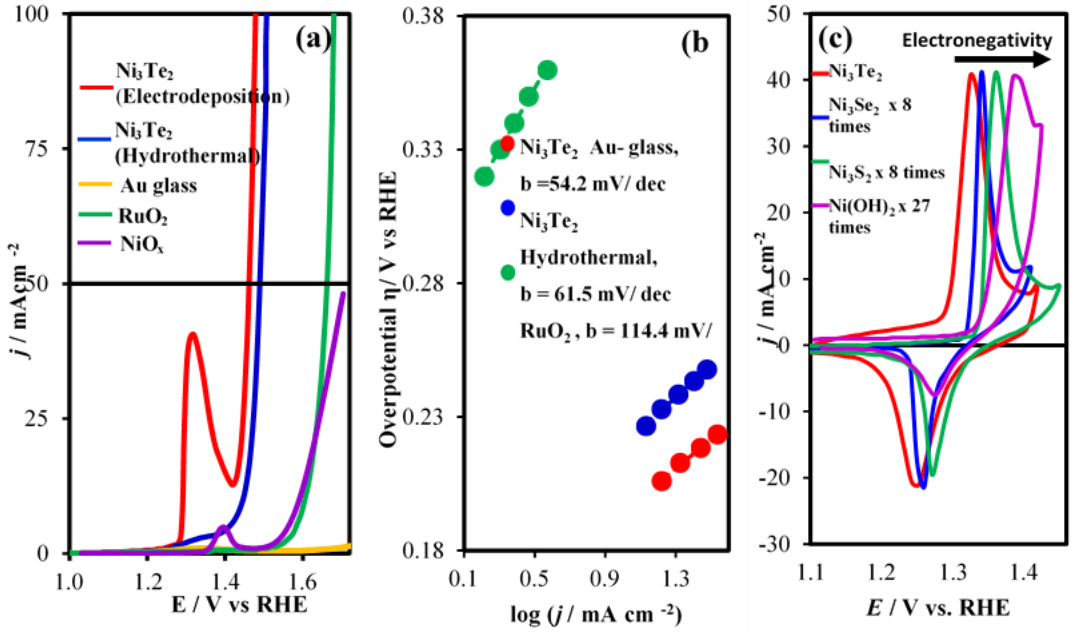

Figure 5. LSVs measured for Ni_3Te_2 catalyst. (a) films in N_2 saturated 1 M KOH at a scan rate of 10 mV s^{-1}. The solid black line shows the current density at 50 mA cm^{-2}. (b) Tafel plots of both electrodeposited and hydrothermally synthesized Ni_3Te_2 compared with RuO_2. (c) Comparison of $Ni^{2+} \rightarrow Ni^{3+}$ oxidation peaks in Ni_3Te_2, Ni_3Se_2, Ni_3S_2 and $Ni(OH)_2$.

Ni_3Te_2, RuO_2 and bare Au-glass collected at a scan rate of 10 mV s^{-1}. Bare Au-coated glass did not show any OER catalytic activity as expected. However, modified Au-glass electrodes coated with electrochemically deposited and hydrothermally synthesized Ni_3Te_2 showed excellent OER catalytic activity as can be seen in Figure 5a. The onset potential for O_2 evolution was at 1.38 V vs. RHE for both electrodeposited and hydrothermally synthesized Ni_3Te_2. Both electrodeposited Ni_3Te_2 and hydrothermally synthesized Ni_3Te_2 showed a pre-oxidation peak before the onset of catalytic activity (Figure S2a and S3c† respectively), which has been commonly observed with most Ni-based electrocatalysts containing Ni^{2+} and has been attributed to the oxidation of Ni(II) to Ni(III). Typically the OER electrocatalysts are benchmarked by comparing their

overpotential, η, required to reach a current density of 10 mA cm^{-2}.[6] Since the larger oxidation peak for the electrodeposited Ni_3Te_2 masked the overpotential at 10 mA cm^{-2}, η was estimated from the reverse sweep of the CV plot (Figure S2a†). It was observed that the overpotential at 10 mA cm^{-2} was at 210 (reverse scan of CV of Figure S2a†) and 220 mV (Figure S3c†) for electrodeposited Ni_3Te_2–Au and hydrothermally synthesized Ni_3Te_2, respectively. The better OER activity for electrodeposited Ni_3Te_2 can be rationalized by considering the fact that the binder free (Nafion free) electrodeposited sample grown directly on the electrodes has better charge transport at the electrode–catalyst interface compared to the catalytic composite containing hydrothermally synthesized Ni_3Te_2 mixed with Nafion. The activity of these catalysts was compared with that of standard RuO_2 which shows an onset potential and η at 10 mA cm^{-2} current density at 1.51 V vs. RHE and 370 mV, respectively, which are comparable with previous reports of RuO_2.[50] It must be noted here that this is the first example of Ni_3Te_2 showing OER catalytic activity; additionally, the onset overpotential and η are both significantly lower than those of other Ni-based electrocatalysts including oxides,[25] sulfides,[29] and selenides[30] in the bulk form.

Since it has been observed in other Ni-based OER electrocatalytic systems that Fe incorporation from impure KOH can significantly boost the catalytic activity, the OER activity of Ni_3Te_2 was tested in purified KOH and compared with that in impure KOH. The KOH purification was done following procedures reported previously and has been described in detail in the ESI.† However, it must be acknowledged that it is hard to remove Fe completely and the presence of extremely low levels of Fe cannot be totally excluded. As shown in Figure S3a and b,† it was observed that there was no significant

difference in catalytic activity between purified and impure KOH electrolyte, indicating the lower influence of Fe incorporation during the OER process for Ni_3Te_2. The effect of electrodeposition time on the OER catalytic activity was probed by measuring LSV curves of Ni_3Te_2 deposited for 60 s, 120 s, 300 s and 600 s on Au/glass substrates as shown in Figure S4.† It was observed that the OER activity gradually increased till 300 s deposition time after which the activity decreased for longer deposition times. This observation has been made earlier with electrodeposited Ni_3Se_2 electrocatalysts and can be explained from the thickness and microstructure of the film.[31] Longer deposition times typically produce thicker films which may lead to the poor electronic conductivity of semiconductor Ni_3Te_2 thus inhibiting charge transport. Lower deposition time on the other hand creates granular film with a high roughness factor that enhances the active site exposure to the electrolytic solution thereby facilitating the catalytic process. The effect of the substrate on the OER catalytic activity was also investigated and the results have been summarized and presented in the ESI (Figure S5† and Table 1).

Table 1. Effect of substrate on OER catalytic activity.

Substrates	**Loading (mg cm^{-2})**	**Onset potential / V**	**η to 10 mA cm^{-2}/ mV**
Au glass	4.1	1.38	210
GC	4.9	1.36	180
Ni foam	40.8	1.45	230
CFP	4.89	1.41	210
C Cloth	24.81	1.42	210

For this study Ni_3Te_2 catalyst was deposited on glassy carbon (GC), carbon fiber paper (CFP), carbon cloth (CC), and nickel foam (NF) for 300 s and compared with the Au-glass substrate. Among these, the catalyst deposited on GC showed the lowest onset potential of 1.36 V (vs. RHE) and the overpotential at 10 mA cm^{-2} was only 180 mV. Surprisingly, the relatively planar substrates (GC and Au-coated glass) showed better OER activity than the porous three-dimensional substrates such as, NF, CC and CFP. This behavior can be explained by the higher loading of catalyst in three-dimensional substrates which might lead to thicker coatings with poor electronic conductivity of the catalyst layer as explained earlier.

Table 2. Comparison of electrocatalytic parameters for OER and HER.

Catalysts	**OER**						**HER**		
	Total loading / mg	**Loading area /mg cm^{-2}**	**Onset potential / V**	**η to 10 mA cm^{-2} / mV**	**TOF@ 270 mV / s^{-1}**	**Tafel slope / mV dec^{-1}**	**Onset potential / V**	**η to 10 mA cm^{-2} / mV**	**Tafel slope / mV dec^{-1}**
Ni_3Te_2 - Au glass (ED)	0.28	4.1	1.38	210	0.023	54.2	- 0.180	237	73.1
Ni_3Te_2 - GC (ED)	0.96	4.9	1.36	180	0.010	64.3	-	-	-
Ni_3Te_2 - Hydrothermal	1.40	4.9	1.38	220	0.010	61.5	- 0.167	304	94.2
RuO_2 (ED)	-	-	1.51	370	-	114.4	-	-	-
Ni_3Te_2 - Ni foam (ED)	-	-	1.45	230	-	-	- 0.149	212	126.2
Pt	-	-	-	-	-	-	0.000	52	38.5

The kinetics of the OER catalytic activity was investigated by analyzing the Tafel plots as shown in Figure 5b. To obtain accurate Tafel slope values, LSV was carried out at a slow scan speed of 2 mV s^{-1} in a non-stirred electrolyte solution. The Tafel slopes of electrodeposited and hydrothermally obtained Ni_3Te_2 were calculated as 54.2 and 61.5 mV dec^{-1}, respectively, whereas for RuO_2 it was 114.4 mV dec^{-1}. The lower Tafel slope reconfirms that the catalysts are catalytically active for the OER, and using the catalyst

loading as mentioned in Table 2. The TOF values were calculated to be 0.010 s^{-1} and 0.023 s^{-1} for hydrothermally synthesized and electrodeposited Ni_3Te_2 catalysts, respectively. The TOF values also indicate better OER performance for electrodeposited Ni_3Te_2.

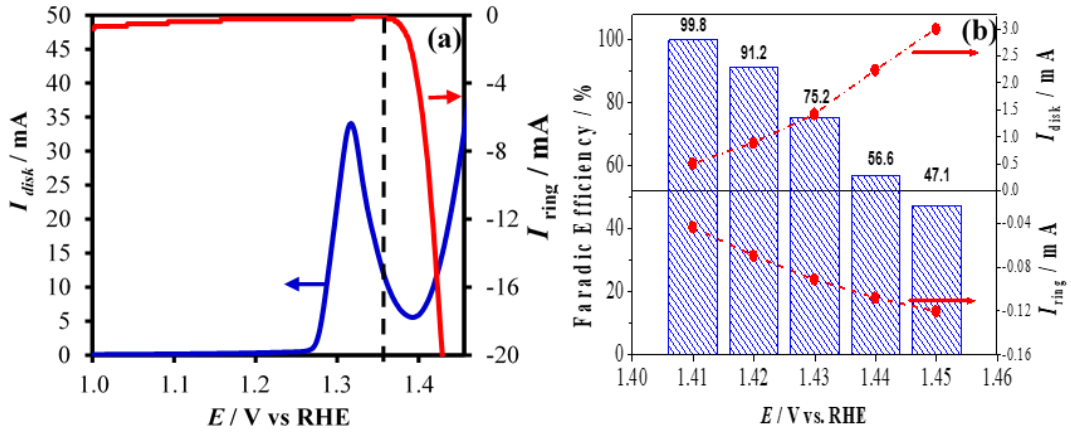

Figure 6. Plots for the ORR-OER reaction. (a) showing OER current density at Ni_3Te_2 /GC disk electrode (area 0.196 cm^2) in N_2-saturated 1 M KOH and ORR current density at Pt ring electrode maintained at 0.2 V vs. RHE as a function of applied disk potential. Black line indicates the onset potential for OER at the disk electrode corresponding with the onset of ORR at the ring electrode. (b) Faradaic efficiency of catalyst measured in N_2 saturated 1 M KOH at 1600 rpm rotation speed.

The evolved gas was analyzed using RRDE experiments where Ni_3Te_2 was deposited on the disc electrode used as the anode, while a Pt ring electrode was used as the cathode. The Pt ring was maintained at 0.2 V vs. RHE, appropriate for the O_2 reduction reaction, ORR, under alkaline conditions. The idea was that if oxygen was being generated at the disc electrode during the anodic scan, the evolved O_2 will be promptly collected and reduced at the Pt ring electrode leading to an increase in the ring current. Figure 6a shows the OER polarization curve of the Ni_3Te_2/GC disk electrode in

1MKOH at 1600 rpm at a scan rate of 10 mV s^{-1} and the ring current is presented as a function of disk potential.

It was observed that below the onset potential there was minimal ring current. However, as soon as the disk electrode was swept past 1.36 V (onset potential), the ring current also increased indicating the ORR. The ring current progressively increased with increasing disk potential. It must be mentioned here that the electrolyte solution was previously purged with N_2 and the whole experiment was performed under a blanket of N_2, thereby ensuring that there was no external source of O_2. This RRDE measurement confirmed that the evolved gas at the anode was definitely O_2.

The faradaic efficiency was measured from the abovementioned RRDE experiment following the procedure detailed in the ESI.† The highest efficiency obtained was about 99.8% which decreased with increasing disk potential (Figure 6b). This decrease in faradaic efficiency at relatively high disk potential is not unusual and can be attributed to poor collection at the Pt ring electrode at high potential where copious quantities of O_2 are generated. Poor collection efficiency by Pt leads to loss of undissolved O_2 resulting in lower faradaic efficiency.[30]

At this point it is necessary to venture deeper into the cause of enhanced OER catalytic activity of Ni_3Te_2. As mentioned previously, our hypothesis was that decreasing the electronegativity of the telluride anions will lead to increased covalency in the Ni–Te bonds. Such a change of anion coordination is expected to alter the chemical potential around the Ni site which can be monitored by observing the redox potential of the Ni sites. In most of these Ni-based electrocatalysts catalyst activation involves Ni(II)/Ni(III) oxidation, which shows up as a peroxidation peak before the onset of catalytic activity

and it has been reported previously that Ni(III) is the actual catalytically active species. It has been observed frequently in the coordination complexes that the oxidation peak potential of the central atom is lowered as the electronegativity of the anions decreases down the chalcogenide series.[43,44] We have measured the Ni(II)/Ni(III) oxidation peak in Ni_3Te_2 by collecting the CV in the range of 1.1 to 1.45 V and compared with that of Ni_3Se_2 and $Ni(OH)_2$. Indeed, it was observed that the Ni^{2+} oxidation peak showed a cathodic shift in Ni_3Te_2 indicating that the catalytically active Ni^{3+} was generated at a lower potential compared to the oxide and selenide (Figure 5c). Availability of the catalytically active site (Ni^{3+}) at a lower potential will definitely enhance the catalytic activity by lowering the onset potential as well as overpotential for the OER activity. In addition to the facile oxidation of Ni^{2+} to Ni^{3+}, the catalytic activity in Ni_3Te_2 can also be facilitated by virtue of its unique crystal structure. As explained before, Ni_3Te_2 comprises of layers containing $NiTe_4$ and $NiTe_5$ polyhedra. The $NiTe_5$ polyhedra are actually square pyramids with an open coordination site in the octahedral position, which might be viewed as functionally similar to an anion vacancy. Such an open coordination site might facilitate the onset of catalytic activity by readily accepting a hydroxyl ligand with minimal distortion to the existing lattice structure. Hence, the enhanced availability of Ni^{3+} along with the presence of accessible, coordinatively under-saturated Ni sites, collectively gives rise to the unprecedented OER catalytic activity of Ni_3Te_2.

Apart from Ni^{2+} to Ni^{3+} oxidation, catalyst activation also involves attachment of the hydroxyl group (OH^-) on the catalyst surface.[51] As has been reported by several groups previously, the oxygen evolution reaction is initiated through the attachment of a hydroxyl (OH^-) anion on the surface-active Ni site.[51] It must be mentioned here that the

nickel telluride surface with bound OH^- is not the same as an oxide-coated surface, but rather can be viewed as a hydroxo-telluride surface akin to the oxyhydroxide formed in the oxide surfaces. Hence, in order to study the activation of the Ni_3Te_2 surface, we have estimated the simple hydroxyl adsorption energies (Ead) through DFT by employing the projected augmented wave (PAW) method, implemented in the Vienna Ab initio Simulation Package (VASP). Details of the calculations have been provided in the ESI.†

However, it must be mentioned here that the OER being a multi-step process, to gain a proper understanding of the reaction kinetics on the catalyst surfaces, energetics of all the elementary steps needs to be estimated and compared. In particular, a more detailed computational-time demanding modeling study is required to determine the actual rate determining step for the OER and follow the energetics to understand the catalytic efficiency as a function of composition with respect to surface energetics. We are currently expanding these DFT based calculations on a wide range of catalyst composition and trying to investigate the energetics of the different elementary steps for the OER and correlate them with the catalytic efficiency in an attempt to construct the volcano-type plot. Such studies will provide a better understanding of how the OER kinetics vary on the different catalyst surfaces. These studies will be disseminated at a later time.

As has been described above, the crystal structure of Ni_3Te_2 contains three crystallographically unique Ni sites, two tetrahedral Ni sites, and one square pyramidal Ni atom. The E_{ad} value for hydroxyl attachment to each of these Ni sites has been estimated in two lattice planes, (001) and (010). The Ni sites have been designated as Ni(1)[Ni(4)], Ni(2)[Ni(5)], and Ni(3) [Ni(6)], for the tetrahedral and square pyramidal

sites on the (001)[(010)] planes, respectively. The calculated cohesive energies of OH^- ions on the (001) surface of Ni_3Te_2 are -2.703 eV (Ni(1)), -2.664 eV (Ni(2)), and -1.949 eV (Ni(3)), while those on the (010) surface are -1.82 eV (Ni(4)), -2.408 eV (Ni(5)), and -2.122 eV (Ni(6)). The calculated data of cohesive energies, bond distances and bond angles after adsorption have been summarized in Table 3 while details of the calculation have been provided in the ESI† along with illustrations depicting the crystallographic planes (Figure S6–S10†).

Table 3. A summary of adsorption energy, bond distances and bond angles. Adsorption energy (E_{ad}), bond distances of O-H and Ni-O (d_{O-H} and d_{Ni-O}), and angle of Ni-O-H (θ_{Ni-O-H}) for OH^- ions adsorbed on different active Ni sites in NiO and Ni_3Te_2.

Active Ni site	**E_{ad} (eV)**	**d_{O-H} (Å)**	**d_{Ni-O} (Å)**	**θ_{Ni-O-H}**
NiO_(001)_Ni	-1.608	0.964	1.808	180°
Ni_3Te_2_(001)_Ni1	-2.703	0.964	1.748	171°
Ni_3Te_2_(001)_Ni2	-2.664	0.965	1.767	172°
Ni_3Te_2_(001)_Ni3	-1.949	0.978	1.910	136°
Ni_3Te_2_(010)_Ni4	-1.820	0.979	1.825	114°
Ni_3Te_2_(010)_Ni5	-2.408	0.975	1.913	108°
Ni_3Te_2_(010)_Ni6	-2.122	0.978	1.920	115°

Interestingly, it was observed that regardless of the differences of calculated OH-ion adsorption energies on different Ni sites in Ni_3Te_2, all of the obtained values were relatively larger than that of the hydroxyl adsorption energy on a Ni-oxide surface (-1.608 eV), as can be directly observed from Figure 7. These results suggest that surface activation of the Ni site through hydroxyl attachment is more facile in Ni_3Te_2 possibly leading to more optimal coverage with OH groups at low activation potential.

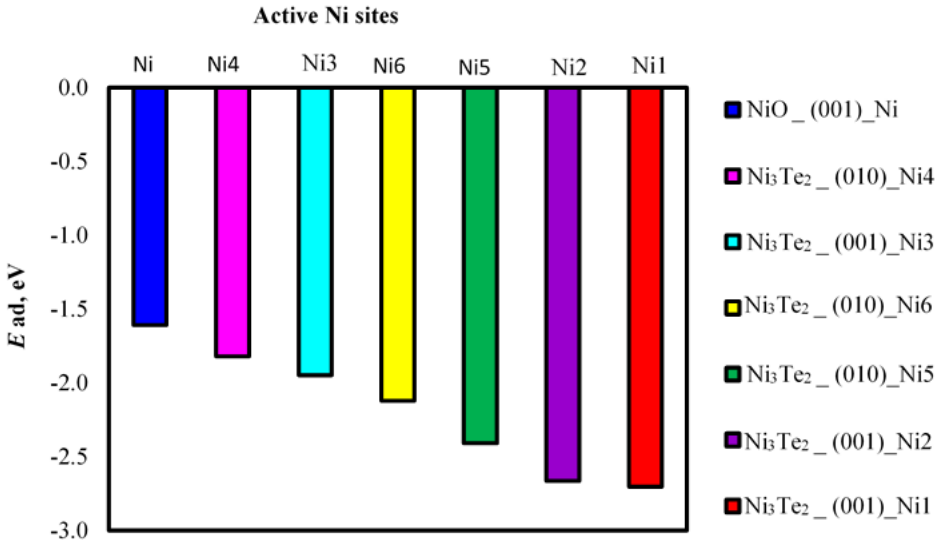

Figure 7. Adsorption energy of OH^- ions adsorbed on various active Ni sites of NiO and Ni_3Te_2. In Ni_3Te_2, Ni(1), Ni(2), Ni(4), Ni(5) correspond to tetrahedral coordination, while Ni(3), Ni(6) are square pyramidal.

This factor coupled with faster generation of Ni^{3+} as shown by electrochemical data may lead to faster onset of catalytic activity at a lower applied potential. This is in very good agreement with lower onset potentials observed in the electrochemical studies, thereby providing further proof that telluride surfaces are indeed energetically more favorable for water oxidation. This study also provides information that the catalytic efficiency of the Ni_3Te_2 films can be further enhanced by growing epitaxial or oriented films with preferred direction of growth, such that lattice planes with more favorable hydroxyl adsorption energy become the terminating plane.

3.4. CATALYTIC STABILITY

The stability of the electrocatalysts was investigated using the constant oxygen evolution condition for an extended period of time and cyclability of the catalyst in 1 M KOH solution. Chronoamperometric studies performed for 24 h in 1 M KOH at 1.41 V

applied potential are shown in Figure 8a. It was observed that there was a large amount of O_2 bubbles generated at the electrode surface and hence the solution was continuously stirred at 1200 rpm to get rid of O_2 bubbles from the catalyst surface and allow progress of the reaction. As can be seen from Figure 8a, both catalysts (electrodeposited and hydrothermally synthesized) showed exceptional stability of the OER catalytic activity for over 24 h in 1M KOH and the current density did not show any degradation. The LSV curves before and after the catalytic activity were also compared to check the catalyst stability and have been shown in Figure 8b and c for electrodeposited and hydrothermally synthesized catalysts, respectively. Interestingly, the LSV curves for Ni_3Te_2 after 24 h of continuous OER did not show any decrease of onset potential and overpotential compared to the as-synthesized catalysts, and the LSV curves before and after catalytic activity were perfectly superimposable.

The composition of the catalysts following catalytic activity was investigated through XPS, EDS, and PXRD analyses. XPS spectra confirmed that the elemental composition of the electrocatalyst was retained after extended periods of catalytic activity as shown in Figure 8e and f for Ni 2p and Te 3d, respectively. Noticeably the XPS peaks before and after catalytic activity did not show any shift of peak positions of Ni 2p and Te 3d (Figure S11†). As can be seen from the XPS peaks after OER activity, there was no evidence for the presence of Ni-oxidic phases, and the Te signal did not show any degradation (Figure 6 and S11†). In addition to the Ni and Te peaks, the O 1s signal was also monitored through XPS. As shown in Figure S11,† the O 1s peak showed characteristics of only surface adsorbed O_2 and traces of Te-oxides, but no Ni-oxide, which stayed the same even after prolonged periods of OER. The surface morphology of

the film checked through SEM imaging after the activity did not reveal major changes in morphology while EDS also confirmed the presence of only Ni and Te in the film after catalytic activity, while no O was detected (Figure S12†). Figure S13b† shows the comparison of PXRD patterns for the electrodeposited Ni_3Te_2 electrocatalyst before and after OER activity for 24 h. As is evident from this figure, there were no changes in peak positions after prolonged chronoamperometry in 1 M KOH, and the Ni_3Te_2 catalyst retained its bulk composition. Figure S13a† shows the PXRD pattern of the hydrothermally synthesized Ni_3Te_2 catalyst after stability tests and no significant difference was observed in the diffraction peak position before and after activity indicating that there was no change in the bulk composition of the catalyst.

The electrochemical stability of the catalyst surface was also probed through CV cycling in 1 M KOH. In particular, surface oxidation has been a lingering doubt for most of these Ni-based OER electrocatalysts. If the chemical coordination around the catalytically active Ni-atoms on the surface changes drastically (such as from telluride coordination to oxide), it is expected that it would lead to a change in the chemical potential and subsequently the Ni^{2+}/Ni^{3+} oxidation potential, which should be detected through CV cycling as a shift of the oxidation peak. Interestingly, in the present case it was observed that the Ni^{2+}/Ni^{3+} oxidation peak on the Ni_3Te_2 surface does not show any shift even with 100 CV cycles and the peaks are exactly superimposable on each other as shown in Figure 8d. If there was surface oxidation and conversion of the Ni_3Te_2 surface to the Ni oxide/oxyhydroxide surface, then the Ni^{2+}/Ni^{3+} oxidation peak would have shown a gradual shift towards more anodic potential.

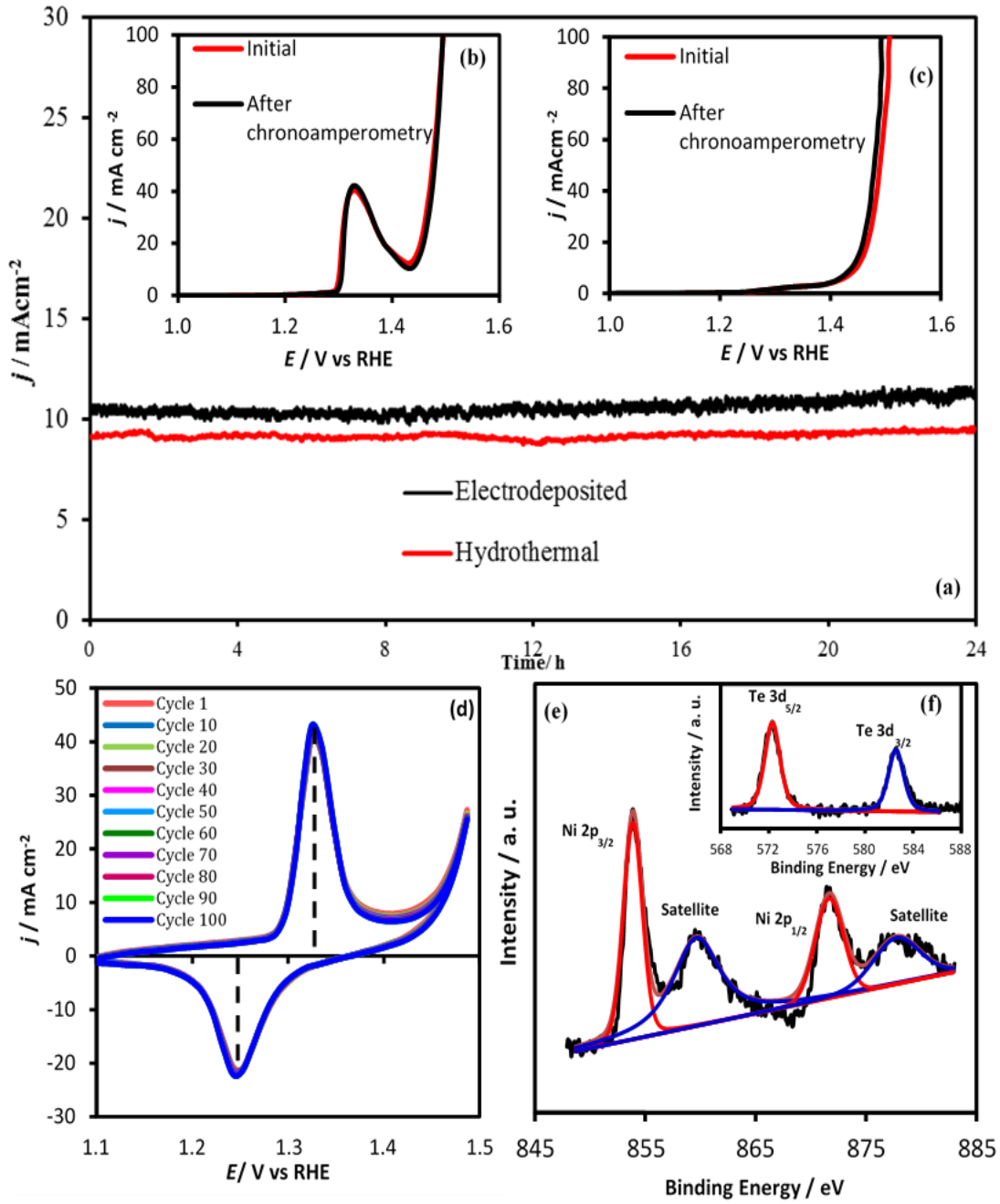

Figure 8. Extended stability study of the Ni_3Te_2 catalyst. (a) under continuous O_2 evolution for 24 h studied through chronoamperometry at constant potential of 1.44 V and 1.45 V vs RHE for elecrodeposited and hydrothermal synthesis catalyst respectively. LSVs of the (b) electrodeposited, and (c) hydrothermally synthesized Ni_3Te_2 in N_2 saturated 1 M KOH before and after chronoamperometry for 24 h. (d) CVs measured for Ni_3Te_2 @ Au- glass for 100 cycles showing the $Ni^{2+} \rightarrow Ni^{3+}$ oxidation peak. (e) Ni 2p XPS spectra, and (f) Te 3d XPS spectra after chronoamperometry for 24 h.

This conclusively proves for the first time that the telluride surface is indeed stable towards surface oxidation in alkaline medium under conditions of the OER. Rather we propose that due to the structural uniqueness of Ni_3Te_2, the Ni^{2+} / Ni^{3+} oxidation is supported through partial hydroxylation leading to a (hydroxy) telluride surface where the telluride coordination remains intact, and there is coordination expansion at the Ni site.

3.5. HER CATALYSIS AND BIFUNCTIONALITY FOR WATER SPLITTING

Ni_3Te_2 has also been studied for possible HER catalytic activity in 1 M KOH by measuring the LSV in the same three-electrode system as has been described above. Electrodeposited Ni_3Te_2 on Au-glass and Ni foam were compared with Pt for HER catalytic activity. Interestingly, both electrodeposited and hydrothermally synthesized Ni_3Te_2 showed good HER catalytic activity as shown in Figure 9a and S16,† respectively. Electrodeposited Ni_3Te_2 on Au-glass showed an onset potential for HER at 0.180 V reaching an overpotential of 237 mV at a current density of 10 mA cm^{-2}. The onset potential and overpotential at 10 mA cm^{-2} for the hydrothermally synthesized (Figure S16†) sample dropcast on Au-glass showed similar values (0.167 V and 304 mV, respectively). The Tafel slopes were calculated from the LSV plots using eqn (4) and have been plotted in Figure 9b. The electrodeposited sample showed a lower Tafel slope possibly due to more facile charge transfer on the catalyst film directly grown on the conducting electrode.

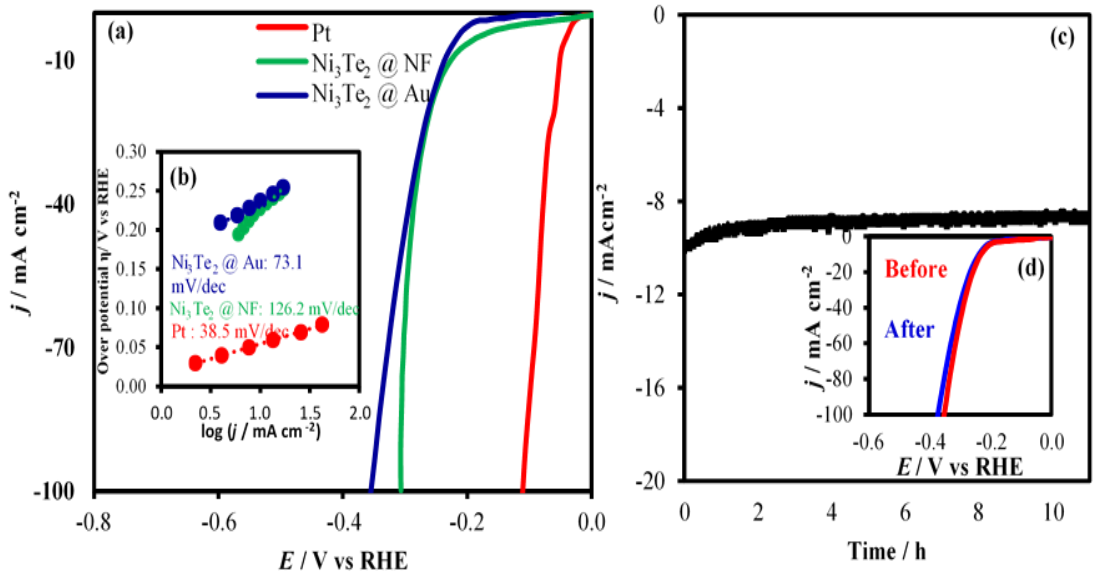

Figure 9. Polarization curves for electrodeposited Ni_3Te_2 catalysts. (a) in N_2 saturated 1 M KOH solution at a scan rate of 10 mV s^{-1} under cathodic scan. (b) Tafel plots of electrodeposited Ni_3Te_2 catalysts. (c) Stability study of electrodeposited Ni_3Te_2 catalyst under continuous H_2 evolution for 11 h at constant potential of -0.237 V vs RHE. (d) LSVs of catalyst in N_2 saturated 1 M KOH for comparison of initial activity and after chronoamperometry for 11h.

The onset potential along with other parameters relevant for HER catalytic activity of Ni_3Te_2 has been listed in Table 2. The stability of the catalyst for the continuous HER process in 1 M KOH was studied through chronoamperometric measurements as shown in Figure 9c. As can be seen from the current vs. time plot, the electrodeposited Ni_3Te_2 on Au-glass is highly stable for HER activities for extended periods of time. The LSV collected after 11 h of continuous HER was similar to the initial LSV plot (Figure 9d) indicating that the catalyst did not suffer any degradation or loss of catalytic activity. The faradaic efficiency of the catalyst for the HER process was confirmed by the water displacement method (details have been provided in the ESI†). A 100% faradaic efficiency was obtained as shown in Figure 10. Since Ni_3Te_2 was active

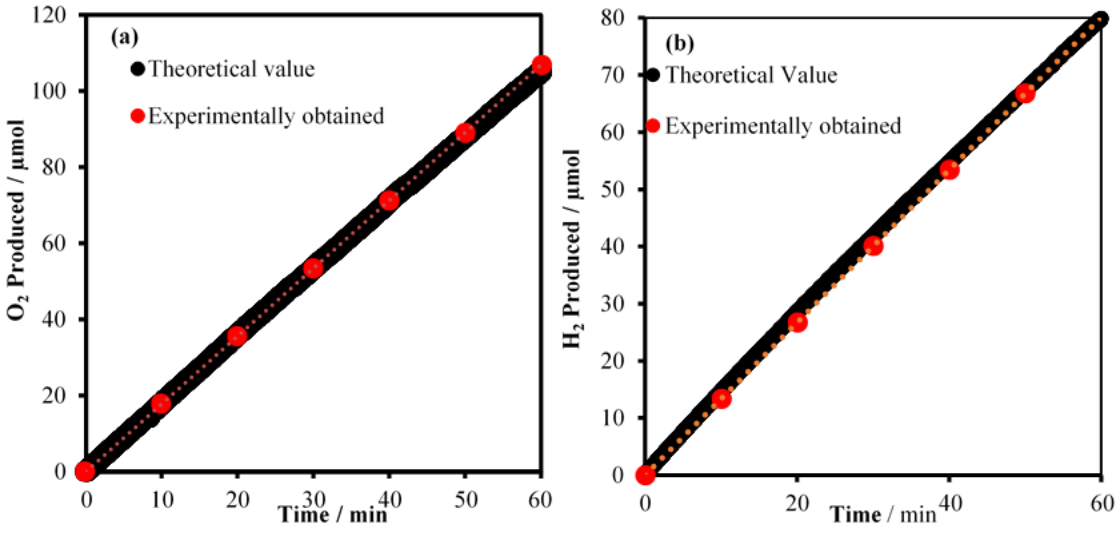

Figure 10. Comparisons of experimentally obtained volumes (a) oxygen and (b) hydrogen with the theoretically calculated amounts.

for both OER and HER in 1 M KOH, a full water electrolysis cell was constructed by coating Ni_3Te_2 on both cathode and anode. It was observed that Ni_3Te_2 could effectively split water producing a current density of 10 mA cm^{-2} at a cell voltage of 1.62 V. The electrolysis energy efficiency was calculated to be 91.8% using the standard method.[52]

Table 4. Comparison of onset, overpotential and electronegativity values of nickel oxide and chalcogenides[a].

	NiO_x	**Ni_3S_2**	**Ni_3Se_2**	**Ni_3Te_2**
η @ 10mA cm^{-2} / mV	360	330	280	180
Onset potential vs RHE / V	1.48	1.46	1.33	1.38
Electronegativity[51]	3.44	2.58	2.55	2.10
[a] NiO, Ni_3S_2, Ni_3Se_2 and Ni_3Te_2 catalysts were electrodeposited on Au-glass				

In this report we have presented the highly efficient OER and HER electrocatalytic activity for Ni_3Te_2 in alkaline medium for the first time. The low onset potential and overpotential at 10 mA cm^{-2} achieved for the OER make this catalyst one of the most efficient electrocatalysts for water oxidation reactions. Moreover, Ni_3Te_2 when compared to other chalcogenides in this series such as Ni_3Se_2 and Ni_3S_2 shows a systematic trend of increasing activity down the chalcogenide series (Table 4, Figure S17†). This trend of increasing OER catalytic activity from oxide to telluride proves the hypothesis for the first time that increasing covalency and decreasing electronegativity of systematic trend of increasing activity down the chalcogenide series (Table 4, Figure S17†). This trend of increasing OER catalytic activity from oxide to telluride proves the hypothesis for the first time that increasing covalency and decreasing electronegativity of the anionic network around the transition metal center will lead to improvement in catalytic efficiency. Through detailed electrochemical studies we have shown that such enhancement in OER catalytic activity can be attributed to the changing redox potential of the catalytically active metal center. Hence, apart from being the first example of Ni-telluride as an OER and HER electrocatalyst, this study also introduces the concept of systematically enhancing the OER catalytic activity through tuning the coordination atmosphere around the catalytically active site. Comparison with other Ni-based OER catalysts reported previously (Table 5) reveals that Ni_3Te_2 is definitely as good as or even better than the best Ni-based OER catalyst. These findings coupled with simple synthesis methods such as electrodeposition and hydrothermal synthesis, and possibilities to tune the catalytic efficiencies even further, make these nonprecious metal-based water splitting catalysts lucrative for various energy-related practical applications.

Table 5. Comparison of the catalytic activities of Ni-based catalysts.

Catalysts	Electrolytes	Onset potential V	η @ 10 mA cm^{-2} (mV *vs* RHE)	Reference
NiO_x nanoparticles[b]	1M KOH	1.52 [a]	331	25
NiO_x/C	1M KOH	1.51 [a]	335	20
Amorphous NiO	1 M KOH	1.54 [a]	>470 [b]	54
α-$Ni(OH)_2$	0.1M KOH	1.54 [a]	331	55
$Ni(OH)_2$ /NiOOH	1 M KOH	1.80 [a]	525	56
$Ni(OH)_2$ nanoparticles[b]	1M KOH	1.48 [a]	299	25
Ni_3S_2–Ni foam	0.1M KOH	1.387	187	27
Ni_3S_2–Ni foam	1M NaOH	1.46 [a]	260	57
NiS/ Ni foam	1 M KOH	1.55	158 [b]	28
Ni_3Se_2–Ni foam	1M KOH	1.48 [a]	270 [b]	33
Ni_3Se_2/Cu foam	1M KOH	1.51	343 [c]	58
$NiSe_2$ /Ti	1 M KOH	1.53 [a]	320 [d]	16
$NiSe_2$	1 M KOH	1.43	250	24
$NiSe_2$-DO	1M KOH	1.46 [a]	241	17
$NiSe_2$ /Ti	1M KOH	1.53 [a]	295 [b]	59
Ni_3Se_2– Au Glass	0.3 M KOH	1.45	320 ±20	30
Ni_3Se_2–Ni foam		1.46	270 ± 20	
Ni_3Se_2 (30 s dissolution) @Au	1M NaOH	1.39	190	31
$Ni_{0.78}Fe_{0.22}(OH)_x$ /C	0.1M KOH	1.45	290	60
$NiSe_2$ nanosheets	1MKOH	1.55	323	61
$Ni_{0.9}Fe_{0.1}O_x$	1M KOH		336	62
$Ni_{62}Fe_{38}O_x$ /C	0.1 M KOH	1.481	290	63
Ni_{45}–Fe_{55}(OOH)	1M KOH	1.43	300	64
Ni_3Te_2– Au Glass	1M KOH	1.38	210 [e]	This work
Ni_3Te_2–Ni foam		1.45	230 [f]	
Ni_3Te_2– CFP		1.41	210	
Ni_3Te_2– C Cloth		1.42	210	
Ni_3Te_2– GC		1.36	180	
Ni_3Te_2 - Hydrothermal		1.38	220	

[a] Calculated from references; [b]@ 20 mA cm^{-2}; [c]@ 50 mA cm^{-2}; [d]@ 100 mA cm^{-2}, [e] supplementary Figure S3a , [f] supplementary Figure S3b.

ACKNOWLEDGEMENT

This research was supported from the National Science Foundation (DMR 1710313), the American Chemical Society Petroleum Research Fund (54793-ND10), and ERDC (Missouri S&T).

SUPPLEMENTARY INFORMATION

1. EXPERIMENTAL PROCEDURE

1.1. ELECTRODEPOSITION OF RuO_2 ON AU-GLASS [S1]

Electrodeposition of RuO_2 on Au-glass substrate was carried out from a mixture of $RuCl_3$ (0.452 g) and KCl (2.952 g) in 40 ml of 0.01M HCl by using cyclic voltammetry from 0.015 to 0.915 V (vs. Ag|AgCl) for 100 cycles at a scan rate of 50 mV s^{-1} . Finally heated at 200 °C for 3 h in presence of Air.

1.2. ELECTRODEPOSITION OF Ni_3S_2 ON AU-GLASS [S2a]

The Ni_3S_2 films were deposited on to the Au-glass substrate by deposition bath containing 50 mM $NiCl_2{\cdot}6H_2O$ and 1 M thiourea. Electrodeposition of Ni_3S_2 on Au-glass substrate was conducted within the potential range between −1.2 V and 0.2 V vs. Ag|AgCl at a scan rate of 5 mV s^{-1} for 6 sweep cycles.

1.3. ELECTRODEPOSITION OF Ni_3Se_2 [S2b]

Ni_3Se_2 was electrodeposited on the substrate by a controlled-potential deposition at −0.80 V (vs. Ag/AgCl) for 300 s from an aqueous solution containing 10 mM $Ni(CH_3CO_2)_2{\cdot}4H2O$, 10 mM SeO_2 and 25 mM LiCl at 25 °C. The pH of the electrolytic bath was adjusted with dilute HCl to be 2.5. After electrodeposition, the substrates were washed with deionized water in order to remove impurities and adsorbents from the surface.

1.4. CALIBRATION OF Ag|AgCl

The Ag|AgCl|KCl(sat.) reference electrode was calibrated by measuring open circuit potential (OCP) at Pt wire in pure H_2 saturated 1.0 M H_2SO_4 solution. A value of -0.197 V was obtained as the OCP which was used as the standard potential of Ag|AgCl in this article. The measured potentials vs the Ag/AgCl at any given pH is were converted to the reversible hydrogen electrode (RHE) scale via Nernst equation:

$$E_{RHE} = E_{Ag|AgCl} + 0.059Ph + E^{o}_{Ag|AgCl}$$

where E_{RHE} is the converted potential vs. RHE, $E_{Ag|AgCl}$ is the experimentally measured potential against Ag|AgCl reference electrode, and $E^{o}_{Ag|AgCl}$ is the standard potential of Ag|AgCl at 25 °C (0.197 V).

1.5. KOH ELECTROLYTE PURIFICATION[S3]

1 M KOH electrolyte was purified following a reported procedure.[S3] In a H_2SO_4-cleaned 50 mL polypropylene centrifuge tube, ~2 g of 99.999% $Ni(NO_3)_2 \cdot 6H_2O$ was dissolved in ~4 mL of 18.2 MΩ·cm H_2O. 20 mL of 1 M KOH were added to precipitate high-purity $Ni(OH)_2$. The mixture was shaken and centrifuged, and the supernatant was decanted. The $Ni(OH)_2$ then underwent three washing cycles by adding ~20 mL of 18.2 MΩ·cm water and ~2 mL of 1 M KOH to the tube, redispersing the solid, centrifuging, and decanting the supernatant. Finally, the tube was filled with 50 mL of 1 M KOH for purification. The solid was redispersed and mechanically agitated for at least 10 min, followed by at least 3 h of resting. The mixture was centrifuged, and the purified KOH supernatant was decanted into a H_2SO_4-cleaned polypropylene bottle for storage.

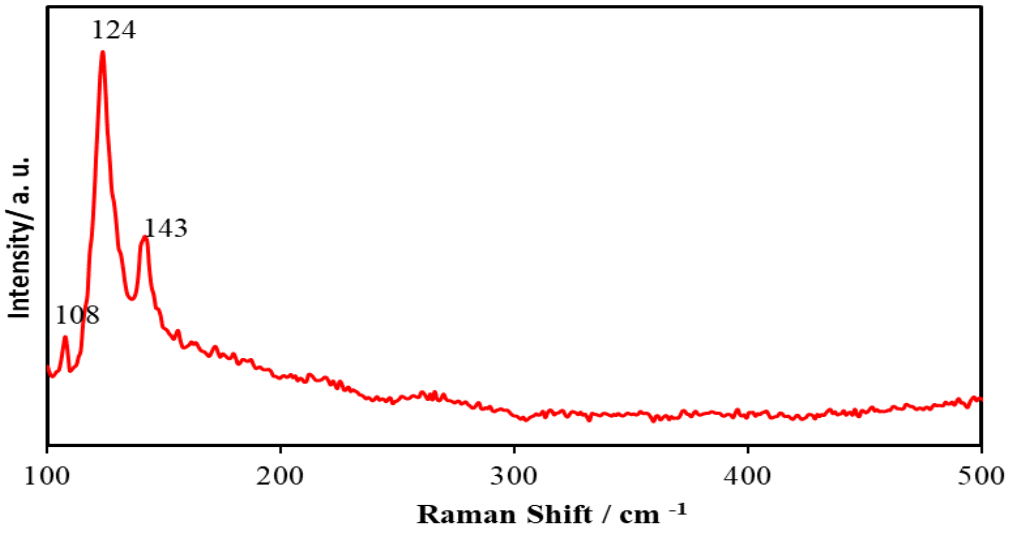

Figure S1. Raman spectrum of the Ni_3Te_2 electrodeposited on Au substrate.

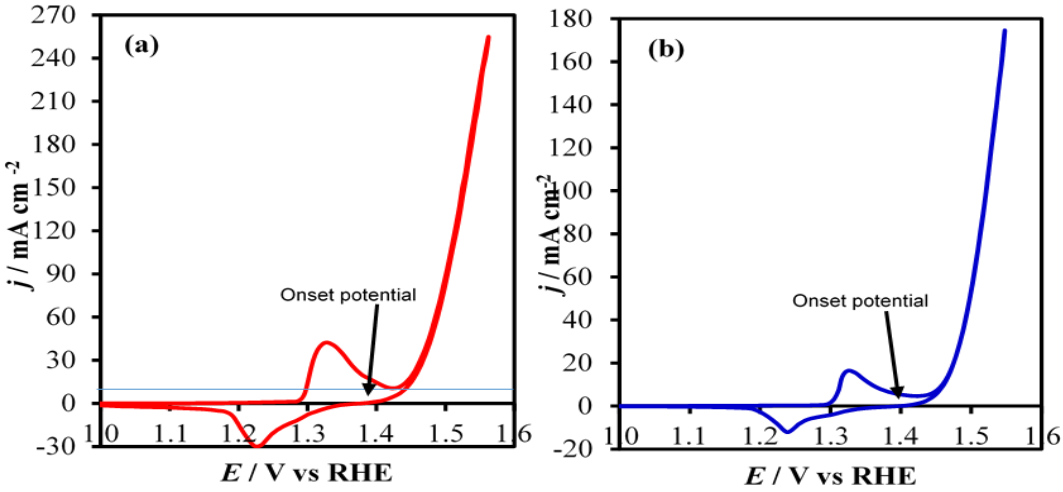

Figure S2. Cyclic voltammograms of Ni_3Te_2 electrodeposited on (a) Au glass (b) Ni foam in N_2 saturated 1M KOH solution.

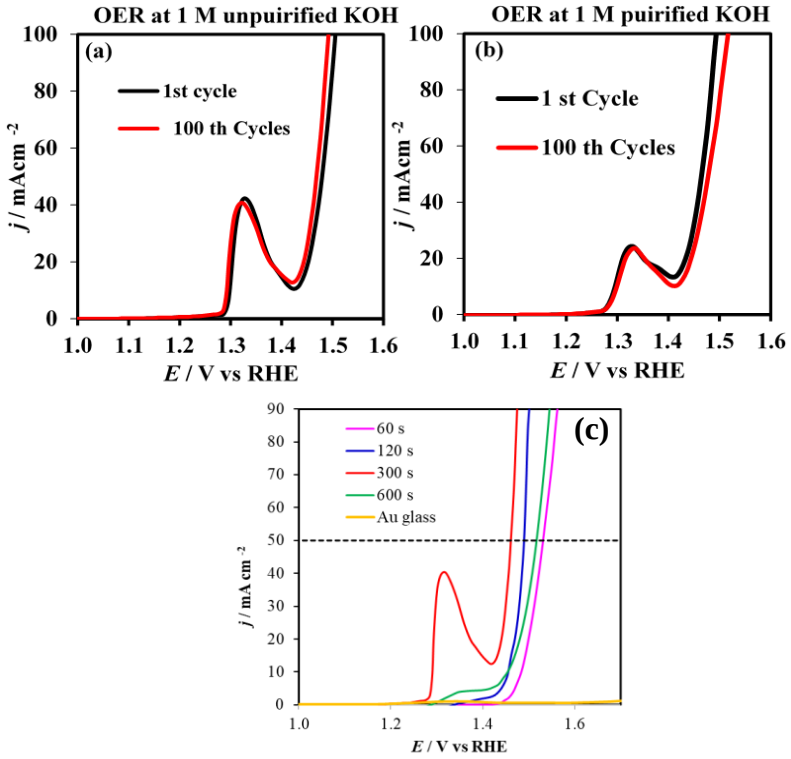

Figure S3. Cyclic voltammograms for OER of 1 st cycle and 100 th cycles for (a) unpurified 1 M KOH (b) purified 1 M KOH prepared as mentioned above (c) LSV measured in N_2 saturated 1M KOH solution at hydrothermally synthesized Ni_3Te_2 on Au electrode to check the Ni preoxidation peak.

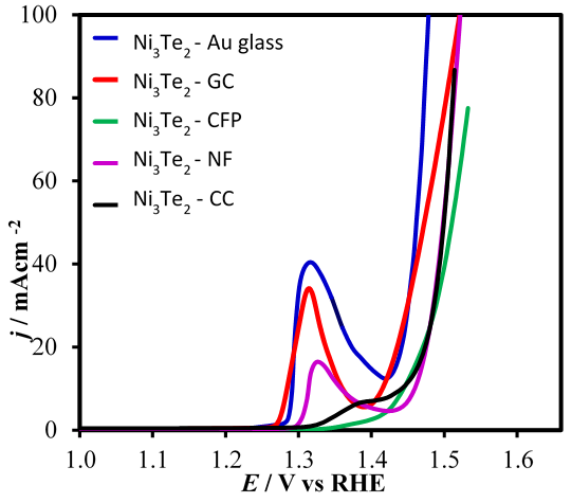

Figure S4. LSVs measured at Ni_3Te_2 @ Au for different electrodeposition times in N_2 saturated 1 M KOH solution at a scan rate of 0.01V s^{-1}.

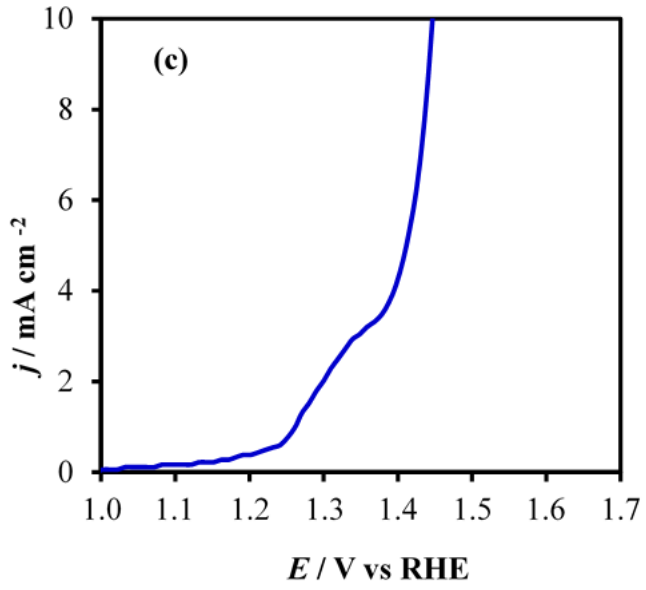

Figure S5. OER activity of Ni_3Te_2 catalysts electrodeposited for 300 s on various substrates.

1.6. COMPARISON OF HYDROXYL ATTACHMENT ON NI SITES (CATALYST ACTIVATION): DENSITY FUNCTIONAL THEORY (DFT) CALCULATIONS

The adsorption energy of the hydroxyl ion on the catalyst surface of NiO and Ni_3Te_2 was calculated by employing DFT calculations using projected augmented wave (PAW) method [S4], that are implemented in the Vienna Ab initio Simulation Package (VASP). [S5,S6] The exchange-correlation interaction was treated in the framework of generalized gradient approximation (GGA) using the Perdew-Burke-Ernzerhof (PBE) functional [S7] and ultrasoft potentials. [S8] Since the rotationally invariant version of the GGA+U method can give a good description of the cohesive energy, electronic structure, and mechanical and magnetic properties of bulk and surfaces of materials, the GGA+U method was used to study the adsorption energy of OH^- ion on various Ni sites of NiO

and Ni_3Te_2. A plane wave cut-off of 400 eV was set up to ensure convergence in energy. The Brillouin zone was sampled using Mokhorst-Pack generated sets of K-points. [S9]

The (001) surface of NiO, and (001) and (010) surfaces of Ni_3Te_2 were selected to estimate the favorable adsorption Ni sites of OH^- ion in the DFT calculations. K-point meshes of 5×5×1, 5×11×1 and 5×5×1 were found to be sufficient to a self-consistent field (SCF) convergence criterion of 1×10^{-4} eV for NiO (001) surface, Ni_3Te_2 (001) surface and Ni_3Te_2 (010) surface, respectively. Free surfaces of Ni_3Te_2 and NiO were simulated using a slab model with 1×1×2 super cells (or 1×2×1, depending on the orientation of free surface), as shown in Fig. S6a and Fig. S7a, respectively. A relatively large vacuum gap of ~20 Å was set between free surfaces to prevent the interactions of the system and its periodically repeated images. Thus, dipole corrections were applied perpendicular to the surface plane. As shown in Fig. S6a and Fig. S7a, the bottom lattice of the model was fixed at the ground-state bulk distances, while the top lattice was set to be free to move in all directions.

The OH^- adsorption energy (E_{ad}) was calculated from equation 1.

$$E_{ad} = E_{\text{NiX-OH}^-} - [E_{clean} + E_{\text{OH}^-}] \quad (1)$$

where, E_{clean} is the internal energy of the slab models for Ni_3Te_2 and NiO (see Figure S6 & S7), E_{OH^-} is the internal energy of the isolated OH^- ion, and $E_{\text{NiX-OH}^-}$ is the total formation energy of NiX surface with bound OH^- (X = O or Te) (see Figure S8, S9, and S10).

By adapting the quasi-Newton scheme as the convergence criterion, the relaxation was first carried out to reconstruct the free surfaces of the slab model, as well to obtain the clean internal energy: E_{NiX}. Thereafter, an OH^- ion was placed on the top of the

active Ni site (on the relaxed free surface) at a distance of 1.86 Å [S10] to calculate the total formation energy $E_{NiX\text{-}OH^-}$.

For the Ni-oxide surface, the OH^- ion was placed right above one Ni-site on NiO (001) surface (Figure S8a). It was observed that after relaxation the three Ni sites on (001) surface slightly move out of the initial plane due to the interaction with the more electronegative OH^- ion (Figure S8b). Such displacement of the metal ions following binding with the hydroxyl anion has been observed previously.[S11] The OH^- ion adsorption energy was calculated to be -1.608 eV using Eq. 1 as mentioned above.

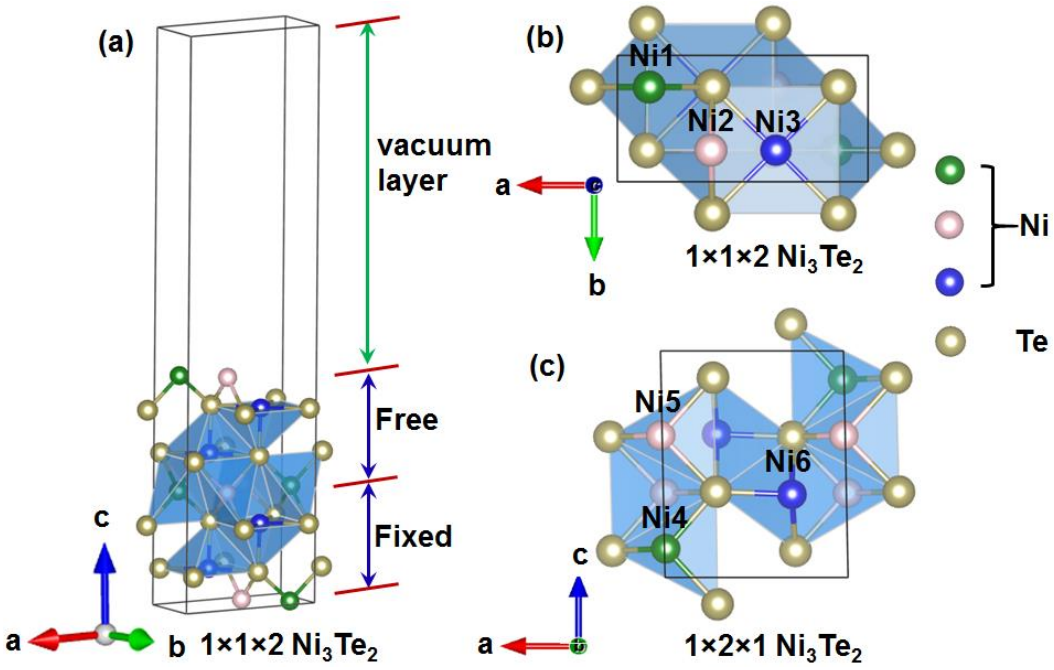

Figure S6. (a) 3-dimensional slab model of Ni_3Te_2 with lattices of 1×1×2; (b) (001) free surface (top-view) of the 1×1×2 Ni_3Te_2 crystal structure; and (c) (010) free surface (side view) of the 1×2×1 Ni_3Te_2 crystal structure. The active Ni sites are denoted as Ni1, Ni2, Ni3, Ni4, Ni5 and Ni6.

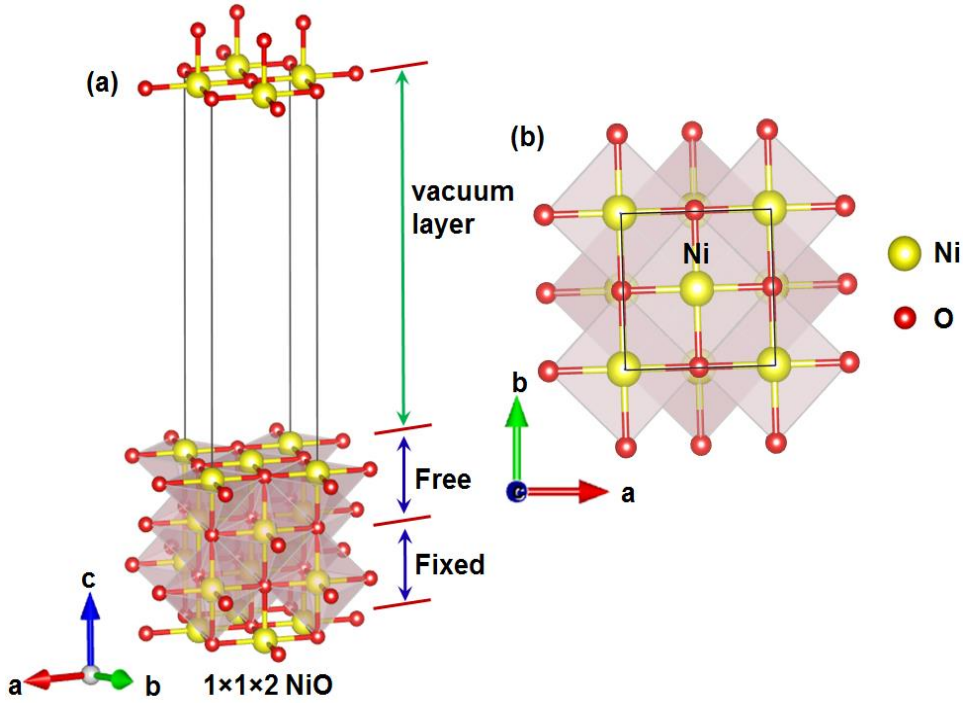

Figure S7. (a) 3-dimensional slab model of NiO with lattices of 1×1×2; (b) (001) free surface (top-view) of NiO crystal structure. The active Ni site has been pointed out.

On the other hand, owing to difference in coordinations, three distinct Ni sites on Ni_3Te_2 (two tetrahedral and one square pyramidal) on (001) and (010) surfaces, respectively, were selected to adsorb OH^- ions, as presented in Figure S9a-c and Figure S10a-c, respectively. These active Ni sites have been denoted as Ni(1), Ni(2) – tetrahedral sites on (001) plane; Ni(3) – square pyramidal on (001) plane; Ni(4), Ni(5) – tetrahedral on (010) plane and Ni(6) – square pyramidal on (010) plane as shown in Figure S9 and S10, respectively. It can be observed from Figure S9a'-c' and Figure S10a'-c' that after relaxation the coordination of OH^- ions and Ni sites, the angle of Ni-O-H, as well as the distance between OH^- ions and active Ni sites have changed owing to the adsorption interaction.

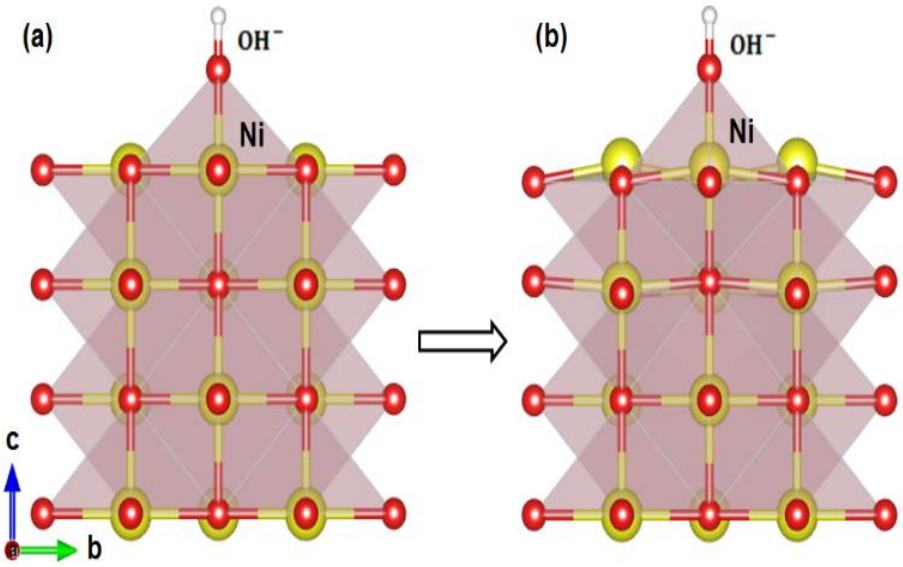

Figure S8. (a) Side view of the original crystal structure of NiO with an OH^- ion placed on the top of the active Ni site, which is located on (001) free surface. The original bond distances of Ni-O and O-H are set as 1.86 Å and 0.96 Å, respectively; (b)The relaxed structure after OH^- ion adsorbed on active Ni site.

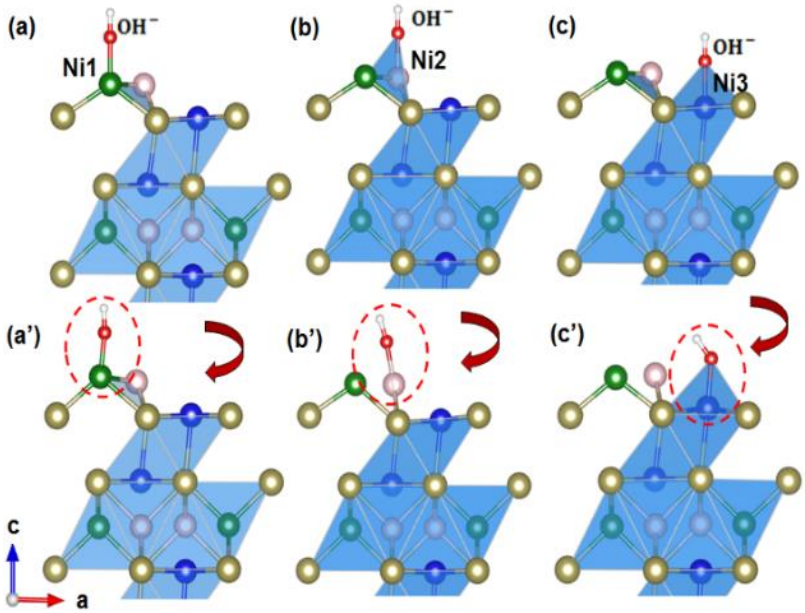

Figure S9. Side views of the original (a-c) and the corresponding relaxed (a'-c') crystal structures of Ni_3Te_2 with OH^- ions placed on the top of active Ni sites: Ni1, Ni2 and Ni3, which are located on (001) plane.

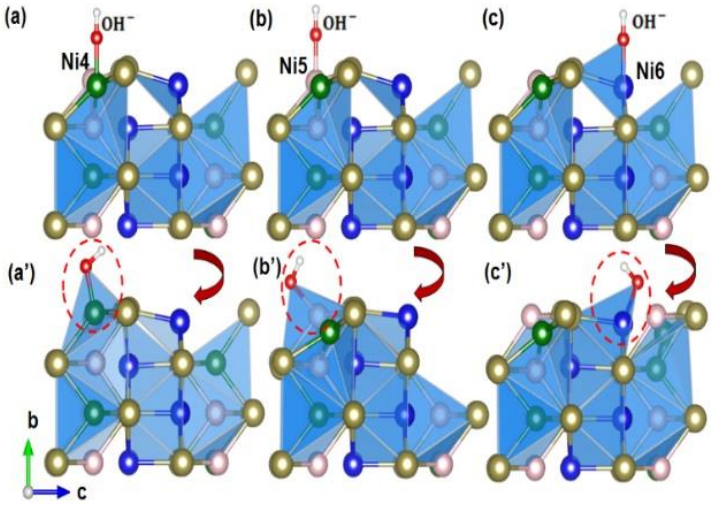

Figure S10. Side views of the original (a-c) and the corresponding relaxed (a'-c') crystal structures of Ni_3Te_2 with OH^- ions placed on the top of active Ni sites: Ni4, Ni5 and Ni6, which are located on (010) plane.

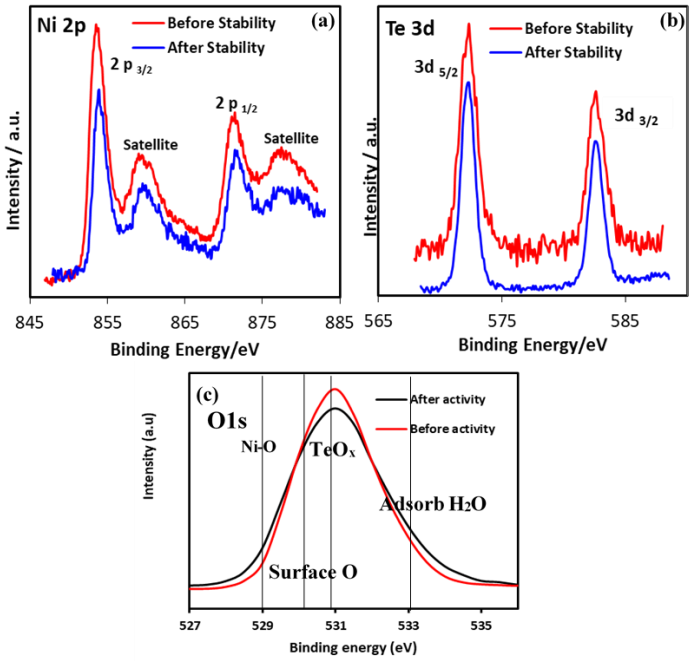

Figure S11. Comparison of (a) Ni 2p and (b) Te 3d XPS spectra of Ni3Te2 catalyst (before and after) for 24 h of stability. (c) Comparison of O1s XPS spectra of Ni3Te2 catalyst (before and after) for 24 h of stability.

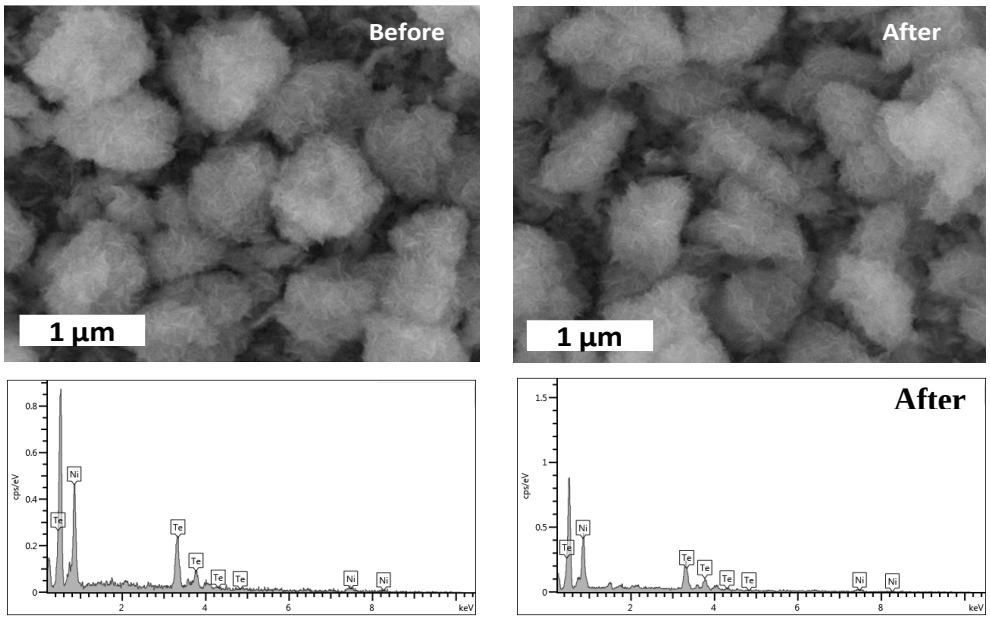

Figure S12. SEM images and corresponding EDAX spectra of Ni_3Te_2 on Au substrate show the identical morphology and composition of catalyst before and after 24h of chronoamperometry.

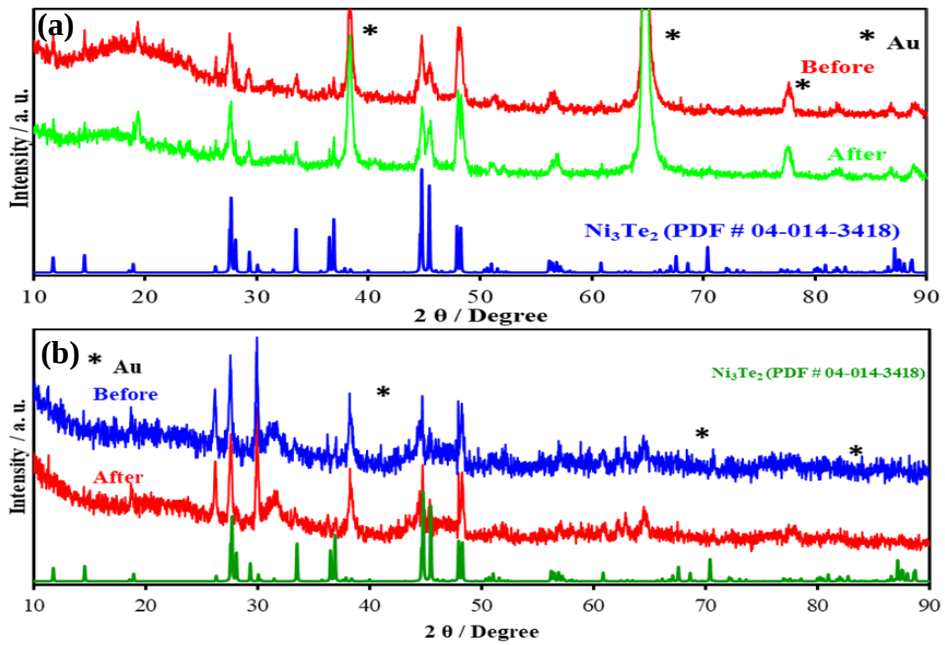

Figure S13. Comparison of XRD patterns from the catalysts after 24 h of OER activity with as prepared Ni_3Te_2 catalyst (a) synthesized from hydrothermal methods, (b) electrodeposited on Au glass.

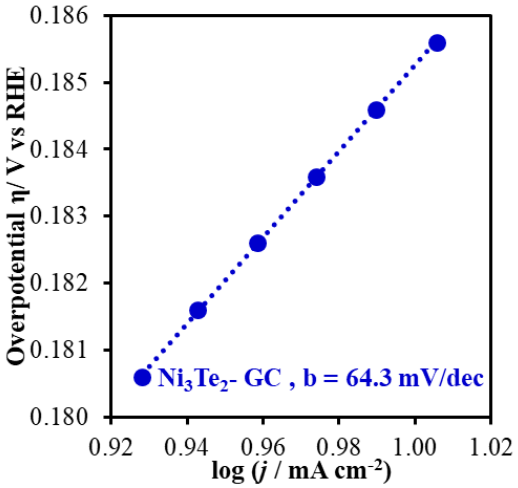

Figure S14. OER Tafel slope of Ni_3Te_2 electrodeposited on GC.

1.7. TESTING OF EVOLVED GAS

Rotating ring disk electrode (RRDE) set up was used in bipotentiostat mode to monitor the gas evolved at the anodic reaction. For this procedure Ni_3Te_2 was electrodeposited on GC disk electrode in a RRDE set-up and scanned at the anodic potential range while Pt ring was held a potential of 0.2 V (vs. RHE). The idea was to hold the Pt ring potential suitable for ORR such that if any O_2 was being produced at the disk electrode, it will be collected and reduced at the ring electrode resulting in an increase of the ring current. Both the ring current and disk current were measured as function of applied disk potential. Initially 1M KOH solution was purged with N_2 gas for 30 min before starting the reaction to remove dissolved O_2 and blanketed in N_2 atmosphere. The disk electrode was scanned from 1.0 to 1. 5 V (vs. RHE) at a scan rate of 10 mV s^{-1} at 1600 rpm. Initially, the ring current was maintained at almost zero current when disk current was almost zero. As soon as the disk current started to increase, the

ring current also increased, indicating that there was indeed oxygen reduction happening at the Pt ring electrode and this O_2 was being generated at the disk electrode (Figure 6a). From this Figure 6a the onset potential of OER was obtained as 1.36 V vs. RHE.

1.8. OER FARADAIC EFFICIENCY

Prior to RRDE measurement, N_2 gas was purged in the cell for 30 min and then blanketed with N_2 during the experiment. The disk electrode was maintained at constant potential steps from 1.41 to 1.45 V (vs RHE) for consecutive periods of 1 min each, while being rotated at a 1600 rpm under a N_2 gas blanket. The ring electrode was held at 0.2 V (vs. RHE) throughout the experiment, which was sufficiently negative to reduce the collected oxygen rapidly. The Faradaic efficiency can be given as:

$$\text{Faradaic Efficiency} = \frac{2i_r}{i_d N}$$

where i_r and i_d are the measured ring and disk currents, respectively, and N is the collection efficiency of RRDE, 0.17 in this work.

The OER faradaic efficiency of the catalyst was calculated from the ratio of ring and disk current and has been presented in Figure 6b. The highest Faradaic efficiency was obtained to be about 99.8% at the applied disk potential of 1.41 V (vs. RHE), and decreased to 47.1% with the disk voltage increasing to 1.45 V (vs. RHE).

1.9. WATER DISPLACEMENT METHOD FOR O_2 AND H_2 FARADAIC EFFICIENCY

The Faradic efficiency of OER and HER catalyst is defined as the ratio of the amount of O_2 and H_2 evolved during the catalytic experiments to the amount of O_2 and

H_2 expected based on theoretical considerations. To measure the Faradic efficiency of OER and HER, we carried out the following experiment. We collected the evolved O_2 and H_2 gas (at constant potential for 1h) by water displacement method. The theoretical amount of O_2 and H_2 were then calculated by applying Faraday law.

1.10. COLLECTION EFFICIENCY

The measured ratio of the ring limiting current to the disk limiting current is known as the collection efficiency (N) of that RRDE electrode and it can be written as:

$$N = -\frac{i_{\boldsymbol{Limiting},Ring}}{i_{Limiting,Disk}}$$

At disk electrode, the reduction of ferricyanide ($Fe(CN)_6^{3-}$) to ferrocyanide (($Fe(CN)_6^{4-}$) took place, on the other hand ferrocyanide is oxidized to ferricyanide at ring at positive potential (0.65 V vs. Ag/AgCl). The value of N was calculated and it was found to be 0.17.

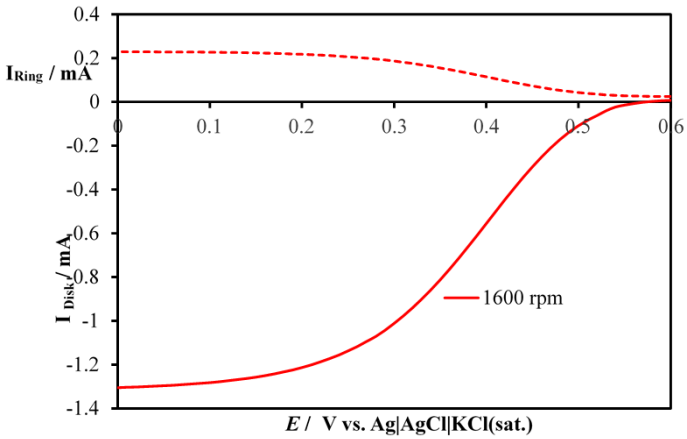

Figure S15. Rotating Ring-Disk voltamograms in N_2 saturated 0.001M $K_3Fe(CN)_6$ containing 1M KOH at 10 mV s^{-1} at different rotation rate. Ring potential was held on 0.65 V vs. Ag/AgCl which is sufficient to oxidize the product rapidly at ring. (Here ring current was shown as a potential of disk electrode).

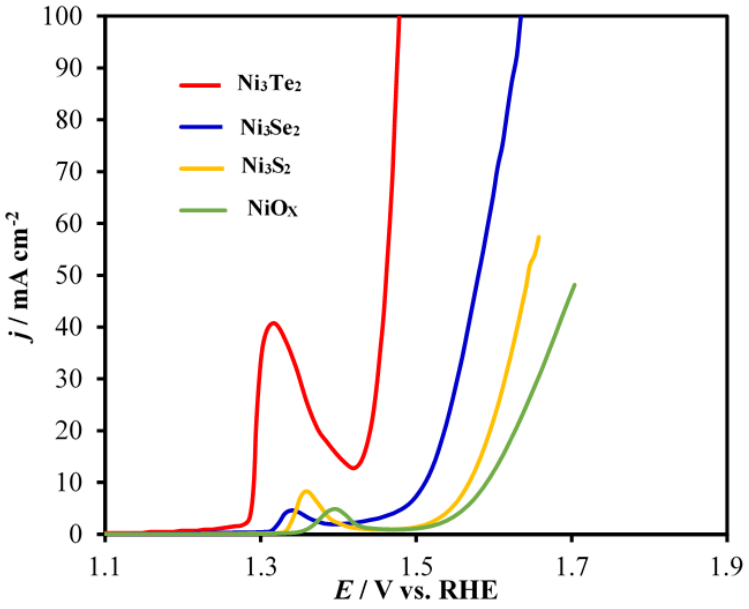

Figure S16. HER polarization curve of hydrothermally synthesized Ni_3Te_2 @ Au in N_2 saturated 1 M KOH solution at a scan rate of 10 mV s^{-1}.

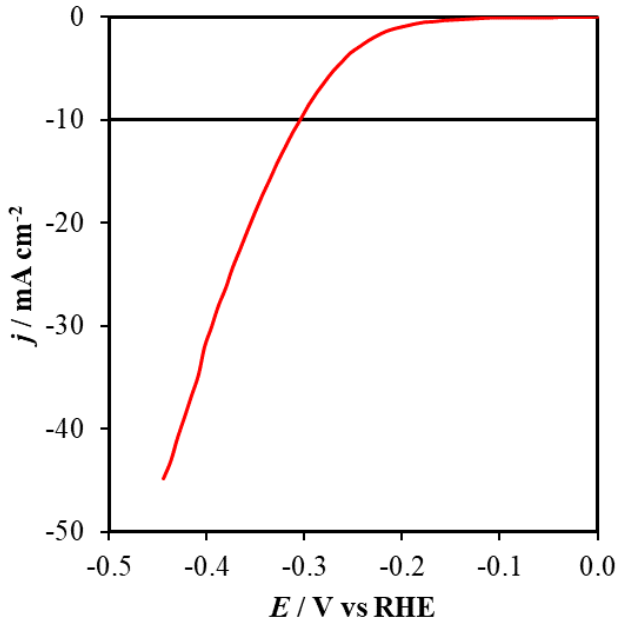

Figure S17. Comparison of polarization curves for NiO_X, Ni_3S_2, Ni_3Se_2 and Ni_3Te_2.

1.11. CALCULATION OF CATALYST LOADING

According to the Faraday's second law of electrolysis, the amount of a material deposited on an electrode is proportional to the amount of electricity used. Thus from the electrodeposition curve, the mass of catalyst can be calculated as:

$$\text{Mass} = \frac{(\text{Molecular weight of Ni3Te2} \times \text{Charge})}{(\text{No.of electron involved in process} \times \text{Faraday Constant})}$$

Here, we can get the total charge from the deposition curve at constant potential (-1.05 V vs. Ag|AgCl). As tellurium cation (Te^{4+}) is electrochemically reduced to Te^{2-}, thus the number of electron involved in the process is 6.

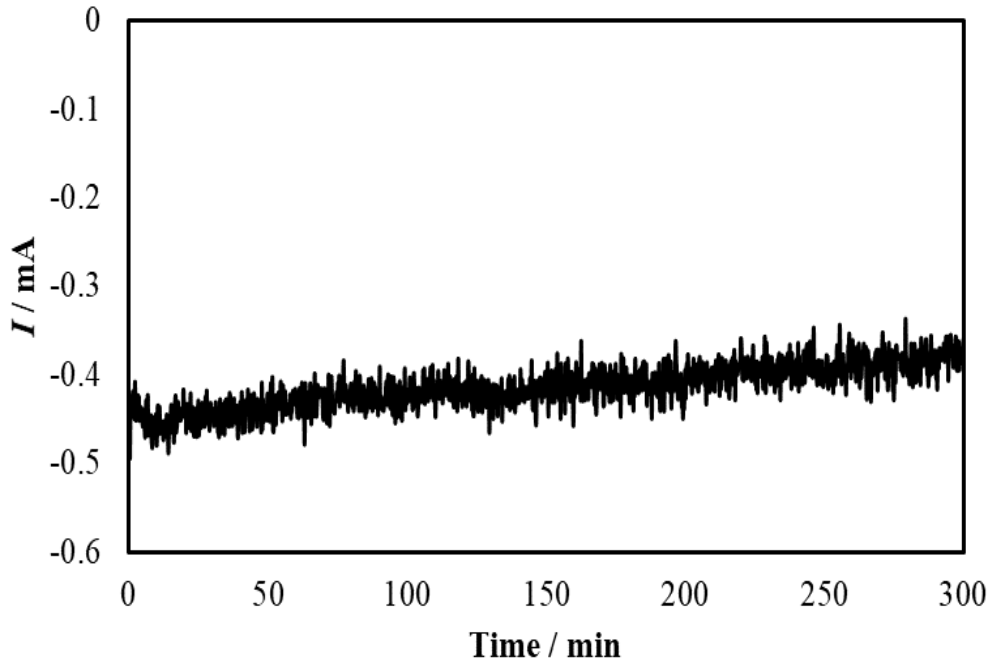

Figure S18. Electrodeposition curve for nickel telluride.

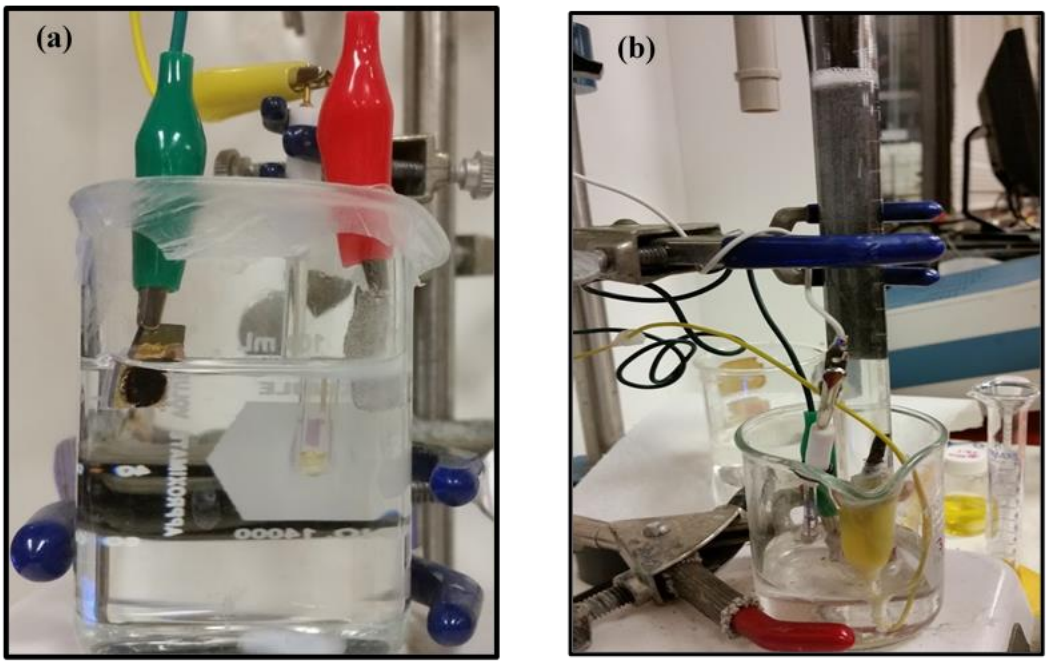

Figure S19. (a) Experimental setup of OER process (b) Image shows experiment to detect production of gaseous oxygen.

SUPPLEMENTARY INFORMATION REFERENCES

S1. C.C.McCrory,S. Jung, S.I.M. Ferrer, S.M. Chatman, J.C. Peters, J.C. and T.F. Jaramillo, *J. Am. Chem. Soc.*, 2015,137, 4347-4357.

S2a. S.W. Chou and J.Y. Lin, J. Electrochem. Soc., 2015, 162, 2762-2769.

S2b. A. T. Swesi, J. Masud and M. Nath, Energy Environ. Sci., 2016, **9**, 1771-1782.

S3. L. Trotochaud, S.L. Young, J.K. Ranney and S. W. Boettcher, J. Am. Chem. Soc., 2014, 136, 6744-6753.

S4. P.E. Blöchl, Phys. Rev. B., 1994, 50, 17953.

S5. G. Kresse and J.Furthmüller, Phys. Rev. B., 1996, 54, 11169.

S6. G. Kresse and D. Joubert, Phys. Rev. B., 1999, 59, 1758.

S7. J.P. Perdew, J.A. Chevary, S.H.Vosko, K.A. Jackson, M.R. Pederson, D.J. Singh and C. Fiolhais, Phys. Rev. B., 1992, 46, 6671.

S8. D. Vanderbilt, Phys. Rev. B., 1990, 41, 7892.

S9. H.J. Monkhorst and J.D. Pack , Phys. Rev. B.,1976,13, 5188.

S10. D. Huang and R.Holm, J. Am. Chem. Soc., 2010, 132, 4693-4701.

S11. H. Ohzuku, H Ikeno, I. Yamada and S.Yagi, AIP Conf. Proc. , 2016,1763, 040005.

REFERENCES

1. I. Dincer, Renew. Sust. Energ. Rev., 2000, 4, 157-175.

2. M. G. Walter, E. L. Warren, J. R. McKone, S. W. Boettcher, Q. Mi, E. A. Santori and N. S. Lewis, Chem. Rev., 2010, 110, 6446-6473.

3. L. Schlapbach and A. Züttel, Nature, 2001, 414, 353-358.

4. R. Subbaraman, D. Tripkovic, K. C. Chang, D. Strmcnik, A. P. Paulikas, P. Hirunsit, M. Chan, J. Greeley, V. Stamenkovic and N. M. Markovic, Nat. Mater. 2012 11, 550-557.

5. M. T. Koper, J. Electroanal. Chem., 2011, 660, 254-260.

6. C. C. McCrory, S. Jung, J. C. Peters and T. F. Jaramillo, J. Am. Chem. Soc., 2013, 135, 16977-16987.

7. A. Marshall, B. Børresen, G. Hagen, M. Tsypkin and R. Tunold, Energy. 2007, 32, 431-436.

8. P. Du and R. Eisenberg, Energy & Environ. Sci., 2012, 5, 6012-6021.

9. Y. Gorlin and T. F. Jaramillo, J. Am. Chem. Soc., 2010, 132, 13612-13614.

10. M. Gong, Y. Li, H. Wang, Y. Liang, J. Z. Wu, J. Zhou, J. Wang, T. Regier, F. Wei and H. Dai, J. Am. Chem. Soc., 2013, 135, 8452-8455.

11. M. Görlin, J. Ferreira de Araújo, H. Schmies, D. Bernsmeier, S. Dresp, M. Gliech, Z. Jusys, P. Chernev, R. Kraehnert, H. Dau, and P. Strasser J. Am. Chem. Soc. 2017, 139, 2070-2082.

12. M. Nath, In Nanotechnology: American Chemical Society, Washington DC, 2, 139-166, 2016.

13. J. Masud, A. T. Swesi, W. P. R. Liyanage and M. Nath, ACS Appl. Mater. Inter., 2016, 8, 17292-17302.

14. C. Xia, Q. Jiang, C. Zhao, M. N. Hedhili and H. N. Alshareef, Adv. Mater., 2016, 28, 77–85.

15. J. Luo, J. H. Im, M. Mayer, M. Schreier, M. Nazeeruddin, N. Park, S. Tilley, H. Fan and M. Gratzel, Science, 2014, 345, 1593–1596.

16. T. Liu, A.M. Asiri and X. Sun, Nanoscale, 2016, 8, 3911- 3915.

17. X. Xu, F. Song and X. Hu, Nat. Commun., 2016, 7, 12324

18. W. Xu, Z. Lu, X. Lei, Y. Li and X. Sun, Phys. Chem. Chem. Phys., 2014, 16, 20402–20405.

19. T. Liu, Q. Liu, A. Asiri, Y. Luo, X. Sun, Chem. Commun., 2015, 51, 16683-16686.

20. Y. Qiu, L. Xin and W. Li, Langmuir., 2014, 30, 7893–7901.

21. C. Tang, A.M. Asiri and X. Sun, Chem. Commun., 2016, 52, 4529-4532.

22. Z. Peng, D. Jia, A. Al-Enizi, A, Elzatahry and G. Zheng, Adv. Energy Mater. 2015, 5, 1402031-1402038.

23. D. Tang, J. Liu, X. Wu, R. Liu, X. Han, Y. Han, H. Huang, Y. Liu and Z. Kang, ACS Appl. Mater. Inter., 2014, 6, 7918–7925.

24. I. H. Kwak, H. S. Im, D. M. Jang, Y. W. Kim, K. Park, Y. R. Lim, E. H. Cha and J. Park, ACS Appl. Mater. Inter., 2016, 8, 5327−5334.

25. L. A. Stern and X. Hu, Faraday Discussions 2014, 176, 363-379.

26. P. D. Tran, S. Y. Chiam, P.P. Boix, Y. Ren, S. S. Pramana, J. Fize, V. Artero and J. Barber, Energy & Environ. Sci., 2013, 6, 2452-2459.

27. W. Zhou, X. J. Wu, X. Cao, X. Huang, C. Tan, J. Tian, H. Liu, J. Wang and H. Zhang, Energy & Environ. Sci., 2013, 6, 2921-2924.

28. W. Zhu, X. Yue, W. Zhang, S. Yu, Y. Zhang, J. Wang and J. Wang, Chem. Commun., 2016, 52, 1486-1489.

29. L. L. Feng, G. Yu, Y. Wu, G. D. Li, H. Li, Y. Sun, T. Asefa, W. Chen and X. Zou, J. Am. Chem. Soc.,2015, 137, 14023-14026.

30. A. T. Swesi, J. Masud and M. Nath, Energy & Environ. Sci., 2016, 9, 1771-1782.

31. A. T. Swesi, J. Masud and M. Nath, J. Mater. Res., 2016, 1-9.

32. J. Masud, P. C. Ioannou, N. Levesanos, P. Kyritsis, and M. Nath, Chem.Sus.Chem.,2016, 9, 3128-3132.

33. C. Tang, N. Cheng, Z. Pu, W. Xing and X. Sun, Angew. Chem. Int. Edit., 2015, 54, 9351 –9355.

34. J. Shi, J. Hu, Y. Luo, X. Sun, and A. Asiri, Catal. Sci. Technol., 2015, 5, 4954-4958.

35. C. Wang, J. Jiang, T. Ding, G. Chen, W. Xu, and Q. Yang, Adv. Mater. Interfaces., 2016, 3, 1500454.

36. K. Xu, P. Chen, X. Li, Y. Tong, H. Ding, X. Wu, W. Chu, Z. Peng, C. Wu and Y. Xie, J. Am. Chem. Soc.,2015, 137, 4119-4125.

37. S.Hu, M.R. Shaner, J.A. Beardslee, M. Lichterman, B. S. Brunschwig and N. S. Lewis, Science. 2014, 344, 1005-1009.

38. J. Masud, S. Umapathi, N. Ashokaan and M. Nath, J. Mater. Chem. A., 2016, 4, 9750-9754.

39. M. Ledendecker, S. K. Calderon, C. Papp, H.P. Steinruck, M. Antonietti and M. Shalom, Angew. Chem. Int. Edit., 2015, 127, 12538–12542.

40. Q. Liu, S. Gu and C. Li, J. Power Sources., 2015, 299, 342-346.

41. Y. Xu and M.A.A. Schoonen, Am. Mineral., 2000, 85, 543-556.

42. F. A. Rasmussen and K.S. Thygesen, J. Phys. Chem. C., 2015, 119, 13169-13174.

43. C. Wombwell and E. Reisner, Chem. Eur. J., 2015, 21, 8096-8104.

44. N. Levesanos, W.P.R. Liyanage, E. Ferentinos, G. Raptopoulos, P. Paraskevopoulou, Y. Sanakis, A. Choudhury, P. Stavropoulos, M. Nath and P. Kyritsis, Eur. J. Inor. Chem., 2016, 34, 5332-5339.

45. Patterson, A.L The Scherrer formula for X-ray particle size determination. Phys. Rev. 56, 978 (1939).

46. E. Ferentinos, D. Maganas, C. P. Raptopoulou, A. Terzis, V. Psycharis, N. Robertson and P. Kyritsis, Dalton T., 2011, 40, 169-180.

47. D. Maganas, J. Krzystek, E. Ferentinos, A.M. Whyte, N. Robertson, V. Psycharis, A. Terzis, F. Neese and P. Kyritsis, Inorg. Chem., 2012, 51, 7218-7231.

48. W. Bensch, W. Heid, M. Muhler, S. Jobic, R. Brec and J. Rouxel, J. Solid. State. Chem., 1996, 121, 87-94.

49. O. Rotlevi, K.D. Dobson, D. Rose and G. Hodes, Thin Solid Films., 2001, 387, 155-157.

50. M.R. Gao, X. Cao, Q. Gao, Y.F. Xu, Y.R. Zheng, J. Jiang and S.H. Yu, ACS Nano., 2014, 8, 3970-3978.

51. T. Shinagawa, A.T. Garcia-Esparza, and K.Takanabe, Sci. Rep.UK., 2015. 5.13801

52. A. L. Allred , J. Inorg. Nucl. Chem., 1961, 17, 215.

53. W. Kreuter and H. Hofmann, Int. J. Hydrogen Energy, 1998, 23, 661-666.

54. L. Kuai, J. Geng, C. Chen, E. Kan, Y. Liu, Q. Wang and B.A. Geng, Angew. Chem. Int. Edit. , 2014.53, 7547–7551 (2014).

55. M.Gao, W. Sheng, Z. Zhuang, Q. Fang, S. Gu, J. Jiang and Y. Yan, J. Am. Chem. Soc., 2014, 136, 7077-7084.

56. S. Klaus, Y. Cai, M. Louie, L. Trotochaud and A. T. Bell, J. Phys. Chem. C., 2015,119, 7243-7254.

57. L. L. Feng, G. Yu, Y. Wu, G. D. Li, H. Li, Y. Sun, T. Asefa, W. Chen and X. Zou, J. Am. Chem. Soc.,2015, 137, 14023-14026.

58. J. Shi, J. Hu, Y. Luo, X. Sun and A. M. Asiri, Catal. Sci. Technol., 2015, 5, 4954 - 4958.

59. Z. Pu, Y. Luo, A. M. Asiri and X. Sun, ACS Appl. Mater. Inter., 2016, 8, 4718- 4723.

60. S. Dresp and P. Strasser, ECS Transactions, 2016, 75, 1113-1119.

61. Z. Wang, J. Li, X. Tian, X. Wang, Y. Yu, K.A. Owusu, L. He and L. Mai, ACS Appl. Mater. Inter., 2016, 8, 19386-19392.

62. L. Trotochaud, J.K. Ranney, K.N. Williams and S. W. Boettcher, J. Am. Chem. Soc., 2012, 134,17253-17261.

63. M. Görlin, M. Gliech, J.F. de Araújo, S. Dresp, A. Bergmann and P. Strasser, Catal. Today., 2016, 262, 65-73.

64. M. Görlin, J. F. de Araújo, H. Schmies, D. Bernsmeier, S. Dresp, M. Gliech, Z. Jusys, P. Chernev, R. Kraehnert, H. Dau and P. Strasser, J. Am. Chem. Soc., 2017, 139, 2070-2082.

II. INTRINSIC ACTIVITY OF TRIFUNCTIONAL ELECTROCATALYST: COBALT TELLURIDE IN ALKALINE MEDIUM

Manuscript has been submitted to Chemistry of Materials

Umanga De Silva[a], Matthew Perkins[b], Wipula P.R. Liyanage[a], Siddesh Umapathi[a], Jahangir Masud[a], Manashi Nath*[a]

[a] Department of Chemistry, Missouri University of Science and Technology, Rolla, MO 65409.

[b] Department of Chemical and Biochemical Engineering, Missouri University of Science and Technology, Rolla, MO 65409.

*Email: nathm@mst.edu

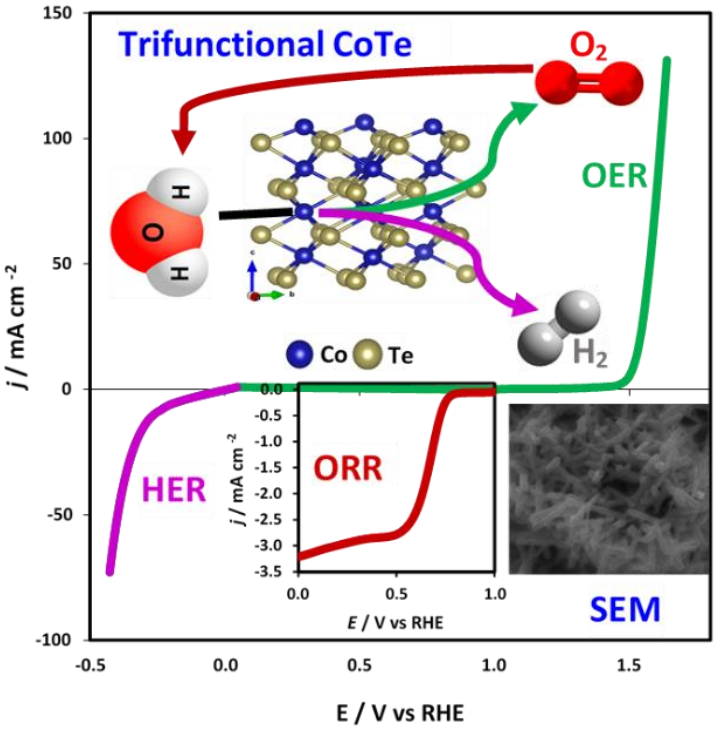

ABSTRACT

Efficient bifunctional electrocatalysts for alkaline oxygen evolution and hydrogen evolution reactions are persuaded the kinetics of water splitting and enhance renewable energy to chemical energy. Among these electrocatalysts, noble metal free $CoTe_2$ catalysts are favored because of their abundance, low cost and similar electronic state of d-orbitals to the traditional, precious state of the art catalysts. Due to the half-filled e_g d orbital density of Co species and higher covalancy of the tellurides in cobalt tellurides increase the higher catalytic performance for OER and HER in water splitting process. Herein, we synthesized two phases of of $CoTe_2$ and CoTe in electrodeposition and hydrothermal methods. The electrodeposited CoTe showed the better performance with the lowest over potential of 200 mV at 10 mA cm^{-2} benchmark potential and low Tafel slope of 43.8 mV dec^{-1}.

Key words: Cobalt telluride, Oxygen evolution reaction, Bi-functional, Electrocatalysts

1. INTRODUCTION

Hydrogen has been identified as clean, zero carbon content, sustainable and promising energy source for the future.[1-3] Currently, hydrogen is mainly produced from steam reforming process which accelerates depletion of fossil fuel reserves and leads to CO_2 emissions. Water electrolysis on the other hand, has long been recognized as an environmentally benign, clean, efficient procedure that can lead to on-demand production for high purity hydrogen.[4-6] Electrochemical water splitting is consists of two half-cell

reactions, oxygen evolution reaction (OER) which occurs at anode and hydrogen evolution reaction (HER) taking place at the cathode. Efficiency of water splitting reaction and consequently hydrogen production from water electrolysis is limited by OER which is an energy-intensive uphill process requiring a large overpotential exceeding the thermodynamic water splitting voltage of 1.23 V.[7-8] Typically electrocatalysts are employed to reduce the overpotentials for HER and OER. An efficient and practically feasible electrocatalyst is expected to exhibit low overpotential, high current density, long-term stability, as well as being economically cost-effective in terms of raw materials availability and processing conditions. Conventionally, Pt-based catalysts have shown superior performance as HER electrocatalysts [9-10] while oxides of Ir and Ru are considered as state-of-the-art electrocatalysts for OER.[11-15] However, Pt, Ir, and Ru belong to the class of precious metal (generically referred to as PGMs) with limited availability on earth's crust which reduces practically useability of these electrocatalysts for large scale water electrolysis set-up. Continued search to replace the PGM-based electrocatalysts has led to the formulation of several non-precious metal based electrocatalysts for OER and HER. Among these transition metal compounds of the ferrous metal group (Fe, Co, Ni), has made a significant impact in this research area owing to their unprecedented high catalytic activity characterized by low overpotential. These transition metal composition include oxides, hydroxides, carbides, nitrides, phosphides, and chalcogenides.[16-25] Among the transition metals, Co deserves special mention since it was predicted that modulating *d*-electron density around the catalytic site, especially a half-filled e_g orbital will lead to more optimal charge transfer at the catalyst-water interface making Co occupy top of the Sabatier plot exhibiting optimal rate

for OER in alkaline medium.[26] Accordingly Co-oxides and hydroxides have been studied extensively for OER activity in alkaline medium.[27-39] In addition to oxides, other composition of Co specifically, N-C composites [40-43], phosphides [44-48] phosphates[49-54], metal organic frameworks [55-57] and chalcogenides [58-72] have also been investigated as potential applicants for electrocatalytic water splitting. Apart from OER, catalysts supporting the complimentary reaction of oxygen reduction reaction (ORR) has also gained importance, since it is the primary process in fuel cells. In ORR, the reactive species is dioxygen molecules that is attached and further reduced on the catalytic site through 2-electron or 4-electron reduction pathway to form hydrogen peroxide or water, respectively.[73] It has been observed that Co shows significantly improved activity for ORR both in Co-based compounds as well as in single atomic site catalysts.[73-75] Hence, ideally designing a OER-ORR multifunctional catalyst with Co-based composition seems quite feasible, since such catalysts can aid both energy conversion and storage.

Previously we had hypothesized that replacing oxide with lesser electronegative chalcogenide anions will lead to improved OER electrocatalytic performance. Such enhancement in electrocatalytic performance was attributes to enrichment of electron density around the transition metal site which leads to lowering of local site electrochemical oxidation potential and facilitates catalyst activation for OER.[76] This hypothesis was confirmed in the family of Ni-based chalcogenides whereby, Ni-tellurides and selenides exhibited significantly better OER electrocatalytic performance compared to Ni-oxide. Since the transition metal site can also ace as the catalytic center for ORR, and since ORR also proceeds via adsorption of reactive O-containing species, it can be expected that decreasing anion electronegativity around the catalytically active transition

metal site will also positively affect the ORR activity. Hence, selenides and tellurides can be expected to exhibit improved ORR performance compared to oxides and this was further confirmed by superior ORR activity of Co_7Se_8.[73]

Among the chalcogenides, tellurides have gained increasing importance in materials chemistry owing to their plethora of widely different properties. Nanostructured metal tellurides as catalysts have gained substantial amount of attention due to their favorable applications in energy conversion and storage devices.[76-80] Few transition metal tellurides have recently been reported as bifunctional electrocatalysts for water splitting showing high catalytic performance. [69,76,81,82]

In this article we have reported multifunctional electrocatalytic properties of two cobalt telluride phases, CoTe and $CoTe_2$. These cobalt tellurides show high catalytic activity for OER, ORR, and HER in alkaline medium. The cobalt tellurides were synthesized by direct electrodeposition and hydrothermal methods. Among these electrodeposited CoTe exhibited better OER property requiring low overpotential of 200 mV to reach 10 mA/cm^2. The electrocatalysts were also studied through DFT calculations specifically to understand catalyst activation through attachment of surface hydroxyl group which revealed that CoTe had better -OH adsorption energy commensurate with its superior OER activity. $CoTe_2$ on the other hand showed slightly better ORR activity, suggesting that not only the coordination, but crystal structure packing also has a definitive role to play in electrocatalytic activities.

2. EXPERIMENTAL SECTION

2.1. MATERIALS

All chemicals used for both synthesis methods were analytical grade and used without any purification. Deionized water (resistivity 18 MΩ cm) was used to prepare all solutions. Cobalt sulfate ($CoSO_4 \cdot 6H_2O$) and cobalt acetate ($Co(CH_3CO_2)_2.4H_2O$) were purchased from Sigma-Aldrich, hydrazine hydrate ($N_2H_4 \cdot H_2O$, 100%) and tellurium dioxide (TeO_2) were purchased from Acros Organics. Au coated glass slides (Au-glass, hereafter) were bought from Deposition Research Laboratory Inc. (DRLI), St. Charles, Missouri. Carbon cloth (CC) substrate and Nafion were purchased from Fuel cells Etc. Company, college station, Texas, and Ion Power respectively.

2.2. CATALYSTS SYNTHESIS

2.2.1. Electrodeposition of Cobalt Tellurides. Cobalt tellurides were electrodeposited on conducting Au-glass substrates using a conventional three-electrode system where Ag|AgCl, graphitic rod and Au-glass were used as a reference, counter, and working electrodes, respectively.

Prior to deposition, the Au-glass substrates were cleaned by ultrasonication for 30 min in a dilute solution of commercial Micro-90 detergent for degreasing. The Au-glass substrates were then thoroughly washed with deionized water and ultra-sonicated again in a mixture of isopropanol, ethanol, and deionized water to remove any residual detergents from the surface. The clean and air-dried Au-glass substrates were masked with a scotch tape, leaving a circular geometric area of known dimensions (0.08 cm^2)

exposed for electrodeposition. Electrodeposition of cobalt tellurides thin films were carried out from an electrolytic bath containing 2.5 mM $Co(CH_3CO_2)_2.4H_2O$ and 2.5 mM TeO_2 maintained at 80 °C. Dilute HCl was added to adjust the pH to 2.5. After mixing, the solution was purged for 30 minutes with N_2 gas to remove all dissolved O_2 from the electrochemical bath. An IviumStat potentiostat was used and cobalt telluride was deposited at an applied potential of −0.60 and -0.65 V (vs. Ag|AgCl) for CoTe and $CoTe_2$, respectively. After deposition, the films were thoroughly washed with DI water to remove any adsorbents from the surface of the film.

2.2.2. Hydrothermal Synthesis of Cobalt Tellurides. In a typical synthesis, $CoSO_4 \cdot 6H_2O$ (0.03 M) was dissolved in 10.0 mL of deionized water under magnetic stirring to form a homogeneous solution. After mixing the solution for 10 min, TeO_2 (0.03 M) was added and stirred vigorously for 20 min. Finally, $N_2H_4 \cdot H_2O$ (1.0 mL) was added to the mixture and stirred continuously for another 10 min. The resulting solution was transferred to a Teflon-lined stainless-steel autoclave. The autoclave was sealed and maintained at 145 °C for 24 h, then naturally cooled to room temperature. The black product formed was centrifuged, washed several times with DI water, and then with a mixture of ethanol and DI water to remove impurities and unreacted precursors. The product was dried in a vacuum oven at 60 °C for 24 h. The methods as described above produced pure phase CoTe. Changing the relative precursor ratio of $CoSO_4 \cdot 6H_2O$ and TeO_2 to 1:2 yielded $CoTe_2$ exclusively.

2.2.3. Electrode Preparation. The hydrothermally synthesized cobalt telluride powders were assembled on electrodes prior to carrying our electrochemical and electrocatalytic studies. A homogeneous catalyst ink was prepared by adding 5.0 mg of

catalyst powder in 100.0 µL of Nafion solution (50 mL of 1% Nafion the solution in 50 mL of 50% IPA in water) followed by ultrasonication for 30 min. 10 µL of the catalyst-Nafion dispersion was drop casted on a carbon cloth electrode inside a confined area (0.08 cm^2). The drop cast film was dried at room temperature followed by heating at 130 °C for 30 min in an oven. The electrodeposited cobalt tellurides directly grown on the electrodes were used as-prepared for electrochemical measurements.

2.3. CHARACTERIZATION

2.3.1. Powder X-Ray Diffraction (PXRD). The electrodeposited cobalt telluride films and hydrothermally synthesized products were characterized by powder X-ray diffraction (pxrd) using a Philips X-Pert X-ray diffractometer (PANalytical, Almelo, The Netherlands) with CuKα (1.5418 Å) radiation. For the electrodeposited film the pxrd pattern was collected from the as-synthesized cobalt telluride layer on the Au-glass substrate. The deposited cobalt telluride layer was very thin on the substrate, therefore, the pxrd pattern was collected at grazing angle incidence in thin film geometry (GI mode with Göbel mirrors). The average particle sizes were calculated from the diffraction peak width using the Scherrer equation, (Eq. 1)

$$L = \frac{K\lambda}{\beta \mathrm{Cos}\theta} \quad (1)$$

where L is the particle or crystalline domain size, λ is the X-ray wavelength in nanometer (0.15418 nm), β is the diffraction peak width at half maxima in radians, and K is a constant, normally taken as 0.94.

2.3.2. Scanning Electron Microscopy (SEM). The SEM image of electrodeposited cobalt tellurides were obtained using a FEI Helios NanoLab 600 FIB/FESEM at an accelerating voltage of 10 kV and a working distance of 5 mm. Energy dispersive spectra (EDS) along with line scan analysis were also obtained from the same SEM.

SEM images of the hydrothermally synthesized cobalt telluride powders were obtained using Hitachi Model S-4700 field-emission microscope.

2.3.3. X-Ray Photoelectron Spectroscopy (XPS). XPS measurements of the cobalt tellurides were carried out using a KRATOS AXIS 165 X-ray photoelectron spectrometer (Kratos Analytical Limited, Manchester, United Kingdom) using a monochromatic Al X-ray source. C 1s signal at 284.5 eV was used as a reference to correct all the XPS binding energies. XPS spectra was collected from the pristine catalyst surface without sputtering.

2.4. ELECTROCHEMICAL PERFORMANCE

2.4.1. Electrocatalytic Activity. The conventional three-electrode system was connected to an IviumStat potentiostat to measure the electrocatalytic performances. Cyclic voltammetry (CV) and linear sweep voltammetry (LSV) were carried out to study the OER catalytic activity and cycling stability. In addition, the catalyst stability was examined by carrying out constant potential chronoamperometry at 10 $mAcm^{-2}$ current density for an extended period of time in N_2-saturated 1.0 M KOH at room temperature. All the electrochemical measurements were carried out with Au-glass electrodes for the electrodeposited thin films and drop casted catalyst ink on carbon cloth for

hydrothermally synthesized catalysts. The catalyst coated electrode was connected as, working electrode, while graphitic rod and Ag|AgCl (KCl saturated) was used as the counter electrode reference electrode, respectively. Nernst equation given in Eq-2 was used to convert the experimentally measured potentials vs Ag|AgCl to the reversible hydrogen electrode (RHE). The standard potential of Ag|AgCl at 25 °C was measured to be 0.197 V. All the potentials reported in this article have been iR corrected.

$$E_{RHE} = E_{Ag|AgCl} + 0.059pH + E^{0}_{Ag|AgCl} \quad (2)$$

2.4.2. Tafel Plot. The Tafel slope, an important parameter to explain the electrokinetic activity of these thin film catalysts for OER and HER processes, was estimated from Tafel slopes. Tafel equation, is given as the dependence of overpotential η on the current density *j* as shown in Eq-3:

$$\eta = a + \frac{2.3RT}{\alpha nF} \log j \quad (3)$$

where α is the transfer coefficient, n is the number of electrons involved in the reaction, and F is the Faraday constant. The Tafel slope is given by 2.3RT/αnF. The Tafel plots in this work were calculated from the reverse scan of CV collected at a scan rate of 2 mV s^{-1} in a non-stirred N_2-saturated 1.0 M KOH solution.

2.4.3. Faradaic Efficiency. The Faradaic efficiency was measured by quantifying the amount of production evolved oxygen gas by electrocatalyst was measured using a rotating ring-disk electrode (RRDE) apparatus which was connected to the IviumStat in bi-potentiostat mode. The Combined ORR-OER experiment was designed to confirm the evolved gas which is oxygen and quantify the amount of oxygen gas production.[83] RRDE composed of glassy carbon (GC) disk (0.196 cm^2) and pt ring (0.1 cm^2) electrodes. OER

occurred in the catalyst ($CoTe/CoTe_2$) coated glassy carbon disk electrode while ORR occurred in the Pt ring maintained at a constant potential for O_2 reduction. The Pt ring and GC disk electrodes were carefully polished with an alumina slurry (0.05 mm) and washed with DI water, sonicated for 5 min, and cleaned by an electrochemical method in N_2-saturated 0.5 M H_2SO_4 at 1600 rpm. Cobalt telluride catalysts were drop casted on a glassy carbon disk electrode. The potential of the disk electrode was scanned over a certain potential range to facilitate OER, while the Pt ring electrode was held at -0.16 V vs RHE appropriate for reducing oxygen being produced in the disk electrode. The Faradaic efficiency was calculated using Eq-4.

$$\text{Faradaic efficiency} = 2i_r / i_d \, \text{N} \qquad (4)$$

where i_r and i_d are the measured ring and disk currents, respectively, and N is the collection efficiency, estimated to be 0.17 in this work.

The Faradaic efficiency was also checked employing a water displacement method wherein, the evolved gases from each electrode are collected at the constant potential for a certain length of time (typically 1h) and quantified by the volume of water displaced. Faradaic efficiency of OER and HER catalyst is then calculated as the ratio of the experimental yield of O_2 and H_2 evolved during the catalytic experiments and theoretical yield of $O_2$and H_2 estimated from catalyst loading and applying Faraday law.

2.4.4. Electrochemical Active Surface Area. The electrochemically active surface area (ECSA) of the catalyst was estimated by measuring electrochemical double-layer capacitance (C_{DL}) at different scan rates in the non-Faradaic region. It was assumed that the current obtained in the non-Faradaic region is caused by double-layer charging instead of electrochemical reactions or charge transfer. The double-layer current (i_{DL}) was

obtained by performing cyclic voltammograms (CVs) with various scan rates in a non-stirred N_2 saturated 1.0 M KOH solution. The ratio of double-layer current (i_{DL}) and the scan rate (ν) of CV yielded specific electrochemical double-layer capacitance (C_{DL}) as described in Eq-5. The C_{DL} was calculated by averaging the absolute values of cathodic and anodic slopes.

$$iDL = CDL \times \nu \quad (5)$$

$$ECSA = CDL / CS \quad (6)$$

$$RF = ECSA / SA \quad (7)$$

The ECSA of the catalyst was calculated using Eq-6 where C_s is the specific capacitance and reported to be between 0.022 and 0.130 mF cm^{-2} in alkaline solution.[83] In this study, we assumed the value of C_s to be 0.040 $mFcm^{-2}$ based on previously reported OER catalysts in alkaline medium.[83] Roughness factor (RF) is another important parameter that defines catalyst surface roughness and can influence observed catalytic properties. RF was estimated from the ratio of ECSA and the geometric electrode area of 0.08 cm^2.

2.4.5. Turnover Frequency. Turnover frequency (TOF) is another critical parameter that can be calculated to illustrate the efficiency of these electrocatalysts. TOF quantifies the specific activity of a catalytically active center for the OER reaction under defined reaction conditions by the number of catalytic cycles occurring at the catalytic site per unit time.

$$TOF = I / 4 F m \quad (8)$$

where I is the current in amperes, F is the Faraday constant and m is the number of moles of the active catalyst.

2.4.6. Oxygen Reduction Reaction Measurements. All electrochemical measurements for ORR were performed using a CHI electrochemical workstation (model 760 b) in a standard three-electrode cell at room temperature. A 5.61 mm diameter glassy carbon rotating disc with Pt ring electrode in RRDE set-up was used as the working electrode in a 0.1 M NaOH solution to determine the electrocatalytic activity for ORR. A graphite rod was used as a counter electrode along with an Ag/AgCl in saturated KCl as a reference electrode. All potentials initially measured vs the Ag/AgCl electrode were converted to RHE by adding 0.950 V (the potential of Ag/AgCl electrode measured against RHE in 0.1 M NaOH solution). Catalyst inks were prepared by ultrasonically mixing 2.5 mg of catalyst samples with 2.5 mg carbon (BP 2000), 500 µl of isopropyl alcohol and 20 µl of 5% Nafion suspension in alcohol (Solution Technology Inc). Catalyst inks were drop casted on the glassy carbon disc of the RRDE (0.6 mg/cm^2 loading) and air-dried at room temperature prior to the measurement of ORR activity. Cyclic voltammetry (CV) was carried out in O_2 or N_2 saturated 0.1 M NaOH at 20 mV/s scan rate. The CV data was recorded after a run of 20 cycles. In RRDE tests, ORR polarization curves were recorded using linear sweep voltammetry in oxygen saturated 0.1 M NaOH solution with a scan rate of 5 mV/s. The disc rotation rates ranged from 400 to 1600 rpm for evaluating the number of electrons transferred (n) according to the Koutecky-Levich equation.[84] The potential of the Pt ring of the RRDE was set at 1.2 V vs RHE to estimate the percentage of peroxide formed on the disc electrode. The peroxide content (% H_2O_2) and the number of electrons transferred per oxygen molecule (n) were calculated from the standard relationships (Eqs. 9 and 10):

$$\%\ (H_2O_2) = 200 \times \frac{i\,R/\,N}{i\,D + i\,R/\,N} \tag{9}$$

$$n = 4 \times \frac{i\,R/\,N}{i\,D + i\,R/\,N} \quad (10)$$

where, i_R is the ring current, i_D is the disc current and N is the collection efficiency (0.37). Chronoamperometric measurements were used to determine the stability of the catalyst.

3. RESULTS & DISCUSSION

3.1. STRUCTURE AND MORPHOLOGY

Pxrd patterns of the as-synthesized products were used to confirm phase purity and crystallinity of the samples. Figure 1 shows the pxrd patterns of hydrothermally synthesized cobalt tellurides. It was observed that hydrothermal synthesis yielded pure CoTe or $CoTe_2$ depending on the relative ratio of $CoSO_4$: TeO_2 in the reaction mixture as has been described in the methods section. The pxrd patterns of the samples matched very well with the standard patterns of CoTe and $CoTe_2$ PDF# 00-034-0420 and 01-074-0245, respectively as shown in Figure 1 CoTe crystallizes in the hexagonal P63/mmc space group. The lattice structure is composed of Co(1) in octahedral coordination with Te(1) atoms. The octahedral are face-shared, edge-shared, and corner-shared to form the 3-dimensional lattice. The short Co(1) – Co(1) the distance of 2.65 Å also indicates significant metal-metal bonding. All Co (1)–Te (1) bond lengths are found to be equivalent (2.62 Å). Te (1) on the other hand shows trigonal prismatic coordination with 6 Co(1) atoms as shown in the inset of Figure 1a.

$CoTe_2$ lattice structure is a mineral analog of Marcasite and crystallizes in the orthorhombic Pnnm space group. Co (1) shows octahedral coordination with six equivalent Te (1) atoms and the resulting CoTe6 octahedra shows corner- and edge-

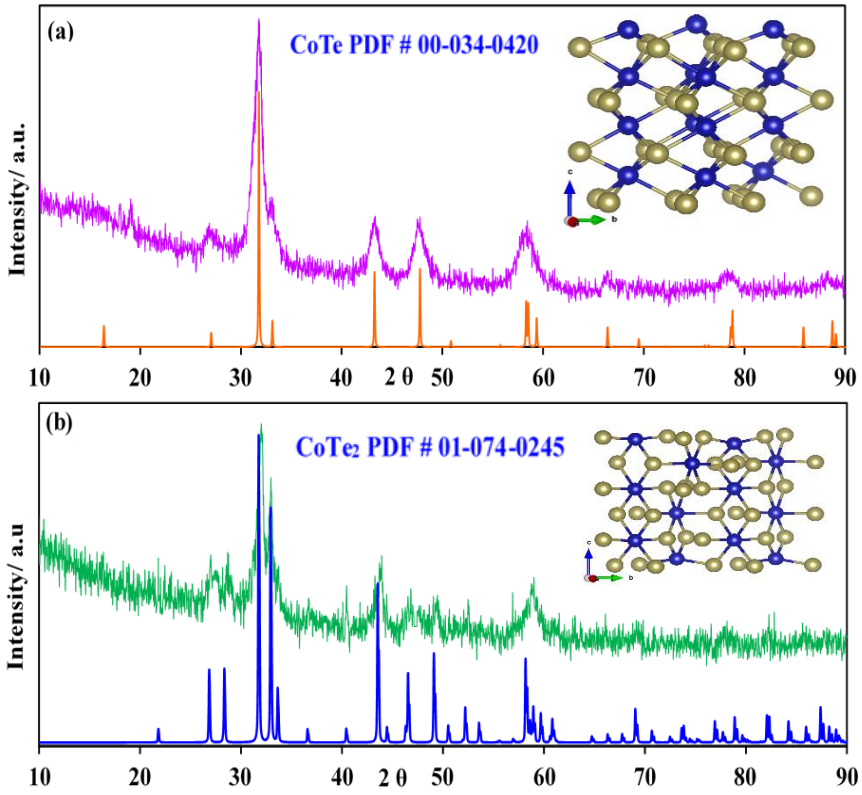

Figure 1. X-Ray diffraction patterns. (a) CoTe and (b) $CoTe_2$. Insets show crystal polyhedra of the CoTe and $CoTe_2$ respectively.

sharing with neighboring polyhedral. Interestingly, it shows a corner-sharing octahedral tilt angle of 56°. All Co (1)–Te (1) bond lengths are 2.59 Å. Te (1), on the other hand, shows a trigonal planar geometry and is bonded to three equivalent Co (1). These trigonal planar units are also connected to the neighboring units through corner and edge-sharing as shown in the inset of Figure 1b.

The pxrd diffraction peaks showed some broadening indicating nanostructuring and the presence of reduced grain/domain size in the sample. The average particle size calculated using the Scherrer equation was approximately 7.5. nm for CoTe and 22 nm for $CoTe_2$ indicating that these are indeed nanostructured catalysts.[85] It must be

mentioned here that from pxrd studies it was apparent that there is no preferred direction of growth for these hydrothermally synthesized cobalt tellurides.

Morphology of the as-synthesized materials was studied through SEM. Figure 2 (a – d) shows the SEM images of electrodeposited and hydrothermally synthesized CoTe phases and $CoTe_2$ phases respectively. Electrodeposited CoTe shows fluffy nanoball-like morphology with smooth edges and an average size of about 100 nm size. Electrodeposited $CoTe_2$ on the other hand, shows fluffy nanostructures with rough edges with average sizes less than 100 nm. Hydrothermally synthesized CoTe shows short nanorods with an average length of about 400nm while $CoTe_2$ shows irregular nanostructures with an average size of about 100 nm size. Interestingly both electrodeposition and hydrothermal synthesis yielded cobalt telluride nanostructures with varying morphology. Nanostructuring is expected to enhance the electrocatalytic performance significantly by increasing exposure of the catalytically active site to the electrolyte. The nanostructures obtained adapted by these cobalt tellurides have high aspect ratio as well as surface area which can have a significant effect on the observed electrocatalytic activity. The catalyst composition was also confirmed through EDS elemental analysis.

Table S1 lists the elemental ratios of electrodeposited and hydrothermally synthesized CoTe and $CoTe_2$ compounds. For hydrothermally synthesized CoTe average atomic ratio for Co: Te was obtained as 53:47 which is closer to the theoretical ratio of 1:1. Similarly, hydrothermally synthesized $CoTe_2$showed an average atomic ratio for Co:Te as 35:65 confirming the composition to be $CoTe_2$. Similarly, electrodeposited CoTe and $CoTe_2$ showed relative atomic ratio of Co:Te as 54:46 and 68:32, respectively

confirming the respective compositions. Figure S1 shows the electrodeposited CoTe and $CoTe_2$ EDS spectra along with the line scan for Co and Te. From the elemental line scans it is apparent that Co and Te are distributed uniformly over the catalyst composition. The Au and Si lines originated from the Au-coated glass substrates. These further confirmed composition of the electrodeposited samples as CoTe and $CoTe_2$. Figure S2 shows similar EDS spectra and line scan analysis for hydrothermally synthesized CoTe and $CoTe_2$ confirming the uniform distribution of Co and Te throughout the sample and their respective compositions.

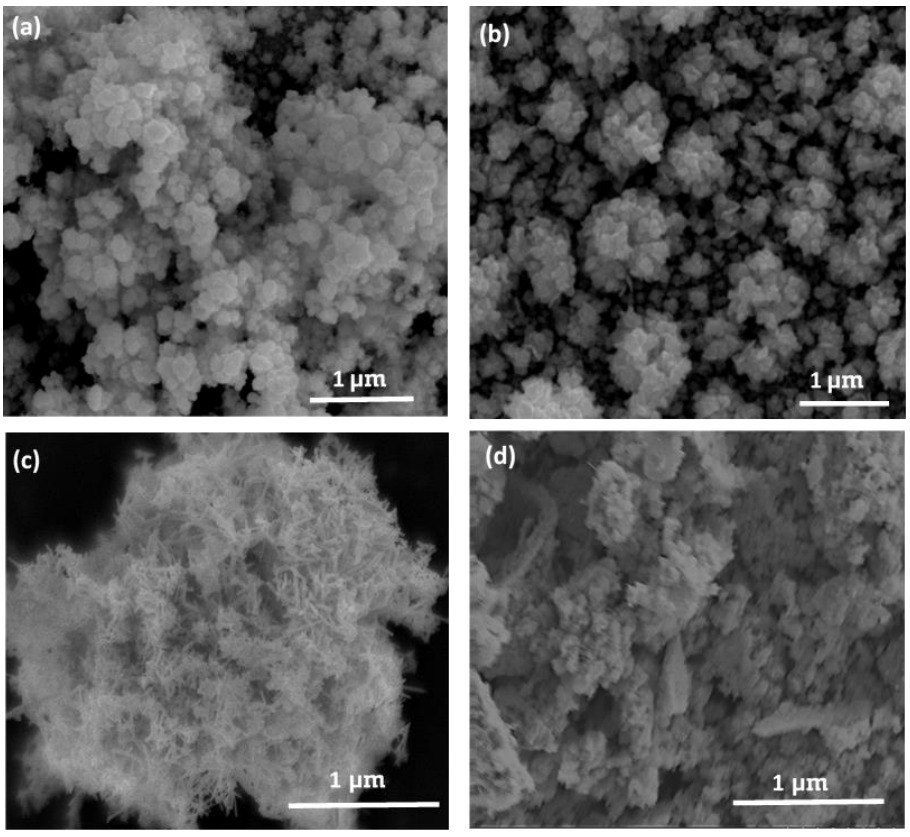

Figure 2. Scanning Electron Microscopy images. (a) electrodeposited CoTe and (b) $CoTe_2$ hydrothermally synthesized (c) CoTe and (d) $CoTe_2$.

The surface composition of the catalyst was also confirmed through XPS studies. Figure 3 shows the XPS spectra of hydrothermally synthesized CoTe (a-b) and $CoTe_2$ (c-d) powders. Survey spectra showed that only Co and Te were present in the sample without any other impurities (Figure S-3).

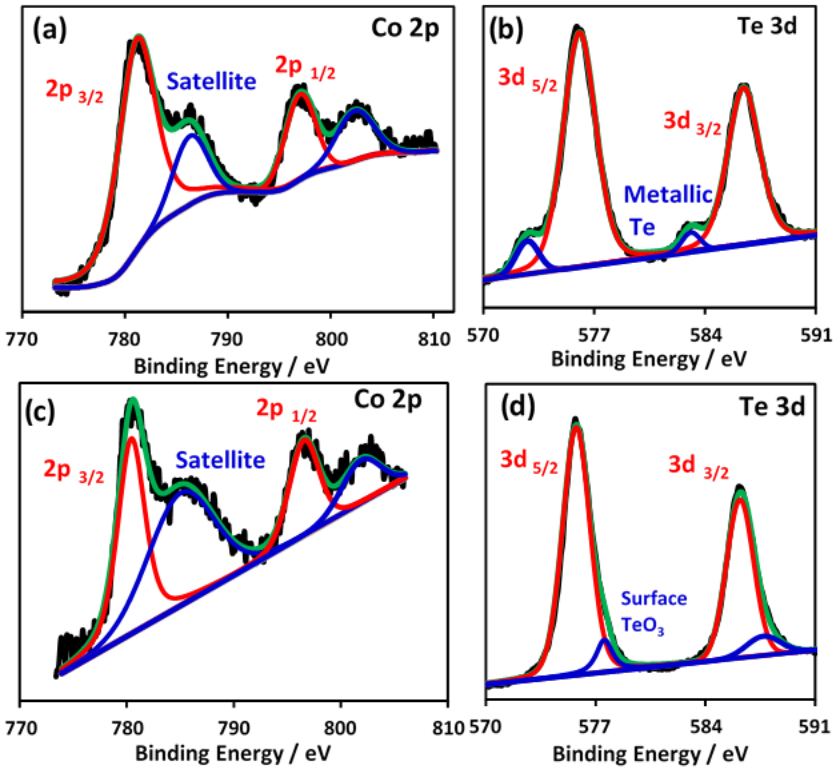

Figure 3. X-Ray photoelectron spectroscopy. CoTe (a) Co 2p and (b) Te 3d; $CoTe_2$ (c) Co 2p and (d) Te 3d.

Figure 3(a & c) and (b & d) shows the Co 2p and Te 3d spectra respectively. Co 2p spectra have two peaks at 780.0 eV and 795.5 eV corresponding to $2p_{3/2}$ and $2p_{1/2}$ which is similar to the literature values for Co^{2+}.[68,86] The satellite peaks are observed at 786.6 eV and 803.0 eV which corresponds well with the published literature.[68,86] The Te XPS shows peaks at 576.3 and 586.6 eV which corresponds to the presence of TeO_2

which may form through subtle surface oxidation at the Te site. The Te spectra also show the presence of metallic Te at 572.8 eV and 583.3eV (Figure 3b).[68] Figure 3d illustrates the Te 3d spectra of $CoTe_2$ consisting of two peaks at 575.9 eV and 586.1 eV also relevant to TeO_2.[68] The O1s spectra of both CoTe and $CoTe_2$ shown in Figure S3 reveal the presence of trace amounts of absorbed surface-oxygen at 530. 3eV and 532.4 eV respectively.[68]

3.2. ELECTROCHEMICAL CHARACTERIZATION

The electrochemical active surface area of electrodeposited and hydrothermally synthesized CoTe and $CoTe_2$ were investigated using the cyclic voltammetry (CV) plots scanned in the range from 0.05 V to 0.25 V vs Ag/AgCl with scan rates between 2.5 $mV.s^{-1}$ to 200 $mV.s^{-1}$ in N_2 saturated 1 M KOH solution (Figure 4 a-d). The anodic and cathodic currents were measured at 0.168 V vs Ag/AgCl and Figure 4e - h shows the anodic and cathodic current plotted as a function of scan rates.

ECSA was calculated using the double layer capacitance of the catalysts and the specific capacitance as described in the methods section. All the calculated ECSA values have been tabulated in Table 1. Higher ECSA value typically signifies larger electrochemically active surface area which provides better catalytic performance for OER. Larger ECSA also results in enhanced surface roughness (exemplified by RF) which can be considered as another parameter affecting the observed catalytic activity. Comparison of the four cobalt telluride based electrocatalysts included in this study

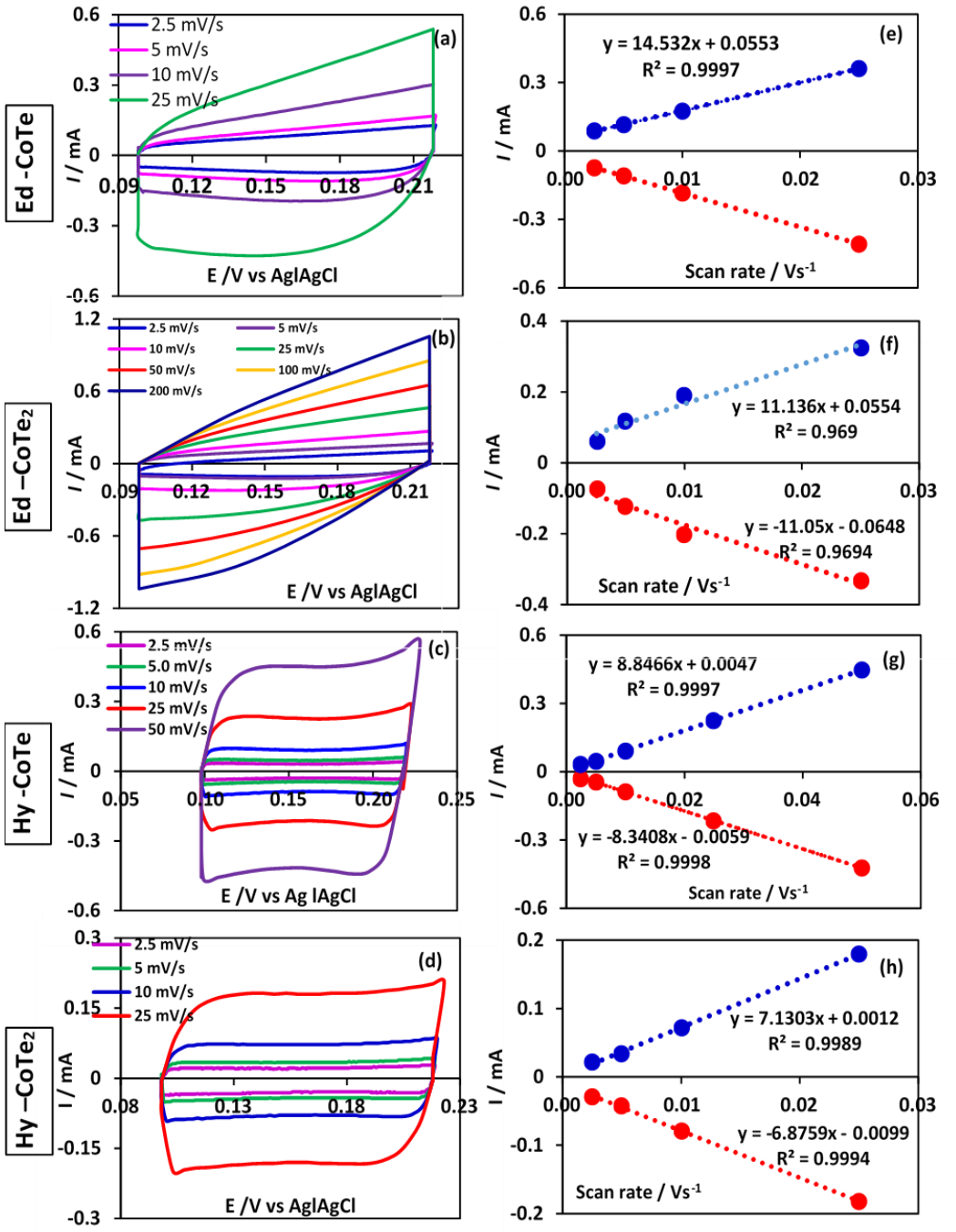

Figure 4. Cyclic voltammograms. Measured at different scan rates (a) Ed- CoTe, (b) Ed- $CoTe_2$, (c) Hy- CoTe, (d) Hy- $CoTe_2$; Plots of anodic and cathodic currents measured as a function of different scan as a function of scan rates for (e) Ed- CoTe (f) Ed- $CoTe_2$,(g) Hy- CoTe , (h) Hy- $CoTe_2$.

shows that electrodeposited catalysts had higher ECSA and RF which also corresponds with the nanostructured morphology observed in SEM. Among the different phases of cobalt telluride, CoTe shows higher ECSA and RF values for both hydrothermally synthesized and electrodeposited samples. This might be one of the reasons why CoTe was observed to have better electrocatalytic activity compared to $CoTe_2$.

The OER electrocatalytic activity of these cobalt telluride phases were studied through LSV measurements (shown in Figure 5a) as described in the methods section. Comparison of OER electrochemical activities of electrodeposited and hydrothermally synthesized CoTe and $CoTe_2$ electrocatalysts is also shown in Table 1. Among all four electrocatalysts, Ed-CoTe shows the best catalytic activity having lowest overpotential of 200 mV at 10 mA cm^{-2}, and highest current density exceeding 150 $mA.cm^{-2}$ at 300 mV. Comparison of the hydrothermally synthesized electrocatalysts showed that CoTe has lower overpotential at 10 $mA.cm^{-2}$ and higher current density than $CoTe_2$ as shown in Figure 6a. The OER onset potential can be considered as an intrinsic property of the electrocatalysts and both CoTe and $CoTe_2$ were observed to have low onset potential for OER. Interestingly CoTe exhibited significantly improved OER catalytic activity compared to $CoTe_2$ illustrating the influence of lattice structure, stoichiometry, and crystal packing on the observed electrocatalytic properties which has been discussed in more detail in later sections.

Tafel slope is an important catalytic parameter in electrochemical performances and it provides the reaction kinetics of the electrocatalytic reaction. Lower Tafel slopes of the catalysts typically signify faster OER kinetics. Tafel slopes were measured in a steady

state of the LSVs in a non-stirred electrolyte solution at a lower scan rate of 2 mVs^{-1}. The Tafel values of electrodeposited cobalt tellurides and the hydrothermally synthesized cobalt tellurides are shown in Figure 5b and Figure 6b respectively. Electrodeposited catalysts have lower Tafel slopes than the hydrothermally synthesized catalysts. The electrodeposited catalysts have direct contact with the substrate, and it is binder free catalysts and as a result, they are expected to have facile charge transfer within the catalyst composite and at the electrode-electrolyte interface leading to lower Tafel slope and improved OER activity. The hydrothermally synthesized samples, on the other hand, were assembled with the help of Nafion that being a non-active component results in large contact resistance and a hindrance to charge flow.

Table 1. Comparison of electrocatalytic parameters.

OER	**Hy-CoTe**	**Ed-CoTe**	**Hy- $CoTe_2$**	**Ed-$CoTe_2$**	**Ed-RuO_2**
Onset potential / V	1.44	1.44	1.48	1.43	1.51
η @ 10 mA cm^{-2} / mV	270	200	320	240	370
Tafel slope / mV dec^{-1}	67.7	43.8	111.8	44.8	114.4
Current density @ 300 mV/ mA	17.01	116.67	9.21	65.73	1.63
ECSA / cm^2	221	368	175	277	-
RF	2800	4600	2216	3647	-
TOF @ 300 mV / s^{-1}	0. 0013	0.0024	0.0011	0.0022	-

Both CoTe and $CoTe_2$ electrocatalysts irrespective of the synthesis conditions showed better OER activity than electrodeposited RuO_2 which has been traditionally known as a state-of-the-art catalyst for OER in alkaline medium. Better electrocatalytic activity of electrodeposited catalysts compared to hydrothermally synthesized catalysts can be attributed to the effect of direct growth on the electrodes which reduces contact resistance as well as the absence of any binder or other additives that restrict exposure of the catalyst site to the electrolyte.

3.3. CATALYTIC STABILITY

Functional stability of these electrocatalysts in the electrolyte was measured by subjecting them to constant oxygen evolution reaction conditions for an extended period of time in the 1M KOH solution. The chronoamperometric experiments were performed for 24h in the alkaline medium at a constant applied potential of 1.43 V and 1.44 V respectively for electrodeposited CoTe and $CoTe_2$ as shown in Figure 5c. The evolution of large amounts of oxygen bubbles from the catalyst surface was observed during the extended period of time. Due to this large amount of gas evolution, it was also observed that the bubbles sometimes stuck to the catalyst surface and needed to be tapped off periodically. As a result, the current response shows some fluctuation during the time period as seen in Figure 5c. Stirring the electrolyte solution did not help much in therapid removal of generated oxygen bubbles from the catalyst surface. The electrodeposited CoTe and $CoTe_2$ electrocatalysts showed outstanding catalytic stability of the OER for 24h in an alkaline medium. The current density with the extended time period did not show any degradation which confirmed the prolonged stability of these catalysts

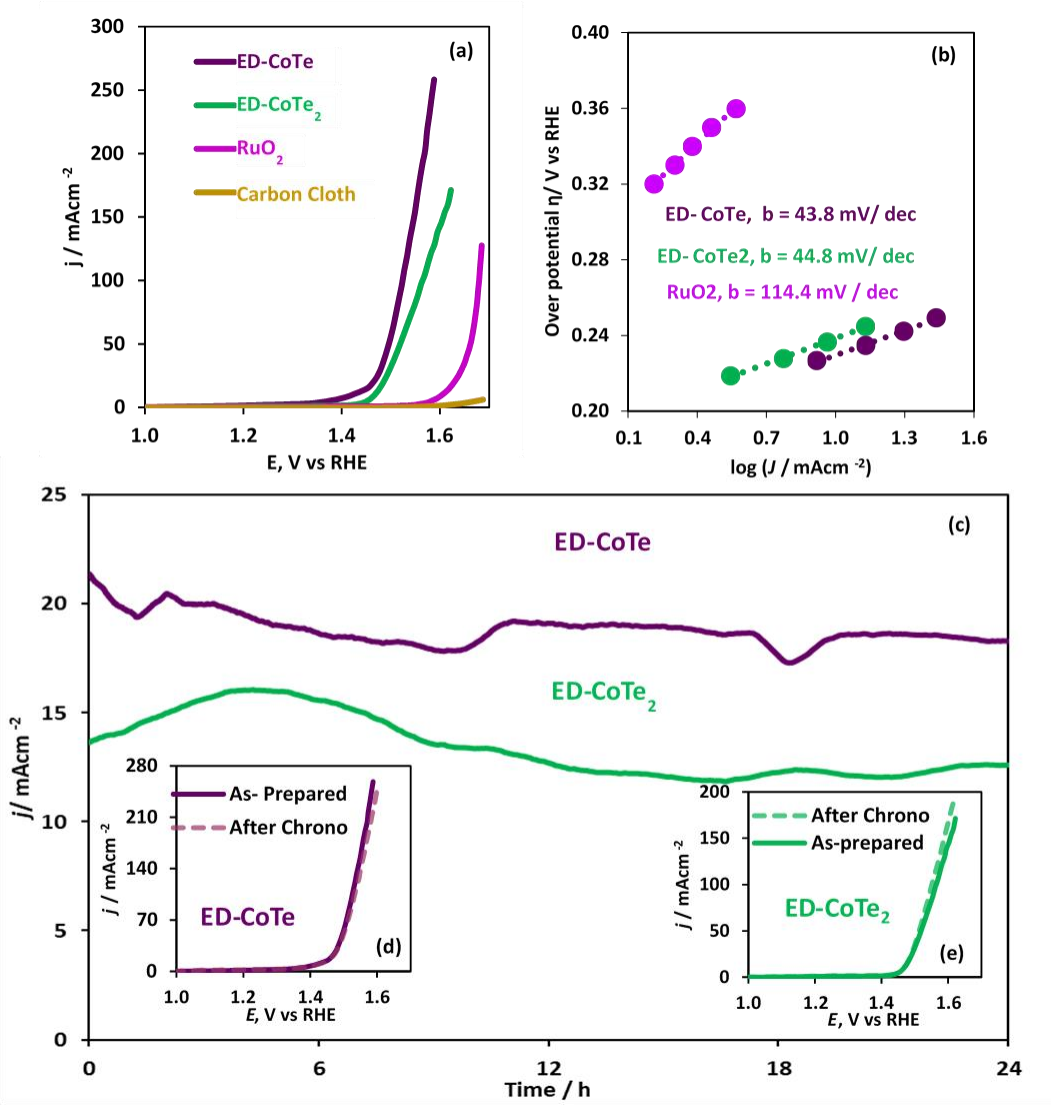

Figure 5. Catalytic stability of electrodeposited cobalt telluride catalysts. CoTe and $CoTe_2$ (a) LSVs measured in N_2 saturated 1 M KOH at a scan rate of 10 mV s^{-1}; (b) Tafel plots of both catalysts compared with RuO_2; (c) Chronoamperometry for extended time periods; The insets are the comparison of electrodeposited cobalt tellurides before and after of chronoamperometry (d) CoTe and (e) $CoTe_2$ respectively.

under conditions of continuous oER in an alkaline medium. Also, the LSV plots of CoTe and $CoTe_2$ before and after the chronoamperometry experiments were almost superimposable and showed almost no change as illustrated by Figure 5 d and 5 e, respectively, indicating no change in catalyst performance for over 24 h.

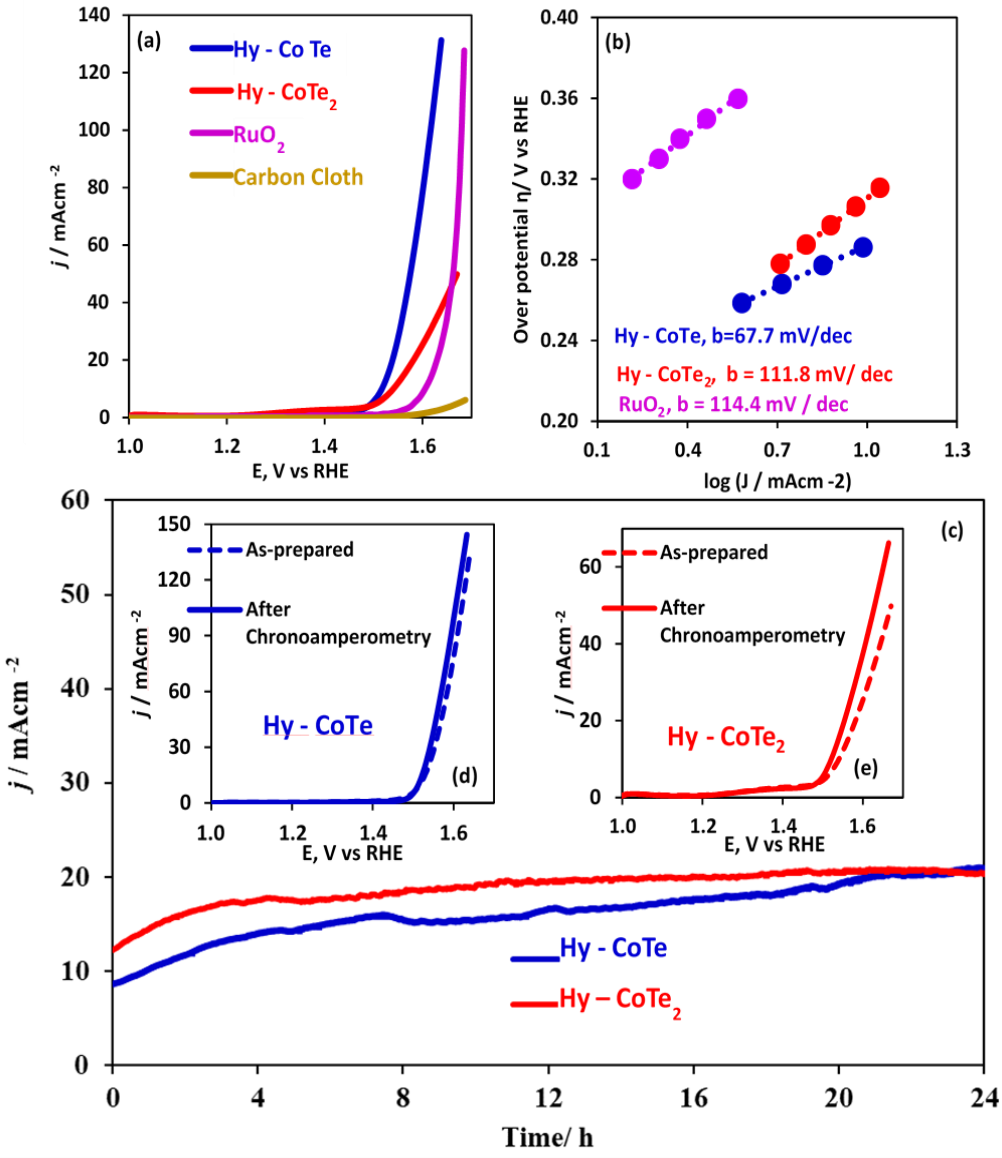

Figure 6. Catalytic stability of hydrothermally synthesized cobalt telluride catalysts. CoTe and $CoTe_2$ (a) LSVs measured in N_2 saturated 1 M KOH at a scan rate of 10 mV s^{-1}; (b) Tafel plots of both catalysts compared with RuO_2; (c) Chronoamperometry for extended time periods; The insets are the comparison of Hydrothermally synthesized cobalt tellurides before and after of chronoamperometry (d) CoTe and (e) $CoTe_2$ respectively.

Similarly, chronoamperometry measurements for 24 h of hydrothermally synthesized CoTe and $CoTe_2$ catalysts and the comparison of LSV plots before and after chronoamperometry are shown in Figure 6c, 6d, and 6e, respectively. The current

density of both hydrothermally synthesized catalysts of CoTe and $CoTe_2$ showed slightly higher current density after the 24 h time period. This can be explained by the common observation that with aging and continuous oxygen evolution, the Nafion film becomes a little bit more permeable leading to more exposure of the catalytic sites to the electrolyte and thereby increasing the observed electrocatalytic activity. The LSV comparison also showed improvement in catalyst performance for both CoTe and $CoTe_2$ with time. For hydrothermally synthesized samples, this seemed really promising that there was not only the catalyst stable for a prolonged period in an alkaline medium, but also the catalyst performance improved with time. The Faradaic efficiency of the CoTe and $CoTe_2$ catalysts for OER activity was measured by the water displacement method. Both CoTe and $CoTe_2$ catalysts exhibited 100% Faradaic efficiency as shown in Figure S4.

The composition of the electrocatalysts after OER stability studies were investigated through XPS analyses. XPS spectra confirmed that the elemental composition of the electrocatalyst was retained after extended periods of catalytic activity as shown in Figure S 5-8. The comparison of Co 2p and Te 3d spectra, before and after chronoamperometry of CoTe has been shown in Figure S5 (a - d) while for $CoTe_2$ it is given in Figure S5 (e - h), respectively. Figure S6 shows the comparison of O1s spectra for before and after chronoamperometry for both CoTe and $CoTe_2$. Remarkably, the XPS peaks before and after catalytic activity did not show any shift of peak positions for Co 2p and Te 3d as shown in Figure S7. Also, the O 1s peaks positions did not show any shift after the 24 h chronoamperometry study (Figure S 8).

3.4. COMPARISON OF HYDROXYL ADSORPTION ENERGY BY DFT CALCULATIONS

The CoTe, $CoTe_2$, and Co_3O_4 (001) surfaces were studied by first-principles density functional theory (DFT) calculations by using the projector augmented wave (PAW) method[87] as implemented in Vienna Ab-initio Simulation Package (VASP)[88] to investigate the favorable adsorption energy of OH ions on these catalyst surfaces. Generalized gradient approximation (GGA)[89] using Perdew–Burke Ernzerhof (PBE)[90] functional and ultra soft potentials were used to treat exchange-correlation interactions. An energy cutoff limit of 500 eV was employed with 10^{-5} eV convergence criteria during electronic minimization steps and all the ions were iteratively relaxed by conjugate gradient algorithm and the atomic forces of all systems were minimized to less than 0.01 eV without any symmetry constraints. A Methfessel–Paxton smearing with σ= 0.05 eV to the orbital occupation is employed during structure relaxation, whilst a tetrahedron method with Blöchl corrections was used during the accurate electronic structure calculations. Gamma-centered Mokhorst-Pack[91] generated sets of K-points were used for sampling the Brillouin zone and K-point meshes of 11x11x11, 6x6x1, and 8x8x3 were used for self-consistent field (SCF) convergence of CoTe, $CoTe_2$, and Co_3O_4 respectively. For each species, the free surfaces of slab models were simulated with 2x2x2, 2x2x2, and 1x1x1 unit cells along with a large vacuum gap of 15 Å along z-direction to avoid interaction between periodic layers and also dipole corrections were applied normal to the surface.

To perform the calculation of -OH adsorption energy, first the surfaces were relaxed to obtain the energy of the clean surfaces, E_{clean}, and then OH^- ions were placed on top of the active metal site at a distance of 1.80 Å, which is very close to the

equilibrium distance of OH- on transition metal sites,[76] and the system was relaxed to calculate, $E_{sys.}$, the total formation the energy of the system. The relaxed surfaces after the OH- attachment on (001) the surface is shown in Figure 7. The adsorption energy of OH^- ions, E_{ad}, was calculated as $E_{ad} = E_{sys} - E_{clean} - E_{OH}$, in which E_{OH} is the energy of free OH^-. As observed in previous studies[76], the active catalyst site was slightly moved upward on the surface after binding to the more electronegative OH^- ions.

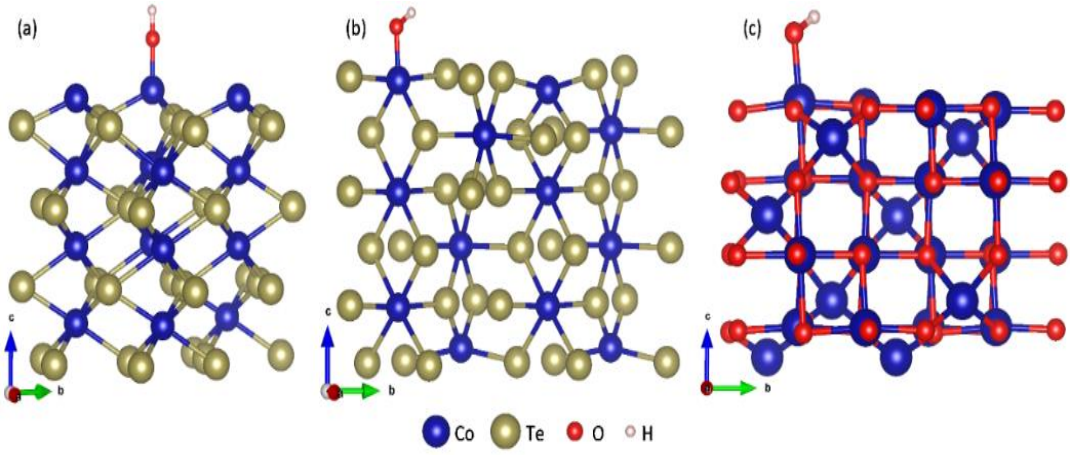

Figure 7. The relaxed crystal structures. (a) CoTe (b) $CoTe_2$ and (c) Co_3O_4 crystal structures after adsorption of OH^- on active Co sites on (001) free surfaces.

The OH^- adsorption energy on (001) surface was found to be -2.49 eV, -2.04 eV, and -1.61 eV for CoTe, $CoTe_2$ and Co_3O_4 respectively as indicated in Figure 8. Higher -OH adsorption energy for CoTe surface indicates more preferential OH attachment on the surface. Since -OH attachment on the surface represents the initiation of OER and can be considered as a catalyst activation step, it can explain the improved catalytic performance of CoTe compared to $CoTe_2$. Interestingly, both CoTe and $CoTe_2$ showed improved -OH adsorption energetics than Co_3O_4 indicating the better electrocatalytic performance of the

tellurides compared to oxide, which further confirms that decreasing anionic electronegativity leads to better OER activity. The calculated partial density of states (PDOS) of CoTe and $CoTe_2$ are given in Figure S9 and S10 in the supporting information.

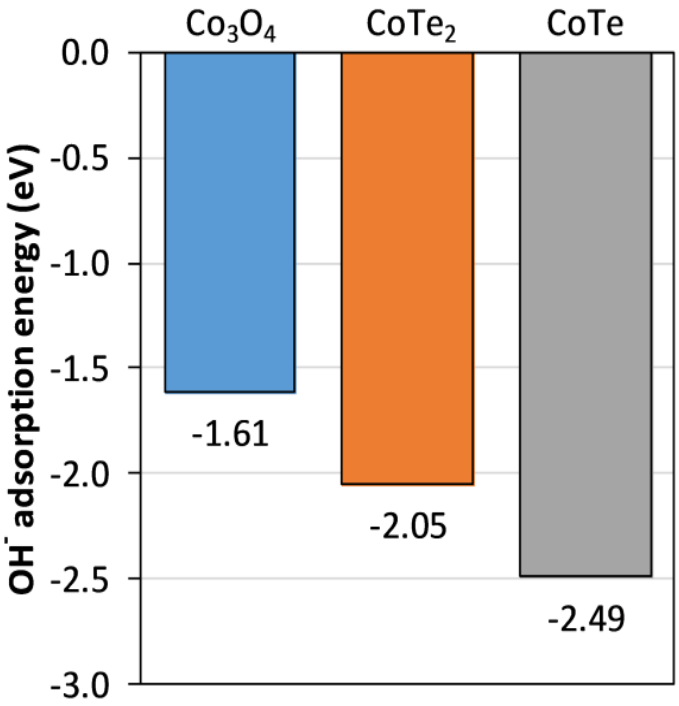

Figure 8. Calculated adsorption energy of OH- ions on CoTe, $CoTe_2$ and CO_3O_4. The negative value indicates the highest adsorption energy on (001) surfaces.

3.5. HER CATALYSIS

Electrodeposited CoTe and $CoTe_2$ have been also studied for HER catalytic activity in 1M KOH alkaline solution using the three-electrode system. These polarization curves were measured under cathodic scan in N_2 saturated 1 M KOH

solution with a scan rate of 10 mVs^{-1}. CoTe and $CoTe_2$ catalysts were electrodeposited on Au-glass HER activity was compared with electrodeposited Pt catalysts. Both catalysts were active for HER catalytic activity as shown in Figure 9. Comparatively, CoTe catalysts exhibited lower overpotential of 283 mV at 10 $mA.cm^{-2}$ than $CoTe_2$. Nevertheless, $CoTe_2$ showed higher current density in HER performances than CoTe. The Tafel slopes were calculated using equation (3) and has been shown in Figures 9 (e-g) s for CoTe, $CoTe_2$, and Pt. HER catalytic parameters have been listed in Table S2. The catalytic stability studies were monitored through chronoamperometry measurements in 1M KOH at a constant potential of - 0.283 V for CoTe and -0.350 V for $CoTe_2$ vs. RHE as shown in Figure 9d. In the chronoamperometry plot, CoTe and $CoTe_2$ catalysts on Au-glass showed high stability for continuous H_2 generation for 24h time period. There was no catalytic degradation after an extended period of time. In Figure 9 (b) and (c) illustrated the comparison of LSVs of before and after chronoamperometry test. The LSVs also do not show any degradation and catalytic loss after the 24 h continuous H_2 gas generation. The faradaic efficiency of the CoTe and $CoTe_2$ catalysts for HER activity was measured by the water displacement method. Both CoTe and $CoTe_2$ catalysts showed 100% faradaic efficiency as shown in Figure S11. The hydrothermally synthesized CoTe and $CoTe_2$ were also studied for HER catalytic activity in 1M KOH alkaline solution. The LSV polarization curves measured under cathodic scan in N_2 saturated 1M KOH solution at a scan rate of 10 mVs^{-1} showed promising HER catalytic activity as shown in Figure 10. Comparatively, CoTe catalysts exhibited lower onset potential at -0.195 V and a lower overpotential of 290 mV at 10 $mAcm^{-2}$ with higher current density of about 80 $mAcm^{-2}$.

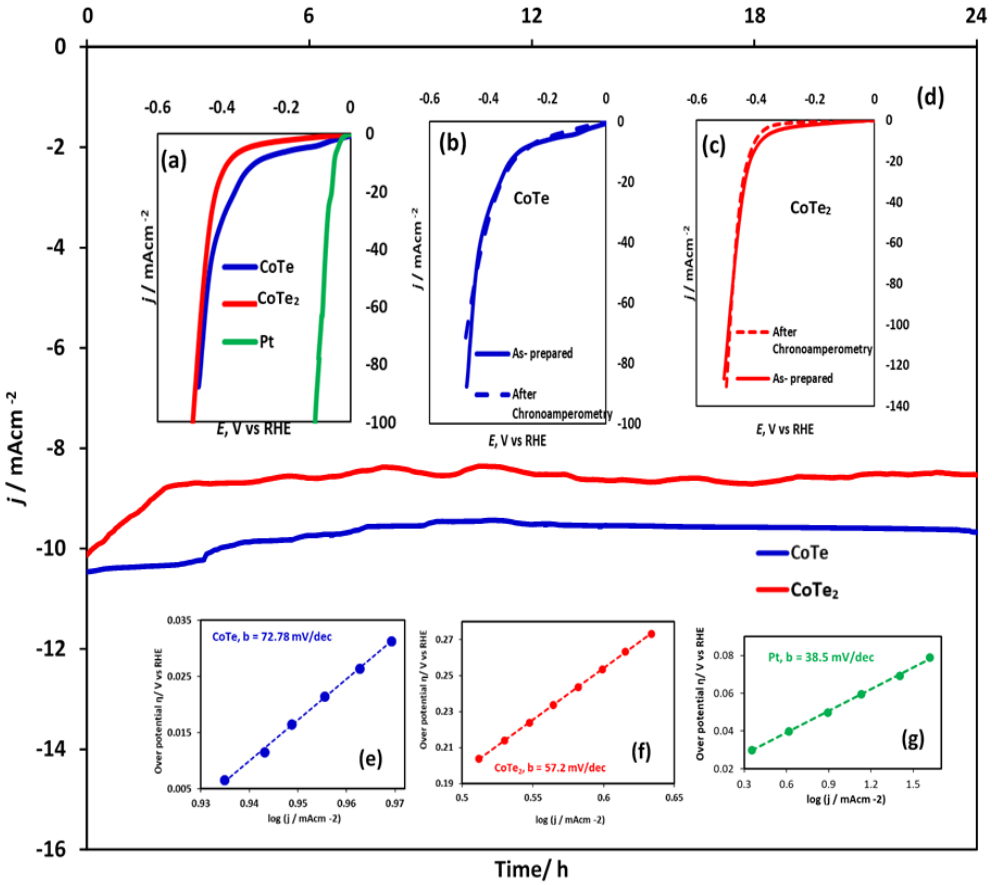

Figure 9. The comparison of HER polarization curves of electrodeposited catalysts. (a) CoTe, $CoTe_2$, and Pt. The comparison of before and after chronoamperometry LSVs of the (b) CoTe and (c) $CoTe_2$ catalysts in 1M KOH alkaline solution. (d) Stability study of the CoTe and $CoTe_2$ catalysts for 24 h. Tafel plots of (e) CoTe, (f) $CoTe_2$, and (g) Pt.

The LSV plots illustrated that the CoTe catalyst showed better catalytic activity toward the HER than $CoTe_2$. Catalytic performance of $CoTe_2$ as a HER catalysts shows -0.250 V onset potential and overpotential of 350 mV at 10 $mAcm^{-2}$. The Tafel slopes were calculated using the equation (3) and have been plotted in Figure 10b. CoTe showed a lower Tafel slope indicating facile charge transfer within the catalyst composite compared to $CoTe_2$. All HER catalytic parameters have been listed in Table S2 in the supplementary document. The catalytic stability studies were monitored through

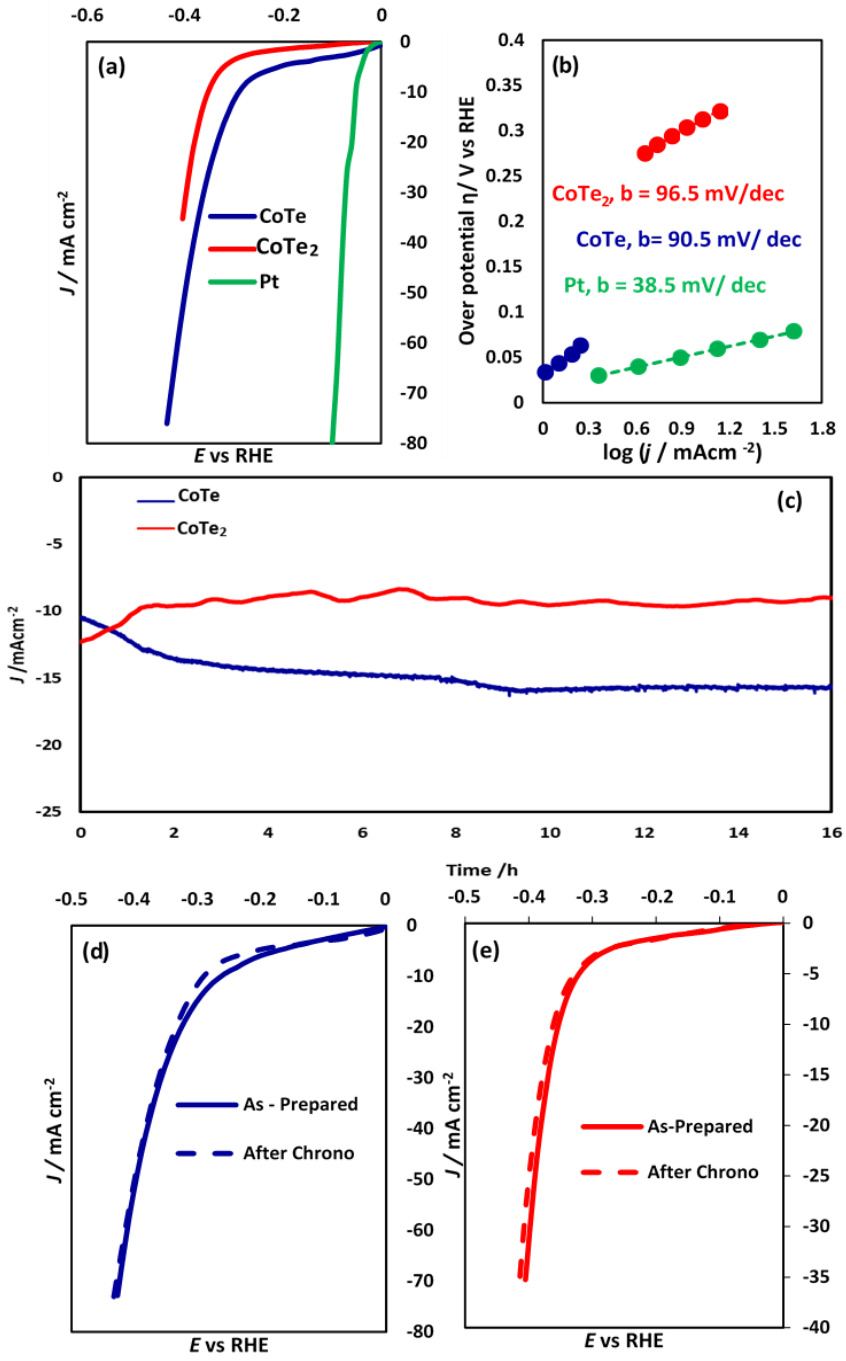

Figure 10. The comparison of HER polarization curves for hydrothermally synthesized cobalt telluride catalysts. (a) CoTe, $CoTe_2$, and Pt. (b) Tafel plots of CoTe, $CoTe_2$, and Pt. (c) Stability study of the CoTe and $CoTe_2$ catalysts for 16 h. The comparison of before and after chronoamperometry LSVs of the (d) CoTe and (e) $CoTe_2$ catalysts in 1M KOH alkaline solution.

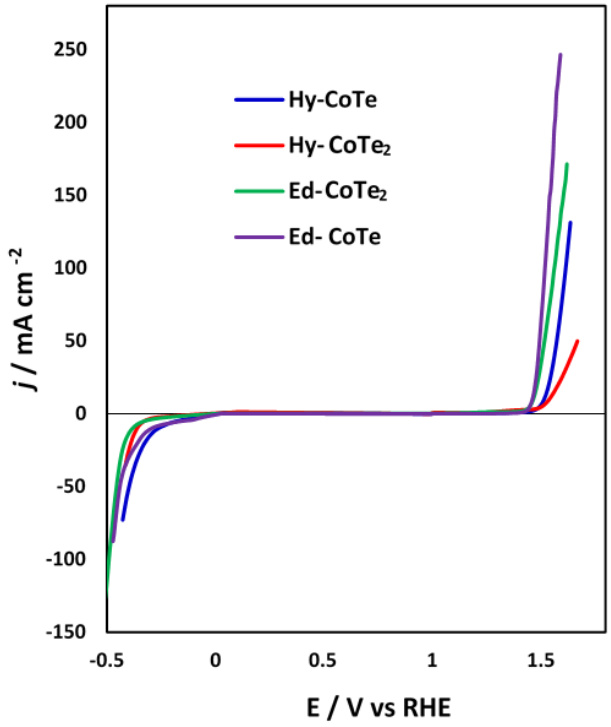

Figure 11. The comparison of water splitting cell voltage for cobalt tellurides.

chronoamperometry measurements in 1M KOH at a constant potential of -0.290 V for CoTe and -0.378 V for $CoTe_2$ vs. RHE and has been plotted in Figure 10c. In the chronoamperometry plot, CoTe and $CoTe_2$ catalysts on Au-glass showed extended stability for continuous H_2 generation for a prolonged time period. There was no catalytic degradation after an extended period of time. In Figure 10 (d) and (e) shows the comparison of LSVs before and after the chronoamperometry test which confirmed that there was no catalyst degradation after 16 h of continuous H_2 gas generation. Both CoTe and $CoTe_2$ catalysts showed 100% Faradaic efficiency as shown in Figure S.11 in the supporting document. Since these cobalt tellurides were active for both OER and HER, full water electrolysis was studied by using cobalt tellurides as both anodic and cathodic catalysts in their electrode system. The comparison of CoTe and $CoTe_2$for full water

electrolysis has been shown in Figure 11. Calculated cell voltages at 10 $mA.cm^{-2}$ revealed that CoTe had a smaller water-splitting voltage of 1.71 V. The electrolysis energy efficiency of the electrodeposited CoTe was estimated to be 86.64 % and was highest among all four catalysts. The calculated data of cell voltage and the electrolysis energy efficiency were tabulated in Table S 3.

3.6. ORR CATALYSIS

CoTe and $CoTe_2$ also was tested as electrocatalyst for ORR in alkaline medium using O_2 saturated and N_2 saturated 0.1M NaOH using cyclic voltammetry (CV) and linear sweep voltammetry (LSV) using RRDE as shown in Figure 12. Figure 12(a) shows a typical CV of CoTe and $CoTe_2$ catalysts which showed a prominent cathodic ORR peak in O_2 saturated 0.1M NaOH. This can be assumed due to the electrocatalytic reduction of O2 since no such peak was observed in the N_2 saturated electrolyte. Additionally, LSV analysis from RRDE measurements were performed in O_2 saturated 0.1M NaOH to evaluate the ORR activity as shown in Figure 12(b) and (c) for CoTe and $CoTe_2$ catalysts, respectively. As the rotation speed was increased the corresponding cathodic current density also was increased linearly. This is the result of decreasing the diffusion layer thickness at higher rotation rates which in turn facilitates the diffusion of O_2 from the bulk electrolyte to the catalyst surface for electroreduction resulting in an increase of the cathodic current. The calculated half-wave potentials (E1/2) of CoTe and $CoTe_2$ were found to be 0.66 V and 0.74 V respectively. The insets of Figure (b) and (c) shows the relevant Koutecky-Levich plots at different potentials and shows good linearity in the given potential range.

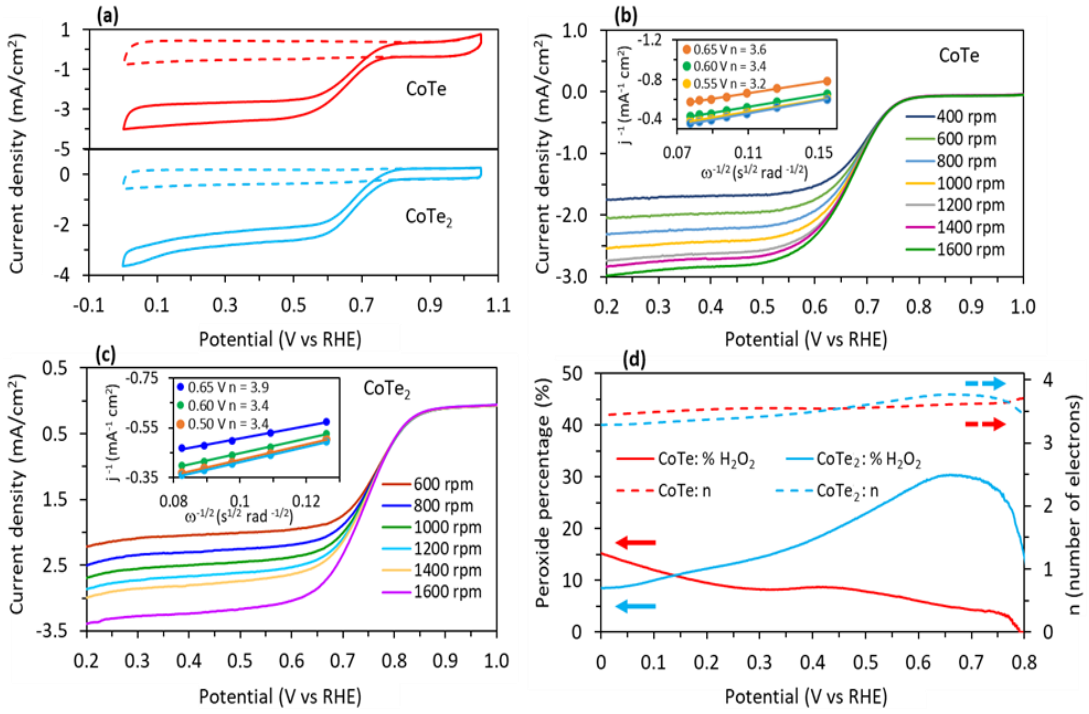

Figure 12. Evaluation of CoTe and $CoTe_2$ as oxygen reduction catalysts. (a) CV curves of CoTe and $CoTe_2$ on glassy carbon disc electrode in O_2 saturated (solid line) or N_2 saturated (dash line) 0.1M NaOH at 1600 rpm and 20 mV/s scan rate. (b) linear sweep voltammograms of CoTe and (c) $CoTe_2$ in O_2 saturated 0.1M NaOH with a scan rate of 5 mV/s at different rotation rates. The insets in (b) and (c) shows corresponding Koutecky-Levich plots at different potentials. (d) H_2O_2 yield and electron count of CoTe and $CoTe_2$ at disc rotation rate of 1600 rpm and scan rate of 5mV/s in O_2 saturated 0.1M NaOH.

The estimated value of n at a typical potential of 0.65 V for CoTe is 3.6 and 3.9 for $CoTe_2$ suggests that the oxygen reduction process follows 4 electron pathways. However, the decrease of this value at low potentials for CoTe suggests that the two-electron process gradually increases as also evident from the increase of H_2O_2 yield shown in Figure 12(d). For $CoTe_2$ this effect is not as evident as for CoTe. Lastly, we studied the stability of the two catalysts under continuous ORR conditions for 10 hours and found that CoTe retains 86% of initial activity while $CoTe_2$ retains 88% of initial activity as shown in Figure S12.

4. CONCLUSION

In this study we have successfully synthesized cobalt tellurides catalysts of CoTe and $CoTe_2$ from two different methods of electrodeposition and hydrothermal synthesis. Also, we have studied both catalysts of CoTe and $CoTe_2$ as trifunctional electrocatalysts for OER, HER and ORR activity in alkaline medium for the first time. This nano morphology of cobalt telluride catalysts exhibit outstanding catalytic performances with greater stability as trifunctional catalysts in 1M KOH alkaline medium. The low onset potentials and over potentials at 10 $mAcm^{-2}$ and higher current densities have confirmed that catalysts are efficient catalysts for water splitting reactions. The catalytic activity is an intrinsic property of the cobalt telluride catalysts that has been already confirmed by two synthesis methods of electrodeposition and hydrothermal synthesis catalysts. Also, the OER and HER catalytic performance were compared with the other reported cobalt telluride catalysts (Table S 4 and S 5). The ORR activity of cobalt telluride electrocatalysts are comparably better than the other cobalt chalcogenide based electrocatalysts. This inexpensive and highly reproducible electrocatalysts works as highly efficient trifunctional electrocatalysts for numerous energy related applications.

CONFLICTS OF INTEREST

There are no conflicts to declare.

ACKNOWLEDGEMENT

This work was supported by the National Science Foundation (DMR 1710313) and the American Chemical Society Petroleum Research Fund (54793-ND10). DFT calculations were performed at the Molecular Foundry supported through standard user proposals (4804 and 6640). ORR measurements were completed at the Los Alamos National Laboratory. The authors would like to acknowledge MRC for equipment usage.

SUPPLEMENTARY INFORMATION

Table S1. EDS elemental ratios of electrodeposited and hydrothermally synthesized cobalt tellurides.

Elements	**Electrodeposited**		**Hydrothermally synthesized**	
	CoTe	**$CoTe_2$**	**CoTe**	**$CoTe_2$**
Te L	54.26	67.78	53.14	65.42
Co K	45.74	32.22	46.86	34.58
Total	100.00	100.00	100.00	100.00

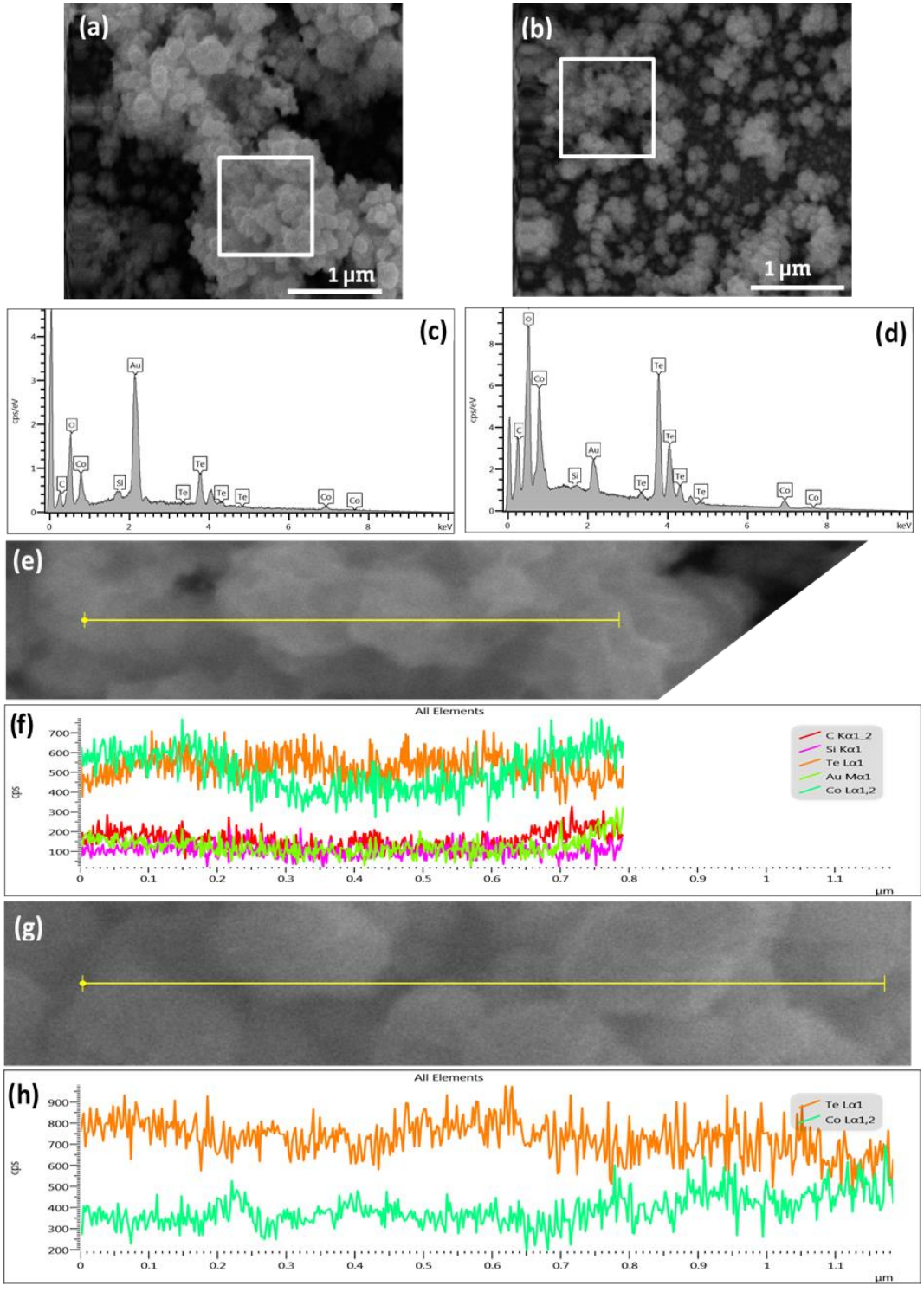

Figure S1. SEM images of electrodeposited (a) CoTe, (b) $CoTe_2$; EDS spectra of (c) CoTe , (d) $CoTe_2$; EDS line scan image of (e) CoTe , (g) $CoTe_2$; EDS line scan elemental ratios spectra of (f) CoTe , (h) $CoTe_2$.

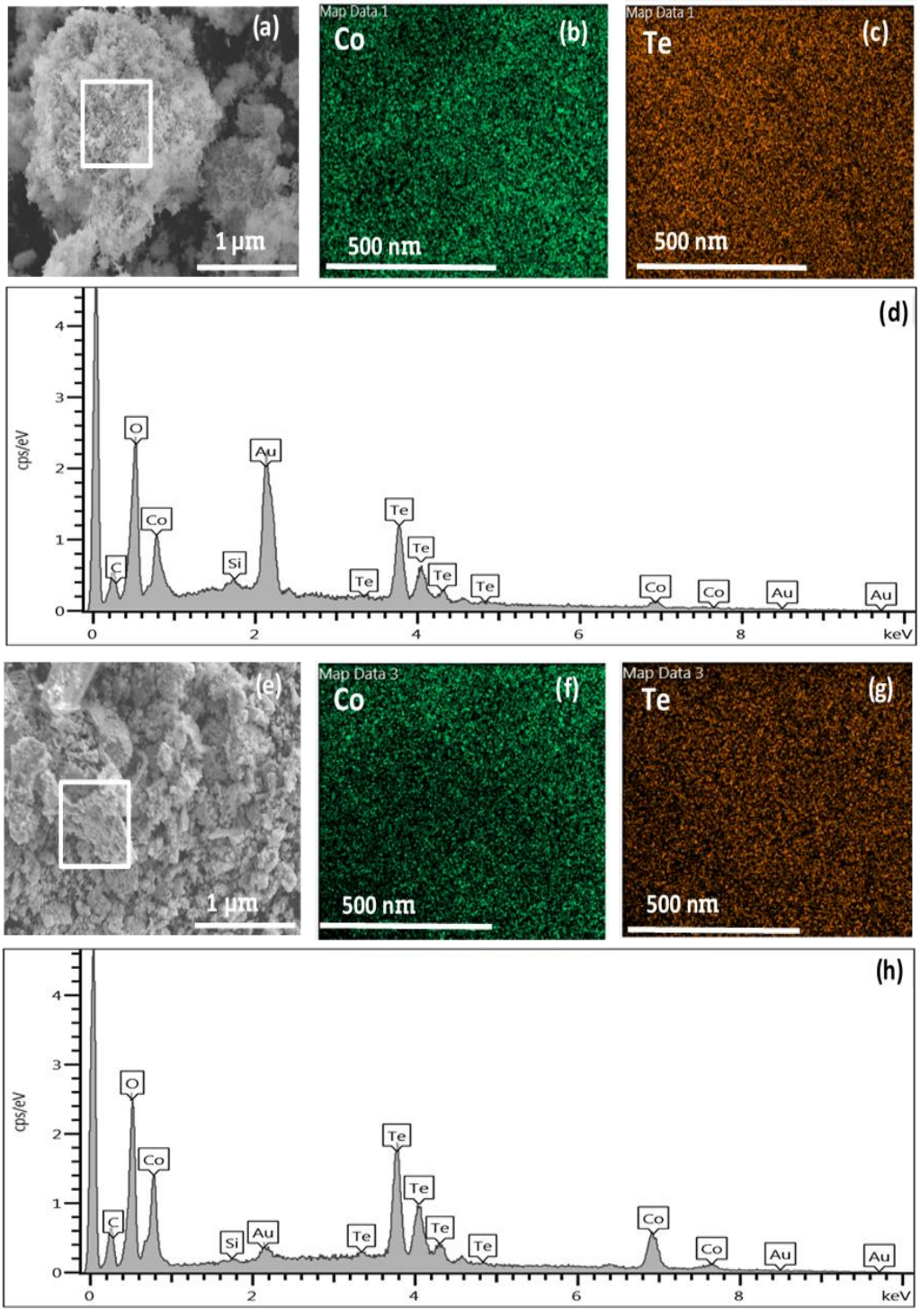

Figure S2. SEM images of hydrothermally synthesized (a) CoTe, (e) $CoTe_2$; EDS elemental mapping of (b) Co and (c) Te in CoTe and (f) Co and (g) Te in $CoTe_2$ respectively; EDS spectra of (d) CoTe , (h) $CoTe_2$.

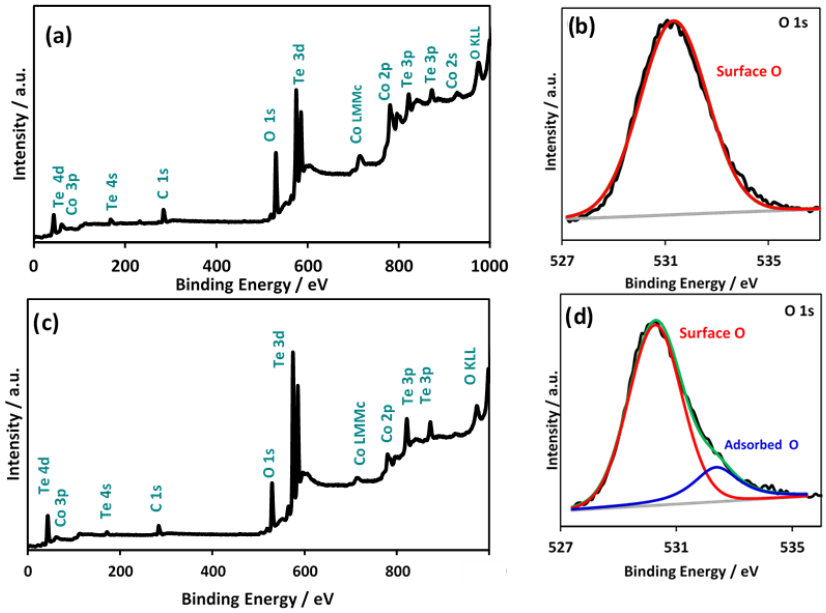

Figure S3. X-ray photoelectron spectroscopy of powdered catalysts of CoTe (a) survey (b) O 1s; $CoTe_2$ (c) survey (d) O 1s

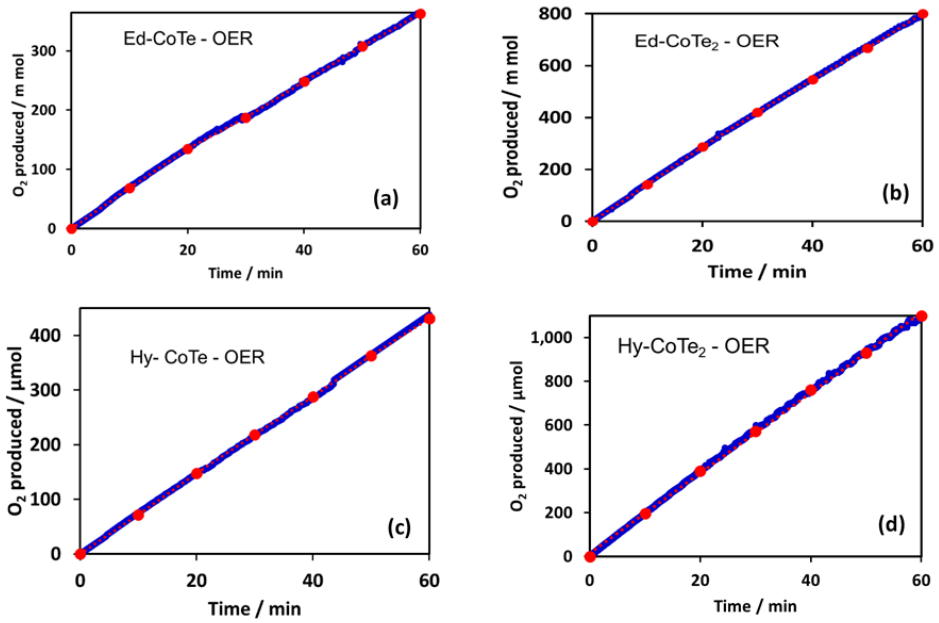

Figure S4. The Comparisons of experimentally obtained volumes of oxygen with the theoretically calculated amounts: electrodeposited (a) CoTe, (b) $CoTe_2$; hydrothermally synthesized (c) CoTe, (d) $CoTe_2$.

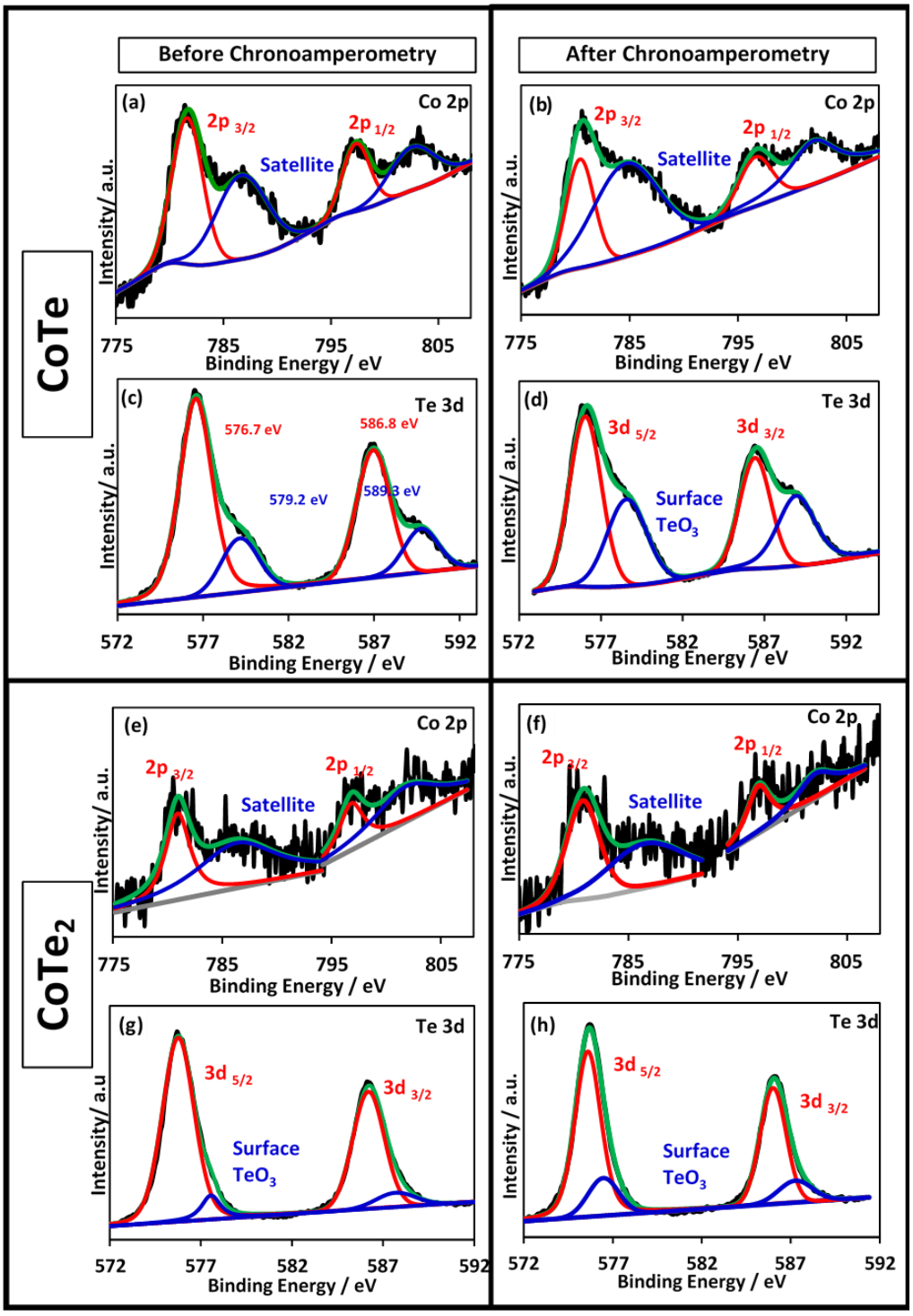

Figure S5. X-ray photoelectron spectra of prepared electrodes of CoTe before chronoamperometry (a) Co 2p (c) Te 3d after chronoamperometry (b) Co 2p (d) Te 3d; … and $CoTe_2$ before chronoamperometry (e) Co 2p (g) Te 3d after chronoamperometry (f) Co 2p (h) Te 3d respectively.

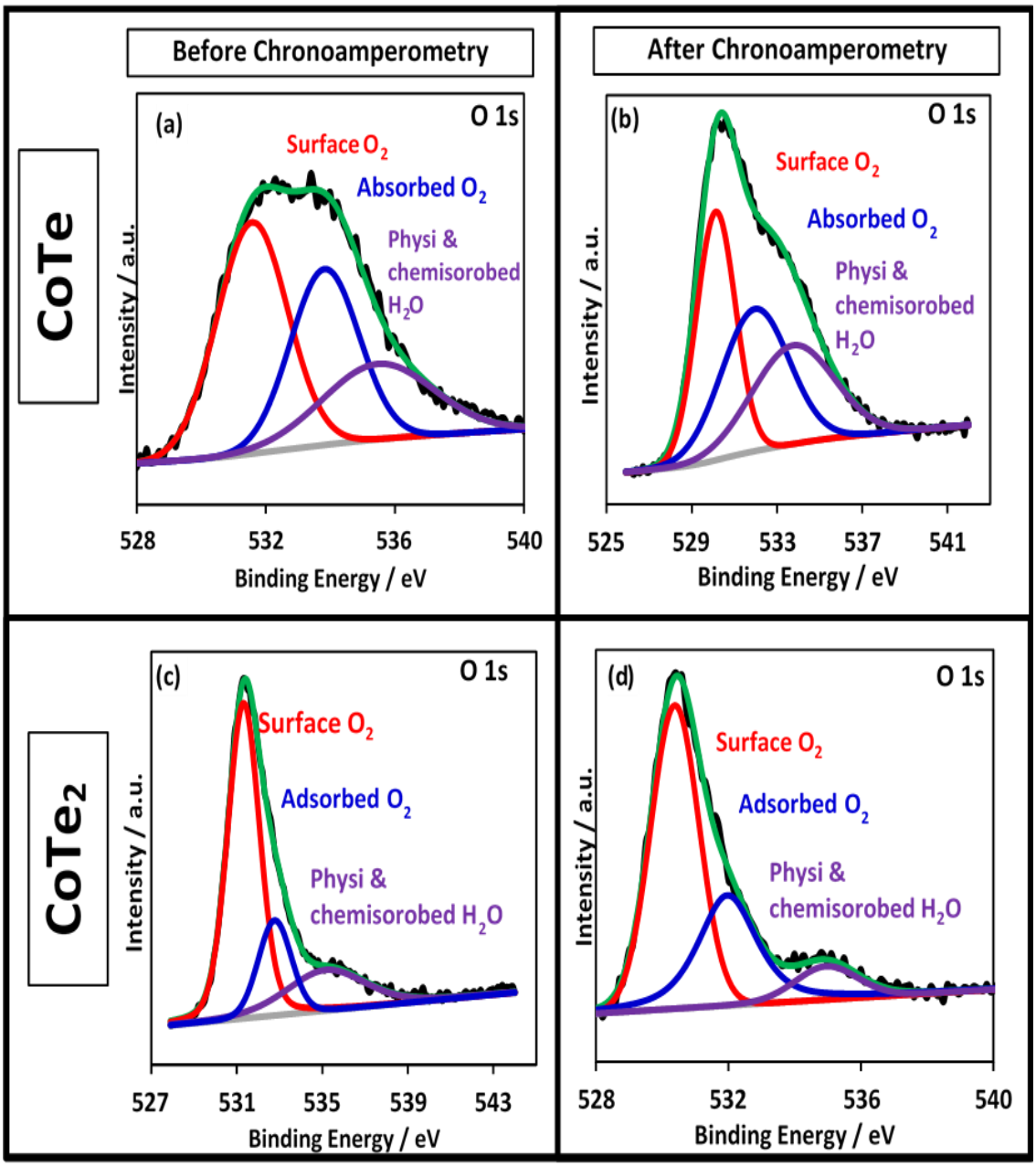

Figure S6. X-ray photoelectron spectra of O 1s prepared electrodes of CoTe (a) before chronoamperometry (b) after chronoamperometry; and $CoTe_2$ (c) before chronoamperometry (d) after chronoamperometry.

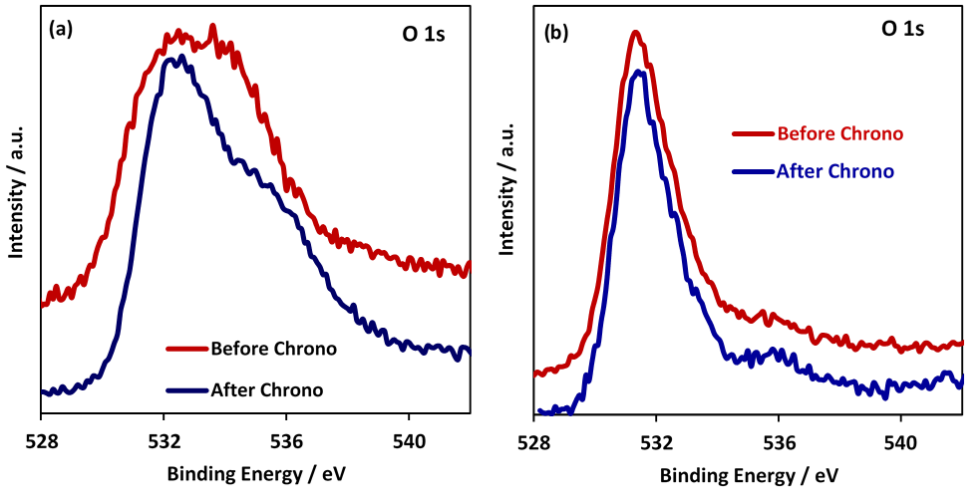

Figure S7. The comparison of O 1s X-ray photoelectron spectra of before and after chronoamperometry for (a) CoTe; (b) $CoTe_2$.

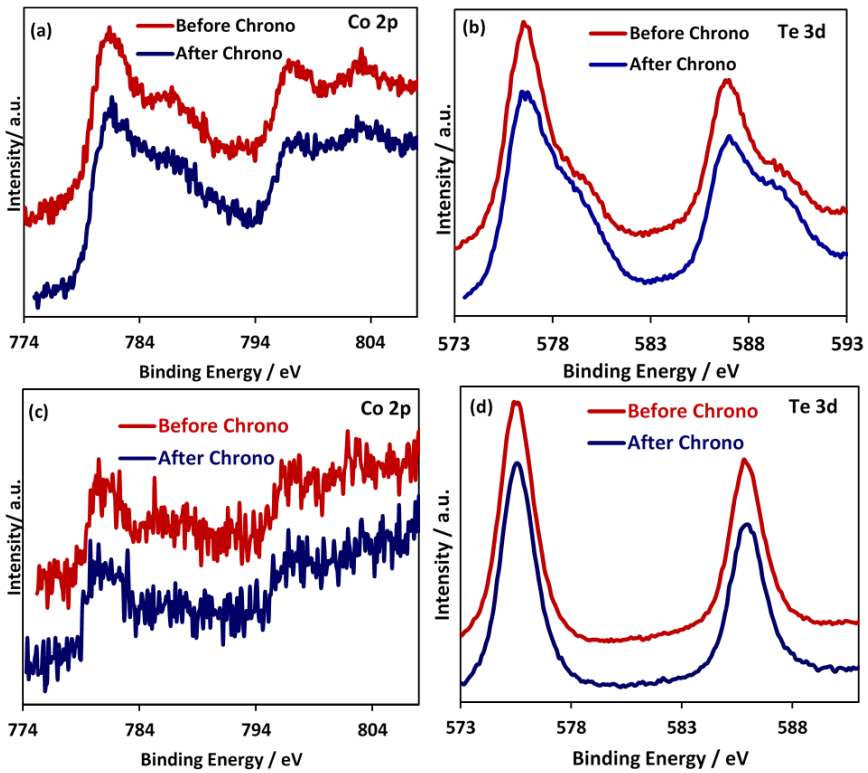

Figure S8. The comparison of X-ray photoelectron spectra of before and after chronoamperometry for CoTe (a) Co 2p , (b) Te 3d ; $CoTe_2$ (c) Co 2p, (d) Te 3d.

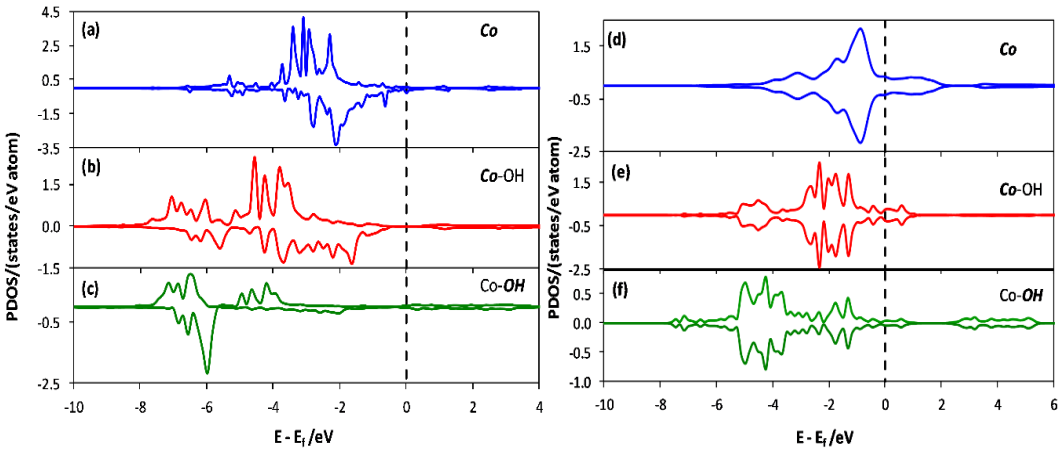

Figure S9. Calculated partial density of states (PDOS) of CoTe in (001) surface (a) Co atom before the attachment of OH^- ion, (b) Co atom after the attachment of OH^- ion, (c) OH^- ions after attachment on Co atom. Similarly, PDOS of $CoTe_2$ (001) surface (d) Co atom before the attachment of OH^- ion, (e) Co atom after the attachment of OH^- ion and (e) OH^- ions after attachment on Co atom.

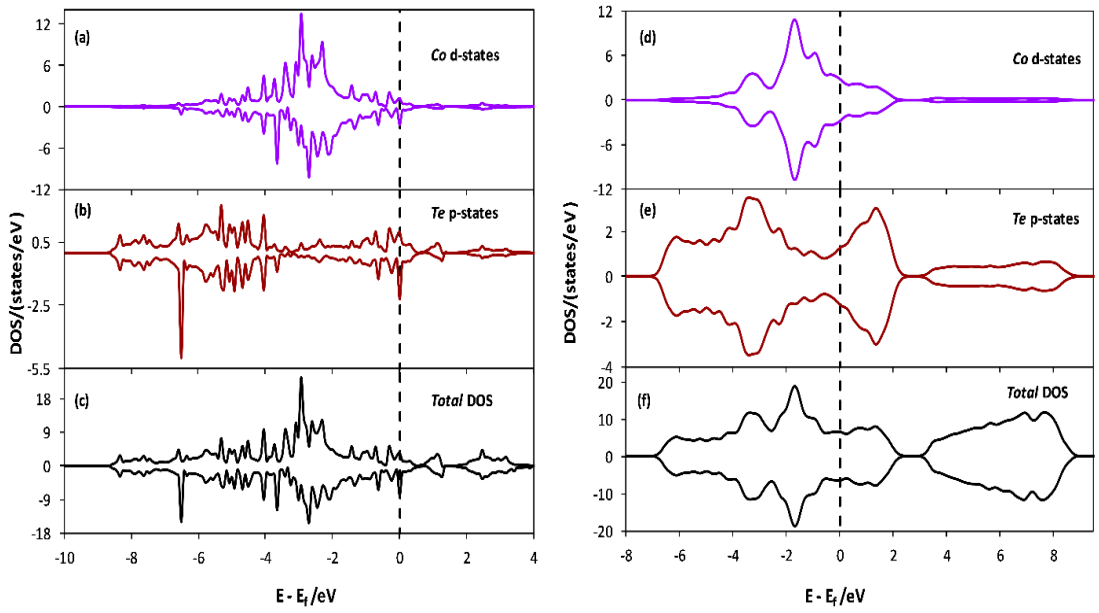

Figure S10. Contribution from (a) Co d-states and (b) Te p-states to the (c) total density of states (DOS) of CoTe in (001) surface. Accordingly, (d) and (e) illustrates the contribution from Co d-states and Te p-states to the (f) DOS of $CoTe_2$ (001) surface.

Table S2. Comparison of electrocatalytic parameters for the OER.

	CoTe-Ed	**$CoTe_2$-Ed**	**CoTe-Hy**	**$CoTe_2$-Hy**	**Pt**
Onset Potentail / V	-0.195	-0.175	-0.207	-0.250	0.000
η to 10mA cm^{-2} / mV	290	350	290	378	52
Tafel slope / mV dec^{-1}	72.8	90.5	57.2	96.5	38.5

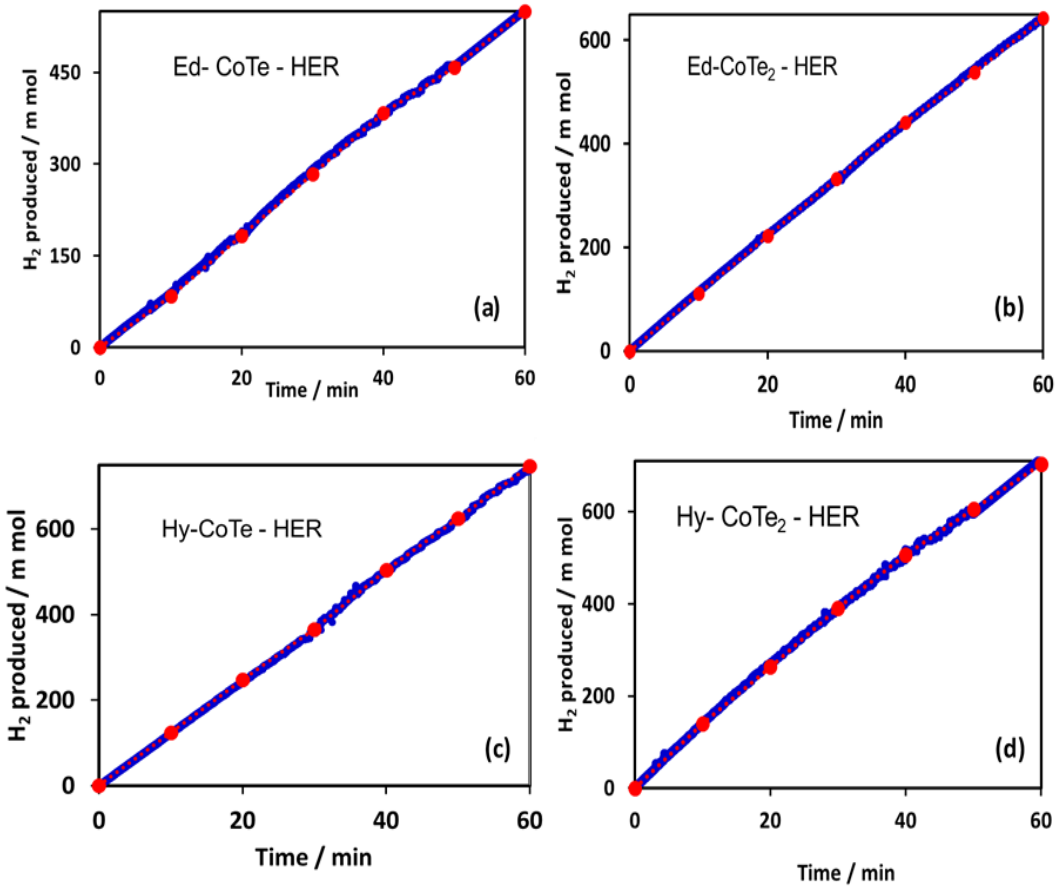

Figure S11. The comparisons of experimentally obtained volumes of hydrogen with the theoretically calculated amounts: electrodeposited (a) CoTe, (b) $CoTe_2$; hydrothermally synthesized (c) CoTe, (d) $CoTe_2$.

Table S3. The comparison of energy efficiency of catalysts.

Catalysts	**OER (V)[a] at at 10 mA cm^{-2}**	**HER (V)[a] at at 10 mA cm^{-2}**	**Water splitting cell voltage at at 10 mA cm^{-2}**	**Energy efficiency (%)[b]**
Ed- CoTe	1.43	0.28	1.71	86.54
Ed- $CoTe_2$	1.47	0.35	1.82	81.31
Hy- CoTe	1.50	0.27	1.77	83.61
Hy- $CoTe_2$	1.54	0.38	1.92	77.08

[a] All voltages are *vs* RHE.
[b] Energy efficiency of water electrolysis ≅ (1.48 $V/Ecell$) ×100.

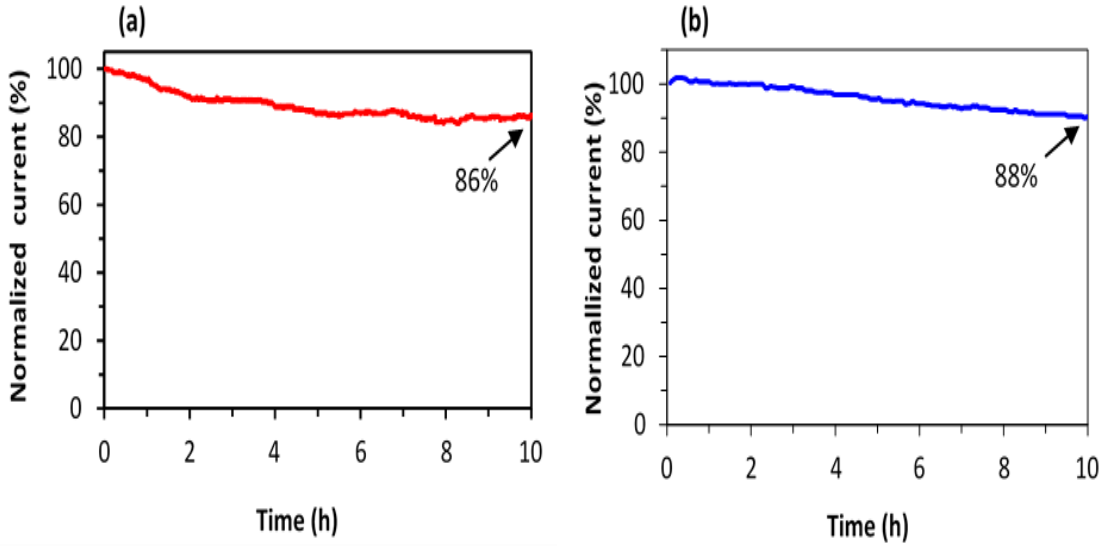

Figure S12. Stability of the (a) CoTe and (b) $CoTe_2$ electrocatalysts (0.6mg/cm^2 loading) under continuous ORR conditions in O_2 saturated 0.1M NaOH solution at 400rpm on RRDE.

Table S4. The comparison of OER activity of reported cobalt telluride catalysts.

OER Catalysts	Electrolytes	Onset potential V	η @ 10 mA cm^{-2} (mV *vs* RHE)	Tafel slope mV dec^{-1}	Loading (mg cm^{-2})	Reference
1-D- CoTe-200 ℃	1M KOH/5mVS^{-1}	1.51	370	-	0.7	1
$CoTe_2$	0.1m KOH	1.53*	357	32	0.25	2
CoTe		1.51*	365	73	0.25	
$CoTe_2$ NA/TM	1.0 M KOH	1.50*	340[b]	67	1.45	3
CoTe	1.0 M KOH/5mVS^{-1}	1.56	370	-	-	4
$CoTe_2$/ CoOx	1.0 M KOH/10 mVS^{-1}	1.45*	380	58	0.28	5
$CoTe_2$@NCNTFs	1.0 M KOH	1.56	330	98.6	0.285	6
$CoTe_2$ / CNT	1.0 M KOH	1.50*	291	44.2	-	7
CoTe-200 ℃	1.0 M KOH	1.52*	370	-	0.7	8
CoTe2@NCNTFs	1.0 M KOH	1.53*	330	82.8	0.285	9
Ed- CoTe	1.0 M KOH/10 mVS^{-1}	1.44	200	43.8	6.25	This work
Hy- CoTe	1.0 M KOH/10 mVS^{-1}	1.44	270	67.7		
Ed- $CoTe_2$	1.0 M KOH/10 mVS^{-1}	1.48	240	44.8		
Hy- $CoTe_2$	1.0 M KOH/10 mVS^{-1}	1.43	320	111.8		

* Calculated from references; [a]@ 20 mA cm^{-2}; [b]@ 50 mA cm^{-2}; [c]@ 100 mA cm^{-2},

Table S5. The comparison of HER activity of reported cobalt telluride catalysts.

HER Catalysts	Electrolytes	Onset potential V	η @ 10 mA cm^{-2} (mV *vs* RHE)	Tafel slope mV dec^{-1}	Loading (mg cm^{-2})	Reference
1-D- CoTe °C	1M KOH /5mVS^{-1}	-0.22*	-450*	-	-	1
CoTe NSs/CoTe2 NTs	0.5 M H_2SO_4 /5mVS^{-1}	-0.16*	-172	57.1	4.85	2
CoTe NTs		-0.24*	-284	58.7	-	
CoTe2 NDs/CoTe2 NTs		-0.27*	-309	63.2	4.57	
CoTe2	0.5 M H_2SO_4 /5mVS^{-1}	-0.48	-508	51	-	3
$CoTe_2$@NCNTFs - 700 °C	1M KOH/5 mV s^{-1}	-0.15*	-208	58.04	0.285	4
	0.5 M H_2SO_4 /5 mV s^{-1}	-0.15*	-240	61.67	0.285	
CoTe - 200 °C	1M KOH/5 mV s^{-1}	-0.50*	-550*	-	0.7	5
CoTe2@NCNTFs	0.5 M H2SO4	-0.2*	-240	61.67	0.285	6
	1.0 M KOH	-0.2*	-208	58.04		
CoTe - Ed	1.0 M KOH /10 mVS^{-1}	-0.195	283	72.8	6.25	This work
CoTe - Hy	1.0 M KOH /10 mVS^{-1}	-0.207	270	57.2		
$CoTe_2$ - Ed	1.0 M KOH /10 mVS^{-1}	-0.175	350	90.5		
$CoTe_2$ - Hy	1.0 M KOH /10 mVS^{-1}	-0.250	378	96.5		

* Calculated from references; [a]@ 20 mA cm^{-2}; [b]@ 50 mA cm^{-2}; [c]@ 100 mA cm^{-2},

REFERENCES

1. Turner, J.A., 2004. Sustainable hydrogen production. *Science*, *305*(5686), pp.972-974.

2. Edwards, P.P., Kuznetsov, V.L., David, W.I. and Brandon, N.P., 2008. Hydrogen and fuel cells: towards a sustainable energy future. *Energy policy*, *36*(12), pp.4356-4362.

3. Hosseini, S.E. and Wahid, M.A., 2016. Hydrogen production from renewable and sustainable energy resources: promising green energy carrier for clean development. *Renewable and Sustainable Energy Reviews*, *57*, pp.850-866.

4. Kothari, R., Buddhi, D. and Sawhney, R.L., 2008. Comparison of environmental and economic aspects of various hydrogen production methods. *Renewable and Sustainable Energy Reviews*, *12*(2), pp.553-563.

5. Steinberg, M. and Cheng, H.C., 1989. Modern and prospective technologies for hydrogen production from fossil fuels. *International Journal of Hydrogen Energy*, *14*(11), pp.797-820.

6. Koper, Marc TM. "Hydrogen electrocatalysis: A basic solution." *Nature chemistry* 5, no. 4 (2013): 255.

7. Zeng, K. and Zhang, D., 2010. Recent progress in alkaline water electrolysis for hydrogen production and applications. *Progress in energy and combustion science*, *36*(3), pp.307-326.

8. Walter, M.G., Warren, E.L., McKone, J.R., Boettcher, S.W., Mi, Q., Santori, E.A. and Lewis, N.S., 2010. Solar water splitting cells. *Chemical reviews*, *110*(11), pp.6446-6473.

9. Kemppainen, E., Bodin, A., Sebok, B., Pedersen, T., Seger, B., Mei, B., Bae, D., Vesborg, P.C.K., Halme, J., Hansen, O. and Lund, P.D., 2015. Scalability and feasibility of photoelectrochemical H 2 evolution: the ultimate limit of Pt nanoparticle as an HER catalyst. *Energy & Environmental Science*, *8*(10), pp.2991-2999.

10. Hou, D., Zhou, W., Liu, X., Zhou, K., Xie, J., Li, G. and Chen, S., 2015. Pt nanoparticles/MoS2 nanosheets/carbon fibers as efficient catalyst for the hydrogen evolution reaction. *Electrochimica Acta*, *166*, pp.26-31.

11. Cherevko, S., Geiger, S., Kasian, O., Kulyk, N., Grote, J.P., Savan, A., Shrestha, B.R., Merzlikin, S., Breitbach, B., Ludwig, A. and Mayrhofer, K.J., 2016. Oxygen and hydrogen evolution reactions on Ru, RuO2, Ir, and IrO2 thin film electrodes in acidic and alkaline electrolytes: A comparative study on activity and stability. *Catalysis Today*, *262*, pp.170-180.

12. Fuentes, R.E., Farell, J. and Weidner, J.W., 2011. Multimetallic electrocatalysts of Pt, Ru, and Ir supported on anatase and rutile TiO2 for oxygen evolution in an acid environment. *Electrochemical and Solid-State Letters*, *14*(3), pp.E5-E7.

13. Paoli, E.A., Masini, F., Frydendal, R., Deiana, D., Schlaup, C., Malizia, M., Hansen, T.W., Horch, S., Stephens, I.E. and Chorkendorff, I., 2015. Oxygen evolution on well-characterized mass-selected Ru and RuO_2 nanoparticles. *Chemical science*, *6*(1), pp.190-196.

14. Ma, L., Sui, S. and Zhai, Y., 2008. Preparation and characterization of Ir/TiC catalyst for oxygen evolution. *Journal of Power Sources*, *177*(2), pp.470-477.

15. Danilovic, N., Subbaraman, R., Chang, K.C., Chang, S.H., Kang, Y., Snyder, J., Paulikas, A.P., Strmcnik, D., Kim, Y.T., Myers, D. and Stamenkovic, V.R., 2014. Using surface segregation to design stable Ru-Ir oxides for the oxygen evolution reaction in acidic environments. *Angewandte Chemie International Edition*, *53*(51), pp.14016-14021.

16. Faber, M.S. and Jin, S., 2014. Earth-abundant inorganic electrocatalysts and their nanostructures for energy conversion applications. *Energy & Environmental Science*, *7*(11), pp.3519-3542.

17. Yan, Y., Xia, B.Y., Zhao, B. and Wang, X., 2016. A review on noble-metal-free bifunctional heterogeneous catalysts for overall electrochemical water splitting. *Journal of Materials Chemistry A*, *4*(45), pp.17587-17603.

18. Galán-Mascarós, J.R., 2015. Water oxidation at electrodes modified with earth-abundant transition-metal catalysts. *ChemElectroChem*, *2*(1), pp.37-50.

19. Wang, F., Shifa, T.A., Zhan, X., Huang, Y., Liu, K., Cheng, Z., Jiang, C. and He, J., 2015. Recent advances in transition-metal dichalcogenide based nanomaterials for water splitting. *Nanoscale*, *7*(47), pp.19764-19788.

20. Sultan, S., Tiwari, J.N., Singh, A.N., Zhumagali, S., Ha, M., Myung, C.W., Thangavel, P. and Kim, K.S., 2019. Single Atoms and Clusters Based Nanomaterials for Hydrogen Evolution, Oxygen Evolution Reactions, and Full Water Splitting. *Advanced Energy Materials*, *9*(22), p.1900624.

21. Sapountzi, F.M., Gracia, J.M., Fredriksson, H.O. and Niemantsverdriet, J.H., 2017. Electrocatalysts for the generation of hydrogen, oxygen and synthesis gas. *Progress in Energy and Combustion Science*, *58*, pp.1-35.

22. Tahir, M., Pan, L., Idrees, F., Zhang, X., Wang, L., Zou, J.J. and Wang, Z.L., 2017. Electrocatalytic oxygen evolution reaction for energy conversion and storage: a comprehensive review. *Nano Energy*, *37*, pp.136-157.

23. Zou, X. and Zhang, Y., 2015. Noble metal-free hydrogen evolution catalysts for water splitting. *Chemical Society Reviews*, *44*(15), pp.5148-5180.

24. Seh, Z.W., Kibsgaard, J., Dickens, C.F., Chorkendorff, I.B., Nørskov, J.K. and Jaramillo, T.F., 2017. Combining theory and experiment in electrocatalysis: Insights into materials design. *Science*, *355*(6321), p.eaad4998.

25. Eftekhari, A., 2017. Tuning the electrocatalysts for oxygen evolution reaction. *Materials Today Energy*, *5*, pp.37-57.

26. Suntivich, J., May, K.J., Gasteiger, H.A., Goodenough, J.B. and Shao-Horn, Y., 2011. A perovskite oxide optimized for oxygen evolution catalysis from molecular orbital principles. *Science*, *334*(6061), pp.1383-1385.

27. Zhong, H., Campos-Roldán, C., Zhao, Y., Zhang, S., Feng, Y. and Alonso-Vante, N., 2018. Recent advances of cobalt-based electrocatalysts for oxygen electrode reactions and hydrogen evolution reaction. *Catalysts*, *8*(11), p.559.

28. Bajdich, M., García-Mota, M., Vojvodic, A., Nørskov, J.K. and Bell, A.T., 2013. Theoretical investigation of the activity of cobalt oxides for the electrochemical oxidation of water. *Journal of the American chemical Society*, *135*(36), pp.13521-13530.

29. Maiyalagan, T., Jarvis, K.A., Therese, S., Ferreira, P.J. and Manthiram, A., 2014. Spinel-type lithium cobalt oxide as a bifunctional electrocatalyst for the oxygen evolution and oxygen reduction reactions. *Nature communications*, *5*, p.3949.

30. García-Mota, M., Bajdich, M., Viswanathan, V., Vojvodic, A., Bell, A.T. and Nørskov, J.K., 2012. Importance of correlation in determining electrocatalytic oxygen evolution activity on cobalt oxides. *The Journal of Physical Chemistry C*, *116*(39), pp.21077-21082.

31. Castro, E.B., Gervasi, C.A. and Vilche, J.R., 1998. Oxygen evolution on electrodeposited cobalt oxides. *Journal of applied electrochemistry*, *28*(8), pp.835-841.

32. Deng, X. and Tüysüz, H., 2014. Cobalt-oxide-based materials as water oxidation catalyst: recent progress and challenges. *ACS catalysis*, *4*(10), pp.3701-3714.

33. Liang, H., Meng, F., Cabán-Acevedo, M., Li, L., Forticaux, A., Xiu, L., Wang, Z. and Jin, S., 2015. Hydrothermal continuous flow synthesis and exfoliation of NiCo layered double hydroxide nanosheets for enhanced oxygen evolution catalysis. *Nano letters*, *15*(2), pp.1421-1427.

34. Hou, Y., Lohe, M.R., Zhang, J., Liu, S., Zhuang, X. and Feng, X., 2016. Vertically oriented cobalt selenide/NiFe layered-double-hydroxide nanosheets supported on exfoliated graphene foil: an efficient 3D electrode for overall water splitting. *Energy & Environmental Science*, *9*(2), pp.478-483.

35. Song, F. and Hu, X., 2014. Ultrathin cobalt–manganese layered double hydroxide is an efficient oxygen evolution catalyst. *Journal of the American Chemical Society*, *136*(47), pp.16481-16484.

36. Jiang, J., Zhang, A., Li, L. and Ai, L., 2015. Nickel–cobalt layered double hydroxide nanosheets as high-performance electrocatalyst for oxygen evolution reaction. *Journal of Power Sources*, *278*, pp.445-451.

37. Zhong, H., Tian, R., Gong, X., Li, D., Tang, P., Alonso-Vante, N. and Feng, Y., 2017. Advanced bifunctional electrocatalyst generated through cobalt phthalocyanine tetrasulfonate intercalated Ni2Fe-layered double hydroxides for a laminar flow unitized regenerative micro-cell. *Journal of Power Sources*, *361*, pp.21-30.

38. Zou, X., Huang, X., Goswami, A., Silva, R., Sathe, B.R., Mikmeková, E. and Asefa, T., 2014. Cobalt-embedded nitrogen-rich carbon nanotubes efficiently catalyze hydrogen evolution reaction at all pH values. *Angewandte Chemie International Edition*, *53*(17), pp.4372-4376.

39. McIntyre, N.S. and Cook, M.G., 1975. X-ray photoelectron studies on some oxides and hydroxides of cobalt, nickel, and copper. *Analytical chemistry*, *47*(13), pp.2208-2213.

40. Han, C., Bo, X., Zhang, Y., Li, M., Nsabimana, A. and Guo, L., 2015. N-doped graphitic layer encased cobalt nanoparticles as efficient oxygen reduction catalysts in alkaline media. *Nanoscale*, *7*(13), pp.5607-5611.

41. Hou, Y., Wen, Z., Cui, S., Ci, S., Mao, S. and Chen, J., 2015. An advanced nitrogen-doped graphene/cobalt-embedded porous carbon polyhedron hybrid for efficient catalysis of oxygen reduction and water splitting. *Advanced Functional Materials*, *25*(6), pp.872-882.

42. Zhou, W., Zhou, J., Zhou, Y., Lu, J., Zhou, K., Yang, L., Tang, Z., Li, L. and Chen, S., 2015. N-doped carbon-wrapped cobalt nanoparticles on N-doped graphene nanosheets for high-efficiency hydrogen production. *Chemistry of Materials*, *27*(6), pp.2026-2032.

43. Su, J., Yang, Y., Xia, G., Chen, J., Jiang, P. and Chen, Q., 2017. Ruthenium-cobalt nanoalloys encapsulated in nitrogen-doped graphene as active electrocatalysts for producing hydrogen in alkaline media. *Nature communications*, *8*, p.14969.

44. Feng, Y., Yu, X.Y. and Paik, U., 2016. Nickel cobalt phosphides quasi-hollow nanocubes as an efficient electrocatalyst for hydrogen evolution in alkaline solution. *Chemical Communications*, *52*(8), pp.1633-1636.

45. Popczun, E.J., Read, C.G., Roske, C.W., Lewis, N.S. and Schaak, R.E., 2014. Highly active electrocatalysis of the hydrogen evolution reaction by cobalt phosphide nanoparticles. *Angewandte Chemie International Edition*, *53*(21), pp.5427-5430.

46. Ha, D.H., Han, B., Risch, M., Giordano, L., Yao, K.P., Karayaylali, P. and Shao-Horn, Y., 2016. Activity and stability of cobalt phosphides for hydrogen evolution upon water splitting. *Nano Energy*, *29*, pp.37-45.

47. Yang, D., Zhu, J., Rui, X., Tan, H., Cai, R., Hoster, H.E., Yu, D.Y., Hng, H.H. and Yan, Q., 2013. Synthesis of cobalt phosphides and their application as anodes for lithium ion batteries. *ACS applied materials & interfaces*, *5*(3), pp.1093-1099.

48. He, P., Yu, X.Y. and Lou, X.W., 2017. Carbon-incorporated nickel–cobalt mixed metal phosphide nanoboxes with enhanced electrocatalytic activity for oxygen evolution. *Angewandte Chemie International Edition*, *56*(14), pp.3897-3900.

49. Kim, H., Park, J., Park, I., Jin, K., Jerng, S.E., Kim, S.H., Nam, K.T. and Kang, K., 2015. Coordination tuning of cobalt phosphates towards efficient water oxidation catalyst. *Nature communications*, *6*, p.8253.

50. Kanan, M.W., Surendranath, Y. and Nocera, D.G., 2009. Cobalt–phosphate oxygen-evolving compound. *Chemical Society Reviews*, *38*(1), pp.109-114.

51. Surendranath, Y., Kanan, M.W. and Nocera, D.G., 2010. Mechanistic studies of the oxygen evolution reaction by a cobalt-phosphate catalyst at neutral pH. *Journal of the American Chemical Society*, *132*(46), pp.16501-16509.

52. González-Flores, D., Sánchez, I., Zaharieva, I., Klingan, K., Heidkamp, J., Chernev, P., Menezes, P.W., Driess, M., Dau, H. and Montero, M.L., 2015. Heterogeneous water oxidation: surface activity versus amorphization activation in cobalt phosphate catalysts. *Angewandte Chemie International Edition*, *54*(8), pp.2472-2476.

53. Xie, L., Zhang, R., Cui, L., Liu, D., Hao, S., Ma, Y., Du, G., Asiri, A.M. and Sun, X., 2017. High-Performance Electrolytic Oxygen Evolution in Neutral Media Catalyzed by a Cobalt Phosphate Nanoarray. *Angewandte Chemie International Edition*, *56*(4), pp.1064-1068.

54. Zhong, D.K., Cornuz, M., Sivula, K., Grätzel, M. and Gamelin, D.R., 2011. Photo-assisted electrodeposition of cobalt–phosphate (Co–Pi) catalyst on hematite photoanodes for solar water oxidation. *Energy & Environmental Science*, *4*(5), pp.1759-1764.

55. You, B., Jiang, N., Sheng, M., Gul, S., Yano, J. and Sun, Y., 2015. High-performance overall water splitting electrocatalysts derived from cobalt-based metal–organic frameworks. *Chemistry of Materials*, *27*(22), pp.7636-7642.

56. Ma, T.Y., Dai, S., Jaroniec, M. and Qiao, S.Z., 2014. Metal–organic framework derived hybrid Co3O4-carbon porous nanowire arrays as reversible oxygen evolution electrodes. *Journal of the American Chemical Society*, *136*(39), pp.13925-13931.

57. Guan, C., Sumboja, A., Zang, W., Qian, Y., Zhang, H., Liu, X., Liu, Z., Zhao, D., Pennycook, S.J. and Wang, J., 2019. Decorating Co/CoNx nanoparticles in nitrogen-doped carbon nanoarrays for flexible and rechargeable zinc-air batteries. *Energy Storage Materials*, *16*, pp.243-250.

58. Liao, M., Zeng, G., Luo, T., Jin, Z., Wang, Y., Kou, X. and Xiao, D., 2016. Three-dimensional coral-like cobalt selenide as an advanced electrocatalyst for highly efficient oxygen evolution reaction. *Electrochimica Acta*, *194*, pp.59-66.

59. Masud, J., Swesi, A.T., Liyanage, W.P. and Nath, M., 2016. Cobalt selenide nanostructures: an efficient bifunctional catalyst with high current density at low coverage. *ACS applied materials & interfaces*, *8*(27), pp.17292-17302.

60. Li, S., Peng, S., Huang, L., Cui, X., Al-Enizi, A.M. and Zheng, G., 2016. Carbon-coated Co3+-rich cobalt selenide derived from ZIF-67 for efficient electrochemical water oxidation. *ACS applied materials & interfaces*, *8*(32), pp.20534-20539.

61. Xu, X., Du, P., Chen, Z. and Huang, M., 2016. An electrodeposited cobalt–selenide-based film as an efficient bifunctional electrocatalyst for full water splitting. *Journal of Materials Chemistry A*, *4*(28), pp.10933-10939.

62. Zhao, X., Zhang, H., Yan, Y., Cao, J., Li, X., Zhou, S., Peng, Z. and Zeng, J., 2017. Engineering the Electrical Conductivity of Lamellar Silver-Doped Cobalt (II) Selenide Nanobelts for Enhanced Oxygen Evolution. *Angewandte Chemie International Edition*, *56*(1), pp.328-332.

63. De Silva, U., Liyanage, W.P.R. and Nath, M., 2016. Magnetic Multifunctional Nanostructures as High-efficiency Catalysts for Oxygen Evolution Reactions. *MRS Advances*, *1*(34), pp.2401-2407.

64. Chen, P., Xu, K., Tao, S., Zhou, T., Tong, Y., Ding, H., Zhang, L., Chu, W., Wu, C. and Xie, Y., 2016. Phase-Transformation Engineering in Cobalt Diselenide Realizing Enhanced Catalytic Activity for Hydrogen Evolution in an Alkaline Medium. *Advanced materials*, *28*(34), pp.7527-7532.

65. Gao, Q., Huang, C.Q., Ju, Y.M., Gao, M.R., Liu, J.W., An, D., Cui, C.H., Zheng, Y.R., Li, W.X. and Yu, S.H., 2017. Phase-Selective Syntheses of Cobalt Telluride Nanofleeces for Efficient Oxygen Evolution Catalysts. *Angewandte Chemie International Edition*, *56*(27), pp.7769-7773.

66. Patil, S.A., Kim, E.K., Shrestha, N.K., Chang, J., Lee, J.K. and Han, S.H., 2015. Formation of semimetallic cobalt telluride nanotube film via anion exchange tellurization strategy in aqueous solution for electrocatalytic applications. *ACS applied materials & interfaces*, *7*(46), pp.25914-25922.

67. McKendry, I.G., Thenuwara, A.C., Sun, J., Peng, H., Perdew, J.P., Strongin, D.R. and Zdilla, M.J., 2016. Water oxidation catalyzed by cobalt oxide supported on the mattagamite phase of $CoTe_2$. *ACS Catalysis*, *6*(11), pp.7393-7397.

68. Ji, L., Wang, Z., Wang, H., Shi, X., Asiri, A.M. and Sun, X., 2018. Hierarchical $CoTe_2$ nanowire array: an effective oxygen evolution catalyst in alkaline media. *ACS Sustainable Chemistry & Engineering*, *6*(4), pp.4481-4485.

69. Kim, E.K., Bui, H.T., Shrestha, N.K., Shin, C.Y., Patil, S.A., Khadtare, S., Bathula, C., Noh, Y.Y. and Han, S.H., 2018. An enhanced electrochemical energy conversion behavior of thermally treated thin film of 1-dimensional CoTe synthesized from aqueous solution at room temperature. *Electrochimica Acta*, *260*, pp.365-371.

70. Wang, K., Ye, Z., Liu, C., Xi, D., Zhou, C., Shi, Z., Xia, H., Liu, G. and Qiao, G., 2016. Morphology-controllable synthesis of cobalt telluride branched nanostructures on carbon fiber paper as electrocatalysts for hydrogen evolution reaction. *ACS applied materials & interfaces*, *8*(5), pp.2910-2916.

71. Chia, X., Sofer, Z., Luxa, J. and Pumera, M., 2017. Unconventionally Layered $CoTe_2$ and $NiTe_2$ as Electrocatalysts for Hydrogen Evolution. *Chemistry-A European Journal*, *23*(48), pp.11719-11726.

72. Wang, X., Huang, X., Gao, W., Tang, Y., Jiang, P., Lan, K., Yang, R., Wang, B. and Li, R., 2018. Metal–organic Framework Derived $CoTe_2$ Encapsulated on Nitrogen-doped Carbon Nanotubes Frameworks: High-efficiency Bifunctional Electrocatalyst for Overall Water Splitting. *Journal of Materials Chemistry A*.,6, 3684.

73. Masud, J. and Nath, M., 2016. Co7Se8 nanostructures as catalysts for oxygen reduction reaction with high methanol tolerance. *ACS Energy Letters*, *1*(1), pp.27-31.

74. Shi, Z., Liu, H., Lee, K., Dy, E., Chlistunoff, J., Blair, M., Zelenay, P., Zhang, J. and Liu, Z.S., 2011. Theoretical study of possible active site structures in cobalt-polypyrrole catalysts for oxygen reduction reaction. *The Journal of Physical Chemistry C*, *115*(33), pp.16672-16680.

75. Patel, A.M., Ringe, S., Siahrostami, S., Bajdich, M., Nørskov, J.K. and Kulkarni, A.R., 2018. Theoretical approaches to describing the oxygen reduction reaction activity of single-atom catalysts. *The Journal of Physical Chemistry C*, *122*(51), pp.29307-29318.

76. De Silva, U., Masud, J., Zhang, N., Hong, Y., Liyanage, W.P., Zaeem, M.A. and Nath, M., 2018. Nickel telluride as a bifunctional electrocatalyst for efficient water splitting in alkaline medium. *Journal of Materials Chemistry A*, *6*(17), pp.7608-7622.

77. Zhang, G., Fang, H., Yang, H., Jauregui, L.A., Chen, Y.P. and Wu, Y., 2012. Design principle of telluride-based nanowire heterostructures for potential thermoelectric applications. *Nano letters*, *12*(7), pp.3627-3633.

78. Liyanage, W.P., Wilson, J.S., Kinzel, E.C., Durant, B.K. and Nath, M., 2015. Fabrication of CdTe nanorod arrays over large area through patterned electrodeposition for efficient solar energy conversion. *Solar Energy Materials and Solar Cells*, *133*, pp.260-267.

79. Krupke, W.F., Page, R.H., DeLoach, L.D. and Payne, S.A., 1996. *Transition-metal doped sulfide, selenide, and telluride laser crystal and lasers*. U.S. Patent 5,541,948.

80. Mitzi, D.B., Copel, M. and Murray, C.E., 2006. High-mobility p-type transistor based on a spin-coated metal telluride semiconductor. *Advanced Materials*, *18*(18), pp.2448-2452.

81. Bhat, K.S., Barshilia, H.C. and Nagaraja, H.S., 2017. Porous nickel telluride nanostructures as bifunctional electrocatalyst towards hydrogen and oxygen evolution reaction. *international journal of hydrogen energy*, *42*(39), pp.24645-24655.

82. McKone, J.R., Marinescu, S.C., Brunschwig, B.S., Winkler, J.R. and Gray, H.B., 2014. Earth-abundant hydrogen evolution electrocatalysts. *Chemical Science*, *5*(3), pp.865-878.

83. McCrory, C.C., Jung, S., Peters, J.C. and Jaramillo, T.F., 2013. Benchmarking heterogeneous electrocatalysts for the oxygen evolution reaction. *Journal of the American Chemical Society*, *135*(45), pp.16977-16987.

84. Wu, G., Chung, H.T., Nelson, M., Artyushkova, K., More, K.L., Johnston, C.M. and Zelenay, P., 2011. Graphene-riched Co9S8-NC non-precious metal catalyst for oxygen reduction in alkaline media. *ECS transactions*, *41*(1), p.1709.

85. Patterson, A.L., 1939. The Scherrer formula for X-ray particle size determination. *Physical review*, *56*(10), p.978.

86. Sivanantham, A., Ganesan, P., Estevez, L., McGrail, B.P., Motkuri, R.K. and Shanmugam, S., 2018. A Stable Graphitic, Nanocarbon-Encapsulated, Cobalt-Rich Core–Shell Electrocatalyst as an Oxygen Electrode in a Water Electrolyzer. *Advanced Energy Materials*, *8*(14), p.1702838.

87. Blöchl, P.E., 1994. Projector augmented-wave method. *Physical review B*, *50*(24), p.17953.

88. Kresse, G. and Furthmüller, J., 1996. Efficient iterative schemes for ab initio total-energy calculations using a plane-wave basis set. *Physical review B*, *54*(16), p.11169.

89. Perdew, J.P., Chevary, J.A., Vosko, S.H., Jackson, K.A., Pederson, M.R., Singh, D.J. and Fiolhais, C., 1992. Atoms, molecules, solids, and surfaces: Applications of the generalized gradient approximation for exchange and correlation. *Physical review B*, *46*(11), p.6671.

90. Perdew, J.P., Burke, K. and Ernzerhof, M., 1996. D. of Physics and NOL 70118 J. Quantum theory group Tulane University. *Phys. Rev. Lett*, *77*, pp.3865-3868.

91. Monkhorst, H.J. and Pack, J.D., 1976. Special points for Brillouin-zone integrations. *Physical review B*, *13*(12), p.5188.

III. UNDERSTANDING STRUCTURAL EVOLUTION OF NICKEL CHALCOGENIDE ELECTROCATALYST SURFACE FOR WATER OXIDATION

Manuscript has been submitted to ACS Applied Energy Materials

Umanga De Silva[a], Jennifer See[a], Wipula P. R. Liyanage[a], Jahangir Masud[a], Jinpeng Wu[b], Wanli Yang[b], Wei-Ting Chen[c], David Prendergast[d], Manashi Nath*[a]

[a]Department of Chemistry, Missouri University of Science and Technology, Rolla, MO 65409.

[b]Advanced Light Source, Lawrence Berkeley National Laboratory, One cyclotron road, Berkeley, CA 94720

[c]Materials Research Center, Missouri University of Science and Technology, Rolla, MO 65409.

[d]Molecular Foundry, Lawrence Berkeley National Laboratory, One cyclotron road, Berkeley, CA 94720

*Email: nathm@mst.edu

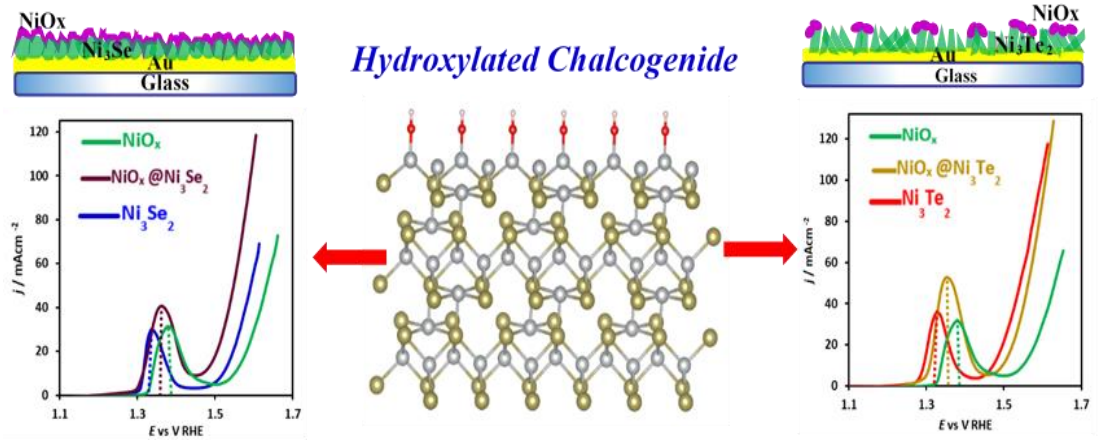

ABSTRACT

Recently nickel selenide and telluride based electrocatalysts have shown promising results toward water electrolysis, exhibiting very low overpotential. However, a major challenge for these chalcogenide-based electrocatalysts has been correct identification of catalytically active species on the surface, with the common concern being that the surface is totally being converted to nickel oxide which becomes the true catalytically active species. In this article we have attempted to understand evolution of the active surface composition for nickel selenide and telluride based electrocatalysts by intentionally creating nickel oxide coated Ni_3Se_2 and Ni_3Te_2 surfaces and comparing their electrocatalytic activity with pristine and aged (subjected to KOH electrolyte for extended period) Ni_3Se_2 and Ni_3Te_2 surfaces, respectively. From such comparison it could be confirmed that catalytically active Ni_3Se_2 and Ni_3Te_2 surfaces were in fact stable in alkaline medium and were not coated with nickel oxide even after prolonged exposure to KOH under anodic potential. Rather active surface for these electrocatalysts can be described as a mixed anionic (hydroxo)chalcogenide surface. The nickel oxide coated nickel selenide and nickel telluride samples were prepared through electrodeposition and characterized with various bulk and surface analytical techniques such as powder X-ray diffraction (pxrd), X-ray photoelectron spectroscopy (XPS), line scan analysis, and soft X-ray absorption spectroscopy (sXAS). The electrochemical properties of these oxide coated chalcogenide surfaces were measured in 1 M KOH under anodic potential scan and compared with that obtained from pristine nickel selenide and nickel telluride films. It was observed that the electrochemical properties were influenced by the coordinating

anion composition and showed significant difference between oxide, selenide, and telluride surfaces. More importantly, it also revealed that an oxide coated chalcogenide surface showed significantly different electrocatalytic response indicating that electrochemical properties can be an appropriate tool for investigating change in composition of the chalcogenide surfaces. This study provides conclusive evidence that surface of the nickel selenide and telluride based OER electrocatalysts evolves into a mixed anionic (hydroxo)chalcogenide surface retaining its predominant chalcogenide coordination.

Keywords: Oxygen evolution reaction, electrocatalysts, nickel selenide, nickel telluride, oxychalcogenide.

1. INTRODUCTION

In recent years, designing efficient electrocatalysts for water splitting under ambient conditions has attracted significant attention due to its potential usage in various applications related to fossil-fuel free sustainable energy conversion and storage technologies such as fuel cells, on demand hydrogen generation systems and solar water splitting.[1-6] Among these electrocatalysts, transition metal chalcogenides has taken the center stage owing to their unprecedented high activity exhibiting some of the lowest overpotentials with high current density compared to precious metal oxides.[7-20] Transition metal chalcogenides, M_xE_y, typically containing chalcogens (E = S, Se, and Te) bonded to various transition metals (M = Fe, Co, Ni, Cu, Mo, W etc.), have been researched extensively owing to their interesting optoelectronic properties.[21,22] The enhanced

electrocatalytic activities of these transition metal chalcogenides towards water oxidation is believed to be due to decreased anion electronegativity of the chalcogen atoms, as well as facile redox tunability of the catalytically active transition metal center.[7,18] Specifically it has been observed that replacing highly electronegative oxide anion with selenide or telluride anions leads to better electrocatalytic activity, i.e. Ni-selenide and Ni-telluride shows better OER activity compared to Ni-oxide/hydroxide.[8,10] However, in spite of tremendous volume of research conducted by several groups of researchers showing unprecedented catalytic activity for these transition metal chalcogenides, little understanding has been gained regarding composition of the active catalyst surface. The Achilles heel of the entire process is based on the perceived lack of stability of chalcogenide surface under conditions of OER in alkaline medium. Some researchers claim that the chalcogenide surfaces are completely hydrolyzed forming a surface oxy-hydroxide phase which is the true catalytically active phase.[23-35]According to this school of thought, the underlying chalcogenide matrix enhances catalytic activity of the (hydroxo)chalcogenides overlayer by improving conductivity of the catalyst composite compared to the bulk oxide phase. In these reports the sulfides and selenides are treated as pre-catalysts that yield the oxide phases upon exposure. The main evidentiary support for such mechanism is offered from XPS studies that show degradation of the chalcogen peak after long-term OER.[36] However, it must be noted here that surface hydrolysis and complete conversion to an oxide/(oxy)hydroxide overlayer involves substitution and replacement of all the chalcogen anions on the surface with O/OH anions. It should be also noted that the metal-chalcogen bonds have a higher degree of covalency following Fajan's rules,[37] compared to metal-oxygen bonds and thereby, have higher bond strength.

Hence, substitution of all the chalcogen anions with O/OH anions will be very energy intensive process especially at ambient temperature and at low applied potential. Based on our previous research on Ni-selenide and Ni-telluride based OER electrocatalysts,[8,10] we propose a different composition of the catalytically active interface for these novel transition metal chalcogenides under alkaline conditions. Previously we have observed that surface XPS signals for Ni-telluride and Ni-selenide show retention of the chalcogen peaks and more importantly does not show significant O 1s and/or Ni peaks corresponding to the buildup of Ni-O/Ni-OH linkages. Moreover, through extensive electrochemical studies for Ni_3Te_2, we have confirmed that the active surface primarily consists of metal-chalcogenide composition even after prolonged OER activity in alkaline medium.[8] Hence, we propose that the active interface comprises mixed anionic composition, metal(hydroxy)chalcogenide M(OH)E, formed through hydroxyl adsorption on the surface during OER, but retaining its chalcogenide lattice. It has been well accepted that the multi-step OER process is initiated by the adsorption of -OH- ions on the catalytically active site followed by subsequent steps of intermediate adsorption and electron transfer.[38-45] This –OH adsorption is considered to be catalyst activation and energetics of –OH adsorption on the surface has significant influence on the observed catalytic activity.[8,18] Such mixed anionic (hydroxo)chalcogenide surface can be expected to retain electronic properties characteristic of the chalcogenide lattice along with enhanced conductivity thereby explaining improved catalytic activity. DFT calculations performed on Ni_3Te_2 surface have also shown favorable adsorption of OH- groups on the catalytically active Ni site compared to NiO.[8] However, in spite of some post-activity and ex situ characterizations that proposes either the completely hydrolyzed (NiO_x /NiOOH)

or (hydroxo)chalcogenides surface model as the interface, there has been limited experimental studies to accurately confirm the active interface composition. In this article, we have attempted to answer the key questions: what is the composition of catalytically active surface for these chalcogenides and how does the surface composition evolve during OER in alkaline medium. We have also attempted to confirm validity of the mixed anionic (hydroxo)chalcogenide surface model by intentionally creating oxide-coated chalcogenide surfaces and comparing their catalytic activity and other properties with that of the pristine chalcogenide surface before and after OER activity. It should be noted here that the oxyhydroxide/oxide phase when formed in situ during oxygen evolution reaction, may have a different thickness depending on the limit of applied potential, and the intentionally deposited NiO_x does not necessarily lead to the same thickness. However, the intent of this manuscript is to propose and validate the idea that growth of any oxide layer on the surface as a function of exposure to alkaline medium, high potential, or reaction time, will be distinctly noticeable through electrochemical measurements such as cyclic voltammetry which shows significant difference between Ni^{2+} coordinated to Te or Se anions and Ni^{2+} coordinated to oxide anions. It should also be noted that surface oxide (or oxyhydroxide) phase refers to the catalyst surface comprising continuous -Ni-O(OH)-Ni- linkages replicating that found in pure oxide or oxyhydroxide phases while surface comprising -Ni(OH)-Te-Ni-Te- linkage has been referred to as mixed anionic (hydroxo)chalcogenide surface and is further being proposed as the active surface formed in situ. Specifically, we have grown Ni_3Se_2 and Ni_3Te_2 by electrodeposition and have further coated these surfaces with a thin layer of NiO_x to yield oxide@selenide and oxide@telluride surfaces (NiO_x@Ni_3Se_2 and NiO_x@Ni_3Te_2,

respectively). Comparison of the electrocatalytic activity of such oxide-coated chalcogenide surfaces with the pristine and aged chalcogenide surfaces revealed significant difference. Moreover, it was also apparent that presence of even minimal amount of NiO_x on the surface of Ni_3Te_2 or Ni_3Se_2 caused prominent shift in overpotential as well as changed surface analytical characterization as expected, making the presence of surface oxide layer easily identifiable. On comparing the electrocatalytic response of Ni_3Te_2 and Ni_3Se_2 surfaces after prolonged OER with the corresponding NiO_x@Ni_3Te_2 and NiO_x@Ni_3Se_2 pre-made surfaces, respectively, it was revealed that the Ni_3Te_2 and Ni_3Se_2 surfaces retained their original behavior and did not show any similarity with performance of the oxide coated surfaces (e.g. overpotentials of Ni_3Te_2 before and after 100 cycles of OER = 210 mV at 10 mA/cm^2, while overpotential for NiO_x@Ni_3Te_2 = 230 mV at 10 mA/cm^2). Hence it can be confirmed that the active interface for these Ni-selenide and Ni-telluride surfaces is not the Ni-oxide layer, but rather a mixed anionic (hydroxo)telluride (/selenide) surface. Even a thin layer of fully grown oxide (or oxyhydroxide) on the surface would lead to substantial changes in the electrochemical response as has been proposed and shown in the manuscript. We have further confirmed composition of the pristine as well as evolved catalytic surface through detailed electrochemical measurements as well as surface analytical techniques such as X-ray photoelectron spectroscopy (XPS), scanning electron microscopy (SEM), EDS, powder X-ray diffraction (pxrd), and soft X-ray absorption spectroscopy (sXAS). Combination of all these characterizations validates the mixed anionic (hydroxo)chalcogenide as the active interface for these electrocatalysts.

2. EXPERIMENTAL SECTION

2.1. MATERIALS

Nickel sulfate ($NiSO_4.6H_2O$) was purchased from Fisher Scientific, nickel acetate tetrahydrate [$Ni(CH_3CO_2)_2.4H_2O$] was purchased from J. T. Baker Chemical Company, USA, tellurium dioxide (TeO_2), selenium dioxide (SeO_2) and hydrazine hydrate ($N_2H_4.H_2O$, 100%) were purchased from Acros Organics and lithium chloride (LiCl) and KOH were purchased from Sigma Aldrich. Au coated glass slides (Au-glass, hereafter) were purchased from Deposition Research Laboratory Inc. (DRLI), St. Charles, Missouri. All the chemicals used for electrodepositions and electrochemical activity were analytical grade and were used without further purification. Deionized water (DI: resistivity 18 Mμ cm) was used to prepare all chemical solutions.

2.2. ELECTRODE PREPARATION

A conventional three-electrode system with IviumStat potentiostat were used for the electrodeposition of catalysts on Au-glass substrates. Ag|AgCl was used as reference electrode, graphite rod was used as counter electrode and Au-glass substrates were used as working electrode. Au-glass substrates were cleaned by using Micro-90 detergent followed by sonication in a mixture of isopropanol, ethanol, and deionized water for 10 minutes. After that, the substrates were thoroughly cleaned with deionized water and dried in a stream of nitrogen gas. The clean and dried Au-glass substrates were masked with a scotch tape, leaving a circular exposed area of known area (0.08 cm^2) for the

electrodeposition. After electrodeposition, the Au-glass substrates were thoroughly washed with deionized water in order to remove electrolyte adsorbents from the surface. Five different types of electrodes were prepared as has been shown in Figure. 1, which consists of two pure binary chalcogenides (i) Ni_3Se_2, and (ii) Ni_3Te_2; two oxide-coated chalcogenides, (iii) $NiO_x@Ni_3Se_2$; and (iv) $NiO_x@Ni_3Te_2$ and (v) NiO_x.

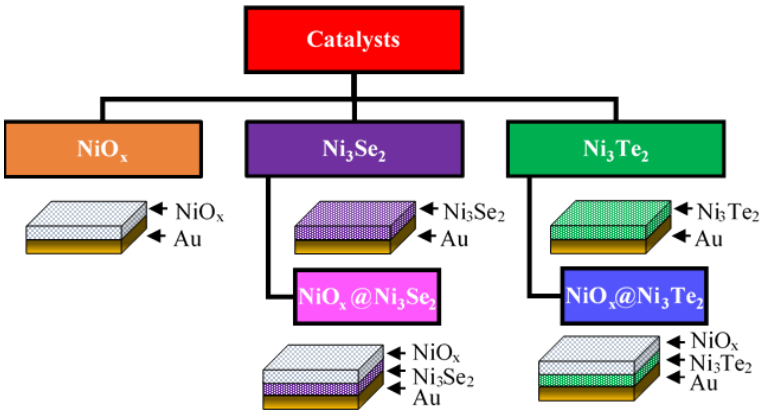

Figure 1. Schematic showing the targeted sample compositions.

2.2.1. Electrodeposition of NiO_x. Nickel oxide (NiOx) was electrodeposited from an aqueous solution of 0.5 M nickel chloride (NiCl2.6H2O), 0.1 M potassium chloride (KCl) and 0.4 M ethylenediaminetetraacetic acid (EDTA) following published report.[46] The electrolyte was maintained at pH=8 by adding appropriate amount of KOH. The electrodeposition was carried out at constant current density of -2.0 mA cm^{-2}at 25 ^{o}C for 10 min on Au-glass substrates.

2.2.2. Electrodeposition of Ni_3Se_2. A previously reported procedure from our group was followed to electrodeposit Ni_3Se_2 thin films.[10] Specifically, Ni_3Se_2 was

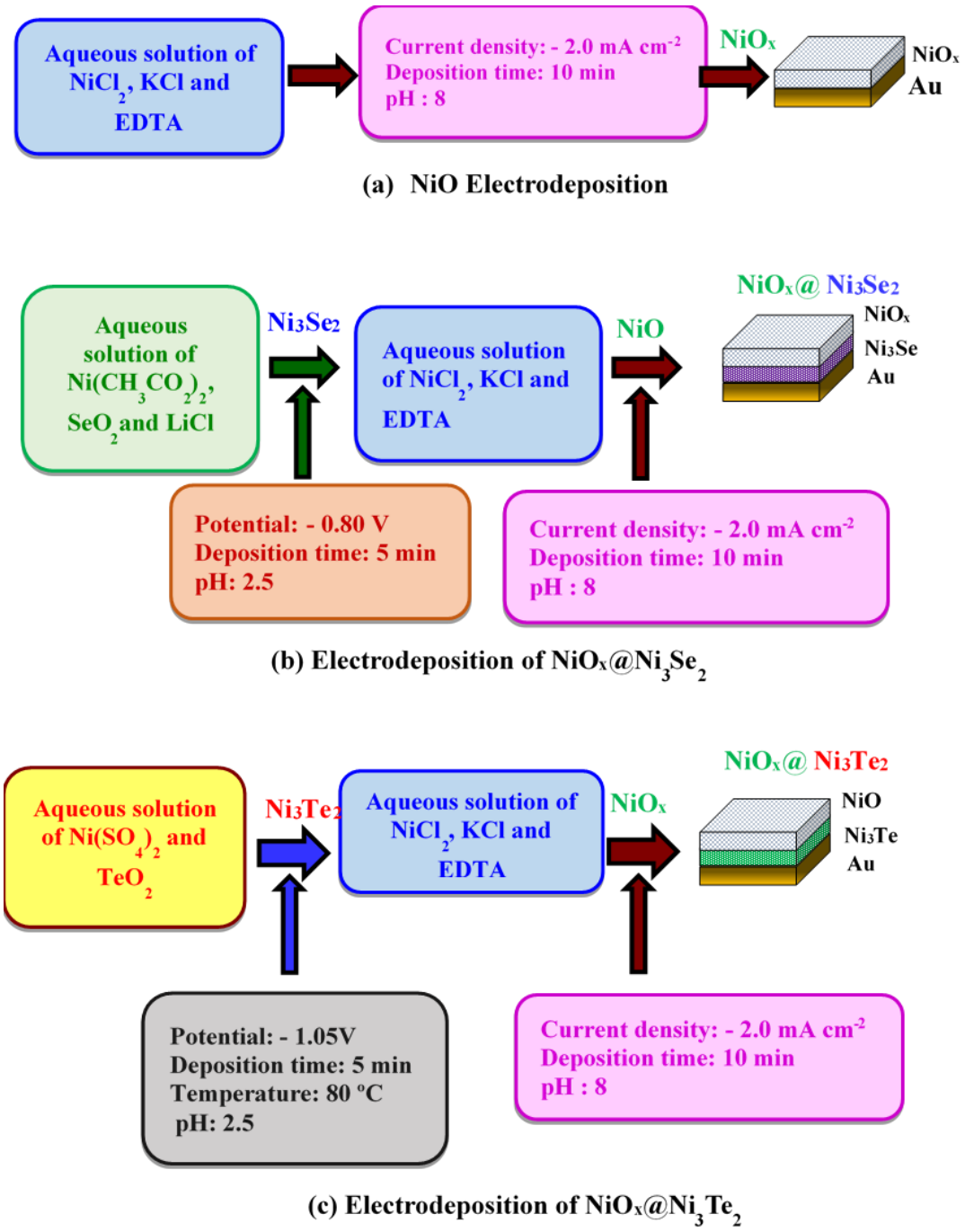

Figure 2. Schematic representation showing detailed electrodeposition conditions. (a) NiO_x; (b) NiO_x coated Ni_3Se_2 catalytic film (NiO_x @Ni_3Se_2), and (c) NiO_x coated Ni_3Te_2 catalytic film (NiO_x @Ni_3Te_2).

electrodeposited on the substrate at constant potential of -0.80 V (vs. Ag/AgCl) for 300 s from an aqueous solution containing 10 mM nickel acetate, $Ni(CH_3CO_2).4H_2O$, 10 mM SeO_2 and 25 mM LiCl at 25 ℃. The solution pH was adjusted to 2.5 using dilute HCl.

2.2.3. Electrodeposition of Ni_3Te_2. A previously reported procedure from our group was followed for electrodeposition of Ni_3Te_2.[8] Typically, Ni_3Te_2 was electrodeposited on the substrate at a constant potential of -1.05 V (vs. Ag/AgCl) for 300s from an aqueous solution containing 15 mM $Ni(SO_4).6H_2O$ and 5 mM TeO_2 25 at 25 ℃. The solution pH was adjusted to 2.5 using dilute HCl.

2.2.4. Electrodeposition of $NiO_x@Ni_3Te_2$ and $NiO_x@Ni_3Se_2$. The oxide-coated telluride and selenide surfaces were prepared by electrodepositing NiO_x on the Ni_3Te_2 and Ni_3Se_2 electrodeposited films by following the nickel oxide deposition procedure as described above. NiO_x layer was deposited for 10 min on these chalcogenide surfaces. Figure 2 shows a schematic for the electrodeposition procedures for NiO_x, Ni_3Se_2, Ni_3Te_2, $NiO_x@Ni_3Se_2$, and $NiO_x@Ni_3Te_2$.

2.3. CHARACTERIZATION

2.3.1. Powder X-Ray Diffraction (PXRD). The as-synthesized electrodeposited thin films were characterized by powder X-ray diffraction (pxrd) using a Philips X-Pert X- ray diffractometer (PANalytical, Almelo, The Netherlands) with Cu Kα (1.5418 A) radiation using grazing angle incidence in thin film geometry.

2.3.2. Scanning Electron Microscopy (SEM). The SEM images were obtained using a FEI Helios NanoLab 600 FIB/FESEM at an accelerating voltage of 10 kV and a

working distance of 4.5 mm. Energy dispersive spectroscopy (EDS) along with element mapping analysis was also obtained from the SEM microscope.

2.3.3. X-Ray Photoelectron Spectroscopy (XPS). XPS measurements were carried out using a KRATOS AXIS 165 X-ray photoelectron spectrometer (Kratos Analytical Limited, Manchester, United Kingdom). Monochromatic Al was used as an X-ray source. C 1s signal at 284.5 eV was used as a reference to correct all the XPS binding energies. XPS signals were obtained from pristine surfaces without any treatment with Ar-ion plasma.

2.3.4. Electrochemical Measurements. Electrochemical measurements were performed on the IviumStat electrochemical workstation using three-electrode system in 1.0 M KOH aqueous solution. Ag|AgCl and graphite rod were used as reference and counter electrodes respectively, while the catalyst coated Au-glass was used as working electrode. All potentials obtained vs. Ag|AgCl were converted to the reversible hydrogen electrode (RHE) by using the Nernst equation:

$$E\text{RHE} = E\text{Ag|AgCl} + 0.059\text{pH} + E^{0}\ \text{Ag|AgCl} \qquad (1)$$

where ERHE is the calculated potential vs. RHE, EAg|AgCl is the experimentally measured potential vs. Ag|AgCl reference electrode, and E^{0}Ag|AgCl is the standard thermodynamic potential of Ag|AgCl at 25 °C (0.197 V).

The OER catalytic performance was measured through linear sweep voltammetry (LSV) and cyclic voltammetry (CV) at a scan rate of 10 $mV.s^{-1}$. Stability of the catalysts were tested both by cyclic voltammetry (CV) by scanning from 0.0 V to 0.5 V (vs Ag/AgCl) at 50 $mV.s^{-1}$ for 100 cycles as well as chronoamperometry which monitored the current at constant applied potential to maintain current density at 10 $mA.cm^{-2}$ for an

extended period of time. LSV curves were measured before and after each chronoamperometry test to confirm stability and activity of the catalyst.

2.3.5. Soft X-Ray Absorption Spectroscopy (sXAS). sXAS measurement was performed at Beamline 8.0.1 of the Advanced Light Source (ALS) in Lawrence Berkeley National Laboratory (LBNL).[47] The undulator and spherical grating monochromator supply a linearly polarized photon beam with resolving power up to 6000. The experimental energy resolution is about 0.15 eV without considering core-hole lifetime broadening. Experiments were performed at room temperature and with the linear polarization of the incident beam at 45° to sample surfaces. All the sXAS spectra have been normalized to the beam flux measured by the upstream gold mesh. Please refer to previously published work for detailed procedures.[48]

3. RESULTS AND DISCUSSION

3.1. STRUCTURAL AND MORPHOLOGICAL CHARACTERIZATION

The electrodeposited films were characterized by pxrd to confirm their composition as well as crystallinity. Figures 3 (a) and (b) shows pxrd patterns of electrodeposited Ni_3Se_2, NiO_x@Ni_3Se_2, Ni_3Te_2, and NiO_x@Ni_3Te_2 films, respectively while Figure S1 shows the pxrd pattern for the NiO_x film. It was observed that electrodeposited nickel oxide typically yields amorphous films, while the selenide and telluride phase form fairly crystalline films. The crystallinity of the NiO_x can be improved when heated to higher temperature such as 350 ºC as has been reported previously.[49]

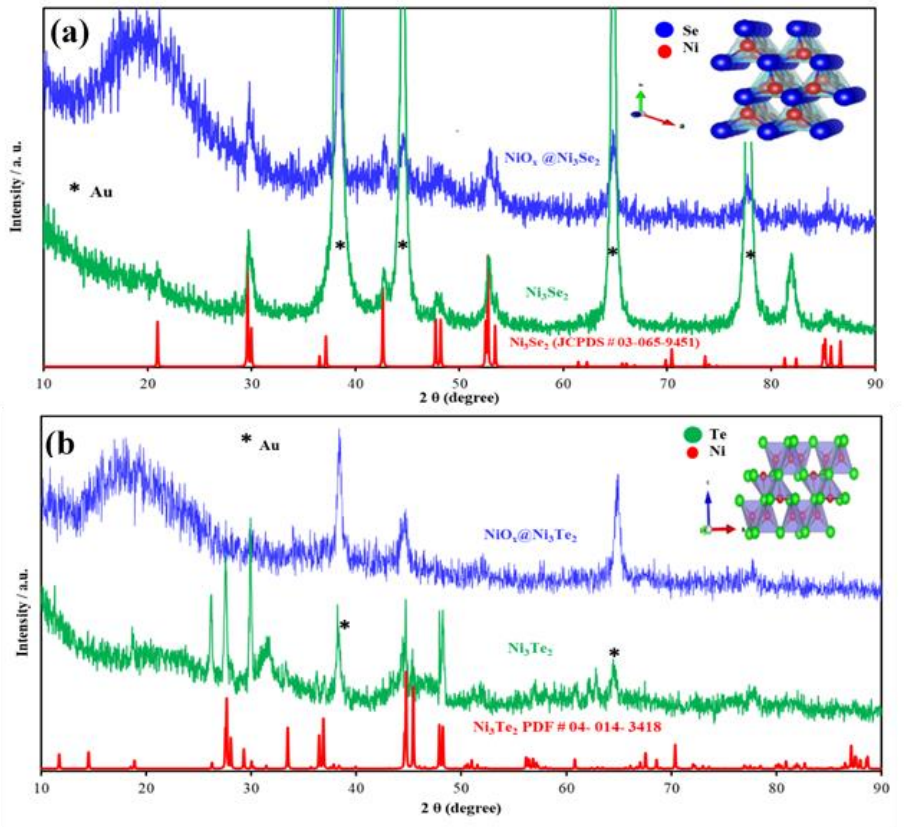

Figure 3. Powder X-Ray diffraction patterns (a) Ni_3Se_2 and $NiO_x@Ni_3Se_2$; (b) Ni_3Te_2 and $NiO_x@Ni_3Te_2$. Au peaks appeared in the XRD patterns are from Au-glass substrates.

However, in the present study, electrodeposition was performed at room temperature. It was also observed that NiO_x films required longer time for deposition (10 min) compared the selenide or telluride films (~5 min each) to achieve comparable layer thickness. This can be explained from the insulator-like behavior of NiO_x which limits charge transport within the film, while both Ni_3Se_2 and Ni_3Te_2 have higher electron conductivity due to their narrow gap semiconductor nature.

The pxrd pattern for Ni_3Se_2 matched very well with the standard diffraction pattern (PDF # 04-004-4574) as shown in Figure 3a. Ni_3Se_2 crystallizes in a Hazelwoodite type

structure which consists of corner- and edge-shared tetrahedral NiSe4 units along with octahedral coordination for Se atoms. In addition to Ni-Se bonds, the structure also contains Ni-Ni metallic bonds. Pxrd pattern of the oxide coated Ni_3Se_2 film (NiO_x@Ni_3Se_2) on the other hand, showed similar diffraction peaks for Ni_3Se_2 with slightly reduced intensity while the NiO_x phase did not show any diffraction peaks The reduction in peak intensity can be possibly explained by the presence of amorphous NiO_x overlayer. In addition, the average crystallite sizes of Ni_3Se_2 in the pristine Ni_3Se_2 and NiO_x@Ni_3Se_2 film were estimated from Scherrer equation.[50]

$$D = \frac{K\lambda}{B\,Cos\,\theta} \quad (2)$$

where D is the average crystal size, β is the FWHM, θ is the Bragg angle of the (110) peak (2θ 20.895º), and λ is the wavelength of X-rays (Cu Kα1, λ = 0.154056 nm). The FWHM values of the (110) peak for Ni_3Se_2 and NiO_x@Ni_3Se_2 were found to be 0.60 º and 0.45 º respectively. It was observed that the average crystallite size was slightly increased upon coating the selenide particles with an overlayer of oxide (Ni_3Se_2 ~ 14.31 nm; NiO_x@Ni_3Se_2 ~ 19.09 nm).

Diffraction peaks of Ni_3Te_2 were also in good agreement with the standard pattern (PDF # 04-014-3418) as shown in Figure 3b. The high intensity of the diffraction peaks revealed that the electrodeposited Ni_3Te_2 film was fairly crystalline and pure since there was no other impurity peaks observed in the pxrd pattern. Ni_3Te_2 shows an interesting crystal structure with two types of Ni coordination: layers of edge-shared $NiTe_4$ tetrahedral moieties and square-pyramidal $NiTe_5$ units edge-shared to form dimers. The $NiTe_4$ and $NiTe_5$ layers are stacked alternately along the *c*-direction. Pxrd pattern of the oxide coated Ni_3Te_2 sample showed peaks corresponding to the Ni_3Te_2 phase with

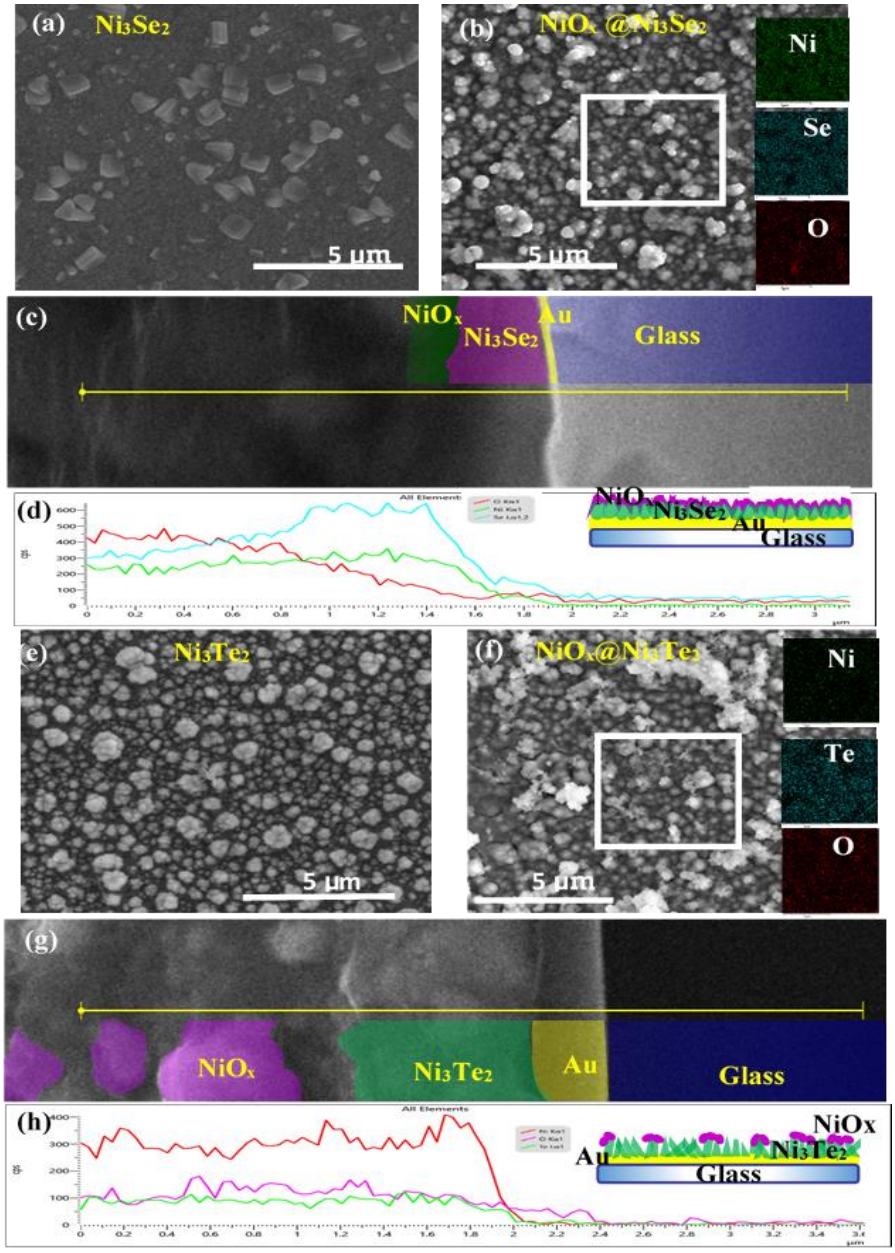

Figure 4. SEM images. (a) Ni_3Se_2; (b) NiO_x@Ni_3Se_2; (e) Ni_3Te_2 and (f) NiO_x @Ni_3Te_2 films. Insets in (b) and (f) shows the elemental mapping for Ni, Se, O and Ni, Te, respectively in NiO_x@Ni_3E_2 films. Cross-sectional SEM images in (c) and (g) were analyzed with EDS line scan (yellow line in (c) and (g)) to investigate distribution of (d) Ni, Se, O and (h) Ni, Te, O respectively, across the interface of NiO_x@Ni_3E_2 films. Insets in (d) and (h) shows schematic representation of the NiO_x@Ni_3Se_2 and NiO_x@Ni_3Te_2 films as deciphered from the cross-sectional elemental analysis.

slightly lower intensity than pristine Ni_3Te_2 while there were no diffraction peaks corresponding to NiO_x (Figure 3b). The average crystallite sizes of Ni_3Te_2 and NiO_x@ Ni_3Te_2 were estimated from Scherrer equation. Table S1 shows comparison of the crystallite sizes in pristine Ni_3Se_2, Ni_3Te_2 as well as the oxide coated films (NiO_x @Ni_3Se_2 and NiO_x@Ni_3Te_2).

Morphologies of the electrodeposited Ni_3Se_2, NiO_x@Ni_3Se_2, Ni_3Te_2, and NiO_x@ Ni_3Te_2 films were analyzed through SEM as shown in Figure 4 (a), (b), (e) and (f) respectively. All of these SEM images showed that films contained mainly irregularly shaped granules with sizes ranging from several hundred nanometers to few micrometers. SEM of Ni_3Se_2 film showed triangular and rectangular shaped granules of about 1µm randomly distributed within the film. The relative atomic percentage obtained from EDS showed a relative atomic ratio of 1.5:1 for Ni:Se confirming the composition to be Ni_3Se_2.[10] Electrodeposited Ni_3Te_2 films on the other hand, showed that surface of the irregular granules was covered with randomly oriented nano-flakes (Figure S3). Such Such vertically oriented nanoflakes can increase surface area of the pristine Ni_3Te_2 film that can enhance electrocatalytic activity. Elemental ratio obtained from EDS showed a Ni:Te average atomic ratio of 1.5:1 confirming the composition to be Ni_3Te_2.[8] Elemental mapping was also performed which showed that Ni, Se, and Te were uniformly distributed throughout the film as shown in Figures S2 and S3, respectively. SEM image of NiO_x showed that it was composed of irregular grains of similar morphology as was observed in the oxide-coated films (Figure S4), while elemental mapping showed uniform distribution of Ni and O.

The oxide coated $NiO_x@Ni_3Se_2$ and $NiO_x@Ni_3Te_2$ films were also analyzed by SEM and EDS. SEM image of $NiO_x@Ni_3Se_2$ showed irregular shaped NiO_x islands uniformly deposited on top of the Ni_3Se_2 (Figure 4b). Similar morphology was also observed for the $NiO_x@Ni_3Te_2$ films which showed NiO_x crystallites randomly deposited on top of Ni_3Te_2 film. Elemental mapping obtained from top of the $NiO_x@Ni_3Se_2$ and $NiO_x@Ni_3Te_2$ films showed co-existence of Ni, Se, Te, and O in the film as shown in Figures 4(b) and (f). Elemental line scan analysis was also performed across the edge of the deposited film to do depth profiling and further analyze the spatial distribution of the elements across the interface. To obtain such line scan analysis across the interface, the substrates were sliced along middle of the deposition. The substrates were then loaded into the SEM specimen holder and studied with a tilt angle of 45 degrees which revealed the cross-sectional edge. Line scan analysis of the $NiO_x@Ni_3Se_2$ films showed that the deposition near the substrate interface was mainly composed on Ni and Se, while the outer coating of the deposition was predominantly Ni and O, as can be seen in Figure 4(c) & (d), where Ni and Se elemental peaks are more concentrated near the substrate interface while O peaks near the film surface. Such elemental distribution and depth profiling suggested that nickel oxide deposited as a uniform, conformal coating on top of Ni_3Se_2 film thereby covering the surface with a thin layer of the oxide as depicted in the schematic shown in inset of Figure 4(d). Line scan analysis across the interface of $NiO_x@Ni_3Te_2$ film however, showed a different elemental distribution. It was observed that Ni, Te, and O were present uniformly across the deposition thickness from the substrate-interface to surface of the film, indicating that unlike $NiO_x@Ni_3Se_2$ film, nickel oxide deposited as isolated grains on the Ni_3Te_2 surface as depicted in the schematic

shown in Figure 4(g). Hence the surface of Ni_3Te_2 was apparently not uniformly coated with NiO_x even after subjecting the film to anodic potential for prolonged period of time. Line scan analysis across the interface of the binary films, NiO_x, Ni_3Se_2 and Ni_3Te_2 is given in the Figure S5 which shows uniform distribution of the elements as expected. It also shows that the binary chalcogenide films (Ni_3Se_2 and Ni_3Te_2) do not contain any significant amount of O.

X-ray photoelectron spectroscopy was performed on each of these electrodeposited films to confirm their surface elemental composition as well as oxidation states of the respective elements. Figure 5 (a) to (d) represent Ni 2p peaks for as-electrodeposited Ni_3Se_2, $NiO_x@Ni_3Se_2$, Ni_3Te_2 and $NiO_x@Ni_3Te_2$, respectively while the insets of (a) and (b) shows Se 3d peaks and (c) and (d) shows the Te 3d peaks in the respective samples as mentioned above. In Figure 5 (a), the XPS peaks at 873.7 eV and 855.4 eV can be attributed to Ni^{3+},[51] while the peaks at 870.1 eV and 852.6 eV corresponded to Ni^{2+} oxidation state in a selenide matrix.[10] The peaks positions of 878.7 eV and 860.4 eV represent Ni $2p_{3/2}$ and Ni $2p_{1/2}$ satellite peaks. The Se 3d spectra was composed of two peaks at 55.5 eV and 54.6 eV corresponding to Se $3d_{3/2}$ and Se $3d_{5/2}$.[7] The oxidation states of Se were identified as Se^{2-} and Se^{4+}, corresponding to nickel selenide and SeO_2 that can form from surface oxidation of the selenide under ambient condition.[52] Interestingly, Ni XPS spectra did not show evidence for the formation of Ni-oxide. O 1s spectra on the other hand, revealed presence of surface adsorbed oxygen as shown in Figure S6. Figure 5 (b) illustrates Ni 2p and Se 3d spectra of $NiO_x@Ni_3Se_2$, where the XPS peaks of 854.1 eV and 871.9 eV corresponds to Ni^{2+} in NiO_x of 2p3/2 and 2p1/2 respectively.[52,54]

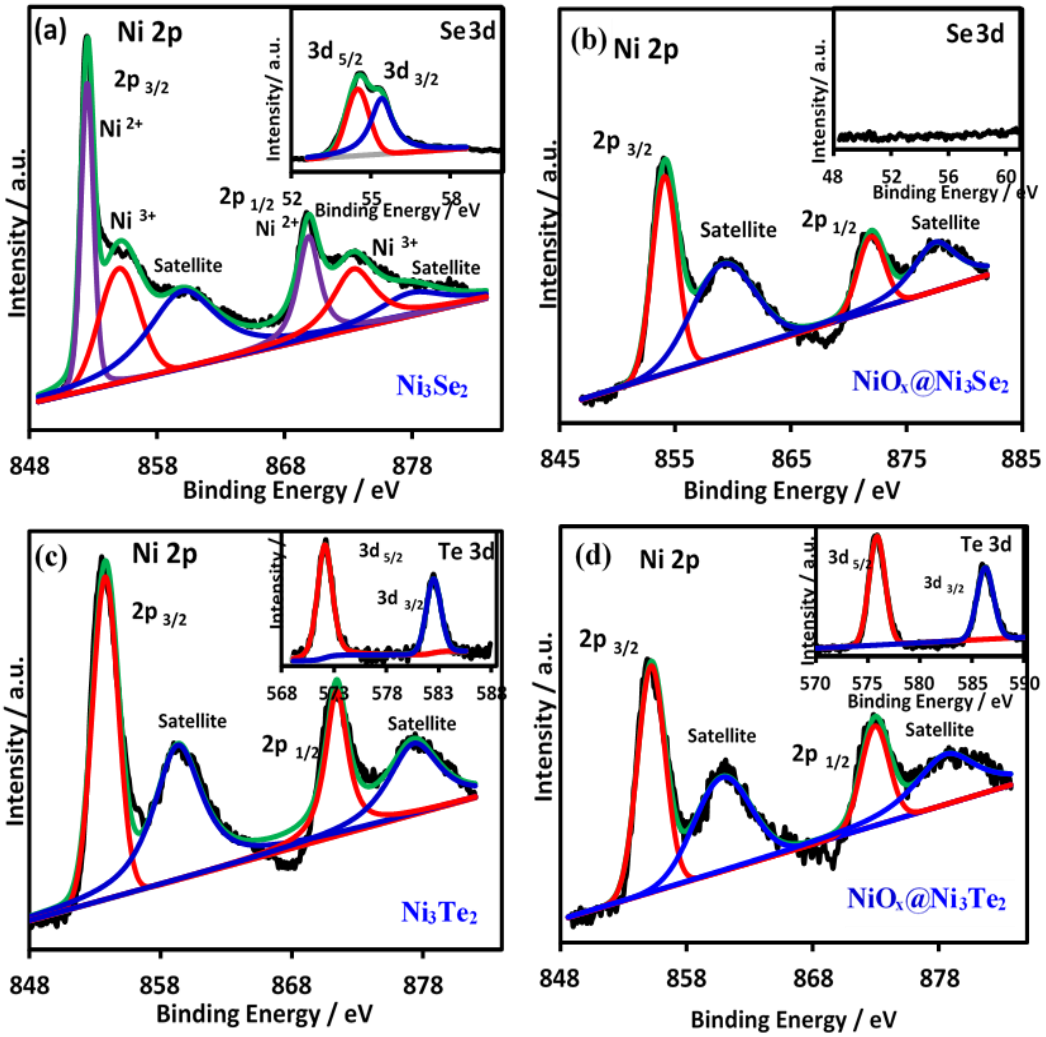

Figure 5. XPS spectra of the catalysts. Showing the Ni 2p peaks of (a) Ni_3Se_2, (b) $NiO_x@Ni_3Se_{2x}$, (c) Ni_3Te_2, (d) $NiO_x@Ni_3Te_2$. Inset of (a) and (b) shows the Se 3d peaks and (c) and (d) shows Te 3d peaks respectively.

It was also observed that Ni 2p peaks of $NiO_x@Ni_3Se_2$ sample were shifted toward higher energies than the peaks position of pristine Ni_3Se_2 and are very close to NiO_x peaks positions because the electrodeposited NiO_x overlayer on top of the pristine Ni_3Se_2. Interestingly, in Se 3d spectrum does not show the characteristic Se peaks indicating that the surface of $NiO_x@$ Ni_3Se_2 film is devoid of Se. This further confirms

that the electrodeposited NiO_x layer forms a thick, conformal coating on the Ni_3Se_2 surface (as represented in scheme shown as inset in Figure 4(d)) that inhibits X-rays to penetrate deeper into the film thickness to detect Se.

Table 1. Comparison of electrocatalytic parameters in nickel selenide and telluride.

Material	Ni_3Se_2 System		Ni_3Te_2 System		NiO_x
	Ni_3Se_2	NiO_x@Ni_3Se_2	Ni_3Te_2	NiO_x@Ni_3Te_2	
Onset potential / V	1.44	1.43	1.42	1.45	1.49
Over potential @ 10 mA cm^{-2} / mV	290	280	230	270	320
Over potential @ 50 mA cm^{-2} / mV	360	355	310	330	400
$Ni^{2+} \rightarrow Ni^{3+}$ Oxidation peak potential / V	1.34	1.36	1.32	1.35	1.38
Current density @ 300 mV / mA cm^{-2}	19.46	23.13	42.62	29.24	9.39

Similar Se XPS spectra was observed in previously reported NiOOH coated NiSe samples.[55] O1s spectra showed two peaks that were attributed to the Ni-O peak at 529.9 eV[56] and the small peak at 531.1 eV[57] was corresponded to absorbed oxygen as shown in Figure S6 (b). Ni 2p and Te 3d spectra of pristine Ni_3Te_2 are shown in Figure 5 (c). In Ni 2p spectra first doublet at 853.5 eV and 871.8 eV specified that the Ni is in Ni^{2+} oxidation state in nickel telluride[8] and the inset shows the Te 3d spectra where the peaks at 572.4 and 582.9 eV were consigned to Te^{2-} in nickel telluride.[8] As shown in Figure S6 (c), O 1s peaks were attributed to surface absorbed oxygen.[8] Figure 5 (d) shows the Ni 2p peak of electrodeposited NiO_x @Ni_3Te_2, and insert shows Te 3d spectra. It was observed that Ni^{2+} peaks positions were shifted towards higher energy relevant to Ni^{2+} in NiO_x indicating that the surface of these films indeed have nickel oxide phase.[58] The peaks at 854.1 eV and 871.9 eV were contributed to Ni $2p_{3/2}$ and $2p_{1/2}$ respectively.[54,58]

Interestingly in the Te spectra, Te 3d peaks were still observed with similar intensity as the pristine Ni_3Te_2 film, however, the peaks were slightly moved toward higher energy. This can be due to the coexistence of the oxide layer on the surface. It should be noted here that unlike $NiO_x@Ni_3Se_2$ sample which showed significant loss of Se on the surface, the $NiO_x@Ni_3Te_2$ showed that Te was still present predominantly on the surface along with O. Hence this also confirmed the proposed morphology of the $NiO_x@Ni_3Te_2$ film as NiO_x islands randomly deposited on the Ni_3Te_2 surface and not forming a conformal coating, as was also suggested from the EDS cross-sectional line scan analysis. Figure S6 (d) shows O 1s spectra and the two peaks can be assigned to Ni-O and absorbed O_2.[56]

3.2. ELECTROCHEMICAL CHARACTERIZATION

Electrochemical performance of the pristine chalcogenide and oxide@chalcogenide films were compared by measuring their linear sweep voltammetries (LSV) and cyclic voltammetries (CV) in N_2 saturated 1M KOH electrolyte. The motivation was to quantify the differences in electrochemical properties observed between pristine chalcogenide and oxide@chalcogenide films. Electrochemical properties of the chalcogenide films after prolonged exposure to 1M KOH under applied anodic potential was then compared with that of the pristine chalcogenide and oxide@chalcogenide films to evaluate probable composition of the active surface, i.e. whether they resembled the oxide@chalcogenide film indicating that the chalcogenide surfaces hydrolyzed over time to grow an oxide layer on top or they

were more closer to the pristine chalcogenide film suggesting that retained their chalcogenide surface composition.

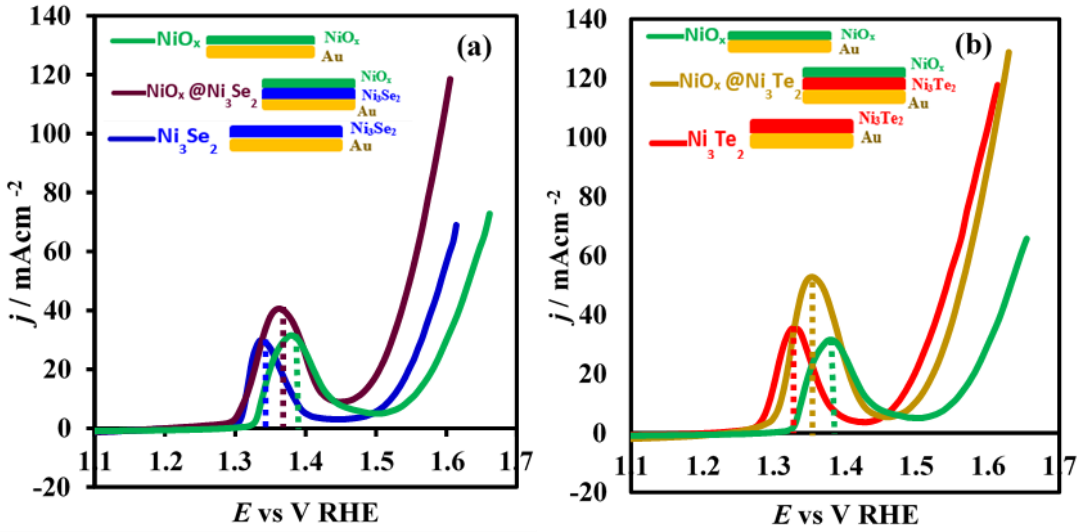

Figure 6. LSVs of catalysts. (a) NiO_x, NiO_x@Ni_3Se_2 and Ni_3Se_2; (b) NiO_x, NiO_x@Ni_3Te_2 and Ni_3Te_2.

Catalyst loadings used for each film has been summarized in Table S2. The catalysts loadings of the Ni_3Se_2 and Ni_3Te_2 electrodeposited catalysts on Au-glass substrates were maintained to be similar to previously published literature,[8,10] while NiO_x catalyst loading was 0.46 $mg.cm^{-2}$. Table 1 lists other electrocatalytic parameters such as onset potentials, overpotentials at 10 $mA.cm^{-2}$ and 50 $mA.cm^{-2}$, oxidation peak potentials and current density at 300 mV observed for all five samples.

Figure 6 (a) & (b) shows the LSV plots for the nickel selenide and telluride samples which illustrates and compares their OER performance. The onset potentials of NiO_x, Ni_3Se_2, and Ni_3Te_2 for OER were comparable to the previously

reported values.[8,10,58] As reported previously, the onset potentials exhibited a decrease from oxide to telluride as a function of decreasing electronegativity. The overpotential at 10 mA.cm^{-2} of nickel selenide and nickel tellurides were also found to be comparable to the previously reported values.[8,10] Overpotential at 10 mA.cm^{-2} for NiO_x was observed at 320 mV and was similar to previously reported literature.[51]

Comparisons of the overpotential shows that NiO_x@Ni_3Se_2 shows slightly lower overpotential at 10 mA/cm^2 compared to pristine Ni_3Se_2 while NiO_x shows the highest overpotential. For the nickel telluride system, pristine Ni_3Te_2 shows the lowest overpotential at 10 mA.cm^{-2} compared to NiO_x@Ni_3Te_2. To understand this observed trend in the pristine chalcogenide and oxide-coated chalcogenide films, we have carried out additional electrochemical measurements offering further insight as mentioned in the following sections. In nickel selenide system, NiO_x@Ni_3Se_2 shows better catalytic performance than the pristine Ni_3Se_2 and pristine NiO_x catalysts due to higher amount of active catalytic materials deposited in this sample. However, in nickel telluride system, pristine Ni_3Te_2 shows better catalytic activity compared to NiO_x@Ni_3Te_2 and pristine NiO_x. As can be clearly observed in Figures 6 and 7, NiO_x@Ni_3Se_2 and NiO_x@Ni_3Te_2 layered catalysts show larger oxidation peaks than pristine catalysts of Ni_3Se_2, Ni_3Te_2 and NiO_x due to higher amount of Ni^{2+} in two catalysts layers of these samples. The comparison of CV's, LSV's and oxidation peaks of all five samples are shown in Figure S7.

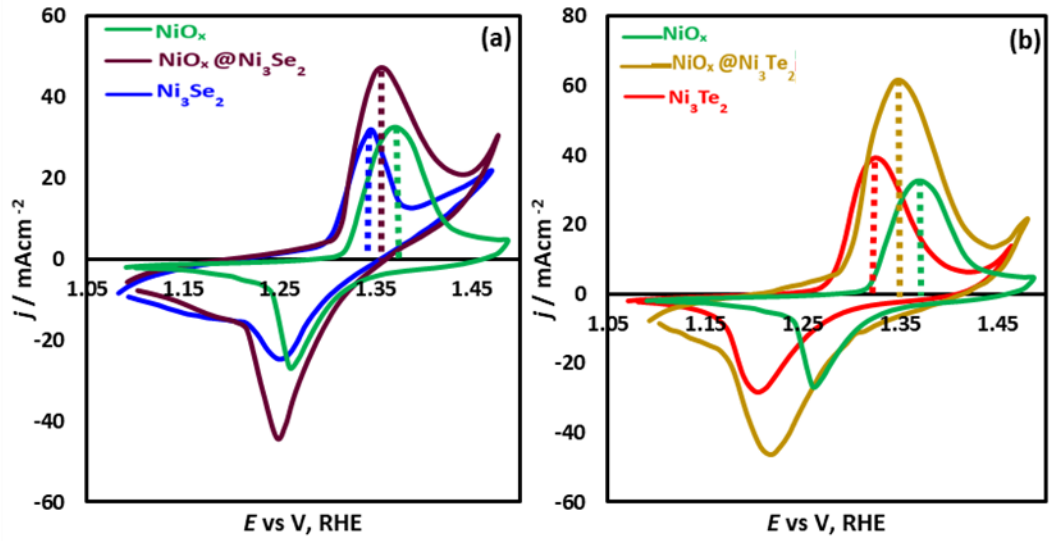

Figure 7. Oxidation peaks comparison. (a) NiO_x, NiO_x @Ni_3Se_2 and Ni_3Se_2; (b) NiO_x, NiO_x @Ni_3Te_2 and Ni_3Te_2.

For Ni-based OER electrocatalysts the pre-oxidation peak corresponding to $Ni^{2+} \rightarrow Ni^{3+}$ conversion, observed before onset of OER as a characteristic peak provides better insight into the intrinsic catalytic property since Ni^{3+} is the actual catalytically active species.[59-61] The Ni^{2+}/Ni^{3+} oxidation peak potential is influenced by the anion coordination and electronegativity and hence shows a shifts towards more cathodic potential as a function of reduced anion electronegativity as has been reported earlier.[8] Thus the Ni^{2+}/Ni^{3+} oxidation peak shows lowest value for Ni_3Te_2 followed by Ni_3Se_2 and NiO_x as has been shown previously.[10] This has a significant influence on the observed OER catalytic activity since Ni^{3+} is the actual catalytically active species, and generating Ni^{3+} at a lower potential makes Ni_3Te_2 the most catalytically active species (lowest onset and overpotential), followed by Ni_3Se_2 and NiO_x. More importantly, as has been explained before the oxidation peak potential is strongly influenced by the coordinating

anion composition and hence can be used to identify surface composition. This can be clearly seen by comparing the oxidation peak potentials for pristine chalcogenide and oxide@chalcogenide films as shown in Figure 7. The Ni_3Se_2 and Ni_3Te_2 films shows lower oxidation potential compared to NiO_x while the oxidation potential for NiO_x@ Ni_3Se_2 and NiO_x@Ni_3Te_2 films were in-between the pristine chalcogenide and oxide films as shown in Figure 7(a) and (b), respectively. It must be noted here that thickness of nickel oxide overlayer on top of the chalcogenide (Ni_3Se_2 or Ni_3Te_2) layers was moderate (as confirmed from EDS line scan analysis). Such observation confirms that even minute change of anion coordination on surface of the catalyst film will lead to shift of the Ni^{2+} oxidation peak potential. Hence, the Ni^{2+} oxidation peak potential can be used as a tool to accurately understand compositional evolution of the active surface. Subsequently it can be expected that if the nickel chalcogenide surface is gradually changed to nickel oxide (or hydroxide) overlayer on the surface during prolonged exposure in alkaline medium, the Ni^{2+} oxidation peak will show an anodic shift to higher potential to resemble the oxide@chalcogenide surfaces as shown in Figure Such shift of the oxidation peak towards more anodic potential therefore would confirm the oxide@chalcogenide surface model as has been suggested in previous reports. [36]

The compositional evolution of the catalytic surface was further investigated through cyclic voltammetry studies using the Ni^{2+}/Ni^{3+} redox peaks as a characterization tool as mentioned above. Figure 8 shows the CV plots for Ni_3Se_2 and Ni_3Te_2 pristine films as well as the NiO_x@Ni_3Se_2 and NiO_x@Ni_3Te_2 films measured for 100 cycles in 1 M KOH (every 10^{th} cycle has been shown for clarity). Insets in the upper right corners in the figures show comparison between the 1^{st} and 100^{th} CV cycle. Interestingly, this CV

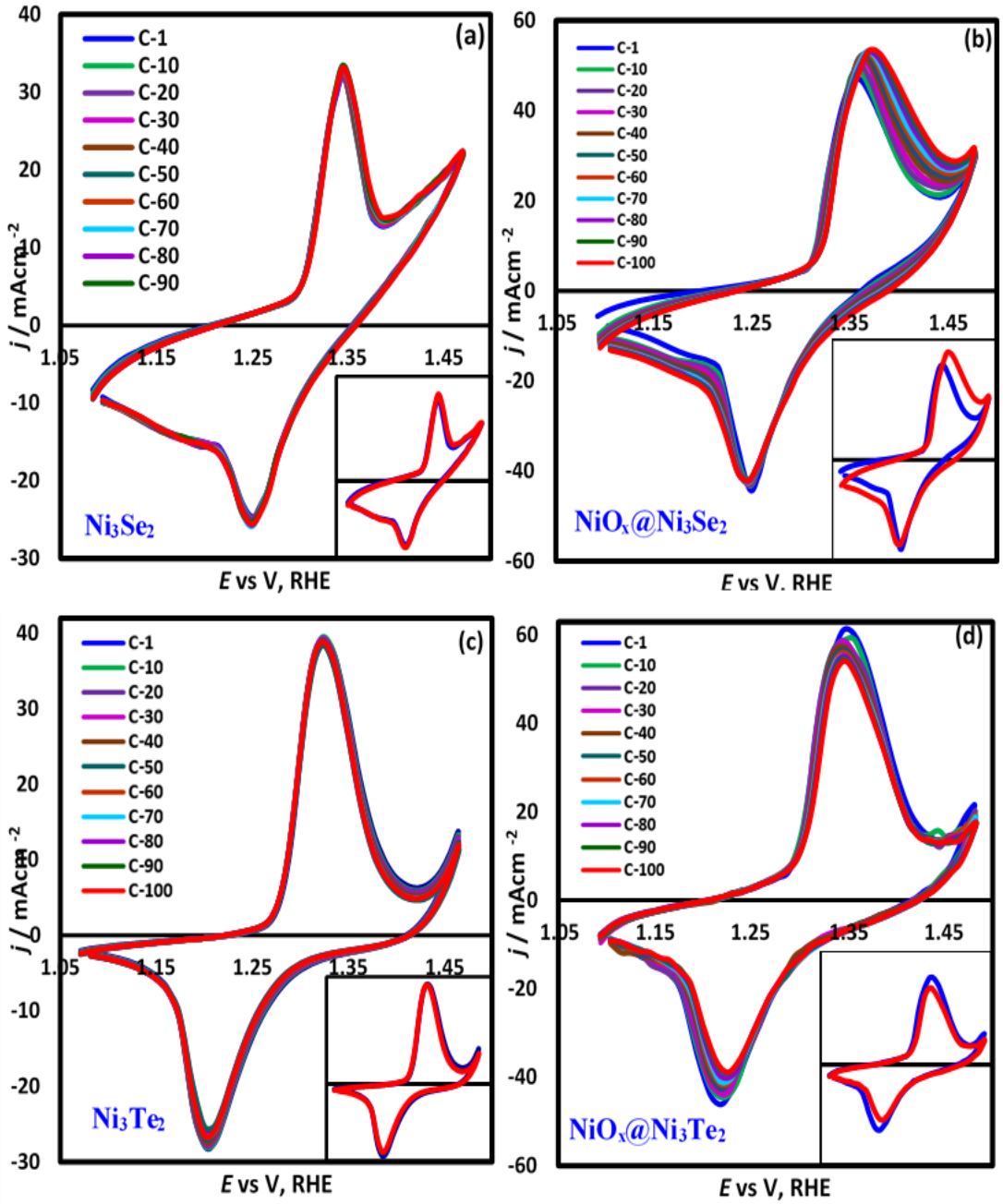

Figure 8. The comparison of CVs. Measured for (a) Ni_3Se_2 (b) $NiO_x@Ni_3Se_2$ (c) Ni_3Te_2 and (d) $NiO_x@Ni_3Te_2$ catalysts for 100 cycles showing the Ni^{2+} / Ni^{3+} oxidation peak. Insets show the comparison between 1st and 100th cycle.

cycling plots show that for pristine Ni_3Se_2 and Ni_3Te_2 films (Figure 8(a)and (d), respectively), the oxidation peak potential does not shift at all during cycling and cycle 1 and cycle 100 are exactly superimposable on each other. This confirms that the Ni_3Se_2 and Ni_3Te_2 surfaces retain their compositional integrity during prolonged OER and are not coated with nickel oxide/hydroxide coating. The CV plots for $NiO_x@Ni_3Se_2$ surface on the other hand, showed a gradual shift of the Ni^{2+} oxidation peak to higher potential with cycling corresponding to the NiO_x overlayer getting thicker. Interestingly, for the $NiO_x@Ni_3Te_2$ film, the oxidation peak potential still did not show a significant shift to higher potential, which can be explained by the fact that NiO_x formed segregated islands on the Ni_3Te_2 layer therefore the catalyst surface exposed both Ni_3Te_2 and NiO_x phases, and while the NiO_x grains got thicker with cycling, Ni_3Te_2 regions do not show much change as explained above. It should be noted here that since purpose of this cycling study was to monitor the oxidation peak position of Ni^{2+}/Ni^{3+} couple, it was performed till 1.47 V. However, to investigate the catalyst surface evolution at higher anodic potential, full scale LSVs were also compared before and after prolonged periods of OER where the potential was scanned to higher anodic region (upto 1.6 V). Such comparisons have been shown as insets (lower right) in Figure 8, which shows that the LSVs of chalcogenide films are superimposable on each other while the oxide coated films show slight shift towards more anodic potential with prolonged exposure to higher anodic potential. These LSV and cycling studies also confirms robustness and enhanced stability of nickel telluride for OER activity in alkaline medium. The 100 CV cycles and the comparison of 1^{st} and 100^{th} cycle for NiO_x films is shown in Figure S8.

Figure S9 shows the chronoamperometry plots of all five samples where current was measured at a constant potential [1.51 V (Ni_3Se_2); 1.52 V (NiO_x@Ni_3Se_2); 1.46 V (Ni3Te2); NiO_x@Ni_3Te_2 (1.50 V) and 1.55 V (NiO_x)] for 10 h and the CVs represent a comparison of electrochemical behavior before and after chronoamperometry tests. All three pristine samples were stable for extended period of time and their CVs before and after prolonged OER activity did not show a significant difference. NiO_x@Ni_3Se_2 and NiO_x@Ni_3Te_2 also showed stable catalytic performance, however, Ni^{2+} oxidation peak shifted towards anodic potential after extended period of catalytic activity indicating thicker NiO_x on the catalyst surface. The chronoamperometry test also confirmed that pristine chalcogenide surfaces retained their compositional integrity during extended OER activity in alkaline medium and did not undergo total surface oxidation.

The composition of the catalyst surface after prolonged OER activity was also confirmed through XPS as shown in Figure 9. The Ni XPS spectra shown in Figure 9(a) shows that the Ni 2p peak in pristine chalcogenide films (Ni_3Se_2 and Ni_3Te_2) did not change position after prolonged chronoamperometry (Figure 9(a), 9(c), and Figure S10, which shows the comparison of the Ni 2p peak before and after chronoamperometry). This suggests that the surface composition did not change significantly for each of these catalytic surfaces during prolonged exposure in alkaline medium during the chronoamperometric measurement, and the Ni_3Se_2 and Ni_3Te_2 surfaces retained predominantly selenide and telluride coordinations. If the NiO_x would have formed on the selenide and telluride surfaces during prolonged OER activity in alkaline medium, the Ni 2p peak would have shown a shift towards peaks position observed in NiO_x@Ni_3Se_2 (or NiO_x@Ni_3Te_2) films. It should be noted here that the Se and Te XPS signals also

confirm retention of surface composition as has been illustrated in the inset of Figure 9(a) and 9(c).

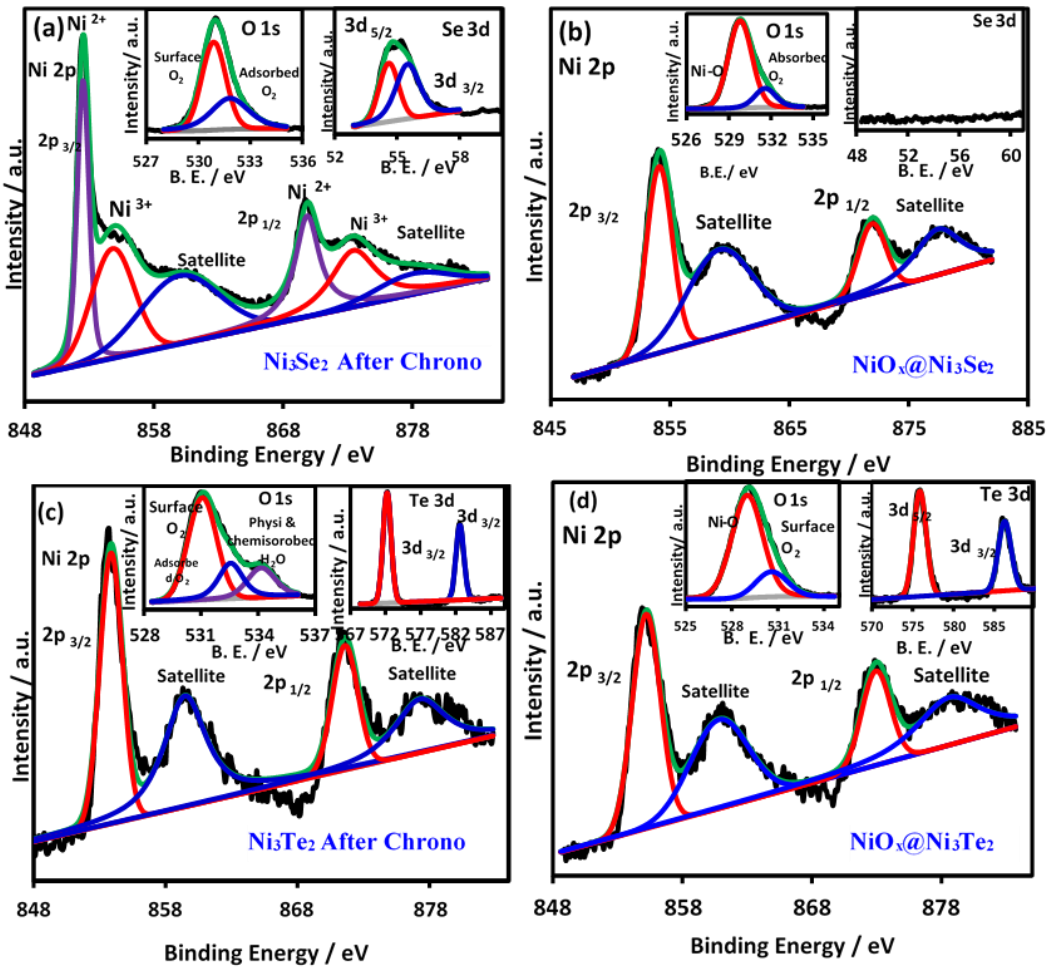

Figure 9. XPS spectra of the catalysts after chronoamperometry. (a) showing Ni 2p peaks of Ni_3Se_2, (b) $NiO_x@Ni_3Se_2$ before chronoamperometry, (c) Ni_3Te_2 after chronoamperometry and (d) $NiO_x@Ni_3Te_2$ before chronoamperometry. Inset of (a) and (b) shows the O 1s and Se 3d peaks; and (c) and (d) shows O 1s and Te 3d peaks.

Ni XPS peaks from the $NiO_x@Ni_3Se_2$ and $NiO_x@Ni_3Te_2$ surfaces on the other hand, shows shift of the Ni 2p peak towards higher binding energy corresponding to the Ni-O bonding. This can be explained by the increasing thickness of the already existing

NiO_x layer in this oxide@chalcogenide films during chronoamperometric studies. Se and Te XPS signals collected from these oxide@chalcogenides films also confirm the compositional changes on the surface, whereby, the Se XPS peaks remains diminished (inset of Figure 9(b)) indicating absence of Se on the surface, while the Te signal remains unchanged after chronoamperometry suggesting that the Ni_3Te_2 regions on the surface remain unchanged after chronoamperometry while the NiO_x regions increase in thickness. It must be noted here that as mentioned above the NiO_x coating is more uniform, continuous, and conformal on the Ni_3Se_2 surface while on Ni_3Te_2 it forms segregated islands as has been depicted in scheme shown as inset in Figure 4h. The O 1s spectra shown as insets in Figures 9(a) – (d) also confirm the compositional changes in the pristine chalcogenide and oxide@chalcogenide films as mentioned above, in which pristine catalysts shows surface adsorbed oxygen at 531.1 eV for both before and after chronoamperometry test while oxide coated chalcogenides show oxygen at 529.9 eV which corresponds to chemically bonded Ni-O in addition to the surface oxygen. Thus, the XPS spectra confirmed that pristine selenide and telluride surfaces retained their compositional integrity and did not grow an oxide overlayer during OER in alkaline medium, validating the mixed anionic surface model as has been explained below.

We have compiled the detailed electrochemical measurements and cycling studies along with the surface analytical characterizations to correctly understand evolution of the active interface.

The OER mechanism in alkaline medium is initiated by the attachment of a hydroxyl group (-OH) on the catalytically active metal site (Ni in this case), and common belief is that with such hydroxyl attachment, these chalcogenide surfaces gets coated with

nickel oxide overlayer. In this article we have proposed a different composition of the active surface based on the detailed electrochemical cycling studies and surface analytical characterization as mentioned above. Figure 10 illustrates these surface models: Figure 10(a) and (c) shows oxide@selenide and oxide@telluride surface, analogous to $NiO_x@Ni_3Se_2$ and $NiO_x@Ni_3Te_2$, respectively, and consistent with common belief of an oxide-coated chalcogenide surface (*Surf-Ox model*), while Figure 10(b) and (d) shows OH^-ions attached directly to the Ni atoms on the surface of pristine nickel selenide and nickel telluride catalysts producing a mixed anionic (hydroxo)selenide or (hydroxo)telluride surface generically referred to as (hydroxo)chalcogenide, (*Surf(OH)E* model). The *Surf(OH)E* model is analogous to the (oxy)hydroxide surfaces that has been observed for nickel oxide based electrocatalysts. As discussed above, electrochemical observations including cycling studies which shows no change of the Ni^{2+}oxidation potential, provide evidence that when OER occurs, it follows the *Surf(OH)E* model for the pristine catalysts. The *Surf-Ox* model which resembles the synthetically created NiO_x $@Ni_3Se_2$ films would have resulted in shift of the Ni^{2+} oxidation peak as has been illustrated in Figures 6 and 7.

The active surface composition and evolution of the interface has been further investigated through soft X-ray absorption spectroscopy (sXAS), which has been widely used to detect oxidation states of transition metals. It is more sensitive to 3*d*-transition metal electronic and chemical states that hard soft X-ray absorption spectroscopy (hXAS) due to strong 2*p*-3*d* dipole-allowed excitation features.[62,63] Ni *L*-edge sXAS spectra of pristine Ni_3Te_2 has been shown in Figure 11(a). Ni *L*-edge spectral features includes two

resonant absorption maxima at *L*3 (~853 eV) and *L*2 (~870 eV) corresponding to 2p3/2 → 3d transition and 2p1/2 → 3d transitions of Ni.[63]

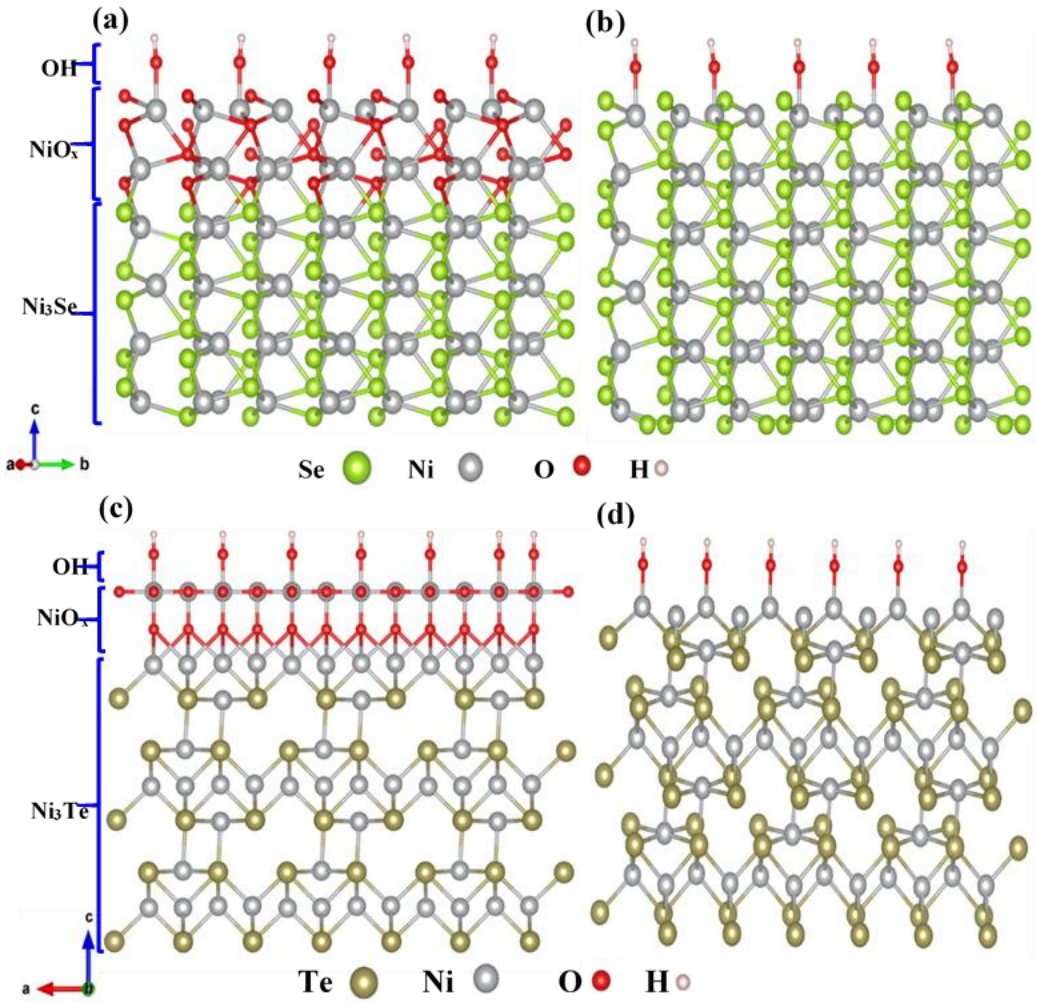

Figure 10. Catalysts models. (a) NiO_x@Ni_3Se_2 surface representing the *Surf*-Ox model. (b) Partially hydroxylated Ni_3Se_2 surface representing *Surf*(OH)Se model. (c) NiO_x@Ni_3Te_2 surface representing the *Surf*-Ox model. (d) partially hydroxylated Ni_3Te_2 surface representing the *Surf*(OH)Te model.

In general, analogous to *K*-edge XAS, *L*3 and *L*2 peak positions moves to the high energy direction when the formal oxidation state of the element increases. Correspondingly, the

features at ~855 eV and ~872 eV indicates the co-existence of Ni^{2+} and Ni^{3+} in the compound.[64] The prominent intensity of this peak means there is some amount of Ni^{3+} present in the catalyst. This observation agrees with the experimentally observed early onset of OER activity of Ni_3Te_2 catalysts since it is well known for Ni based chalcogenide catalysts that OER process starts after the electrochemical oxidation of Ni^{2+} to Ni^{3+} and the presence of Ni in the form of Ni^{3+} in the catalyst can promote OER activity at lower potential.

To observe possible nickel oxide formation on surface of the catalyst aged in alkaline electrolyte, O *K*-edge sXAS spectra was also collected after OER catalytic activity and compared with the sXAS spectra obtained from as-deposited film before catalytic activity as shown in Figure 11(b). O *K*-edge spectrum, which originates from oxygen 1s-2p dipole transition, can be utilized to study the local bonding and symmetry properties of the X-ray excited oxygen.[65] In a typical O *K*-edge spectra of nickel based OER catalysts where oxide or oxyhydroxide formation was observed, there are two main regions in the spectra i.e. the pre-edge region from 527 to 536 eV region that originates from the hybridization of O-2*p* orbitals with Ni-3*d* orbitals, and the broad region above eV that represents Ni-(4*s*/4*p*)-O(2*p*) hybridizations.[64,66,67,68] Hence pre-edge features of the spectrum is associated with the ligand to metal charge transfer excitations, while the spectrum is sensitive to the oxidation state of the cation (3*d* state).[69] In a typical O K-edge XAS of NiO_x, the main low energy feature is observed at 532 eV corresponding to Ni^{2+} ($3d^8$).[64,67]

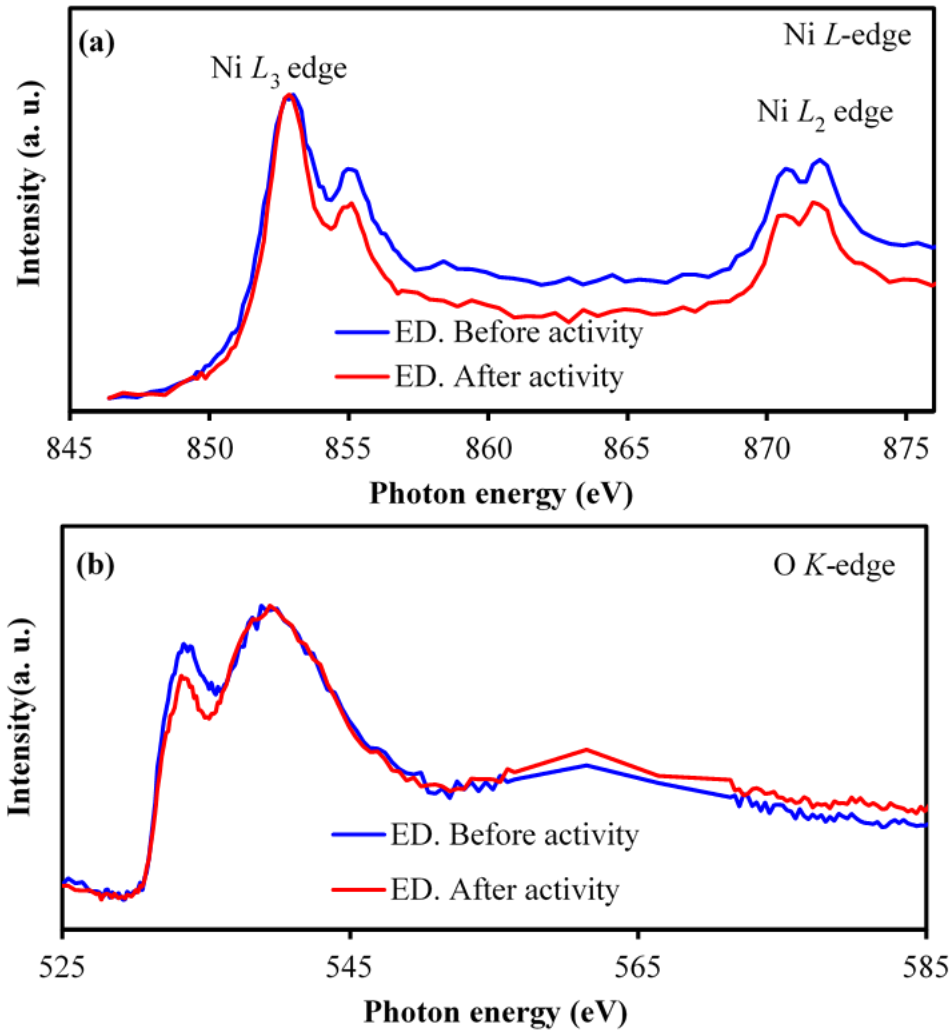

Figure 11. Comparison of sXAS of electrodeposited Ni_3Te_2. (a) Ni *L*-edge and (b) O *K*-edge before and after OER activity.

In the present study, if there was a formation of nickel oxide on Ni_3Te_2 catalyst, a prominent peak should have been observed at ~532 eV in O-*K* sXAS after the catalytic activity. Additionally, for β-NiOOH it has also been reported that a single peak at 528.7 eV, is observed due to formation of NiO_6 octahedral domains initiated from low spin d^7 states (Ni^{3+}) with *eg* orbital symmetry.[67] According to previous reports, after formation of NiO_6 octahedra, it has not been reduced back easily to Ni^{2+} states.[67] However, these

features were not detected in XAS even after prolonged catalytic activity in spite of having Ni^{3+} in the catalyst as suggested from Ni L-edge spectra. In some reports of O-*K* sXAS in Ni-oxides, a prominent peak observed at 530.5 eV has been attributed to the presence of oxygen in the form of O^- as a result of strong localization of holes near the oxygen as a result of formation of Ni^{3+} due to cation vacancies in the material,[64] although, other researchers have shown that oxidized oxygen can only be reliably probed by O-*K* mRIXS.[68] However, the prominent peaks at 533.5 eV observed in present sXAS spectrum does not correspondent with the presence of O^- either. The O-*K* edge XAS studies of Ni_3Te_2 has not been reported yet as per our knowledge, hence, we could not compare the current O-*K* sXAS studies of Ni_3Te_2 catalyst with previous data. It should also be noted that Te 1*s* to 4*p* transition shows a sXAS peak at ~533 eV (*K*-edge). Hence, authors assume that the observed peak at 533.5 eV corresponds to Te *K*-edge in both the samples as shown in Figure 11(b). Interestingly, the O-*K* sXAS peak positions did not change after prolonged OER indicating that there was no change of local coordination around the active site. Therefore, from this O-*K* sXAS study, it was confirmed that a nickel oxide overlayer did not form on the surface of the Ni_3Te_2 catalyst even after prolonged OER activity. Additionally, based on the observation that oxide overlayer grows as segregated islands instead of conformal coating on Ni_3Te_2 surface during anodic electrodeposition, it can be inferred that Ni_3Te_2 has inherent inhibition towards surface oxidation.

The propensity for formation of the mixed anionic (hydroxo)chalcogenide surface can also be investigated from the hydroxyl ion (-OH) adsorption energy, (*E*ads)OH, on the catalytically active Ni site on chalcogenide surface. Typically, a more favorable -OH

adsorption on the chalcogenide surface leading to higher adsorption energy can be correlated with energetically favorable formation of the (hydroxy)chalcogenide surface. In our previous studies we have also observed that higher (*Eads*)OH leads to lower OER onset potential and overpotential at 10 $mA.cm^{-2}$, thereby, could be correlated to improved catalytic activity.

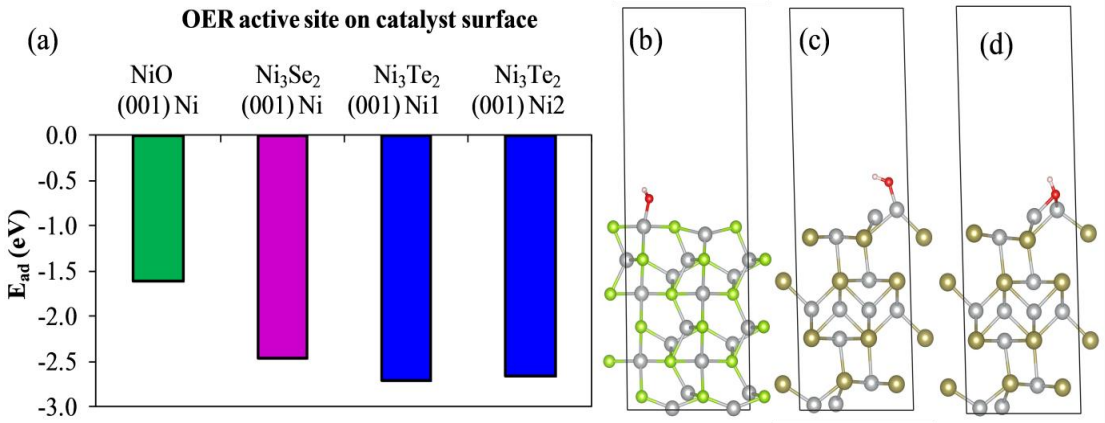

Figure 12. Comparison of OH^- adsorption energy on catalytically active Ni sites. (a) on (001) terminated surfaces of Ni_3Se_2, Ni_3Te_2-Ni1 and Ni_3Te_2-Ni2. (b), (c) and (d) show the corresponding slab model with (001) as the terminating plane.

Hence, we have calculated the -OH adsorption energy for NiO_x, Ni_3Se_2 and Ni_3Te_2 surfaces using DFT as described in supporting information. Specifically, a (001) terminated surface was created for each of this system and the -OH ion was adsorbed on the Ni site. Comparison of the (*Eads*)OH showed that Ni_3Te_2 had the most favorable -OH adsorption energy followed by Ni_3Se_2, while NiO_x showed the smallest adsorption energy, as shown in Figure 12 and Table S3. As has been explained previously, the -OH adsorption can be viewed as catalyst activation and initiates OER process on the surface. A more favorable –OH adsorption leads to better coverage of the catalytic sites leading to

enhanced catalytic activity. Hence, it can be observed here that formation of the mixed anionic (hydroxo)chalcogenide surface is energetically more favorable for nickel telluride. The enhancement in observed OER catalytic activity for the chalcogenide surfaces can thus be correlated with the preferential formation of such mixed anionic (hydroxo)chalcogenide surfaces through facile -OH adsorption.

4. CONCLUSION

The interface evolution of the transition metal chalcogenide electrocatalytic surfaces have been deciphered by creating hypothetical surface models, viz. an oxide@chalcogenide surface (*Surf-Ox*) and partially hydroxylated mixed anionic (*Surf(OH)E*) surface. Surface analogous to the *Surf-Ox* model was synthesized by anodic electrodeposition of a nickel oxide layer on nickel selenide and telluride films (NiO_x@Ni_3Se_2 and NiO_x@Ni_3Te_2, respectively). Comparison of the electrocatalytic activity of aged and pristine Ni_2Se_3 and Ni_2Te_3 films with the NiO_x@Ni_3Se_2 and NiO_x@Ni_3Te_2 films revealed that *Surf-Ox* model does not accurately explain the observed electrocatalytic activity. On the other hand, *Surf(OH)E* model for the active interface was confirmed through extensive surface analytical techniques such as XPS, sXAS etc., as well as through electrochemical measurements. Hence it was confirmed that the transition metal chalcogenide surfaces, specifically, nickel selenide and nickel telluride are indeed stable electrocatalysts for OER in alkaline medium where the active interface can be described as a partially hydroxylated mixed anionic surface formed *in situ*.

CONFLICTS OF INTEREST

There are no conflicts to declare.

ACKNOWLEDGEMENT

This work was supported by National Science Foundation (DMR 1710313) and the American Chemical Society Petroleum Research Fund (54793-ND10). DFT calculations were perfomed at the Molecular Foundry supported through standard user proposal (4804 and 6640). Authors would like to acknowledge MRC for equipment usage.

SUPPLEMENTARY INFORMATION

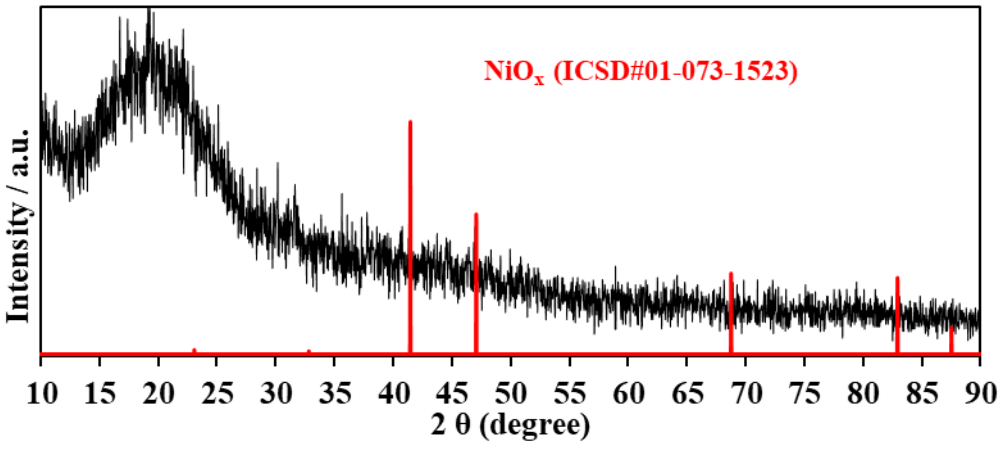

Figure S1. Powder X-ray diffraction of NiO_x

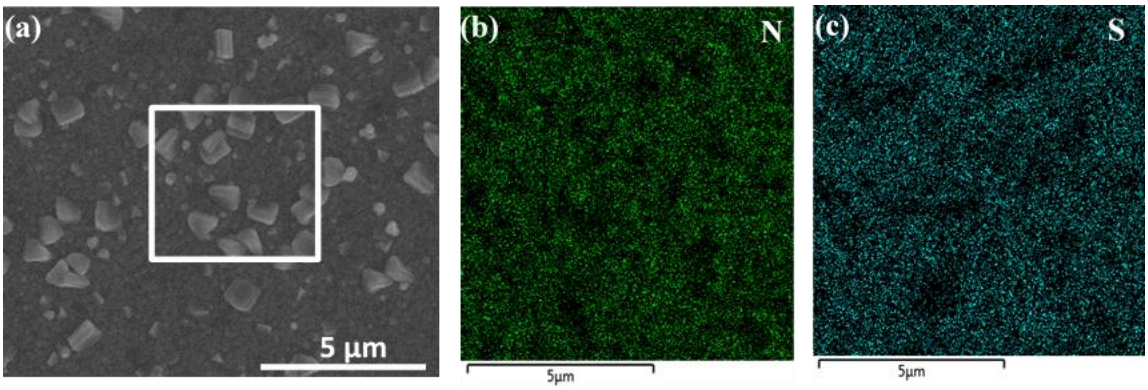

Figure S2. (a) Scanning electron microscope image of Ni_3Se_2 catalyst; Elemental mapping of selected area in SEM image for (b) Ni and (c) Se.

Table S1. Comparison of oxide coated catalysts and pristine catalysts XRD peaks.

Peaks	**θ/ °**	**FWHM/ °**	**D/ nm**
	Ni_3Se_2		
110	29.775	0.60	14.31
201	42.705	0.48	18.57
	$NiO_x@Ni_3Se_2$		
110	29.805	0.45	19.09
201	42.795	0.27	33.03
	Ni_3Te_2		
212	45.375	0.39	23.08
	$NiO_x@Ni_3Te_2$		
212	45.705	0.28	32.77

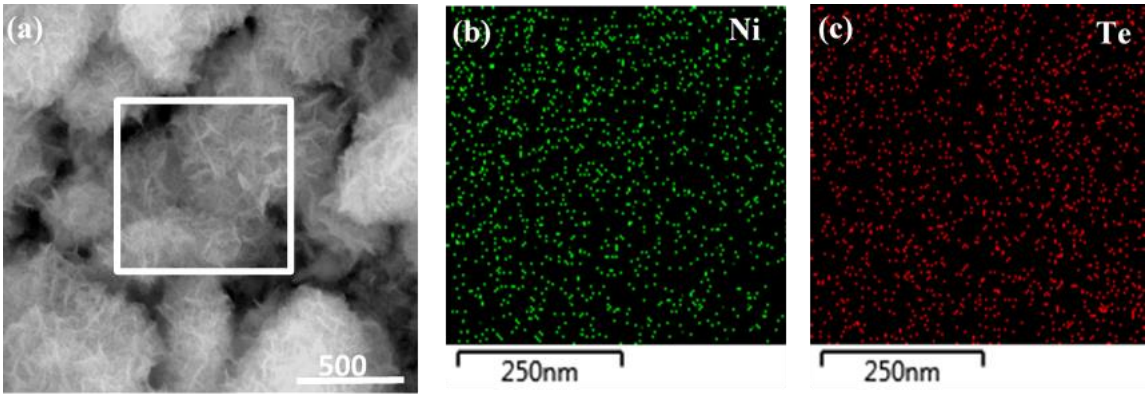

Figure S3. (a) Scanning electron microscope image of Ni_3Te_2 catalyst; Elemental mapping of selected area in SEM image for (b) Ni and (c) Te.

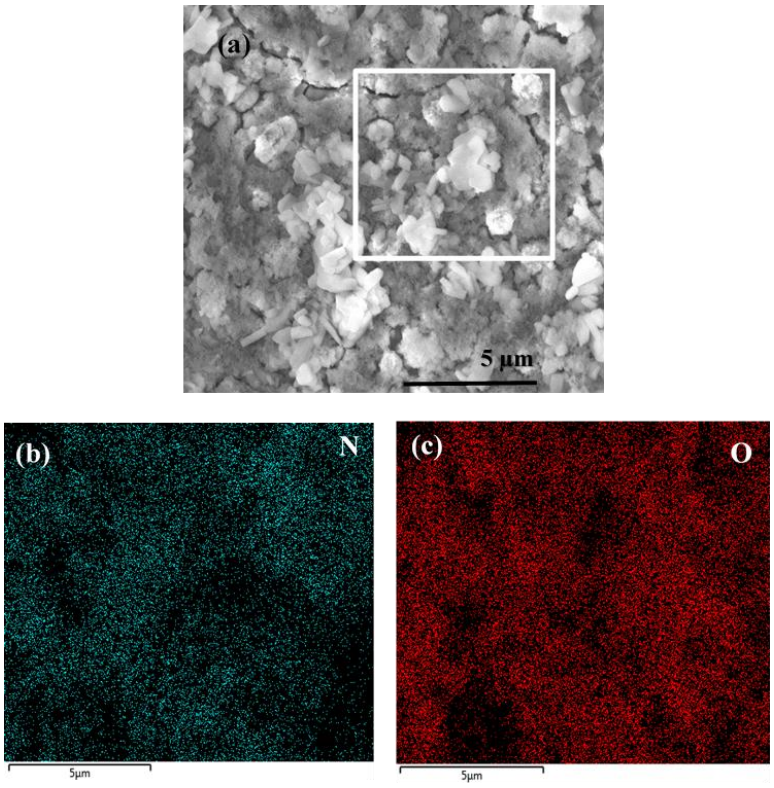

Figure S4. (a) Scanning electron microscope image of NiO catalyst; Elemental mapping of selected area in SEM image for (b) Au ; (c)Ni and (d) O.

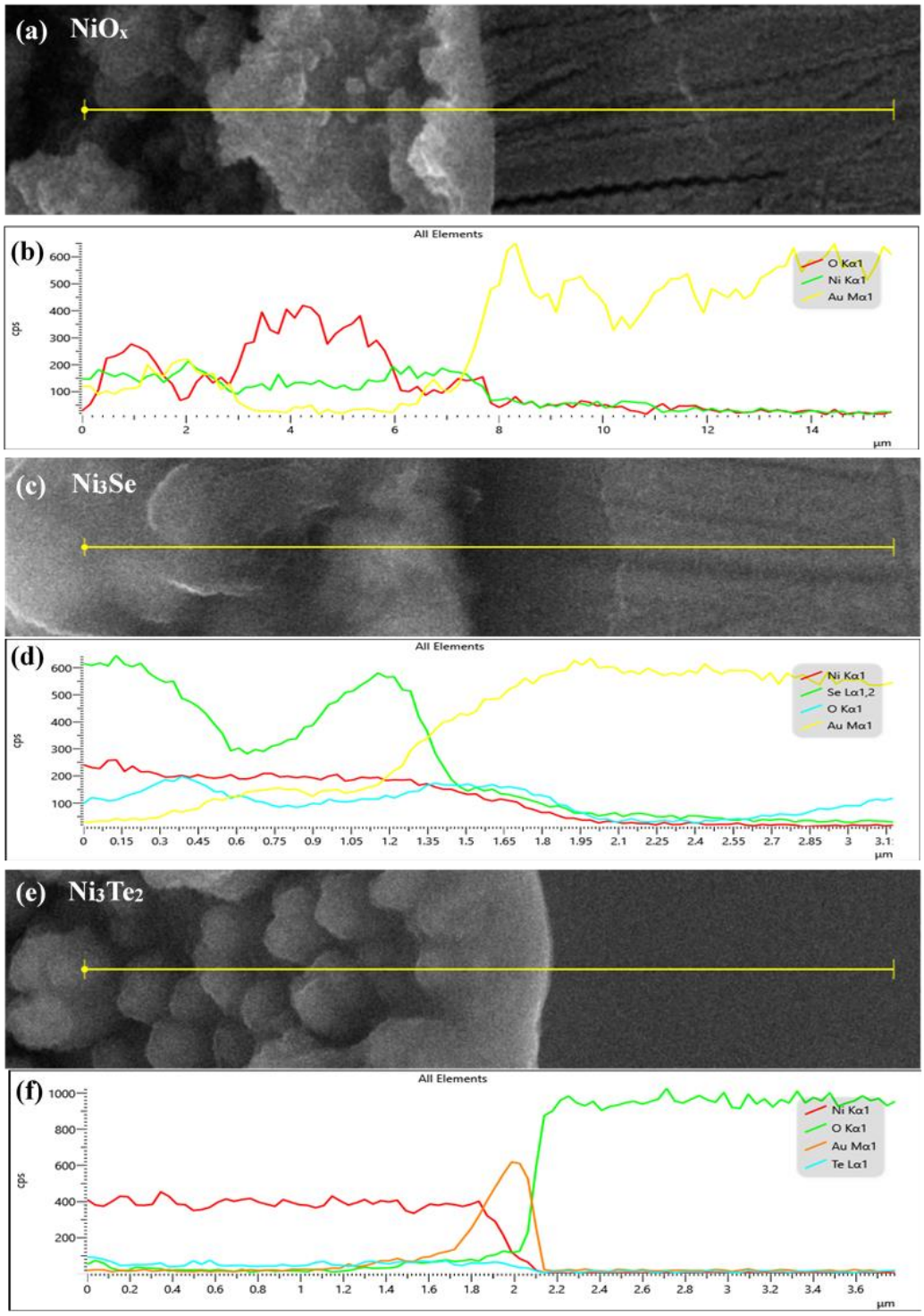

Figure S5. Thickness of the electrodeposited films of (a) NiO_x , (c)Ni_3Se_2 and (e)Ni_3Te_2; (n) Elemental line scan of edge of the electrodeposited films of (b) NiO_x , (d)Ni_3Se_2 and (f)Ni_3Te_2 respectively.

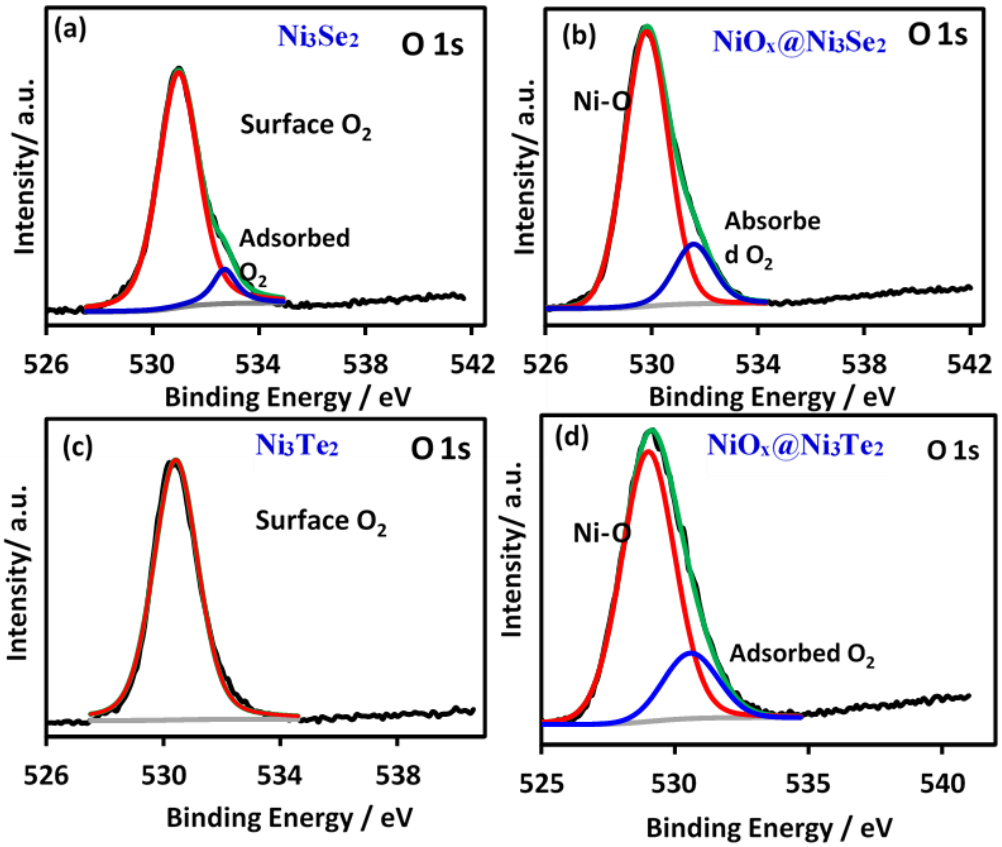

Figure S6. XPS spectra of O 1s peak of (a) Ni_3Se_2, (b) NiO_x@Ni_3Se_2, (c) Ni_3Te_2, (d) NiO_x@Ni_3Te_2.

Table S2. Catalysts loadings of the pristine catalysts.

Catalysts	**Total loading (mg)**	**Loading Area (mg/cm^2)**
Ni_3Se_2	0.64	0.81
Ni_3Te_2	0.29	0.41
NiO_x	0.037	0.46

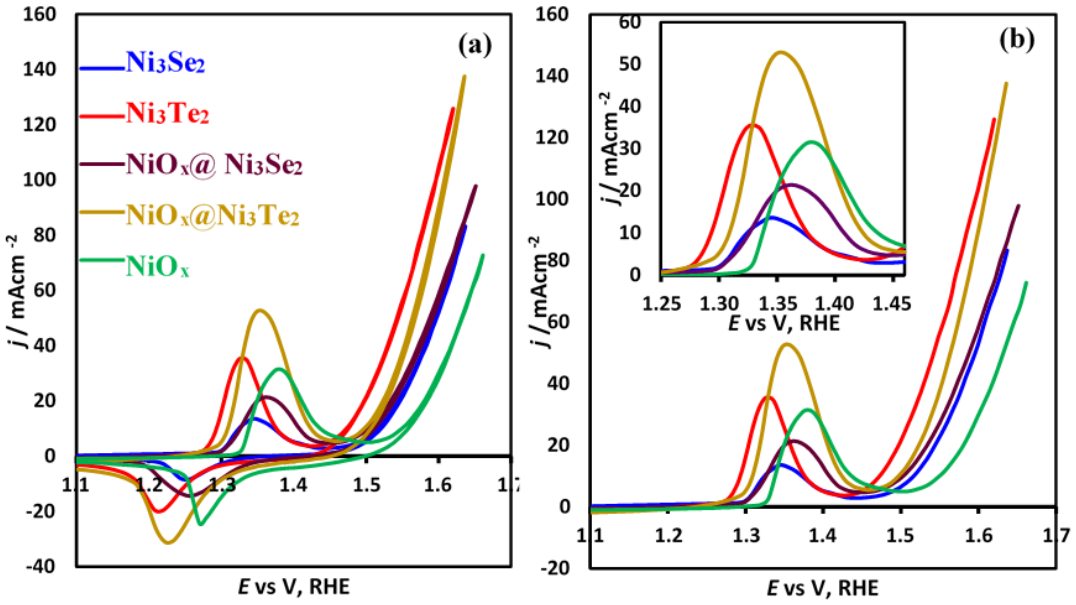

Figure S7. (a) CV (b) LSVs measured for Ni_3Se_2 , Ni_3Te_2, NiO_x@Ni_3Se_2, NiO_x@Ni_3Te_2 and NiO_x catalyst films in N_2 saturated 1 M KOH at a scan rate of 10 mV s^{-1}. Inset in (b) shows the comparison of oxidation peak positions of all catalysts (color scheme for the different catalyst is shown in (a).

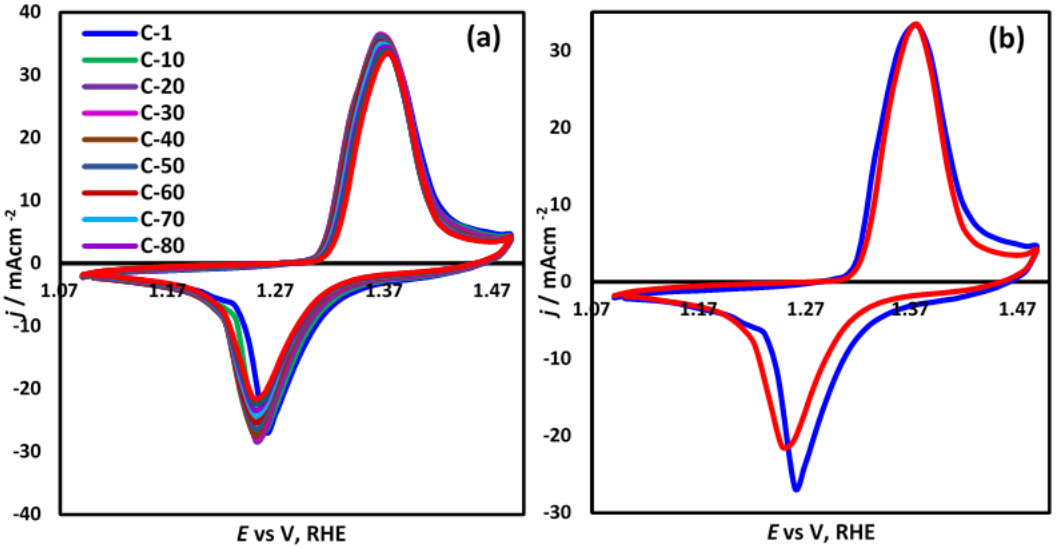

Figure S8. The comparison of Ni^{2+} / Ni^{3+} oxidation peak positions for pristine NiO catalyst @Au-glass (a) CVs measured for 100 cycles; plotted every 10^{th} cycle for clarity (b) Comparison of 1^{st} and 100^{th} CV cycles.

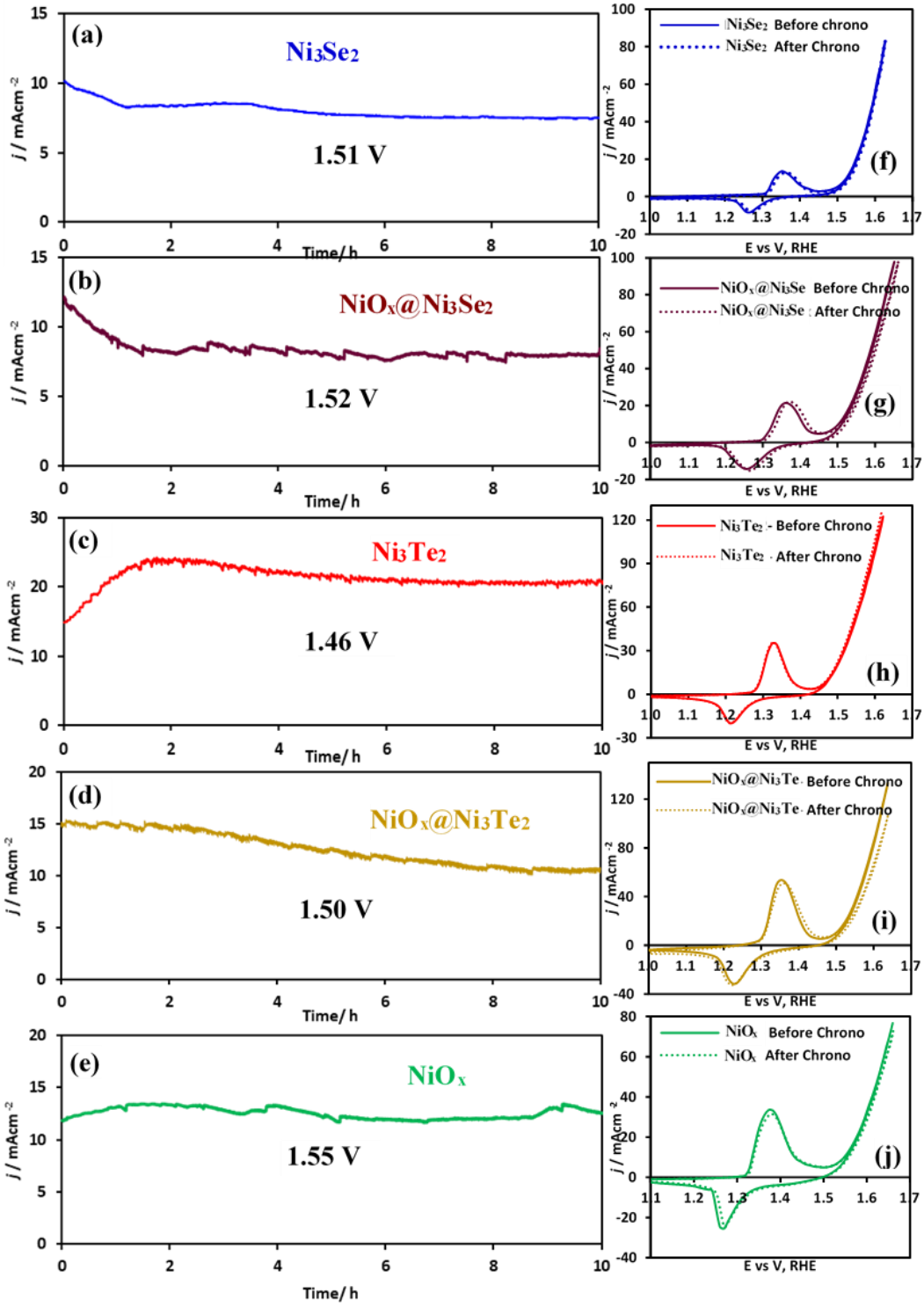

Figure S9. Chronoamperometry of (a) Ni_3Se_2, (b) $NiO_x@Ni_3Se_2$, (c) Ni_3Te_2, (d) $NiO_x@Ni_3Te_2$ and (e)NiO_x ; Comparison of LSVs before and after chronoamperometry (f) Ni_3Se_2 , (g) $NiO_x@Ni_3Se_2$, (h) Ni_3Te_2, (i) $NiO_x@Ni_3Te_2$ and (j) NiO_x .

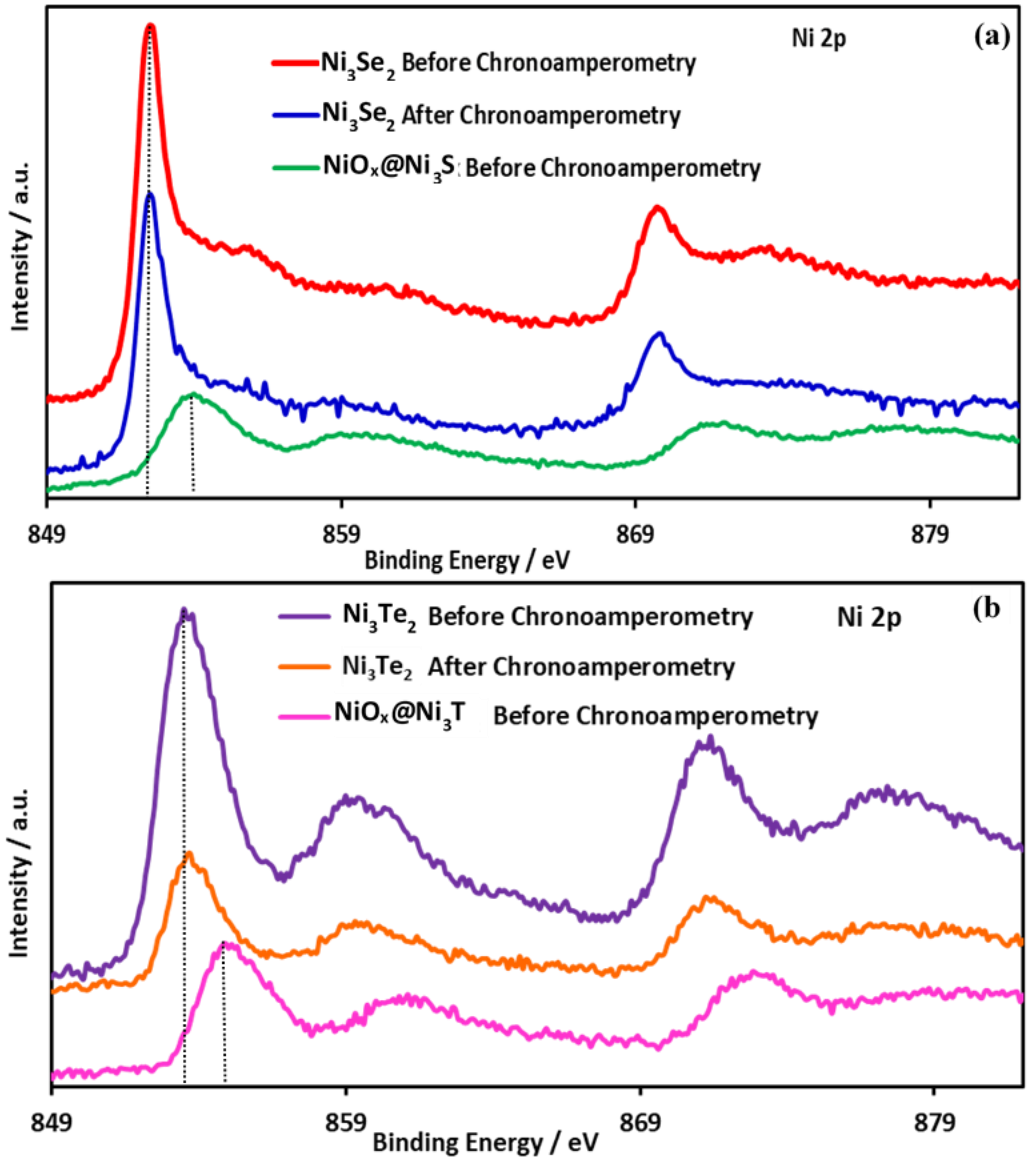

Figure S10. Comparison of Ni 2p peaks (a) Ni_3Se_2 before and after chronoamperometry, and $NiO_x@Ni_3Se_2$ before chronoamperometry; (b) Ni_3Te_2 before and after chronoamperometry, and $NiO_x@Ni_3Te_2$ before chronoamperometry.

1. COMPARISON OF OH^- ADSORPTION ENERGY ON NICKEL SITES ON CATALYST SURFACES: DENSITY FUNCTIONAL THEORY (DFT) CALCULATION

We have employed DFT to calculate the adsorption energy of OH^- ions on active Ni sites on (001) surface of Ni_3Se_2 catalyst and compared the results with OH^- adsorption on active Ni sites on Ni_3Te_2 and NiO (001) surfaces by following a similar process reported earlier[1]. The results have been tabulated in Table S3. Projected augmented wave method (PAW) implemented in Vienna Ab initio Simulation Package (VASP)[2,3] was used and Perdew–Burke–Ernzerhof (PBE) was chosen as the exchange and correlation function within generalized gradient approximation (GGA)[4]. A Monkhorst–Pack mesh of 7x7x1 was used to sample the brillouin zone with plane wave cut-off energy of 400 eV. Free surface of Ni_3Se_2 was simulated using a slab model with 1×1×2 super cell and a relatively large vaccum gap of 20 Å was added to the upper layer under periodic boundary condition to separate layers. The slab was allowed to relax under quasi-newtonial convergence criterion to obtain the energy of the clean slab, E_{clean}. Then OH^- was placed at a distance of 1.8 Å on top of active Ni sites and allowed to fully relax to obtain the total energy of the system, E_{system}. The OH^- adsorption energy, E_{ad}, was calculated as: $E_{ad} = E_{system} - E_{clean} - E_{OH^-}$ where, E_{OH^-} is the energy of free OH^- ion. Ni_3Te_2 (001) surface contain 2 different active Ni sites owing to difference in tetrahedral coordination and denoted as Ni1, Ni2[1].

Table S3. Summary of adsorption energy (E_{ad}), bond lengths of O-H and Ni-O (d_{O-H} and d_{O-H}) for OH^- ions adsorbed on active Ni sites on (001) surfaces of different catalysts.

Active site	**E_{ad} (eV)**	**d_{O-H} (Å)**	**d_{Ni-O} (Å)**	**Reference**
NiO (001) Ni	-1.608	0.964	1.808	1
Ni_3Se_2 (001) Ni	-2.468	0.981	1.814	This work
Ni_3Te_2 (001) Ni1	-2.703	0.964	1.748	1
Ni_3Te_2 (001) Ni2	-2.664	0.965	1.767	1

SUPPLEMENTARY INFORMATION REFERENCES

1. De Silva, U., Masud, J., Zhang, N., Hong, Y., Liyanage, W. P., Zaeem, M. A., & Nath, M. (2018). Journal of Materials Chemistry A, *6*(17), 7608-7622.

2. G. Kresse and J.Furthmüller, Phys. Rev. B.,1996, 54, 11169

3. G. Kresse and D. Joubert, Phys. Rev. B.,1999, 59, 1758.

4. J.P. Perdew, J.A. Chevary, S.H.Vosko, K.A. Jackson, M.R. Pederson, D.J. Singh and C. Fiolhais, Phys. Rev. B., 1992, 46, 6671.

REFERENCES

1. Walter, M.G.; Warren, E.L.; McKone, J.R.; Boettcher, S.W.; Mi, Q.; Santori, E.A.; Lewis, N.S. Solar water splitting cells. *Chem. Rev.* **2010,** *110*, 6446-6473.

2. Sharma, S.; Ghoshal, S.K. Hydrogen the future transportation fuel: From production to applications. *Renew. Sust. Energ. Rev.* **2015,** *43*, 1151-1158.

3. Hosseini, S.E.; Wahid, M.A. Hydrogen production from renewable and sustainable energy resources: promising green energy carrier for clean development. *Renew. Sust. Energ. Rev.* **2016,** *57*, pp.850-866.

4. Anantharaj, S.; Ede, S.R.; Sakthikumar, K. ; Karthick, K. ; Mishra, S. ; Kundu, S. Recent trends and perspectives in electrochemical water splitting with an emphasis on sulfide, selenide, and phosphide catalysts of Fe, Co, and Ni: a review. *ACS Catal.* **2016,** *6*, 8069-8097.

5. Yan, Y.; Xia, B.Y.; Zhao, B.; Wang, X.; A review on noble-metal-free bifunctional heterogeneous catalysts for overall electrochemical water splitting. *J. Mater. Chem. A*, **2016,** *4*, 17587-17603.

6. Ahmad, H., Kamarudin, S.K., Minggu, L.J. and Kassim, M., Hydrogen from photo-catalytic water splitting process: A review. *Renew. Sust. Energ. Rev.* **2015,** *43*, 599-610.

7. Masud, J.; Ioannou, P.C.; Levesanos, N.; Kyritsis, P.; Nath, M. A Molecular Ni-complex Containing Tetrahedral Nickel Selenide Core as Highly Efficient Electrocatalyst for Water Oxidation. *Chem Sus Chem*. **2016,** *9*, 3128-3132.

8. De Silva, U.; Masud, J.; Zhang, N.; Hong, Y.; Liyanage, W.P.; Zaeem, M.A.; Nath, M. Nickel telluride as a bifunctional electrocatalyst for efficient water splitting in alkaline medium. *J. Mater. Chem. A.* **2018,** *6*, 7608-7622.

9. Masud, J.; Swesi, A.T.; Liyanage, W.P.; Nath, M. Cobalt selenide nanostructures: an efficient bifunctional catalyst with high current density at low coverage. *ACS Appl. Mater. Inter.* **2016,** 8(27), 17292-17302.

10. Swesi, A.T.; Masud, J.; Nath, M. Nickel selenide as a high-efficiency catalyst for oxygen evolution reaction. *Energ. Environ. Sci.* **2016,** *9*, 1771-1782.

11. Sivanantham, A.; Shanmugam, S.; Nickel selenide supported on nickel foam as an efficient and durable non-precious electrocatalyst for the alkaline water electrolysis. *Appl. Catal. B-Environ.* **2017,** *203*, 485-493.

12. Cao, X.; Medvedeva, J. E.; Nath, M. Copper Cobalt Selenide as a High-Efficiency Bifunctional Electrocatalyst for Overall Water Splitting: Combined Experimental and Theoretical Study, *ACS Appl. Energy Mater.* **2020,** *3*, 3092-3103.

13. Wang, F.; Li, Y.; Shifa, T.A.; Liu, K.; Wang, F.; Wang, Z.; Xu, P.; Wang, Q.; He, J. Selenium-Enriched Nickel Selenide Nanosheets as a Robust Electrocatalyst for Hydrogen Generation. *Angew. Chem. Int. Edit.* **2016,** *55*, 6919-6924.

14. Bhat, K.S.; Barshilia, H.C.; Nagaraja, H.S. Porous nickel telluride nanostructures as bifunctional electrocatalyst towards hydrogen and oxygen evolution reaction. *Int. J. Hydrogen Energ.* **2017,** *42*, 24645-24655.

15. Gao, Q.; Huang, C.Q.; Ju, Y.M.; Gao, M.R.; Liu, J.W.; An, D.; Cui, C.H.; Zheng, Y.R.; Li, W.X.; Yu, S.H. Phase-Selective Syntheses of Cobalt Telluride Nanofleeces for Efficient Oxygen Evolution Catalysts. *Angew. Chem. Int. Edit.* **2017,** *56*, 7769-7773.

16. Patil, S.A.; Kim, E.K.; Shrestha, N.K.; Chang, J.; Lee, J.K.; Han, S.H. Formation of semimetallic cobalt telluride nanotube film via anion exchange tellurization strategy in aqueous solution for electrocatalytic applications. *ACS Appl. Mater. Inter*. **2015,** *7*, 25914-25922.

17. Masud, J.; Liyanage, W.P.; Cao, X.; Saxena, A.; Nath, M. Copper selenides as high-efficiency electrocatalysts for oxygen evolution reaction. *ACS Appl. Energ. Mater.* **2018,** *1*, 4075-4083.

18. Cao, X.; Hong, Y.; Zhang, N.; Chen, Q.; Masud, J.; Zaeem, M.A.; Nath, M. Phase Exploration and Identification of Multinary Transition-Metal Selenides as High-Efficiency Oxygen Evolution Electrocatalysts through Combinatorial Electrodeposition. *ACS Catal.* **2018,** *8*, 8273-8289.

19. De Silva, U.; Liyanage, W.P.R.; Nath, M. Magnetic Multifunctional Nanostructures as High-efficiency Catalysts for Oxygen Evolution Reactions. *MRS Advances*, **2016,** *1*, 2401-2407.

20. Umapathi, S.; Masud, J.; Swesi, A.T.; Nath, M. FeNi2Se4–Reduced Graphene Oxide Nanocomposite: Enhancing Bifunctional Electrocatalytic Activity for Oxygen Evolution and Reduction through Synergistic Effects. *Adv. Sust. Sys.* **2017,** *1*, 1700086.

21. Baugher, B.W.; Churchill, H.O.; Yang, Y.; Jarillo-Herrero, P. Optoelectronic devices based on electrically tunable p–n diodes in a monolayer dichalcogenide. *Nat. Nanotechol.* **2014,** *9*,262-267.

22. Wang, Q.H., Kalantar-Zadeh, K., Kis, A., Coleman, J.N. and Strano, M.S., Electronics and optoelectronics of two-dimensional transition metal dichalcogenides. *Nat.Nanotechnol.* **2012**,*7*, 699-712.

23. Gong, M.; Dai, H. A mini review of NiFe-based materials as highly active oxygen evolution reaction electrocatalysts, *Nano Research.* **2015**, *8*, 23-39.

24. Bode, H.; Dehmelt, K.; Witte, J. Nickel hydroxide electrodes. 2. oxidation products of nickel(II) hydroxides. *Z. Anorg. Allg. Chem.* **1969**, *366*, 1-2.

25. Wang, H. Y.; Hsu, Y. Y.; Chen, R.; Chan, T. S.; Chen, H. M.; Liu, B. Oxygen Evolution Reaction: Ni3+-Induced Formation of Active NiOOH on the Spinel Ni–Co Oxide Surface for Efficient Oxygen Evolution Reaction, *Adv. Energy Mater.* **2015**, *5*, doi: 10.1002/aenm.201570058.

26. López Fernández, E.; Gil-Rostra, J.; Espinos, J.P.; Gonzalez-Elipe, A.R.; de Lucas-Consuegra, A.; Yubero, F. Chemistry and Electrocatalytic Activity of Nanostructured Nickel Electrodes for Water Electrolysis. *ACS Catal*. 2020, *10*, 6159–6170.

27. Jin, Y.; Huang, S.; Yue, X.; Du, H.; Shen, P.K. Mo-and Fe-modified Ni (OH) 2/NiOOH nanosheets as highly active and stable electrocatalysts for oxygen evolution reaction. *ACS Catal.* **2018,** *8*, 2359-2363.

28. Li, X.; Han, G.Q.; Liu, Y.R.; Dong, B.; Hu, W.H.; Shang, X.; Chai, Y.M.; Liu, C.G.; NiSe@ NiOOH core–shell hyacinth-like nanostructures on nickel foam synthesized by in situ electrochemical oxidation as an efficient electrocatalyst for the oxygen evolution reaction. *ACS Appl. Mater. Inter.* **2016,** *8*, 20057-20066.

29. Konkena, B.; Masa, J.; Botz, A.J.; Sinev, I.; Xia, W.; Koßmann, J.; Drautz, R.; Muhler, M.; Schuhmann, W. Metallic NiPS3@ NiOOH core–shell heterostructures as highly efficient and stable electrocatalyst for the oxygen evolution reaction. *ACS Catalysis*, **2017,** *7*, 229-237.

30. Klaus, S.; Cai, Y.; Louie, M.W.; Trotochaud, L.; Bell, A.T. Effects of Fe electrolyte impurities on Ni (OH) 2/NiOOH structure and oxygen evolution activity. *J. Phys. Chem. C*, **2015,** *119*, 7243-7254.

31. Xiao, M.; Tian, Y.; Yan, Y.; Feng, K.; Miao, Y. Electrodeposition of Ni (OH) 2/NiOOH in the presence of urea for the improved oxygen evolution. *Electrochim. Acta*, **2015,** *164*, 196-202.

32. Kim, B.; Oh, A.; Kabiraz, M.K.; Hong, Y.; Joo, J.; Baik, H.; Choi, S.I.; Lee, K. NiOOH exfoliation-free nickel octahedra as highly active and durable electrocatalysts toward the oxygen evolution reaction in an alkaline electrolyte. *ACS Appl. Mater. Interf.* **2018,** *10*, 10115-10122.

33. Jin, Y.; Huang, S.; Yue, X.; Shu, C.; Shen, P.K. Highly stable and efficient non-precious metal electrocatalysts of Mo-doped NiOOH nanosheets for oxygen evolution reaction. *Int. J. Hydrogen Energ.* **2018,** *43*, 12140-12145.

34. Zhao, J.; Ren, X.; Han, Q.; Fan, D.; Sun, X.; Kuang, X.; Wei, Q.; Wu, D. Ultra-thin wrinkled NiOOH–NiCr 2 O 4 nanosheets on Ni foam: an advanced catalytic electrode for oxygen evolution reaction. *Chem. Commun.* **2018,** *54*, 4987-4990.

35. Tkalych, A.J.; Zhuang, H.L.; Carter, E.A. A density functional+ U assessment of oxygen evolution reaction mechanisms on β-NiOOH. *ACS Catal.* **2017,** *7*, 5329-5339.

36. Wygant, B.R.; Kawashima, K.; Mullins, C.B. Catalyst or precatalyst? The effect of oxidation on transition metal carbide, pnictide, and chalcogenide oxygen evolution catalysts. *ACS Energ. Lett*. **2018,** *3*, 2956-2966.

37. Miessler, G.L.; Fischer, P.J.; Tarr, D.A. *Inorganic Chemistry.* ***2014,*** 5rd edition, Prentice Hall.

38. Reier, T.; Nong, H.N.; Teschner, D.; Schlögl, R.; Strasser, P. Electrocatalytic oxygen evolution reaction in acidic environments–reaction mechanisms and catalysts. *Adv. Energ. Mater.* **2017,** *7*, 1601275.

39. Favaro, M.; Yang, J.; Nappini, S.; Magnano, E.; Toma, F.M.; Crumlin, E.J.; Yano, J.; Sharp, I.D. Understanding the oxygen evolution reaction mechanism on CoO x using operando ambient-pressure X-ray photoelectron spectroscopy. *J. Ameri,Chem. Soc.* 2017, *139*, 8960-8970.

40. Ping, Y.; Nielsen, R.J.; Goddard III, W.A. The reaction mechanism with free energy barriers at constant potentials for the oxygen evolution reaction at the IrO2 (110) surface. *J. Ameri. Chem. Soc*. **2017,** *139*, 149-155.

41. Miles, M.H.; Kissel, G.; Lu, P.W.T.; Srinivasan, S. Effect of temperature on electrode kinetic parameters for hydrogen and oxygen evolution reactions on nickel electrodes in alkaline solutions. *J. Electrochem. Soc.* **1976,** *123*, 332.

42. Matsumoto, Y.; Sato, E. Electrocatalytic properties of transition metal oxides for oxygen evolution reaction. *Mater. Chem.Phys.* **1986,** *14*, 397-426.

43. Fabbri, E., Habereder, A., Waltar, K., Kötz, R. and Schmidt, T.J., 2014. Developments and perspectives of oxide-based catalysts for the oxygen evolution reaction. *Catal. Sci.Technol.* **2014,** *4*, 3800-3821.

44. Suen, N.T., Hung, S.F., Quan, Q., Zhang, N., Xu, Y.J. and Chen, H.M., Electrocatalysis for the oxygen evolution reaction: recent development and future perspectives. *Chem. Soc. Rev.***2017,** *46*, 337-365.

45. Grimaud, A.; Diaz-Morales, O.; Han, B.; Hong, W.T.; Lee, Y.L.; Giordano, L.; Stoerzinger, K.A.; Koper, M.T.; Shao-Horn, Y. Activating lattice oxygen redox reactions in metal oxides to catalyse oxygen evolution. *Nat. Chem.* **2017**, *9*, 457.

46. Basharat, F.; Rana, U.A.; Shahid, M.; Serwar, M. Heat treatment of electrodeposited NiO_x films for improved catalytic water oxidation. *RSC Adv.* **2015,** *5*, 86713-86722.

47. Qiao, R.; Li, Q.; Zhuo, Z.; Sallis, S.; Fuchs, O.; Blum, M.; Weinhardt, L.; Heske, C.; Pepper, J.; Jones, M.; Brown, A.; Spucces, A.; Chow, K.; Smith, B.; Glans, P.-A.; Chen, Y.; Yan, S.; Pan, F.; Piper, L. F. J.; Denlinger, J.; Guo, J.; Hussain, Z.; Chuang, Y.-D.; Yang, W., High-efficiency in situ resonant inelastic x-ray scattering (iRIXS) endstation at the Advanced Light Source. *Rev. Sci. Instrum.* **2017,** *88*, 033106.

48. Wu, J.; Sallis, S.; Qiao, R.; Li, Q.; Zhuo, Z.; Dai, K.; Guo, Z.; Yang, W., Elemental-sensitive Detection of the Chemistry in Batteries through Soft X-ray Absorption Spectroscopy and Resonant Inelastic X-ray Scattering. *J. Vis.Exp.* **2018,** *134*, e57415.

49. Rossmeisl, J.; Logadottir, A.; Nørskov, J.K. Electrolysis of water on (oxidized) metal surfaces. *Chem. Phys.* **2005,** *319*, 178-184.

50. Patterson, A.L. The Scherrer formula for X-ray particle size determination. *Phys. Rev.* **1939,** *56*, 978.

51. Zheng, X.; Han, X.; Liu, H.; Chen, J.; Fu, D.; Wang, J.; Zhong, C.; Deng, Y.; Hu, W. Controllable Synthesis of Ni x Se ($0.5 \leq x \leq 1$) Nanocrystals for Efficient Rechargeable Zinc–Air Batteries and Water Splitting. *ACS Appl. Mater. Inter.* **2018,** *10*, 13675-13684.

52. Swesi, A.T.; Masud, J.; Liyanage, W.P.; Umapathi, S.; Bohannan, E.; Medvedeva, J.; Nath, M.Textured NiSe2 film: bifunctional electrocatalyst for full water splitting at remarkably low overpotential with high energy efficiency. *Sci. Rep.* **2017**, *7*, 1-11.

53. Dufresne, P.; Payen, E.; Grimblot, J.; Bonnelle, J.P. Study of nickel-molybdenum-.gamma.-aluminum oxide catalysts by x-ray photoelectron and Raman spectroscopy. Comparison with cobalt-molybdenum-. gamma.-aluminum oxide catalysts. *J. Phys. Chem.* **1981,** *85*, 2344-2351.

54. Mansour, A.N. Characterization of NiO_x by XPS. *Surf. Sci. Spect.* **1994,** *3*, 231-238.

55. Li, X.; Han, G.Q.; Liu, Y.R.; Dong, B.; Hu, W.H.; Shang, X.; Chai, Y.M.; Liu, C.G. 2016. NiSe@ NiO_x OH core–shell hyacinth-like nanostructures on nickel foam synthesized by in situ electrochemical oxidation as an efficient electrocatalyst for the oxygen evolution reaction. *ACS Appl. Mater. Inter*. **2016,** *8*, 20057-20066.

56. Khawaja, E.E.; Salim, M.A.; Khan, M. A.; Al-Adel, F.F.; Khattak, G.D.; Hussain, Z. XPS, auger, electrical and optical studies of vanadium phosphate glasses doped with nickel oxide. *J.Non-Cryst. Solids***. 1989,** *110*, 33-43.

57. Parkinson, C.R.; Walker, M.; McConville, C.F. Reaction of atomic oxygen with a Pt (111) surface: chemical and structural determination using XPS, CAICISS and LEED. *Surf. Sci.* **2003,** *545*, 19-33.

58. Stern, L.A.; Hu, X. Enhanced oxygen evolution activity by NiO_x and Ni(OH)2 nanoparticles. *Faraday Discuss.* **2015,** *176*, 363-379.

59. Trotochaud, L.; Young, S.L.; Ranney, J.K.; Boettcher, S.W. Nickel–iron oxyhydroxide oxygen-evolution electrocatalysts: the role of intentional and incidental iron incorporation. *J.A.C.S.* **2014,** *136*, 6744-6753.

60. Burke, M.S.; Zou, S.; Enman, L.J.; Kellon, J.E.; Gabor, C.A.; Pledger, E.; Boettcher, S.W. Revised oxygen evolution reaction activity trends for first-row transition-metal (oxy) hydroxides in alkaline media. *J. Phys. Chem. Lett.* **2015**, *6*, 3737-3742.

61. Batchellor, A.S.; Boettcher, S.W. Pulse-electrodeposited Ni–Fe (oxy) hydroxide oxygen evolution electrocatalysts with high geometric and intrinsic activities at large mass loadings. *ACS Catal.* **2015**, *5*, 6680-6689.

62. Yang, W.; Liu, X.; Qiao, R.; Olalde-Velasco, P.; Spear, J. D.; Roseguo, L.; Pepper, J. X.; Chuang, Y.-d.; Denlinger, J. D.; Hussain, Z., Key electronic states in lithium battery materials probed by soft X-ray spectroscopy. *J.Electron Spectros.* **2013,** *190*, 64-74.

63. Gu, W.; Wang, H.; Wang, K.. Nickel L-edge and K-edge X-ray absorption spectroscopy of non-innocent Ni [S2 C2 (CF3)2]2 n series (n=− 2,− 1, 0): direct probe of nickel fractional oxidation state changes. *Dalton T*. **2014**, *43*, 6406-6413.

64. Cho, D. Y.; Song, S. J.; Kim, U. K.; Kim, K. M.; Lee, H. K.; Hwang, C. S.; Spectroscopic investigation of the hole states in Ni-deficient NiO films. *J. Mater. Chem. C.* **2013**,*1*, 4334-4338.

65. Drevon, D; Görlin, M.; Chernev, P.; Xi, L.; Dau, H.; Lange, K. M. Uncovering The Role of Oxygen in Ni-Fe (OxHy) Electrocatalysts using In situ Soft X-ray Absorption Spectroscopy during the Oxygen Evolution Reaction. *Sci. Rep*. **2019**, 9.

66. Qiao, R.; Wray, L. A.; Kim, J. H.; Pieczonka, N. P.; Harris, S. J.;Yang, W. Direct experimental probe of the Ni (II)/Ni (III)/Ni (IV) redox evolution in LiNi0. 5Mn1. 5O4 electrodes. *J. Phys. Chem. C.* **2015**, *119*, 27228-27233.

67. Yoshida, M.; Mitsutomi, Y.; Mineo, T.; Nagasaka, M.; Yuzawa, H.; Kosugi, N.; Kondoh, H. Direct observation of active nickel oxide cluster in nickel–borate Electrocatalyst for Water oxidation by In Situ O K-edge X-ray absorption spectroscopy. *J. Phys. Chem. C*. 2015, *119*, 19279-19286.

68. Wu, J.; Li, Q.; Sallis, S.; Zhuo, Z.; Gent, E. W.; Chueh, C. W.; Yan, S.; Chuang, Y.-d.; Yang, W., Fingerprint Oxygen Redox Reactions in Batteries through High-Efficiency Mapping of Resonant Inelastic X-ray Scattering. *Condens. Matter*. **2019,** *4*, 5.

69. Gilbert, B.; Kim, C. S.; Dong, C. L.; Guo, J.; Nico, P. S.; Shuh, D. K.. Oxygen K-Edge Emission and Absorption Spectroscopy of Iron Oxyhydroxide Nanoparticles. *AIP Conf. Proc.* **2007**, *1* 721-725.

IV. MAGNETIC MULTIFUNCTIONAL NANOSTRUCTURES AS HIGH-EFFICIENCY CATALYSTS FOR OXYGEN EVOLUTION REACTIONS

MRS Advances 1, no. 34 (2016): 2401-2407.

Umanga De Silva, W. P. R. Liyanage, Manashi Nath*

Department of Chemistry, Missouri University of Science and Technology, Rolla, MO 65409.

*Email: nathm@mst.edu

ABSTRACT

The search for high-efficiency and environmentally benign water splitting catalysts has been on the rise since this process is a source of renewable, clean energy. However the process is inherently slow, especially for the production of O_2 from H_2O (water oxidation) due to the high electron count and energy intensive bond formation of the reaction. Hence the search for novel catalysts for oxygen evolution reactions (OER) has led researchers to focus on various families of compounds including oxides and recently selenides. Multifunctional nanostructures containing the semiconductor electrocatalyst grafted onto an optically active metallic component might boost the catalytic activity even further due to efficient charge injection. Magnetically active catalysts will also be lucrative since that might induce better adhesion of the oxygenated species at the catalytically active site. In this report we introduce multifunctional, magnetic Au_3Pd–CoSe nanostructures as high-efficiency OER electrocatalysts. These multifunctional nanostructures were synthesized by a chemical vapor deposition (CVD)

reaction with cobalt acetylacetonate and elemental selenium on Au-Pd sputter coated silica substrate at 800°C. The morphology of these multifunctional nanostructures were mostly bifunctional *Janus*-like nanoparticles as seen through scanning and transmission electron microscopy. They also showed soft ferromagnetic behavior. These bifunctional nanoparticles were coated on the anodes of a water oxidation cell and it was observed that these nanoparticles showed a higher OER activity with lower onset potential for O_2 evolution as compared to the conventional oxide-based OER electrocatalysts.

1. INTRODUCTION

Water splitting is a vital topic of interest in present days since it offers a solution for alternative energy generation without depleting fossil fuel. Water splitting can utilize both solar and/or electric energy for a cleaner, recyclable, and cheaper production of hydrogen and oxygen. The water-splitting reaction has two half-reactions: the hydrogen evolution reaction (HER) and oxygen evolution reaction (OER), both of which are fundamental for the overall efficiency of water splitting [1, 2]. Currently OER has been a prime area of research for energy generation from water oxidation, because of the inherently sluggish rate of the reaction. The OER process is inherently slow, due to the high electron count (4e) and energy intensive bond formation.

Typically, catalysts are required to reduce the activation energy barrier for this uphill reaction. Some of the commonly used catalysts for OER in electrolysis cells are state-of-the-art noble metals of Pt, Ru, and Ir and their oxides.[3,4] However, there are some critical problems with the noble metal electrocatalysts including low abundance,

high cost as well as catalyst poisoning with small organic molecules, and sluggish kinetics.[5, 6] Therefore, partial or complete replacement of noble metal in the electrocatalysts has become a prime activity in recent research. Consequently, researchers focus on novel OER catalysts including earth abundant transition metal based compounds because of their low cost and enhanced catalytic activity.[7,8] In recent times, the most efficient catalytic activity towards OER was obtained by using nickel oxides or hydroxides [9, 10, 11, 12,13], as well as transition metal chalcogenides (ME_x, M = Fe, Co, Ni; E = S, Se) which incidentally showed activity towards HER, and oxygen reduction reaction (ORR) too.[14, 15] Among these transition metal chalcogenides, Nickel selenide (Ni_3Se_2) was shown to have good catalytic activity for OER from our group.[16] CoSe is a semiconducting material with the band gap of 1.52 eV and the valence and conduction band edges being close to the water oxidation-reduction levels. Recently cobalt selenides have shown lot of promise as catalysts for oxygen reduction [17, 18, 19] as well as decomposition of hydrazine hydrate, magnetic refrigeration and as electrodes for Li-ion batteries [20]. Multifunctional nanostructures containing semiconductor electrocatalyst grafted onto an optically active metallic component might boost the catalytic activity even further due to efficient charge injection. Magnetically active catalysts will also be beneficial since that might induce better adhesion of the oxygenated species at the catalytically active site.

In this presentation, we have created multifunctional magnetic Au_3Pd-CoSe nanostructures [21] and have investigated their potential as OER electrocatalysts. These nanoparticles have been produced by a simple chemical vapor deposition (CVD) reaction. OER electrocatalytic activity has been studied through detailed electrochemical

characterization providing some insight into mechanistic details. It was observed that indeed the Au_3Pd-CoSe nanostructures showed a low onset potential for O_2 evolution as well low overpotential at 10mA.cm^{-2}, characteristic of high catalytic efficiency.

2. EXPERIMENTAL

2.1. MATERIALS & METHODS

Gold coated Silicon (Au-Si) and doped silicon (d-Si) substrates used for CVD reactions were purchased from Deposition Research Lab. Inc. These substrates were cut into pieces of 1 x 1 cm^2. Au-Si was prewashed with isopropanol and acetone in order to remove any contaminants. d-Si substrate was etched with HF acid to remove any native SiO_2 layer and then cleaned thoroughly with DI water. These substrates were then sputter coated with Au–Pd (3: 2) for 120 seconds creating a layer of Au–Pd particles over the substrates. Cobalt acetylacetonate ($Co(acac)_3$) and Se shots were used as precursors for the synthesis and they were obtained from Sigma-Aldrich and used without further purification.

2.1.1. Synthesis of CoSe. These Au-CoSe nanostructures were synthesized in a horizontal tube furnace by chemical vapor deposition (CVD) technique at 800°C under a flow of N_2 as carrier gas (120 sccm). Schematic of CVD furnace and its setup is shown in Figure 1. Precursors and substrate were kept in the middle area of the horizontal furnace at 800 °C. Selenium shots were located at 400 °C and $Co(acac)_3$ was kept at a 250 °C region. Initially, the $Co(acac)_3$ and Se were kept outside the heating zone by pushing the ceramic liner to the extreme left.

When the central zone of the furnace reached at the reaction temperature of 800 °C, the ceramic liner was pushed to the right to get the appropriate sublime temperature regions for Se and $Co(acac)_3$ at 400 °C and 250 °C respectively. The reaction was carried out for 30 minutes, and the furnace was cooled down at the rate of 8 °C min^{-1}. This deposition was further characterized for the morphology and composition of the product

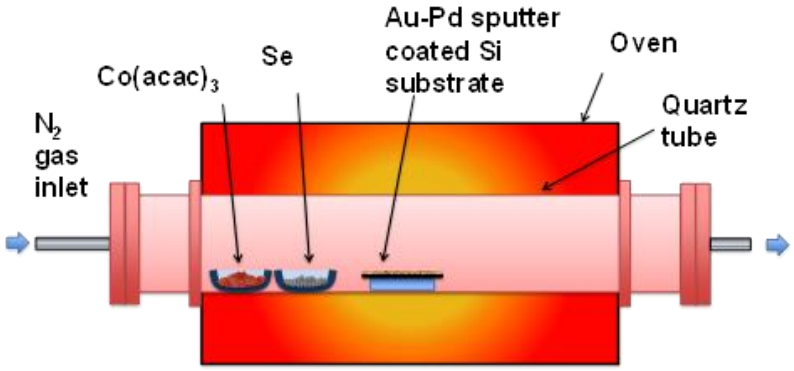

Figure 1. Schematic diagram of CVD apparatus. Used for the synthesis Au_3Pd-CoSe nanostructures.

2.2. CHARACTERIZATION

2.2.1. Powder X-Ray Diffraction. The as-synthesized product from the CVD reactions were characterized by powder X-ray diffraction (pxrd) with Philips X-Pert diffractometer using Cu Kα (1.5418 Å) radiation.

2.2.2. Electron Microscopy. For transmission electron microscopy (TEM) imaging, the sample was prepared by scratching the deposition on substrate and dispersing it in ethanol by sonicating for one hour. A drop from the “as prepared” dispersion was placed a holey carbon coated Cu TEM grid and dried thoroughly in a

vacuum oven prior to TEM imaging and Energy dispersive X-ray spectroscopy (EDS). TEM images were obtained on FEI Tecnai F20 and Tecnai Osiris TEM operating at 200 kV. For FEI Tecnai Osiris TEM the probe current is 1 nA with a spot size of less than 1 nm. The convergence angle is 10.3 mrad and the camera length is 200 mm for HAADF imaging. Scanning electron microscope (SEM) imaging was performed using FEI Helios NanoLab 600 FIB/FESEM directly onto the substrates covered with the CoSe layer.

3. DISCUSSION

Figure 2a shows the pxrd pattern obtained from the product, confirming the presence of hexagonal CoSe (JCPDS card no. 42541) along with Au_3Pd (JCPDS no. 180872). The sharp intensity of the pxrd peaks proves that highly crystalline nature of the product could be obtained. Purity of the product was very high and it did not show existence of any crystalline impurity from other cobalt selenide phases. Figure 1b shows an illustration of the typical crystal structure of CoSe showing the anion close packing and octahedral coordination of Co.

Figure 3a shows the SEM image of CoSe nanostructures grown on d-Si. As can be seen from these images, the CoSe on d-Si grew mostly as vertically oriented nanorods with a rectangular cross section. Closer inspection of the nanorods also revealed that they have a core-shell like morphology (inset of Figure 3a). The CoSe nanostructures grown on Au-Si on the other hand showed elliptical nanostructures as shown in Figure 3b. The shape and nature of these nanostructures are very representative of the bifunctional Janus

particles [22]. The different contrasts in the SEM images exhibits the presence of heterocomposition zones in the nanostructures. Most of the nanostructures were oval shape with the short axis ranging from 100–150 nm while the catalyst tip was less than 100 nm. Brighter tip in Figure 3a represents Au_3Pd, while darker region contains CoSe. Particle size distribution showed that the particle sizes (along the long axis) were mostly in the range 200–250 nm. The size of the oval shaped nanostructure could be manipulated by altering size of the Au–Pd nanoalloy catalyst particles.

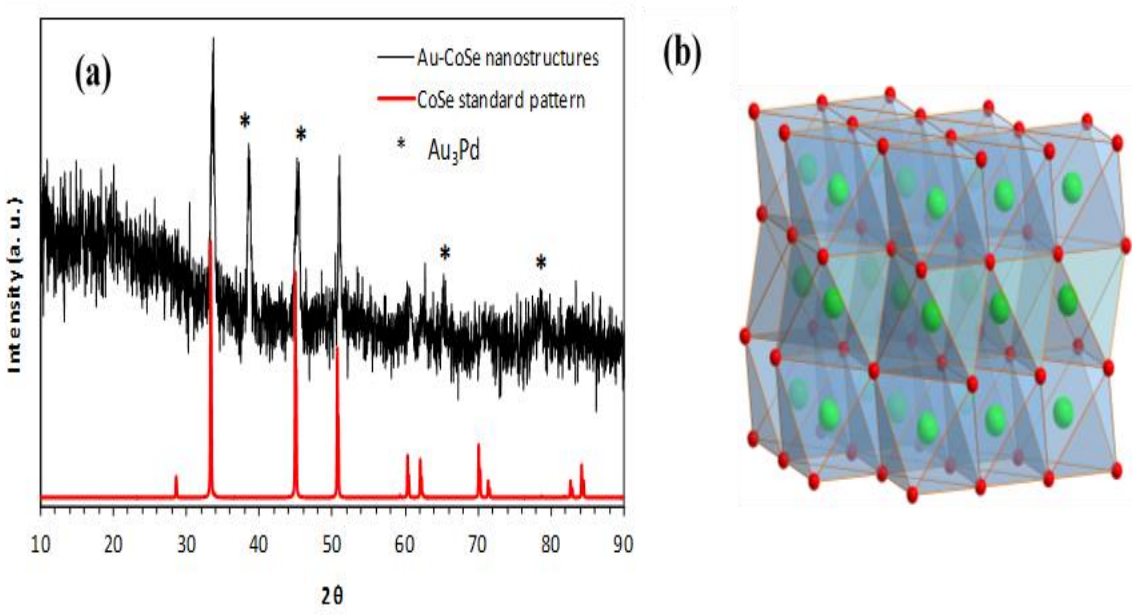

Figure 2. Au_3Pd-CoSe nanostructures. (a) PXRD pattern (b) Crystal structure.

The Au_3Pd-CoSe nanostructures were also characterized with high-resolution TEM imaging which revealed the single crystalline nature of the nanostructures with lattice fringes along the <111> crystallographic direction as shown in Figure 3c. The EDS line scan and mapping as given in Fig. 4 was carried out on an FEI Tecnai F20 TEM

operated at 200 keV in STEM mode. The probe current is 1.2 nA with a spot size of less than 2 nm. The convergence angle is 13 mrad and the camera length is 30 mm for dark Field imaging. This scope is equipped with an Oxford ultra-thin (UTW) window EDS

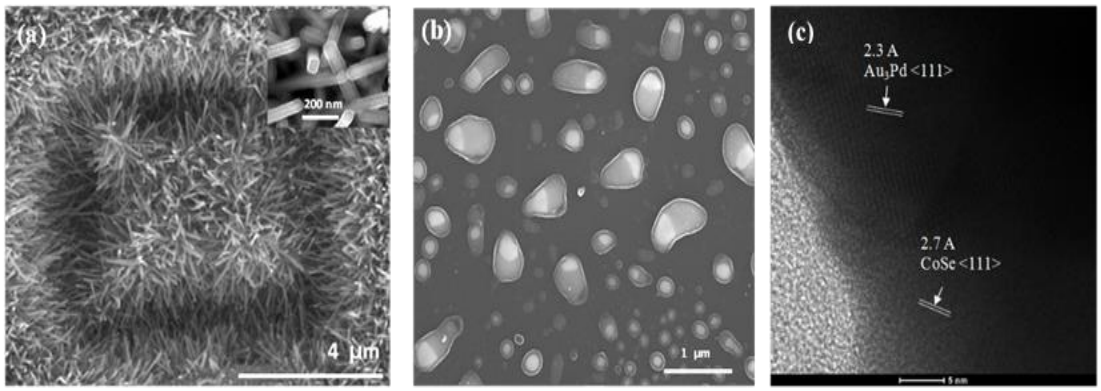

Figure 3: SEM and TEM images. (a) the rod-like CoSe nanostructures; and (b) bifunctional Au_3Pd-CoSe nanoparticles. (c) High resolution TEM image of Au_3Pd–CoSe nanoparticles.

detector, which allows detection of carbon. The X-ray transmission efficiency for carbon with this window is 42%. Table 1 is given the EDS line scanning of the Au_3Pd-CoSe nanostructures and it has a stoichiometric ratio of Co: Se. The elemental mapping of the nanostructures illustrated (figure 4) that brighter tip represents Au_3Pd, while darker region contains CoSe. The Au(Pd) and Co–Se regions shared a common interface. There was no noticeable mixing of Au in the Co–Se regions, and likewise there was almost no mixing of Co–Se in the Au region which indicates that the phase purity of the individual phases.

3.1. ELECTROCHEMICAL CHARACTERIZATION AND CATALYTIC STUDIES

The OER catalytic activity was estimated from LSV graphs. Electrochemical measurements were performed in a three-electrode system with an IviumSoft potentiostat using the Ag/AgCl as reference electrode and Pt mesh as a counter electrode and the substrate with nanoparticles as the working electrode. All measured potentials vs. the Ag/AgCl were converted to the reversible hydrogen electrode (RHE) scale.

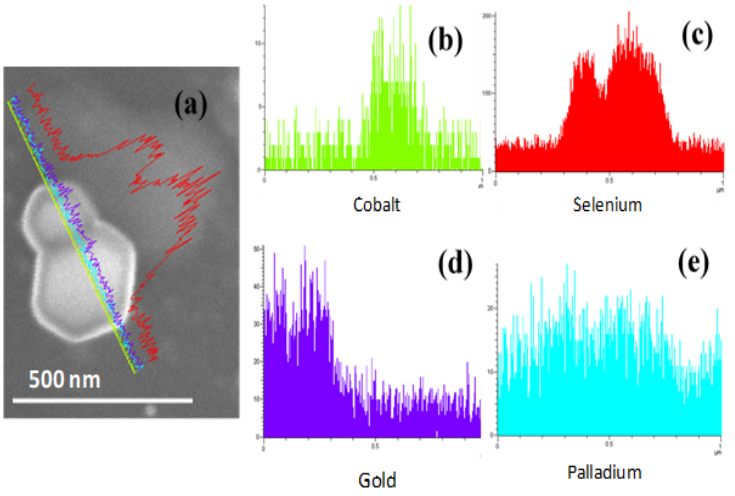

Element	Atomic %
O	12.14
Si	79.61
Co	2.31
Se	2.29
Pd	0.88
Au	2.77
Total	100

Figure 4. Elemental mapping of Au_3Pd-CoSe nanostructures. (a)- (e) Preferential location of Au, Pd, Co and Se.

To study the electrocatalytic activity of the CoSe for OER, linear sweep voltammetry (LSV) measurements were conducted in N_2-saturated 0.3 M KOH solution, at a scan rate of 10 mV s^{-1}. Figures 5 (a) and (b) show the LSVs of electrochemical oxygen evolution with CoSe nanostructured catalysts. Typically rapid oxygen evolution from the CoSe catalyst surface was observed during the electrochemical studies. The

blank substrates of Au- coated Si and doped Si (d-Si) substrates show poor catalytic activity toward the OER as expected. The CoSe nanorods on d-Si substrate revealed that higher onset potential for O_2 evolution compared to the CoSe @ Au-Si (1.27 V *vs* RHE). However, CoSe@d-Si showed a lower overpotential at 10 $mA.cm^{-2}$ (300 mV *vs* RHE) compared to CoSe@Au-Si (430 mV *vs* RHE). The overpotential for CoSe@d-Si is significantly lower that of bulk $CoSe_2$ (590 mV) and ultrathin $CoSe_2$ (320 mV) [23] reported in literature as well as of NG-$CoSe_2$ (366 mV).[24]

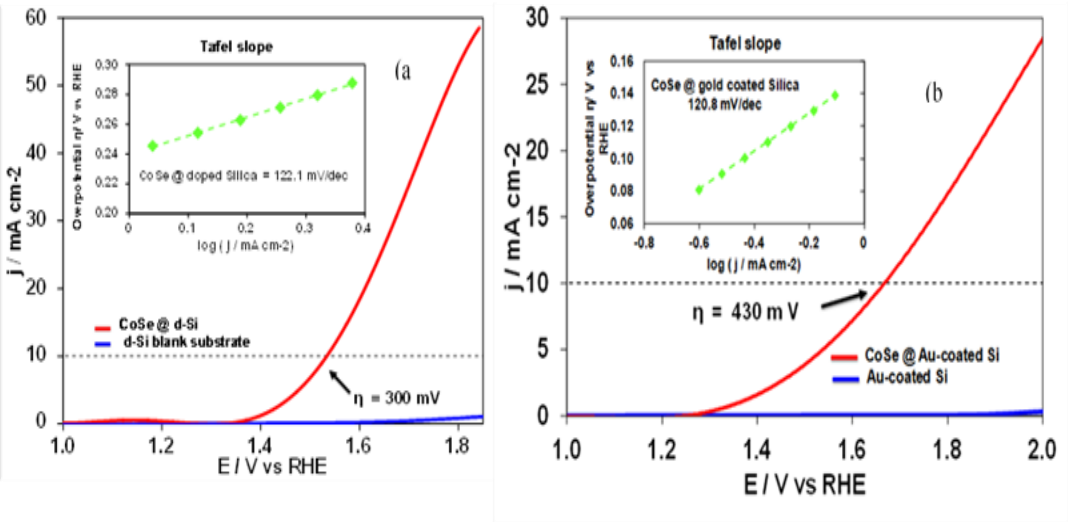

Figure 5. OER activity and Tafel slope. (a) CoSe nanorods on d-Si substrate and (b) bifunctional Au-CoSe nanostructures. Inset shows Tafel slope for each nanostructure ensemble.

Nanostructuring the catalyst increases the functional surface area which is a vital part in catalytic reactions. Yang *at el* also showed that synthesis of a three-dimensional (3D) ternary hybrid $Co_{0.85}Se$ nanosheet array and successively grown NiFe-LDH on electrochemically exfoliated graphene which shows lower overpotential of 150mA cm^{-}

^{2}.[25] In addition RGO/$CoSe_2$ also shows the very low onset potentials than bare $CoSe_2$ [2] due to reduction of the activation barrier when support the nanoparticle of RGO.

CoSe@d-Si substrate shows approximately two-fold exchange current densities compared to CoSe@Au-Si substrate which can be attributed to the growth of grass like square shaped nanorods which significantly increase the functional surface area and also facilitate release of the generated oxygen bubbles away from the electrode surface, particularly at high current densities. [26]

The catalytic performance of the CoSe catalysts toward the OER was further evaluated by measuring the Tafel plots. The Tafel equation is a fundamental equation which acquires from the kinetically controlled region of oxygen evolution reaction and relates the overpotential of the reaction with the current density. In addition, Tafel slope also provides inset into the number of electrons involved in the rate determining step of the catalytic process. For both of the CoSe nanostructures grown on d-Si and Au-Si, a Tafel slope of 120 mV dec^{-1} Tafel slope was obtained as has been shown in the inset of Figures 5 (a) and (b), respectively. A comparison of all the catalytic parameters has been listed in Table 2.

Table 1. Comparison of catalytic activity of Au3Pd-CoSe on two substrates.

Sample	**Onset potential (V vs RHE)**	**Tafel slope (mV dec^{-1})**	**Overpotential at 10 mA cm^{-2} (mV vs RHE)**
Au_3Pd-CoSe@d-Si	1.32	122.1	300
Au_3Pd-CoSe@Au-Si	1.27	120.8	430

4. CONCLUSION

In conclusion, we have synthesized multifunctional magnetic nanostructures of the composition Au_3Pd-CoSe and have shown that these nanostructures are very active towards water oxidation. Moreover, the morphology of these nanostructures could be altered by changing the growth substrate from highly conducting Au-Si to doped-Si, and the catalytic activity also showed a change. Importantly, the CoSe based nanostructures on d-Si showed a very low overpotential at 10 $mAcm^{-2}$ of exchange current density, which is typically a signature of a high efficiency catalyst. Such high catalytic efficiency might be attributed to the existence of an interface with metallic Au_3Pd which can facilitate charge injection and transport within these semiconducting nanostructures. It should be noted that in general these nanostructures showed a higher OER activity with lower onset potential for O_2 evolution reaction as compared to the conventional oxide-based OER electrocatalysts.

ACKNOWLEDGEMENT

Authors would like to acknowledge to the donors of American Chemical Society Petroleum Research Fund (ACS PRF# 54793-ND10) for support of this research and the Materials Research Center at MS&T.

REFERENCES

1. Kwak, I. H., Im, H. S., Jang, D. M., Kim, Y. W., Park, K., Lim, Y. R., & Park, J, *ACS Appl. Mater. Interfaces* **2016**, *8*, 5327-5334.

2. Millet, P., Mbemba, N., Grigoriev, S.A., Fateev, V.N., Aukauloo, A. and Etiévant, C., *Int. J. Hyd. Energy* **2011**, *36*, 4134-4142.

3. Yang, J., Shen, X., Ji, Z. and Zhu, G., 2013., *J. Mater. Sci.* **2013**, *48*, 7913-7919.

4. Gorlin, Yelena, Jaramillo, T. F. *J. Am. Chem. Soc.* **2010**, *132*, 13612-13614

5. Lee, Y., Suntivich, J., May, K.J., Perry, E.E. and Shao-Horn, Y.,*J. Phys. Chem. Lett.* **2012**, *3*, 399-404.

6. Rabis, Annett, Paramaconi Rodriguez, Schmidt, T. J. *ACS Catalysis* **2012**, *2*, 864-890.

7. Faber, M., Matthew S., Song J. *Energy & Environ. Sci.* **2014**, *7*, 3519-3542.

8. Gong, Ming, Dai, H. *Nano Research* **2015**, *8*, 23-39.

9. Li, Y., Panitat H., Wu, Y. *Adv. Mater.* **2010**, *22*, 1926-1929.

10. Corrigan, D. A. *J. Electrochem. Soc.* **1987**, *134*, 377-384.

11. Corrigan, D. A., Bendert, R. M. *J. Electrochem. Soc.* **1989**, *136*, 723-728.

12. Chialvo, D., Gennero, M. R., Chialvo, A. C. *Electrochim Acta* **1988**, *33*, 825-830.

13. Liang, Z. H., Zhu, Y. J., Hu, X. L. *J. Phys. Chem. B* **2004**, *108*, 3488-3491.

14. Xu, W., Lu, Z., Lei, X., Li, Y. and Sun, X., *Phys. Chem. Chem. Phys.* **2014**, *16*, 20402-20405.

15. Feng, Y., Gago, A., Timperman, L. and Alonso-Vante, N., *Electrochim. Acta* **2011**, *56*, 1009-1022.

16. Swesi, A. T., Masud, J., Nath, M. *Energy Environ. Sci.* **2016**, doi: 10.1039/C5EE02463C.

17. Feng, Y., He, T., Alonso-Vante, N. *Electrochim. Acta* **2009**, *54*, 5252-5256.

18. Nekooi, M., Parisa, J., Akbari, M., Amini, M. K. *Int. J. Hyd. Energy* **2010**, *35*, 6392-6398.

19. Feng, Y., Alonso-Vante, N. *Electrochimica Acta* **2012**, *72*, 129-133.

20. Zhang, L. F., Zhang, C. Y. *Nanoscale* **2014**, *6*, 1782-1789.

21. Liyanage, W. P. R., Mishra, S., Song, K. A., Nath, M, *RSC Advances* **2014**, *4*, 28140-28147.

22. Langlois, C., Li, Z.L., Yuan, J., Alloyeau, D., Nelayah, J., Bochicchio, D., Ferrando, R. and Ricolleau, C., *Nanoscale* **2012**, *4*, 3381-3388.

23. Liu, Y., Cheng, H., Lyu, M., Fan, S., Liu, Q., Zhang, W., Zhi, Y., Wang, C., Xiao, C., Wei, S. and Ye, B.,*J. Am. Chem. Soc.* **2014**, *136*, 15670-15675.

24. Gao, M.R., Cao, X., Gao, Q., Xu, Y.F., Zheng, Y.R., Jiang, J. and Yu, S.H., *ACS Nano* **2014**, *8*, 3970-3978.

25. Hou, Y., Lohe, M.R., Zhang, J., Liu, S., Zhuang, X. and Feng, X., *Energy Environ. Sci.* **2016**, *9*, 478-483.

26. Xia, C., Jiang, Q., Zhao, C., Hedhili, M.N. and Alshareef, H.N., *Adv. Mater.* **2016**, *28*, 77-85.

V. SYNTHESIS AND CHARACTERIZATION OF A SERIES OF NICKEL SELENIDES FOR HIGH EFFICIENT WATER OXIDATION CATALYSTS

Manuscript has been submitted to Nan-Micro Letters

Umanga De Silva [a], Diya Allada [a], Matthew Perkins[b], Jahangir Masud [a], Manashi Nath [a]*

[a]Department of Chemistry, Missouri University of Science and Technology, Rolla, MO 65409, USA.

[b]Department of Chemical and Biochemical Engineering, Missouri University of Science and Technology, Rolla, MO 65409.

*Email: nathm@mst.edu

ABSTRACT

The synthesis of an active catalyst series for oxygen evolution reaction is a promising route towards clean and renewable energy. In this paper, we have synthesized a series of nickel selenides of NiSe, $NiSe_2$, Ni_3Se_2, and Ni_3Se_4 as active electrocatalysts for the most crucial step for efficient electrocatalytic water splitting, which is the oxygen evolution reaction (OER) that takes place at the anode. These pure nickel selenides are synthesized by hydrothermal reactions and show low overpotential at 10 mA cm^{-2} and early onset as well as high current density during the OER in 1.0 M KOH. The overpotential at 10 mA cm^{-2} for a series of nickel selenides is 220, 200, 240 and 250 mV for NiSe, $NiSe_2$, Ni_3Se_2, and Ni_3Se_4, respectively. In addition, we discuss in this paper the synthesis of electrocatalysts, characterization techniques of XRD, SEM, TEM, and STEM, and electrochemical investigations of catalysts. Additionally, this paper discusses the stability of this catalyst during long-term OER conditions under 1.0 M KOH.

1. INTRODUCTION

Over the last several decades rapid depletion of fossil fuels has led researchers to focus on finding renewable energy sources for meeting future energy demands. A result of this continuous quest has been to develop technologies for harvesting energy from the sun (solar energy conversion) as well as other renewable sources such as water. Water splitting reaction, in particular has been of considerable interest in recent times due to the promise of generation of clean fuel (hydrogen) through environmentally benign methods.[1] Both solar and electrical energy can be used for water splitting reactions wherein clean hydrogen gas is generated through hydrogen evolution reaction (HER) while the other by-product is oxygen gas from oxygen evolution reaction (OER).[2] Water splitting reaction efficiency slows down to a greater extent due to the kinetically sluggish OER where O−H bond breaking and O=O bond formation occurs with a high electron count (4e).[3, 4, 5] The OER process is goes through multiple steps of proton-coupled electron transfer processes ,[6,7,8] consequently, requires an efficient catalyst to pull the reaction forward. Hence, the development of an efficient and highly active OER electrocatalyst is a major challenge in the water splitting process.[9,10] Generally, catalysts are engaged to decrease the activation energy barrier of the uphill water splitting reaction.[11] The most commonly used catalysts for OER in electrolysis are comprised of precious noble metals such as Pt, Ru, and Ir.[12-16] Researchers over the last few decades have made an attempt to design a durable, cheap, and efficient OER electrocatalyst based on earth-abundant transitions metals due to several reasons: (i) they have available *d* orbitals which can facilitate electron transfer in high electron count reactions such as

OER, (ii) transition metals can shuttle easily between various oxidation states, (iii) the possibility of single occupancy of the e_g orbital at the catalytically active metal site on the catalyst surface; (iv) high degree of covalency between transition metal site and anions.[4] It is the ability of the transition metal to be in a variety of oxidation states, to undergo facile transitions between these oxidation states, to coordinate to a substrate, and to be a good source/sink for electrons that makes transition metals such good catalysts.

Over the last decade, considerable amount of research was reported on pyrite materials MX_2 (M= Ni, Co, Mn, Fe; X=S, Se), which give rise to a wide variety of magnetic, optical and electrical properties due to their crystal field splitting, solid state properties, and intrinsic 3d bandwidth.[17] Consequently, McCrory *et al* have reported transition metals of Ni, Co, Fe, Cu, Mo, and Mn-based electrocatalysts having more proficient catalytic activity towards OER than precious noble metals.[18] Particularly, Ni-based catalytic materials are promising prospective OER catalysts in alkaline media because they show (i) high reaction rates, (ii) high stability and (iii) low-cost earth abundant material.[19] Several research groups are working with Ni-based oxides, hydroxides or composites with other transition metals doping for OER. In 2014, Gao *at el* reported that highly nanostructured α-$Ni(OH)_2$ catalyst which shows 331 mV overpotential at 10 mA cm^{-2} current density.[20] Nickel oxide and nickel hydroxide nanoparticles were investigated for excellent catalytic activity towards OER in alkaline solutions with 330 mV and 300 mV overpotential (η) at 10 mA cm^{-2}, respectively.[21] In 2015, porous Ni–Fe catalyst with overpotentials of 328 mV and 420 mV at 10 mA cm^{-2} and 50 mA cm^{-2} current densities, respectively were reported.[22] Lu and Zaho reported that an efficient OER catalyst can be developed by electrodepositing nickel-

iron composites onto Ni-foam which only require overpotential of 200 mV to initiate the reaction in alkaline solutions.[23] However, catalysts based on metal oxides have some constraints in water oxidation, such as high overpotential required to activate the catalytic site prior to the evolution of oxygen.[24] On the other hand, it has been proposed that the metal chalcogenides might show better electrocatalytic activity due to their increased electrochemical activity and higher degree of lattice covalency.[25] Semiconducting transition metal selenides have recently attracted enormous attention due to their distinctive electrical and magnetic properties and variety of potential applications in, e.g., optical recording materials, solar cell, superionic materials, sensors, laser materials, optical filters, and conductivity fields, etc.[26] Metal selenides, tend to form covalent, often low-dimensional structures in contrast to the ionic, 3D-type structures of the oxides. The greater covalency of the metal–selenide interaction reduces the relative charge on the metal ion thus enhancing metal orbital delocalization and favors M–M bond formation.[27] In addition, due to the higher degree of covalency of Ni-Se bond than the Ni-O bond, later elements of the chalcogenides series have better preference for water oxidation.[4] Consequently, the selenides show higher catalytic efficiencies towards water oxidation.[28]

Recently our group reported electrodeposited Ni_3Se_2 on Au-coated glass as a very good catalyst for OER having 10 mA cm^{-2} current density at an overpotential as low as 290 mV in alkaline solutions[29] and 190 mV for nanostructured Ni_3Se_2 on Au-coated glass.[30] $Ni^{II}Se_4$ complex exhibits excellent OER activity in 1.0 M KOH with an overpotential of 200 mV at 10 mA cm^{-2},[31] and <311> textured $NiSe_2$ shows catalytic activity with the onset potential for O_2 evolution at 1.36 V (vs RHE) and overpotential of

140 mV to get 10 mA cm^{-2} current density in alkaline medium.[32] In 2016, Pu *et al* demonstrated that electrodeposited $NiSe_2$ nanoparticles on Ti plate is an efficient and robust electrode to catalyze water oxidation in basic media which affords 20 mA cm^{-2} at 295 mV overpotential with strong durability in 1.0 M KOH.[33] while, Wu *et al* showed that electrodeposited hexagonal phase as-synthesized $Ni_{0.85}Se$ films supported on graphite substrate exhibited excellent activities for OER which needs overpotential of 302 mV to achieve 10 mA cm^{-2} in 1.0 M NaOH.[34] The growth of NiSe nanowire on nickel foam exhibits high activity with an overpotential of 270 mV required to achieve 20 mA cm^{-2} and strong durability in basic medium.[35] Ni_3Se_2@Ni foam electrode delivers an OER overpotential of 315 mV at a current density of 100 mA cm^{-2} in 1 M KOH.[36] Nickel and selenium are able to create diverse compositions having different stoichiometric ratios due to the smaller electronegativity difference of nickel and selenium (Ni =1.9, Se=2.4) and enhanced charge delocalization.[37] These various nickel selenide compound compositions, crystal structures, and morphologies strongly influence their physical and chemical properties and their applications.[38] We have hydrothermally synthesized four types of nickel selenide nanostructures of composition NiSe, $NiSe_2$, Ni_3Se_2, and Ni_3Se_4. Nanostructures are expected to increase the catalyst surface area as well as the electrochemically active surface area and expose more active sites resulting in enhanced catalytic activity. The nickel selenide nanostructures reported in this article show higher current densities, higher mass activity and very low onset potential and overpotential at 10 mA.cm^{-2} for OER in 1m KOH. In addition, they also show extended functional and compositional stability of under conditions of continuous OER for over 12 h.

2. EXPERIMENTAL SECTION

2.1. MATERIALS

All the syntheses were carried out with analytical grade chemicals and they were used without any further purification. All reagents were prepared using deionized (DI) water. Nickel sulfate ($NiSO_4 \cdot 6H_2O$–Fisher Scientific), Selenium dioxide (SeO_2- Acros Chemicals), and hydrazine hydrate ($N_2H_4 \cdot H_2O$, 100%) were purchased from the Acros Organics company, USA. Carbon cloth (CC) substrate and Nafion were purchased from Fuel cells Etc. Company, college station, Texas and Ion Power respectively.

2.2. SYNTHESIS OF NICKEL SELENIDE NANOSTRUCTURES

Synthesis of nickel selenides was carried out using a reported procedure with some modifications. In a typical synthesis of NiSe, $NiSO_4 \cdot 6H_2O$ and SeO_2 were used in 4:1 stoichiometric ratio. $NiSO_4.6H_2O$ (4.0 mM) was dissolved in 12.0 ml of deionized water under magnetic stirring to form a homogeneous solution. After mixing the solution for 10 min, SeO_2 (1.0 mM) was added and stirred vigorously for 20 min. Ultimately, $N_2H_4.H_2O$ (3.0 ml) was added to the mixture and stirred constantly until the solution becomes transparent. The resulting transparent solution was transferred into a Teflon-lined stainless-steel autoclave. The autoclave was sealed and maintained at 185 °C for 7 h, then naturally cooled to room temperature. The formed black product was centrifuged, washed several times with distilled water and absolute ethanol to remove impurities. The product was dried in a vacuum oven at 60°C for 24 h. Similarly, $NiSe_2$, Ni_3Se_2, and

Ni_3Se_4 were prepared by changing the Ni: Se molar ratio of precursors, reaction times and reactions temperatures which are summarized in Table 1.

Table 1. The reactions parameters of nickel selenides series.

Product	Ni: Se ratio	Time/ h	Temperature / °C
NiSe	4:1	7	185
$NiSe_2$	3:1	7	185
Ni_3Se_2	3:1	24	145
Ni_3Se_4	1:3	31	145

2.3. CHARACTERIZATION METHODS

As-synthesized nickel selenides were characterized by powder X-ray diffraction (PXRD) with Philips X-Pert X-ray diffractometer (PANalytical, Almelo, The Netherlands) using CuKα (1.5418 Å) radiation. The surface morphology was examined with an FEI Helios NanoLab 600 FIB/FESEM. The chemical composition of the films was examined using an energy dispersive X-ray analyzer (EDX) and X-ray photoelectron spectroscopy (XPS) were obtained through a KRATOS AXIS 165 X-ray Photoelectron Spectrometer (Kratos Analytical Limited, Manchester, United Kingdom) using the monochromatic Al X-ray source.

Crystal structure of the catalyst was confirmed using high-resolution transmission electron microscopy (HR-TEM) and selected area electron diffraction (SAED) analysis with an FEI Tecnai F20. The spot size was less than 2 nm and probe current was 1.2 nA. STEM mode in the TEM was also used for imaging with a camera length of 30 mm and

the convergence angle of 13 mrad. Oxford ultra-thin (UTW) window EDS detector was used to detect the elements in TEM mode.

2.4. ELECTRODE PREPARATION

To analyze the activity of hydrothermally synthesized nickel selenides, a homogeneous catalyst ink was prepared by adding finely ground 4.0 mg of catalyst powder in 100.0 μL of 50% IPA in water followed by ultra-sonication for 30 min. Then, 10 μL of the dispersion was drop cast on a confined area (0.08 cm^2) on carbon cloth. The drop-casted film was then dried at room temperature. After that, 5 μL of 0.1% Nafion in IPA solution was drop casted on the catalyst film and allowed to dry overnight in room temperature.

2.5. ELECTROCHEMICAL MEASUREMENTS

Electrochemical studies were carried out in a three-electrode system using an IviumStat potentiostat having Ag/AgCl as the reference electrode, a Pt mesh as the counter electrode and the prepared nickel selenide electrode as the working electrode. 1.0 M KOH was used as the electrolyte for electrochemical studies. Before all the electrochemical measurements, the electrolyte was deaerated by continuously purging with N_2 gas for 30 minutes. The linear scan voltammetry (LSV) was carried out to find the OER catalytic activity at a scan rate of 10 mV s^{-1}. The stability of the catalyst was monitored by chronoamperometry. Following equation was used to convert the potentials

measured from Ag/AgCl electrode to convert in to RHE scale (reversible hydrogen electrode).

$$E_{RHE} = E_{Ag/AgCl} + 0.059pH + E^{o}_{Ag/AgCl} \quad (1)$$

In this equation, $E^{o}_{Ag/AgCl}$ is the standard potential of Ag/AgCl at 25 ºC (0.197 V), $E_{Ag/AgCl}$ is the measured potential, by the potentiostat, with the Ag/AgCl reference electrode and E_{RHE} is the potential vs. RHE. The turnover frequency (TOF) was calculated from the following equation (2).

$$TOF = (I)/(4 \times F \times m) \quad (2)$$

where I is the current in Amperes, F is the Faraday constant and m the number of moles of the active catalyst. The catalytic performance of the Ni_3Se_2 catalysts toward the OER has been carried out by measuring the Tafel plots based on the equation given below equation (3).

$$\eta = a + (2.3R\ T)/\alpha nF \log j \quad (3)$$

where η is the overpotential, j is the current density, α is transfer coefficient, n is number of electron involved in the reaction and F is Faraday constant. The Tafel equation as shown in equation (3) is a fundamental equation which acquires from the kinetically controlled region of OER. To calculate Tafel slopes, LSV plots were obtained with a slow scan speed of 2 mV s^{-1} in non-stirred solution.

The electrochemically active surface area of the catalyst was estimated by measuring electrochemical double layer capacitance (C_{DL}) of the electrode-electrolyte interface of the double layer region in the cyclic voltammogram. The cyclic voltammogram of the electrode was cycled from -0.025 to 0.05V vs Ag/AgCl at scan rates between 2.5 and 40 mV s^{-1} in N_2 saturated 1.0 M KOH solution. The capacitive

current (i_{DL}) was estimated from the non- faradic double layer region in the cyclic voltammogram. This capacitive current mainly accounts more for charge accumulation than charge transfer or chemical reactions and it is directly proportional to scan rate (υ). Capacitive current is the product of the double layer capacitance and scan rate.

$$i_{DL} = C_{DL} \times \upsilon \quad (4)$$

The electrochemical active surface area (ECSA) is the product of double layer capacitance and specific capacitance (Cs) which is shown in equation 5 and is reported from 0.022 mF cm-2 to 0.130 mF cm-2 in alkaline solution.[39] In this study, we have assumed the value of specific capacitance to be 0.040 mF cm^{-2} based on reported Ni-based OER catalysts.[39] The roughness factor (RF) was calculated by using ECSA and the geometric area of the different catalytic electrodes given in Table 2.

$$ECSA = C\ DL / Cs \quad (5)$$

3. RESULTS & DISCUSSION

When $NiSO_4 \cdot 6H_2O$ and SeO_2 are dissolved in the DI water, H_2SeO_3 acid can be obtained as a clear solution. This H_2SeO_3 acid can be reduced to Se by hydrazine hydrate. In the alkaline condition, H_2SeO_3 can easily be converted into Se^{2-} upon quick heating. The dissolved Ni^{2+} ions can react with Se^{2-} ions to form various phases of Ni_xSe_y compounds. Different morphologies and sizes of nickel selenides nanostructures were formed by the hydrothermal process by varying the Ni: Se reactant ratio, reaction temperature and reaction time. This solution-phase reaction system has provided a feasible and homogeneous environment for the nucleation and growth of the nickel

selenide nanostructures. It was found that the molar ratio between the two stable precursors, the reaction temperature and time played important roles in the formation of the nickel selenide series and these products are black in color.[38] Table 1 shows the effect of reaction conditions on the product composition for the synthesis of nickel selenides. The proposed mechanism for the synthesis of nickel selenides can be explained using the following equation:

$$SeO_2 + H_2O \rightarrow H_2SeO_3 \quad (7)$$

$$H_2SeO_3 + N_2H_4 \cdot H_2O \rightarrow Se + N_2 + 4H_2O \quad (8)$$

$$3Se + 6OH^- \rightarrow 2Se^{2-} + SeO_3^{2-} + 3H_2O \quad (9)$$

$$Ni^{2+} + Se^{2-} \rightarrow Ni_xSe_y \quad (10)$$

3.1. STRUCTURAL CHARACTERIZATION

Powder X-ray diffraction (pxrd) is a powerful nondestructive technique for characterizing crystalline materials. It provides information on crystal structures, preferred crystal orientations, phases, and other structural parameters, such as crystallinity, strain and average grain size. XRD peaks are produced by constructive interference of a monochromatic beam of X-rays scattered at specific angles from each set of lattice planes in a sample. The peak intensities are determined by the distribution of atoms within the lattice.[27] The pxrd phase analysis confirmed the reaction between selenium and nickel ions towards the formation of pure nickel selenide electrocatalyst without any impurities such as selenium or other phases of nickel selenides. In fact all the diffraction patterns collected by different samples can be indexed as pure-phase compounds of trigonal/rhombohedral NiSe (PDF no: 04-003-5475), cubic $NiSe_2$ (PDF

no: 00-041-1495), trigonal/rhombohedral Ni_3Se_2 (PDF no: 04 -007-3698) and monoclinic Ni_3Se_4 (PDF no: 04 -007-3699) as shown in Figure 1.

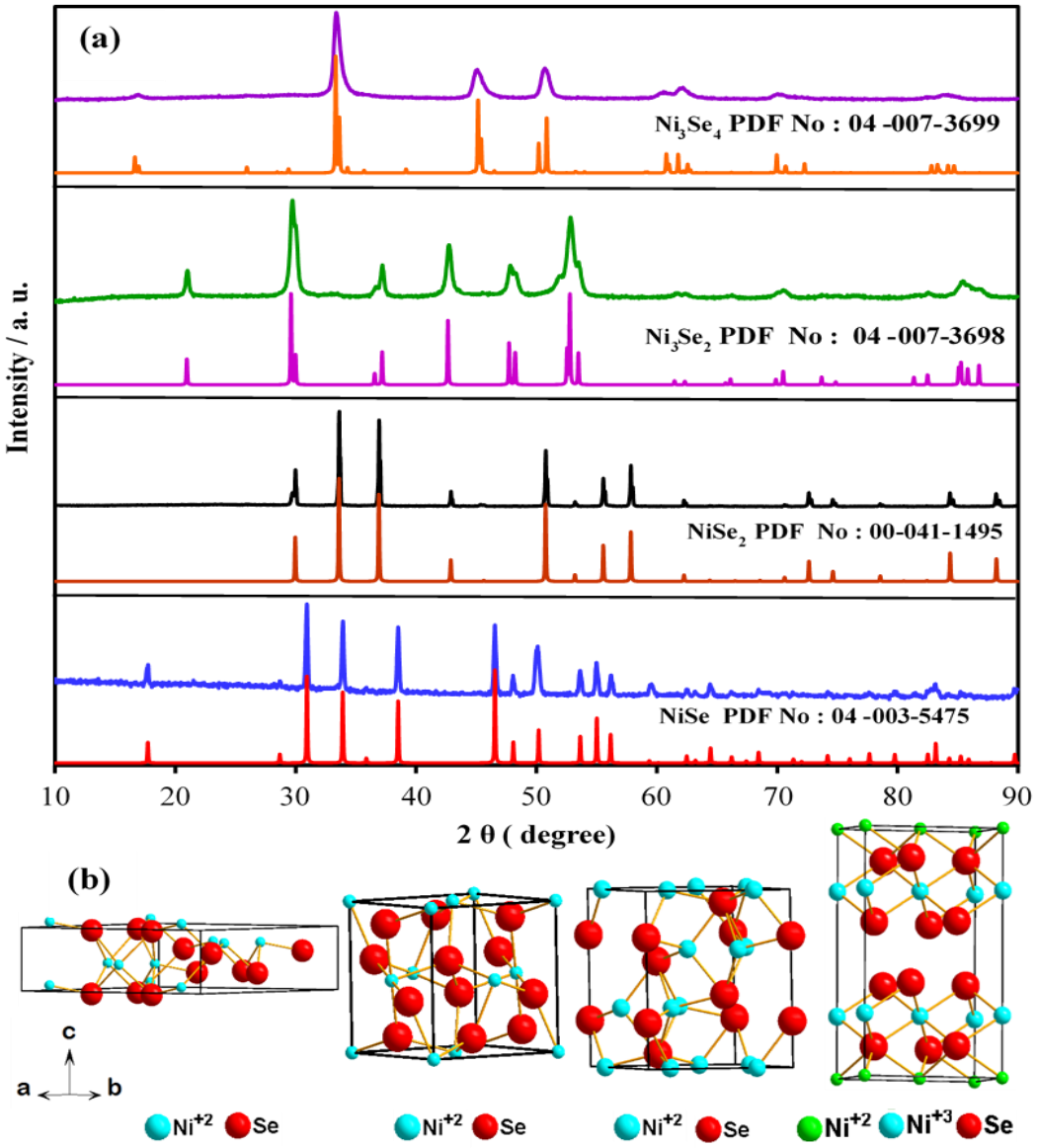

Figure 1. PXRD patterns and crystal structures of nickel selenides. (a) hydrothermally synthesized Ni_3Se_4 , Ni_3Se_2 , $NiSe_2$ and NiSe compounds, (b) Schematic illustration of the crystal structure of NiSe, $NiSe_2$, Ni_3Se_2 and Ni_3Se_4.

The sharp, strong and narrow peaks indicated a high degree of crystallization of the as-prepared products[3] and the broadening of these diffraction peaks indicates that the sample consists of nanocrystallites.[17] The average crystallite size of different morphology of nanostructures was calculated using the Scherrer formula;[40]

$$D = K\lambda/\beta Cos\theta \quad (8)$$

where D is crystallite size, λ is the wavelength of X-ray used, β is the peak width at half maximum in radian, θ is the Bragg's diffraction angle and K is a constant. The average grain size was found to be 40 nm, 100 nm, 16 nm and 12 nm for NiSe, $NiSe_2$, Ni_3Se_2, and Ni_3Se_4, respectively.

NiSe has a trigonal/ rhombohedral crystal structure with R3mH space group that contains each Ni and Se atoms in square pyramidal coordination. Typically, one Ni atom consists of five Se atoms and vice versa. $NiSe_2$ consists of a cubic crystal structure with Pa-3 space group which consists of each Ni atom bonded with six selenium atoms in an octahedral environment, and each Se atom is bonded with four Ni atoms in a tetrahedral environment. In addition, this $NiSe_2$ crystal structure has a Se-Se dimer which increases the magnetic behavior at high temperature since unpaired electrons populates the available 3d orbitals.[41] Ni_3Se_2 also has a trigonal/ rhombohedral crystal structure and belongs to the R32H space group. This crystal structure has rhombohedral coordination for the Se environment and tetrahedral coordination for the Ni environment. Ni_3Se_4 is a monoclinic crystal structure that has I12/m space group. This crystal structure consists of two types of Ni atoms which have Ni^{2+} and Ni^{3+} oxidation states. These Ni atoms are arranged in layers in the crystal structure with octahedral coordination while Se atoms

arrange in prismatic coordination. This layered arrangement increases the unpaired electron localization along the lattice.

Scanning electron microscopy (SEM) was employed to investigate the morphologies of these hydrothermally prepared nickel selenide samples. Figure 2a shows that the NiSe samples are agglomerated and densely packed with many exposed sides which can help to bring more active points onto the surface area. Figure 2b illustrates nearly monodispersed $NiSe_2$ rods. The average length of the edge of these microcrystals is approximately 5 μm. Figure 2C illustrates the Ni_3Se_2 quasi-triangle-shaped morphology, further confirming such a pyramid-like configuration with the uniform formation of Ni_3Se_2. The pyramid-like structure has a considerable surface roughness, thus possessing a high specific surface area. In addition, having many facets with active edge sites, which facilitates charge/mass transport and oxygen diffusion during the OER process.[42] Ni_3Se_4 is arranged into flower-like sphere assemblies of nanoflakes shown in Figure 2D. It is interesting that the sphere-like puffy balls are composed of a large quantity of small Ni_3Se_4 nanoflakes. These nanoflakes have many active points on its surface and make the spheres have a larger surface area than that of smooth spheres, which make this type of structure more suitable for catalytic applications. Consequently, the higher surface area of these structures may provide an ideal host material for the insertion and extraction of ions, to realize region-dependent surface reactivity.[27,43]

Furthermore, flake kind of geometry can make a good path for formed gas bubbles to escape from the electrode surface without any damage to the electrocatalyst material on the surface of the electrode. Because of the slower rate of reduction by

hydrazine hydrate, ample time is there for Ni_3Se_4 to agglomerate and grow into more regular shapes of flower-like spherical geometry.[44]

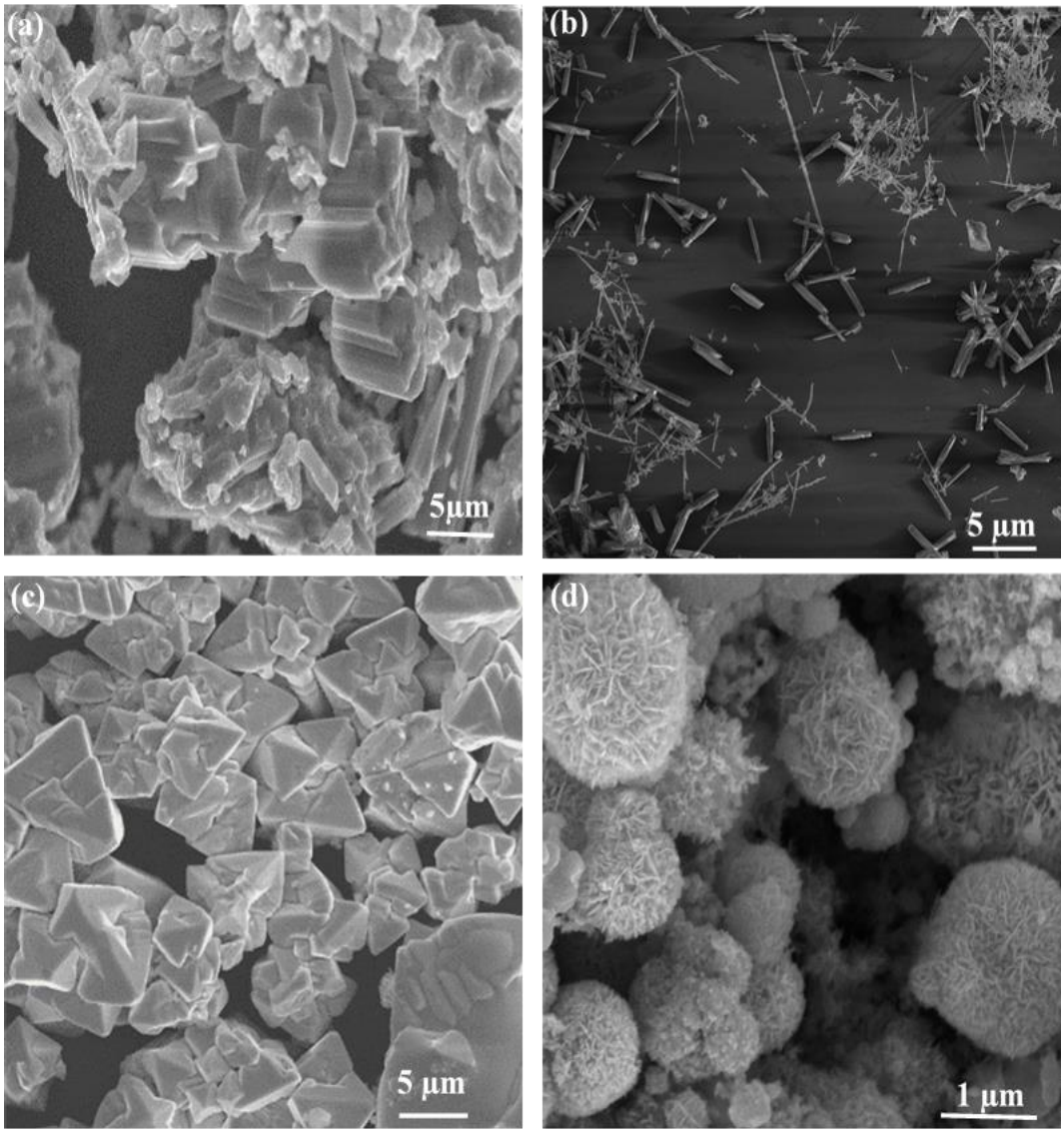

Figure 2. SEM images of nickel selenides. (a) NiSe, (b) $NiSe_2$ rods, (c) Ni_3Se_2 pyramid structures and (d) Ni_3Se_4 flaky structures.

The structural properties of the nickel selenide samples were further characterized by TEM, HRTEM and SAED to better understand the morphology, crystallinity and

crystallographic data of the hydrothermally synthesized nickel selenide samples. NiSe TEM image is given in Figure 3 (a-c) and the high-resolution TEM (HRTEM) image is given in Figure 3c.

The corresponding selected-area electron diffraction (SAED) pattern (Figure 3b) shows diffraction discrete spots corresponding to the high crystallinity of the hydrothermally synthesized NiSe with a distinct single crystalline structure. The well-resolved lattice fringes with interplanar spacings of 1.95 nm can be indexed readily to the <131> plane of rhombohedral NiSe. The associated STEM EDX elemental maps demonstrate the fairly homogeneous distribution of Ni and Se without discernible segregation throughout the NiSe structure as given in Figure S1a. The atomic ratio of Ni: Se was calculated to be 1: 1, in good agreement with a stoichiometry of NiSe (Figure S1a). Figure S1b-f illustrates the atomic percentile and the elemental mapping of NiSe. These NiSe structures have considerable surface roughness and, thus, possesses a high specific surface area and active edge sites, facilitating charge/mass transport and oxygen diffusion during the OER process.[42] Figure 3 b(1) shows the TEM image of the $NiSe_2$, and the SAED pattern in Figure 3 (d-f) shows the diffraction discrete spots corresponding to crystalline $NiSe_2$. Figure 3f revealed two types of crystallographic planes intersected in the HREM image and these planes correspond to a <200 > plane with a d-spacing of 2.95 Å from the cubic $NiSe_2$ system. The STEM EDX analysis of the $NiSe_2$ confirmed the presence of nickel and selenium in a 1:2 ratio (Figure S2a), and it further confirmed that the (Figure S2b) atomic distribution mainly consists of Ni and Se atoms agreeing with the element mappings showed in Figure S2c-f.

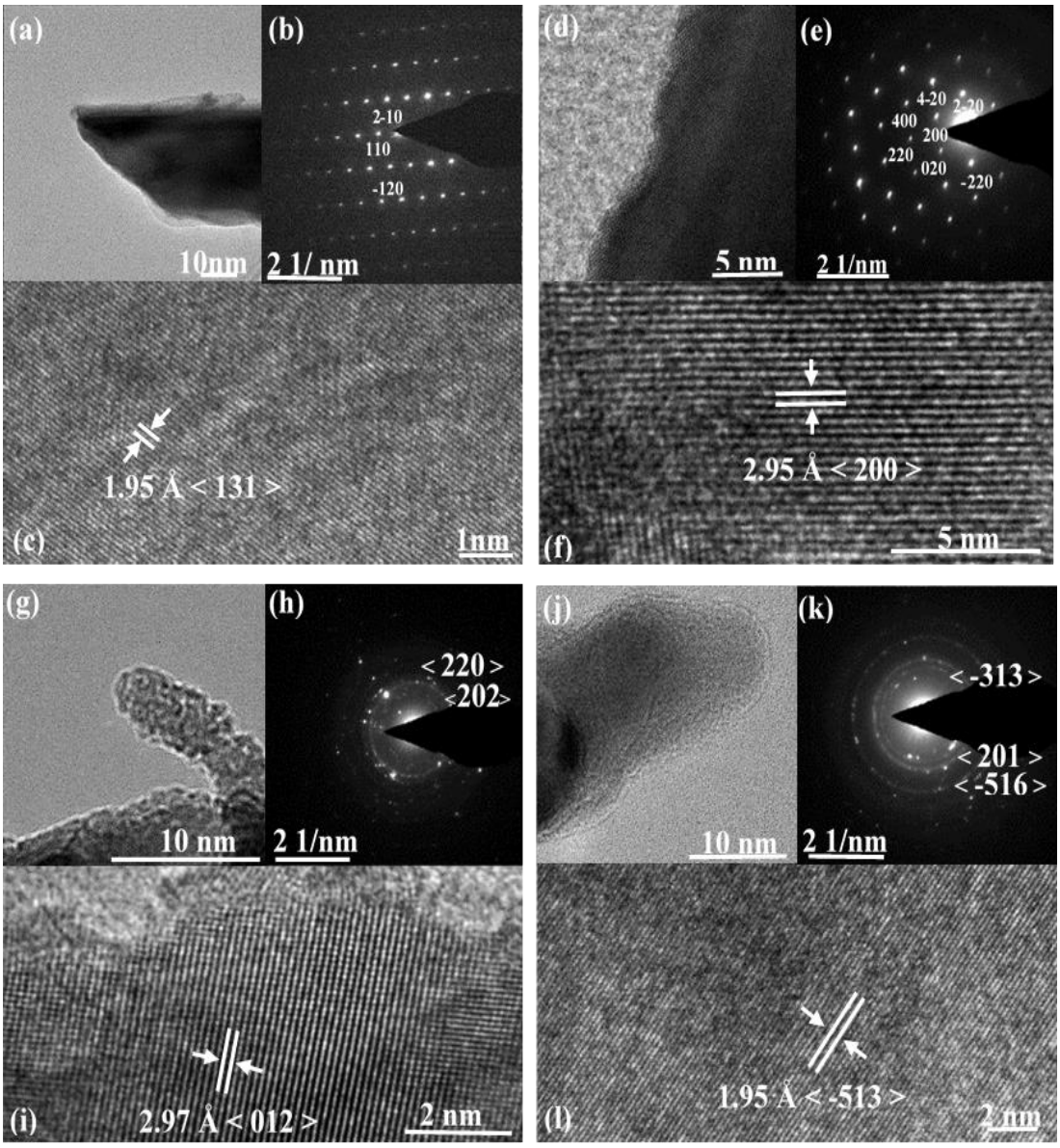

Figure 3. TEM images, SAED patterns and HRTEM images of nickel selenides. (a-c) NiSe (d-f) $NiSe_2$ (g-i) Ni_3Se_2 and (j-l) Ni_3Se_4

The Ni_3Se_2 TEM image is shown in Figure 3g while SAED patterns collected from these pyramid-like structures showed diffraction rings (Figure 3(g-i) corresponding to the presence of polycrystalline crystals. The indicated <202> and <220> lattice planes confirms the presence of crystalline Ni_3Se_2 rhombohedral system, and HRTEM images

revealed that these structures are highly crystalline with lattice fringes prominently corresponding to <012> lattice spacing of Ni_3Se_2 (Figure 3i). The STEM EDX showed a Ni:Se 3:2 atomic ratio (Figure S3a), and the atomic distribution in Figure S3b shows the elemental mapping of Ni, Se and C. Figure S3c-f shows the uniform distribution of these elements. Figure 3j illustrated the TEM image of Ni_3Se_4, and the HRTEM (Figure 3l) showed the lattice plane corresponding to the <-513> plane with a lattice spacing of 1.95 Å of the monoclinic Ni_3Se_4. SAED pattern (Figure 3k) collected from the nanoflakes of puffy balls showed diffraction rings indicating the polycrystalline nature of these flakes. Some of the lattice planes e.g. <201>, <-516>, and <-313> are identified for reference. Elemental composition was confirmed by the elemental mapping and elemental distribution showed in Figure S4 a-e.

The different electronic states of Ni and Se atoms in the near surface region of the hydrothermally synthesized Nickel selenide electrocatalysts was further investigated using XPS. All tested nickel selenide samples were prepared as electrodes which consisted of nafion binder and catalysts. In hydrothermally synthesized NiSe, the observed Ni 2p 1/2 and Ni 2p 3/2 centred at 873.5 and 856 eV correspond to Ni^{3+} (Figure 4a) and the peaks at 852.5 and 867.6 eV can be assigned to Ni^{2+} agree with the previously reported NiSe nanocrystals.[45] The Se 3d spectrum of NiSe shows doublet peaks of $3d_{5/2}$ and $3d_{3/2}$ which correspond to Se and surface oxidation of SeO_x peaks[45], which are related to surface oxidation (Figure 4e). In $NiSe_2$, the Ni 2p spectrum binding energy of $2p_{3/2}$ and $2p_{1/2}$ doublets due to spin-orbit coupling with two satellite peaks were observed in Figure 4b at 853.1 eV and 870.5 eV, and these peaks positions match previous $NiSe_2$ reports.[46-48] The Ni 2p spectrum also shows peaks of Ni^{3+}. It clearly

shows that Ni exists in the form of Ni^{2+} and Ni^{3+}oxidation states. The Se 3d spectrum of $NiSe_2$ shows the $3d_{5/2}$ and $3d_{3/2}$ doublet peaks (Figure 4f) at 54.1 eV and 54.9 eV[49] and its energy separation is ~ 0.8 eV, which is matched with the electrodeposited $NiSe_2$ XPS. It confirms the −2 valance state of Se (Se^{2-}), which means there is only one kind of possible metal-selenide bond (Ni-Se)[36]. In addition, surface oxidation of SeO_x was, also, observed at 59 eV[46] in the selenium spectrum. From these observations, we believe we have successfully formed a Ni-Se compound in the form of $NiSe_2$ without forming any metal oxides, which was confirmed from XRD analysis.

Figures 4c and 4g show Ni 2p and Se 3d spectra for hydrothermally synthesized Ni_3Se_2. The XPS binding energy observed at 852.4 and 870.1eV, as shown in Fig. 2e, corresponds well to the Ni $2p_{3/2}$ and Ni $2p_{1/2}$, respectively, and the peak positions confirmed that it consists of only Ni^{2+}oxidation states.[29] In Figure 4g, the peak at 54.5 eV and 53.5eV is representative of the Se $3d_{3/2}$ and $3d_{5/2}$ binding energy, indicating $^{-2}$ valence state of Se.

In Figures 4d and h are the spectra of Ni 2p and Se 3d of Ni_3Se_4. The oxidation states of Ni and Se prove the formation Ni_3Se_4 which would have Ni^{2+} and Ni^{3+} ions with Se^{2-}. The low-intensity peaks located at a lower binding energy of Ni $2p_{3/2}$ and $2p_{1/2}$ at 852.9 eV and 870.7 eV are due to the Ni^{2+} and high-intensity peaks at 856.2eV and 873.8eV are attributed to the Ni^{3+} ion $2p_{3/2}$ and $2p_{1/2}$ from the Ni 2p spectra.[50] Figure 4h shows the Se 3d spectra and its Se $3d_{3/2}$ and $3d_{5/2}$ binding energy, indicating -2 valence state of Se, and surface oxidation of SeO_x was observed around 59 eV in the selenium spectrum.[50]

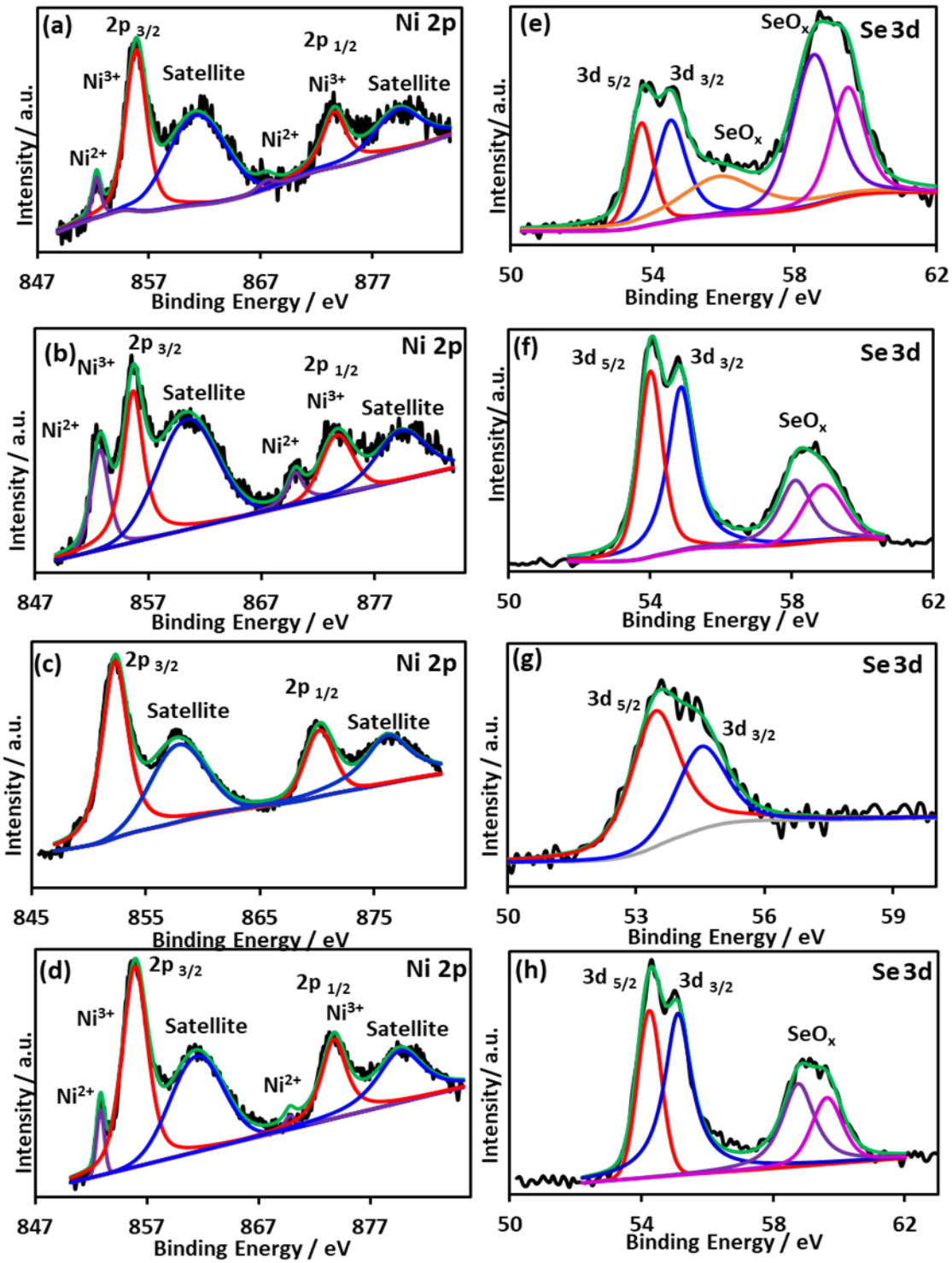

Figure 4. XPS spectra of nickel selenides. The catalysts showing the Ni 2p peaks of (a) NiSe, (b) $NiSe_2$, (c)Ni_3Se_2 and (d) Ni_3Se_4 ; Se 3d peaks of (e) NiSe, (f) $NiSe_2$, (g)Ni_3Se_2 and (h) Ni_3Se_4.

Figure S5 shows the O 1s spectra of all four nickel selenides samples. Among them, NiSe and Ni_3Se_4 spectra (Figures S5 (a) and (d) respectively) show surface oxygen peaks around 530-531 eV.[29,32] The peak at 533 eV in Figures S5 (b) and (c) was attributed to nafion oxygen which is C-O-C.[51]

3.2. ELECTROCHEMICAL CHARACTERIZATION

The electrocatalytic activity of the hydrothermally synthesized nickel selenide catalysts was examined through detailed electrochemical studies in 1.0 M KOH. The electrochemically active surface areas (ECSA) of the catalysts were calculated by measuring the electrochemical capacitance of the electrode-electrolyte interface in the non-faradic double-layer region of the cyclic voltammograms. Using N_2-saturated 1.0 M KOH, the electrode was scanned from -0.25 to -0.10 V vs. Ag/AgCl at scan rates between 5 and 40 mVs^{-1} for $NiSe_2$ given in Figure 5. The cathodic and anodic current was measured at -0.15 V vs. Ag|AgCl (Figure 5a) and plotted as a function of scan rates (Figure 4b). The average of the anodic and cathodic slopes, C_{DL}, was obtained and ECSA was calculated using equation 5. It was observed that the electrodeposited $NiSe_2$ had a moderate ECSA value of 32.2 cm^2. Roughness factor was calculated using ECSA and the geometric area of the electrode. The comparatively high roughness factor of the $NiSe_2$ (403.8) and the elongated rod morphology might be one of the factors responsible for high catalytic activity among four nickel selenides. The other three nickel selenides' (NiSe, Ni_3Se_2, and Ni_3Se_4) ECSA graphs are shown in Figure S6 (a), (c) and (e) respectively. The comparison of electrochemically active surface area and roughness factor is given in Table 2. Comparatively, Ni_3Se_4 shows the highest ECSA value among

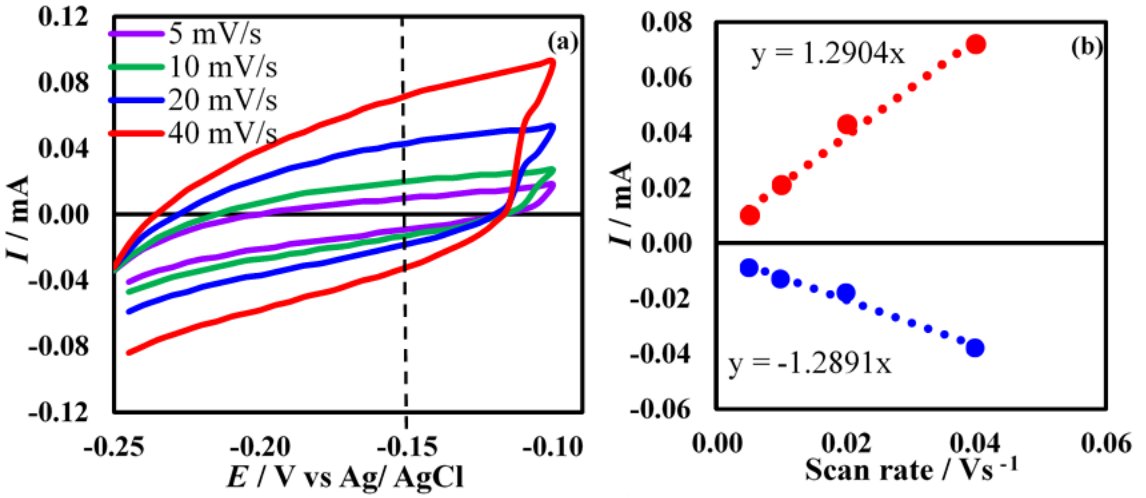

Figure 5. Cyclic voltammograms measured for the $NiSe_2$ catalyst. (a) in N_2 saturated 1.0 M KOH solution at different scan rates from 5 to 40 mV s^{-1}. (b) Plot of anodic and cathodic currents measured at −0.15 V as a function of scan rate.

all four nickel selenides and this was confirmed by its morphology which was the spongy ball like morphology consisting of flakey geometry. Ni_3Se_4 also has a higher roughness factor which further confirmed that higher surface area composes in a small volume. Also, NiSe, relatively, shows a higher roughness factor and ECSA value among other nickel selenides which might be the reason NiSe shows better catalytic activity. Ni_3Se_2 shows lower ECSA value that was further confirmed by its morphology which shows triangular shapes masses. We have tested the oxygen evolution activity of hydrothermally synthesized nickel selenides of NiSe, $NiSe_2$, Ni_3Se_2, and Ni_3Se_4 electrocatalysts by preparing electrodes using drop casting on carbon cloth (CC) and testing electrochemical activity in nitrogen saturated 1.0M KOH electrolyte solution. A scan rate of 10 mV s^{-1} was used in LSV measurements with a three-electrode system using an IviumStat potentiostat having Ag/AgCl as a reference electrode, Pt mesh as a counter electrode

Table 2. Comparison of nickel selenides electrochemically active surface area.

Catalyst	**ECSA / cm^2**	**RF**
NiSe	39.9	498.9
$NiSe_2$	32.3	403.8
Ni_3Se_2	15.1	188.8
Ni_3Se_4	45.4	567.5

and the as-prepared electrode as the working electrode. For the comparison purposes, bare carbon cloth and RuO_2 electrocatalyst were assessed. Figure 6(a) shows the linear sweep voltammetry polarization curves of oxygen evolution reactions. All the measured potentials with Ag/AgCl reference electrode were converted to the reversible hydrogen electrode (RHE) using equation 1. All the potentials are corrected by compensating for IR drop and current densities are given by considering the geometric area of the working electrode. It is seen that hydrothermally synthesized nickel selenides show much greater catalytic activity than the RuO_2 and the bare CC, indicating early onset, higher current density, and a lower overpotential at 10 mA cm^{-2}. The oxidation peak around 1.35V vs RHE was observed for $NiSe_2$ and Ni_3Se_2 while Ni_3Se_4 has an early onset at 1.33 V vs RHE, but NiSe does show an elongated oxidation peak after 1.36 V vs RHE. The oxidation peak is due to conversion of Ni^{2+} to Ni^{3+} during the oxygen evolution reaction which proved that surface Ni atoms partially oxidized into NiOOH on the surface of nickel selenide working electrodes. Interestingly, $NiSe_2$ shows an oxidation peak higher than other nickel selenide electrocatalysts and implies the formation of more active sites

(NiOOH) on the $NiSe_2$ surface.[52] All oxidations of nickel selenide electrocatalysts are reversible as shown in cyclic voltammograms of nickel selenides given in supporting information (Figure S7 a-d). The onset potentials, Tafel plots (Figure 6b), the overpotential at 10 mA cm^{-2} (Figure 6c), and current density at overpotential 300 mV (Figure 6d) were obtained from the reverse scan of cyclic voltammograms of nickel selenides as shown in Figure S7 a-d and also given in Table 3. All the nickel selenides in this experiment show an earlier onset potential than the RuO_2, which is 1.51 V vs RHE under the same experimental conditions. Similarly, the overpotential (η) required to achieve at 10 mA cm^{-2} for OER is also less for hydrothermally synthesized nickel selenides than the RuO_2. $NiSe_2$ requires 200 mV to achieve 10 mA cm^{-2} current density while RuO_2 needs 370 mV to achieve the same, which is 170 mV higher than $NiSe_2$. In addition, $NiSe_2$ shows the lowest overpotential at10 mA cm^{-2} of the nickel selenide electrocatalysts of NiSe, Ni_3Se_2, and Ni_3Se_4. Comparison of this data is summarized in Table 3. Oxygen evolution reaction's kinetics was examined by analyzing the Tafel slopes of the electrocatalytic reactions, as shown in Figure 6b, which was acquired by leaner sweep voltammetry carried out with the catalysts at a slow scan speed (2 mV s^{-1}) in a non-stirred 1.0 M KOH solution. The calculated Tafel value for $NiSe_2$ was 55.2 / mV dec^{-1}, which was the lowest value among the other nickel selenides, and that assumes two-electron transfer reaction is the rate-limiting reaction. Tafel slope for RuO_2 was 114.4 mV dec^{-1} and it is a single-electron transfer rate-limiting reaction. As mentioned in Table 3, the lower Tafel slopes of the nickel selenides confirm observed enhanced kinetics and higher catalytic activity than RuO_2. $NiSe_2$ also shows the highest current

density at η 300 mV, which is more than four times the current density than other nickel selenides and it is more than sixty times higher than the RuO_2 standard catalyst.[53]

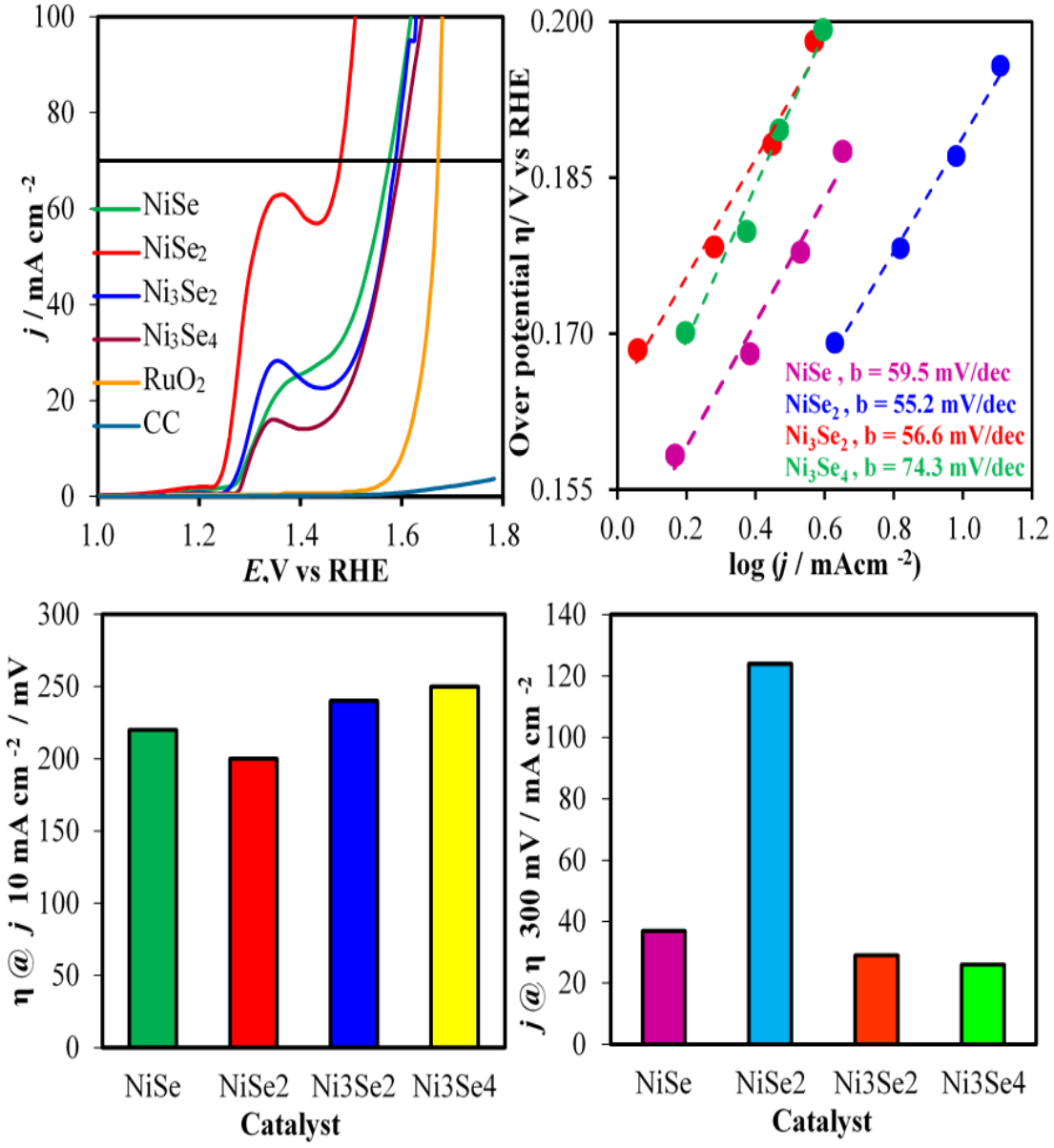

Figure 6. LSVs and tafel plots of nickel selenides. (a) LSV curves of NiSe, $NiSe_2$, Ni_3Se_2 and Ni_3Se_4 ,(b) Tafel plots (c) overpotential at current density 10 mA cm^{-2} (d) current density at overpotential 300 mV.

3.3. ELECTROCHEMICAL STABILITY

The electrochemical stability of the catalyst is another crucial parameter for the oxygen evolution process which can be measured by chronoamperometry for a long duration under a continuous electrochemical reaction. We have evaluated the long-term stability of nickel selenide working electrodes with chronoamperometry at 10 mA cm^{-2} in a 1.0 M KOH electrolyte solution. It was observed that O_2 bubbles were forming on the working nickel selenide electrode surfaces, and, therefore, the electrolyte solution was stirred continuously during the experiment to remove the O_2 bubbles generated on the catalyst surface to help the reaction continue without disturbances. Figure 7a shows a 12 h continuous stability plot and its leaner sweep voltammetry curves, given in Figures 7 b-e, show the behavior of the catalyst before and after the chronoamperometry test for NiSe, $NiSe_2$, Ni_3Se_2, and Ni_3Se_4, respectively. It was seen that there is no overpotential difference between before and after the chronoamperometry test at 10 mA cm^{-2} for the 12h duration. It was observed that LSV curves before and after catalytic activity were perfectly superimposable. Similarly, the stability and corresponding LSV curves of the other nickel selenides before and after the test are shown in Figure 7. It should be noted that these nickel selenides were very stable under the experimental conditions and no degradation of the current density was seen during long-term stability tests. Figure S8 shows the comparison of four nickel selenide XRDs before and after 12h chronoamperometry. The intensity of all nickel selenide XRD peaks is lower than the powdered XRD samples shown in Figure 1 because these samples consisted of catalyst and nafion binder. There is no difference observed in before and after XRD spectra. That means these catalysts even when exposed for a certain period to OER its crystalline

properties have no change. It further confirmed that nickel selenides exist as a catalyst after chronoamperometry. Figure S9 shows the deconvoluted Ni2p, Se3d and O1s XPS spectra for four nickel selenides after chronoamperometry for 12h. There is no difference before and after chronoamperometry for all Ni2p spectra. This condition is seen in Se 3d spectra. NiSe and Ni_3Se_4 catalysts' O1s spectra have a surface oxygen peak around 530-531eV [29,32] and Ni_3Se_2 and $NiSe_2$ catalysts show nafion C-O-C bond in O1s spectrum at 533 eV.[51] In contrast, $NiSe_2$ catalysts show the physisorbed and chemisorbed water around 535 eV.[32] These XPS spectrum further confirmed the catalyst is still nickel selenide after 12h chronoamperometry.

Table 3. Comparison of nickel selenides'electrocatalytic parameters for oxygen evolution reaction.

Catalyst	**Total loading / mg**	**Loading area / mg cm^{-2}**	**Onset potential / V**	**η @ 10 mA cm^{-2} / mV**	**Tafel slope / mV dec^{-1}**	**η @70 mA cm^{-2}/ mV**	**j @ η 300 mV / mA cm^{-2}**	**TOF @300 mV/ s^{-1}**
NiSe	0.4	5	1.37	220	59.5	350	37	0.0026
$NiSe_2$	0.4	5	1.38	200	55.2	250	124	0.0137
Ni_3Se_2	0.4	5	1.39	240	56.6	360	29	0.0016
Ni_3Se_4	0.4	5	1.38	250	74.3	370	26	0.0021
RuO_2	-	-	1.51	370	114.4	440	2	-

Table 4. Comparison of the electrocatalytic activity of nickel selenide electrocatalysts with reported nickel catalysts in literature.

Catalysts	Electrolytes	Onset potential V	η @ 10 mA cm^{-2} (mV *vs* RHE)	Reference
NiO_x particles[b]	1.0 M KOH	1.52*	331	21
NiO_x/C	1.0 M KOH	1.51*	335	54
Amorphous NiO	1.0 M KOH	1.54*	>470 [a]	55
α-$Ni(OH)_2$	0.1M KOH	1.54*	331	20
$Ni(OH)_2$ /NiOOH	1.0 M KOH	1.80*	525	56
$Ni(OH)_2$ particles[b]	1.0 M KOH	1.48*	299	21
Ni_3S_2–Ni foam	1.0M NaOH	1.46*	260	57
Ni_3S_2–Ni foam	0.1M KOH	1.387	187	58
NiS/ Ni foam	1.0 M KOH	1.55	158[a]	59
Ni_3Se_2–NF	1.0 M KOH	1.48*	270 [a]	35
NiSe nanowires		1.49*	270[a]	
Ni_3Se_2/Cu foam	1.0 M KOH	1.51	343 [b]	60
$NiSe_2$ /Ti	1.0 M KOH	1.53*	295 [a]	33
$NiSe_2$ nanosheets	1.0 MKOH	1.55	323	50
$NiSe_2$ /Ti	1.0 M KOH	1.53*	320 [c]	61
$NiSe_2$-DO	1.0 M KOH	1.46*	241	62
$Ni_{0.85}Se$/ Graphite	1.0 M NaOH	1.55*	302	34
$NiSe_2$	1.0 M KOH	1.43	250	2
Ni_3Se_2– Au Glass	0.3 M KOH	1.45	320 ±20	29
Ni_3Se_2– Ni foam		1.46	270 ± 20	
Ni_3Se_2 @Au	1.0 M NaOH	1.39	190	30
$Ni^{II}Se_4$/CFP	1.0 M KOH	1.40	200	31
Ni_3Se_4 assemblies	1.0 M KOH	1.47*	244[b]	63
$NiSe_2$– Au Glass	1.0 M KOH	1.36	140	32
$NiSe_2$ / CFP		1.38	220	
Ni_3Se_2 / NF	1.0 M KOH	1.52*	315[c]	36
NG/$NiSe_2$ pyramids/NF	0.1 M KOH	1.45*	307[a]	64
Ni_3Se_2 nano/NF	1.0 M KOH	1.48*	353 [c]	65
NiSe nanowire/Ni	1.0 M KOH	1.51*	300	66
$Ni_{1-y}Se$	1.0 M KOH	1.57*	355	67
NiSe / CC	1.0 M KOH	1.37	220	This work
$NiSe_2$ / CC		1.38	200	
Ni_3Se_2/ CC		1.39	240	
Ni_3Se_4/ CC		1.38	250	
* Calculated from references, [a] @ 20 $mAcm^{-2}$, [b] @ 50 $mAcm^{-2}$, [c] @ 100 $mAcm^{-2}$				

4. CONCLUSION

In this article, we have reported the OER electrocatalytic activity of a series of nickel selenide nanostructures, NiSe, $NiSe_2$, Ni_3Se_2 and Ni_3Se_4 for oxygen evolution reaction in alkaline medium. These nickel selenide nanostructures were synthesized through hydrothermal techniques. The as-prepared samples exhibited showed excellent catalytic activity and durability for OER process in the alkaline electrolyte. The early onset potentials, low overpotential at 10 mA cm^{-2} and the high current density of these nanostructured nickel selenides make them efficient electrocatalysts for oxygen evolution reaction in water splitting. The comparison of these nanostructured catalysts to other nickel-based OER catalysts reported till date (Table 4), reveals that these hydrothermally synthesized nickel selenides have outstanding performance as an electrocatalyst for OER. The exceptional catalytic activity and durability along with the simple synthesis process of nickel selenides offer a better path for use of earth abundant metal water oxidation electrocatalysts.

ACKNOWLEDGEMENT

This research was supported from the National Science Foundation (DMR 1710313), the American Chemical Society Petroleum Research Fund (54793-ND10), and ERDC (Missouri S&T).

SUPPLEMENTARY INFORMATION

1. EXPERIMENTAL PROCEDURE

1.1. ELECTRODEPOSITION OF RuO_2 ON AU-GLASS. [S1]

Electrodeposition of RuO_2 on Au-glass substrate was carried out from a mixture of $RuCl_3$ (0.452 g) and KCl (2.952 g) in 40 ml of 0.01M HCl by using cyclic voltammetry from 0.015 to 0.915 V (vs. Ag|AgCl) for 100 cycles at a scan rate of 50 mV s^{-1} . Then it was heated at 200 ^oC for 3 h in presence of Air.

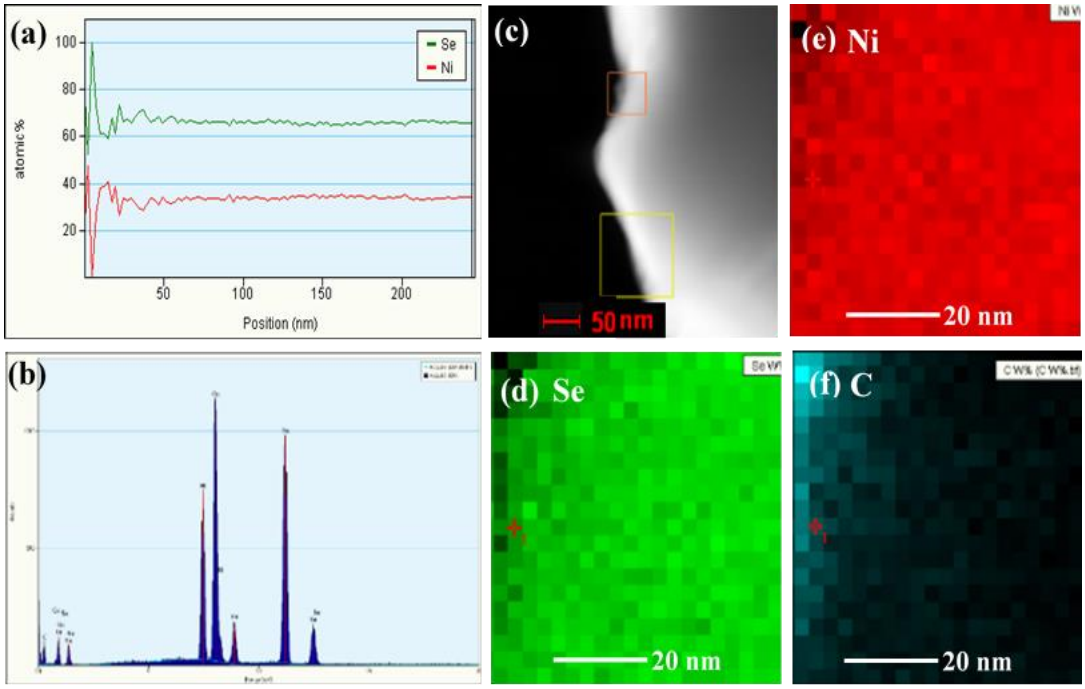

Figure S1. STEM images of NiSe (a) EDX atomic ratio (b) EDX element spectra (c) Drift collected spectrum image for element mapping (d) Se (e) Ni (f) C.

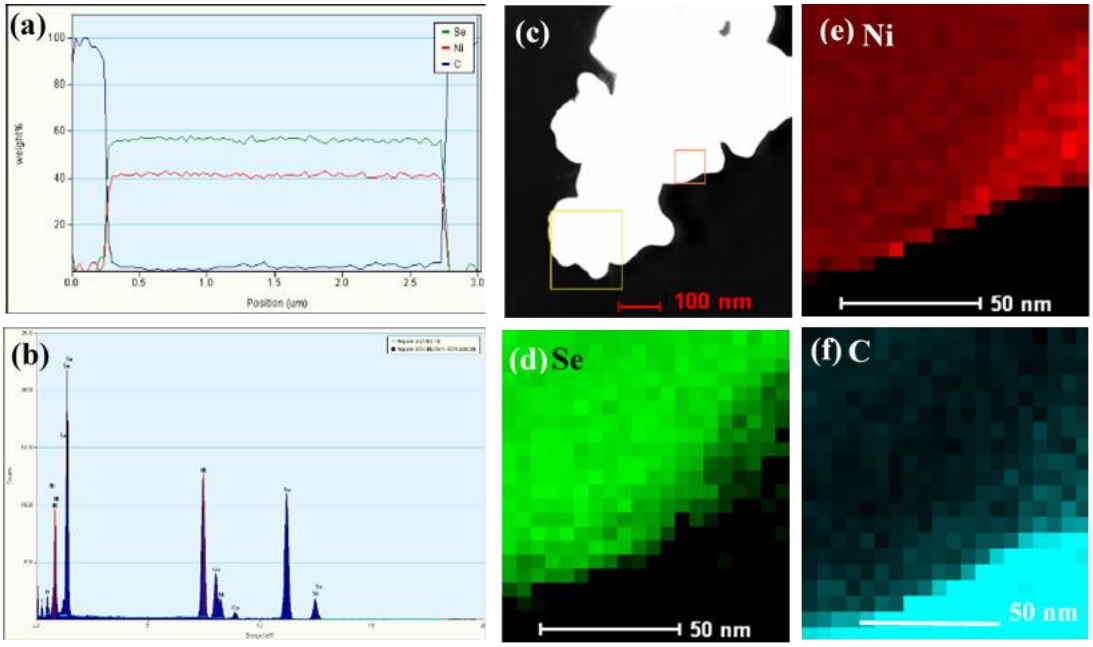

Figure S2. STEM of $NiSe_2$ (a) EDX atomic ratio (b) EDX element spectra (c) Drift collected spectrum image for element mapping (d) Se (e) Ni (f) C.

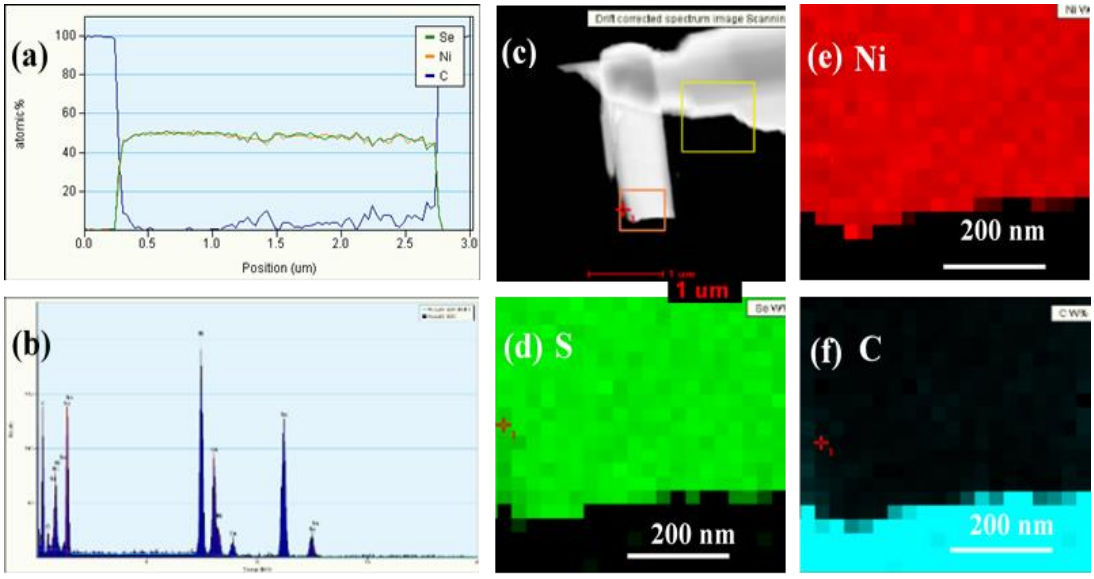

Figure S3. STEM of Ni_3Se_2 (a) EDX atomic ratio (b) EDX element spectra (c) Drift collected spectrum image for element mapping (d) Se (e) Ni (f) C.

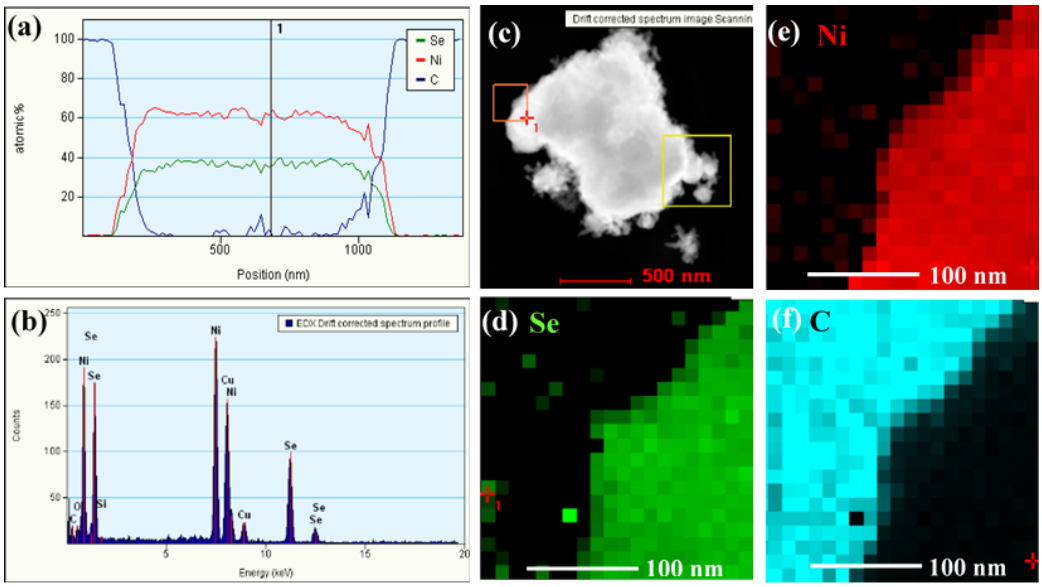

Figure S4. STEM of Ni_3Se_4 (a) EDX atomic ratio (b) EDX element spectra (c) Drift collected spectrum image for element mapping (d) Se (e) Ni (f) C.

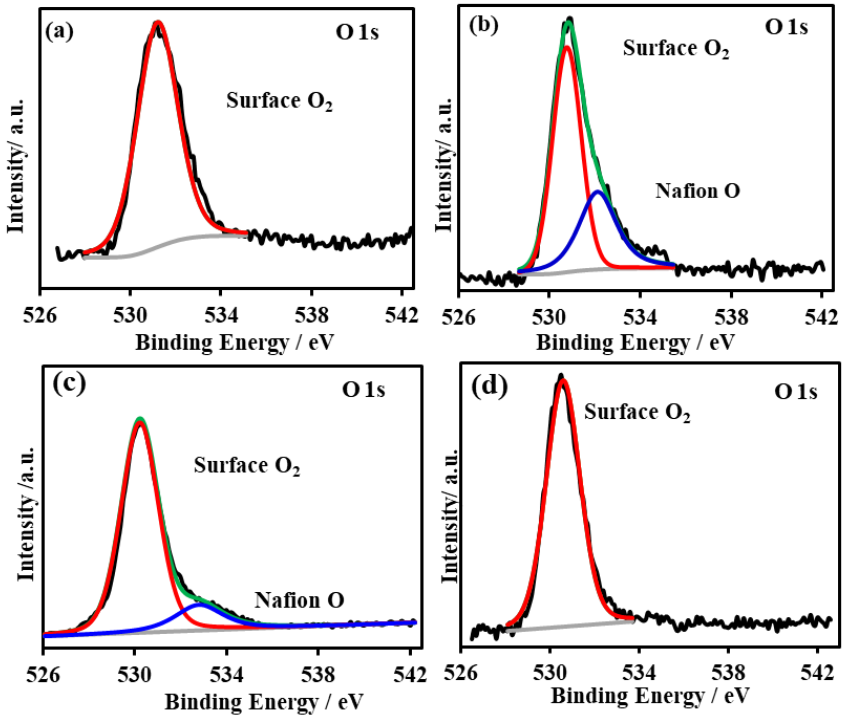

Figure S5. XPS spectra of the catalysts showing the O 1s peaks of (a) NiSe, (b) $NiSe_2$, (c) Ni_3Se_2 and (d) Ni_3Se_4.

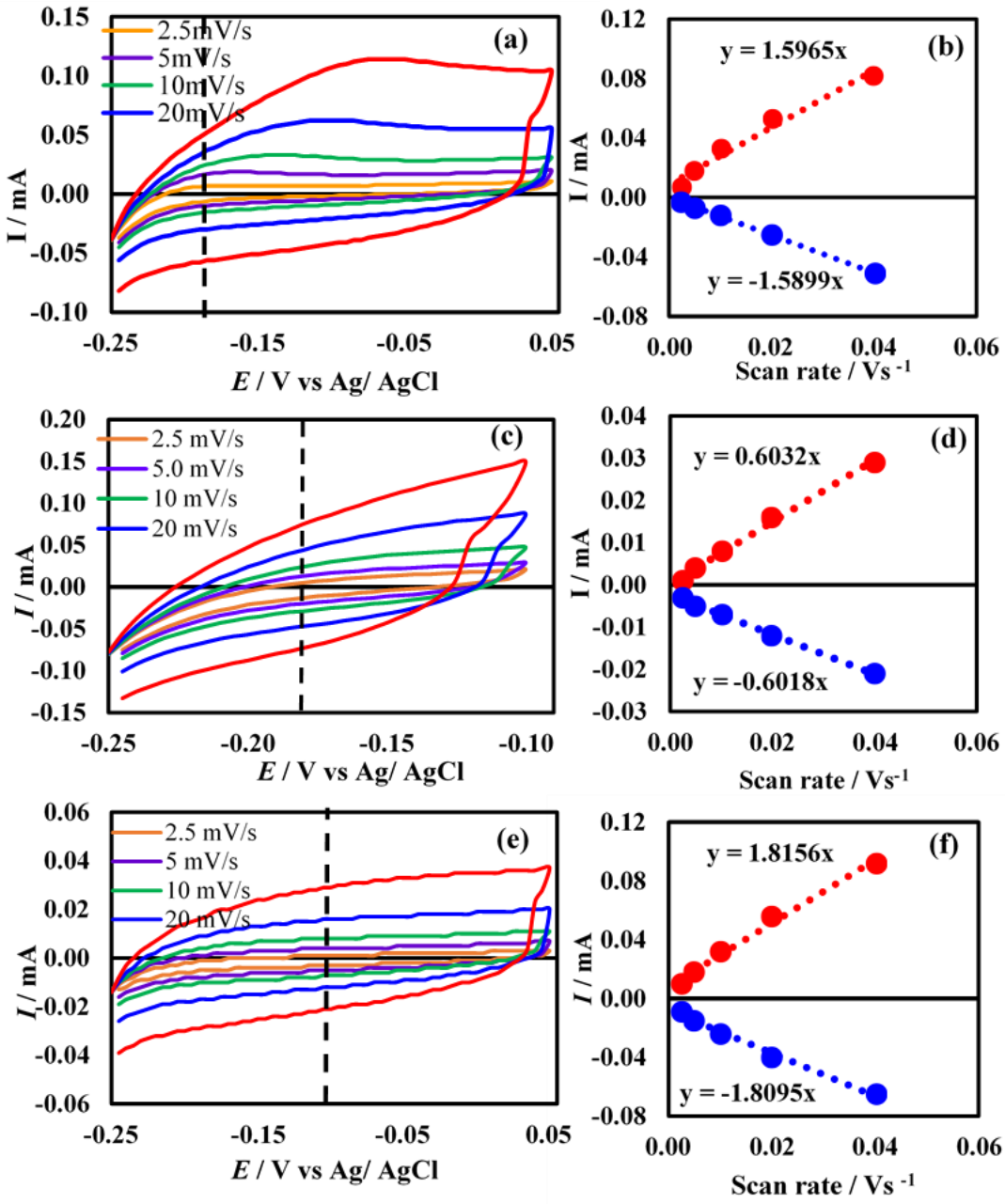

Figure S6. Cyclic voltammograms measured for the (a) NiSe (c) Ni_3Se_2 (e) Ni_3Se_2 catalysts in N_2 saturated 1.0 M KOH solution at different scan rates from 2.5 to 40 mV s^{-1}. Plot of anodic and cathodic currents measured at (b) -0.15 V for NiSe (d) -0.10 V for Ni_3Se_2 (f) -0.18 V for Ni_3Se_4 as a function of scan rate.

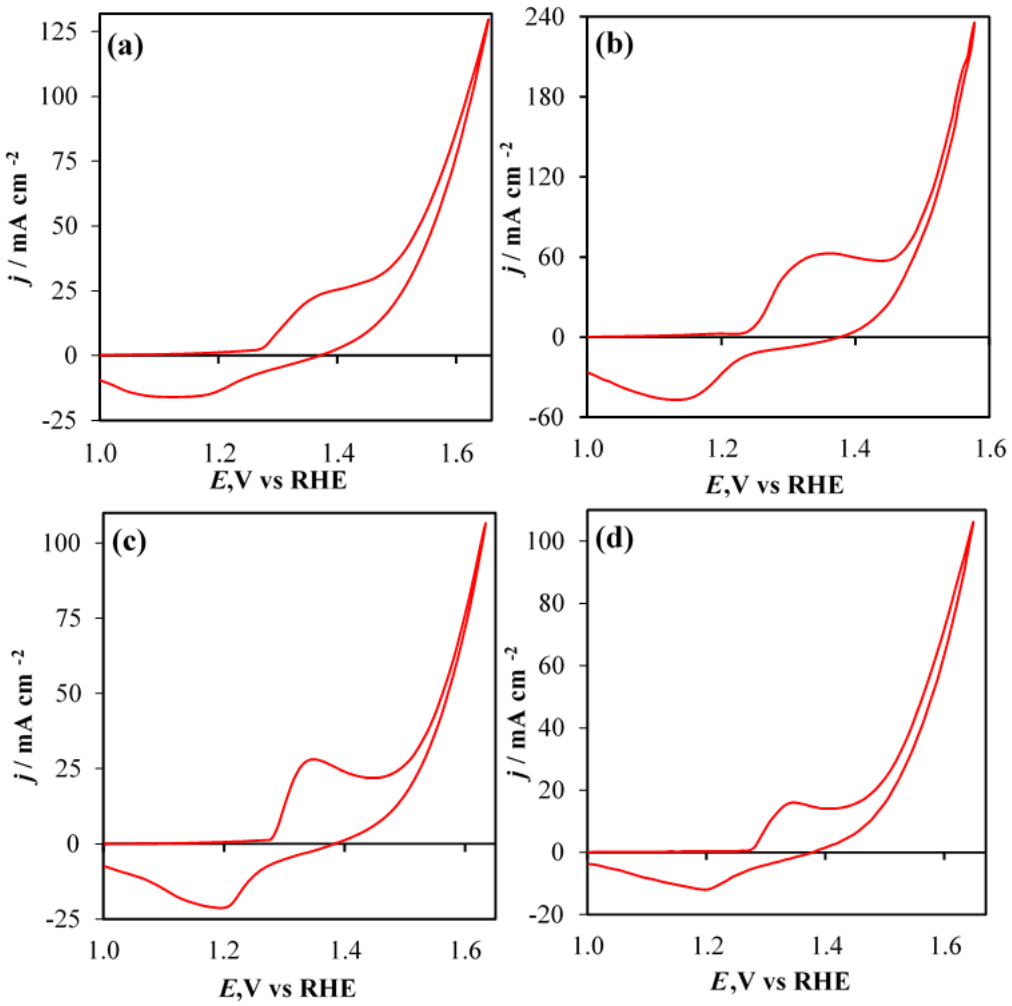

Figure S7. Cyclic voltammetry of nickel selenides (a) NiSe (b) $NiSe_2$ (c) Ni_3Se_2 (d) Ni_3Se_4.

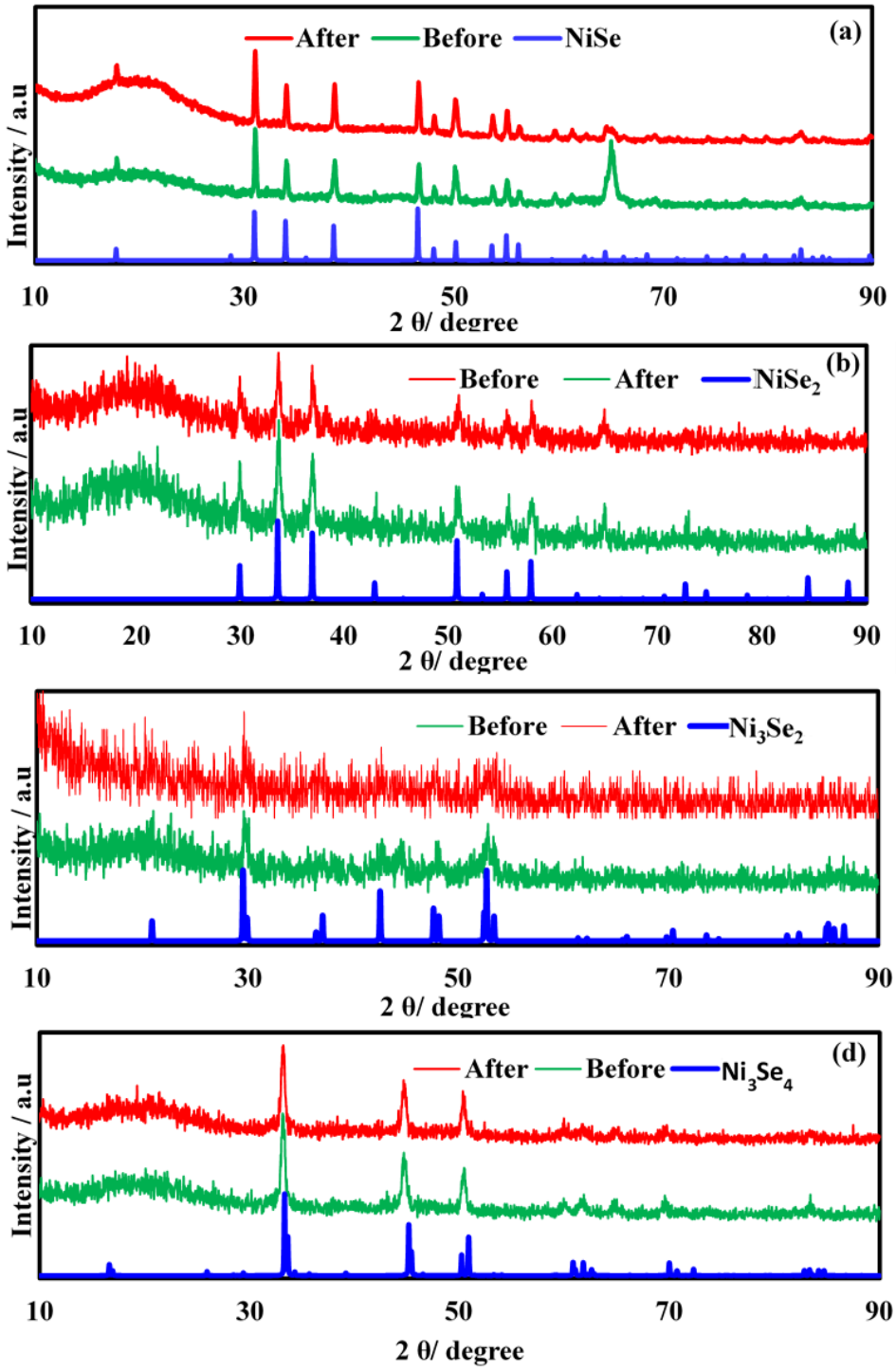

Figure S8. Comparison of XRD patterns of catalyst films after 12h of hronoamperometry and as prepared catalysts (a) NiSe (b) $NiSe_2$ (C) Ni_3Se_2 and (d) Ni_3Se_4

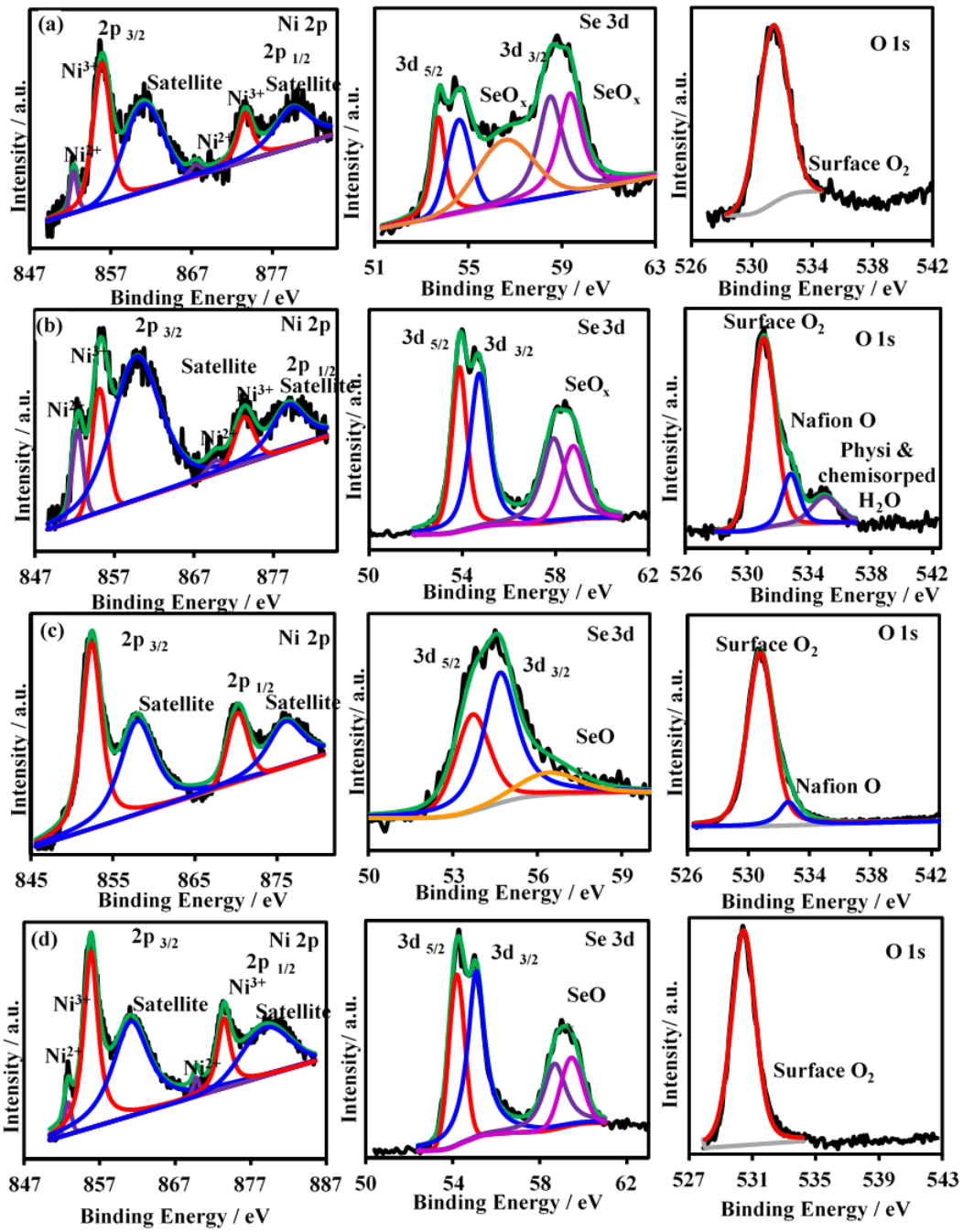

Figure S9. XPS spectra of Ni 2p, Se 3d and O 1s peaks obtained from the catalyst after chronoamperometry (a) NiSe, (b) $NiSe_2$, (c)Ni_3Se_2 and (d) Ni_3Se_4 respectively.

SUPPLEMENTARY INFORMATION REFERENCES

S1. Tsuji, E., Imanishi, A., Fukui, K.I. and Nakato, Y., 2011. Electrocatalytic activity of amorphous RuO2 electrode for oxygen evolution in an aqueous solution. *Electrochimica Acta*, *56*(5), pp.2009-2016.

REFERENCES

1. Simon, P., & Gogotsi, Y. (2008). Materials for electrochemical capacitors. *Nature materials*, *7*(11), 845-854.

2. Kwak, I.H., Im, H.S., Jang, D.M., Kim, Y.W., Park, K., Lim, Y.R., Cha, E.H. and Park, J., 2016. $CoSe_2$ and $NiSe_2$ nanocrystals as superior bifunctional catalysts for electrochemical and photoelectrochemical water splitting. *ACS applied materials & interfaces*, *8*(8), pp.5327-5334.

3. Gerken, J. B., McAlpin, J. G., Chen, J. Y., Rigsby, M. L., Casey, W. H., Britt, R. D., & Stahl, S. S. (2011). Electrochemical water oxidation with cobalt-based electrocatalysts from pH 0–14: the thermodynamic basis for catalyst structure, stability, and activity. *Journal of the American Chemical Society*, *133*(36), 14431-14442.

4. Suntivich, J., May, K. J., Gasteiger, H. A., Goodenough, J. B., & Shao-Horn, Y. (2011). A perovskite oxide optimized for oxygen evolution catalysis from molecular orbital principles. *Science*, *334*(6061), 1383-1385.

5. Dau, H., Limberg, C., Reier, T., Risch, M., Roggan, S. and Strasser, P., 2010. The mechanism of water oxidation: from electrolysis via homogeneous to biological catalysis. *ChemCatChem*, *2*(7), pp.724-761.

6. Koper, M. T. (2011). Thermodynamic theory of multi-electron transfer reactions: Implications for electrocatalysis. *Journal of electroanalytical chemistry*, *660*(2), 254-260.

7. Gong, M., Li, Y., Wang, H., Liang, Y., Wu, J.Z., Zhou, J., Wang, J., Regier, T., Wei, F. and Dai, H., 2013. An advanced Ni–Fe layered double hydroxide electrocatalyst for water oxidation. *Journal of the American Chemical Society*, *135*(23), pp.8452-8455.

8. Cheng, Y. and Jiang, S.P., 2015. Advances in electrocatalysts for oxygen evolution reaction of water electrolysis-from metal oxides to carbon nanotubes. *Progress in Natural Science: Materials International*, *25*(6), pp.545-553.

9. Yang, J., Shen, X., Ji, Z., & Zhu, G. (2013). Reduced graphene oxide/$CoSe_2$ nanocomposites: hydrothermal synthesis and their enhanced electrocatalytic activity. *Journal of Materials Science*, *48*(22), 7913-7919.

10. Xia, C., Jiang, Q., Zhao, C., Hedhili, M.N. and Alshareef, H.N., 2016. Selenide-Based Electrocatalysts and Scaffolds for Water Oxidation Applications. *Advanced Materials*, *28*(1), pp.77-85.

11. Umanga De Silva, W. P. R. Liyanage and Manashi Nath Magnetic Multifunctional Nanostructures as High-efciency Catalysts for Oxygen Evolution Reactions. *MRS Advances*, *1*(34), pp.2401-2407.

12. Gorlin, Y. and Jaramillo, T.F., 2010. A bifunctional nonprecious metal catalyst for oxygen reduction and water oxidation. *Journal of the American Chemical Society*, *132*(39), pp.13612-13614.

13. Song, F. and Hu, X., 2014. Exfoliation of layered double hydroxides for enhanced oxygen evolution catalysis. *Nature communications*, *5*(1), pp.1-9.

14. Rossmeisl, J., Qu, Z.W., Zhu, H., Kroes, G.J. and Nørskov, J.K., 2007. Electrolysis of water on oxide surfaces. *Journal of Electroanalytical Chemistry*, *607*(1), pp.83-89.

15. Lee, Y., Suntivich, J., May, K.J., Perry, E.E. and Shao-Horn, Y., 2012. Synthesis and activities of rutile IrO_2 and RuO_2 nanoparticles for oxygen evolution in acid and alkaline solutions. *The journal of physical chemistry letters*, *3*(3), pp.399-404.

16. Thomsen, J.M., Huang, D.L., Crabtree, R.H. and Brudvig, G.W., 2015. Iridium-based complexes for water oxidation. *Dalton Transactions*, *44*(28), pp.12452-12472.

17. Zhang, W., Hui, Z., Cheng, Y., Zhang, L., Xie, Y. and Qian, Y., 2000. A hydrothermal method for low-temperature growth of nanocrystalline pyrite nickel diselenide. *Journal of crystal growth*, *209*(1), pp.213-216.

18. McCrory, C.C., Jung, S., Ferrer, I.M., Chatman, S.M., Peters, J.C. and Jaramillo, T.F., 2015. Benchmarking hydrogen evolving reaction and oxygen evolving reaction electrocatalysts for solar water splitting devices. *Journal of the American Chemical Society*, *137*(13), pp.4347-4357.

19. Kauffman, D.R., Alfonso, D., Tafen, D.N., Lekse, J., Wang, C., Deng, X., Lee, J., Jang, H., Lee, J.S., Kumar, S. and Matranga, C., 2016. Electrocatalytic Oxygen Evolution with an Atomically Precise Nickel Catalyst. *ACS Catalysis*, *6*(2), pp.1225-1234.

20. Gao, M., Sheng, W., Zhuang, Z., Fang, Q., Gu, S., Jiang, J. and Yan, Y., 2014. Efficient water oxidation using nanostructured α-nickel-hydroxide as an electrocatalyst. *Journal of the American Chemical Society*, *136*(19), pp.7077-7084.

21. Stern, L.A. and Hu, X., 2015. Enhanced oxygen evolution activity by NiOx and $Ni(OH)_2$ nanoparticles. *Faraday discussions*, *176*, pp.363-379.

22. Qi, J., Zhang, W., Xiang, R., Liu, K., Wang, H.Y., Chen, M., Han, Y. and Cao, R., 2015. Porous nickel–iron oxide as a highly efficient electrocatalyst for oxygen evolution reaction. *Advanced Science*, *2*(10),1500199.

23. Lu, X. and Zhao, C., 2015. Electrodeposition of hierarchically structured three-dimensional nickel–iron electrodes for efficient oxygen evolution at high current densities. *Nature communications*, *6*(1), pp.1-7.

24. Rossmeisl, J., Logadottir, A. and Nørskov, J.K., 2005. Electrolysis of water on (oxidized) metal surfaces. *Chemical physics*, *319*(1), pp.178-184.

25. Hansen, H.A., Rossmeisl, J. and Nørskov, J.K., 2008. Surface Pourbaix diagrams and oxygen reduction activity of Pt, Ag and Ni (111) surfaces studied by DFT. *Physical Chemistry Chemical Physics*, *10*(25), pp.3722-3730.

26. Liu, X., Zhang, N., Yi, R., Qiu, G., Yan, A., Wu, H., Meng, D. and Tang, M., 2007. Hydrothermal synthesis and characterization of sea urchin-like nickel and cobalt selenides nanocrystals. *Materials Science and Engineering: B*, *140*(1), pp.38-43.

27. Sobhani, A. and Salavati-Niasari, M., 2014. Synthesis and characterization of a nickel selenide series via a hydrothermal process. *Superlattices and Microstructures*, *65*, pp.79-90.

28. Hong, W.T., Risch, M., Stoerzinger, K.A., Grimaud, A., Suntivich, J. and Shao-Horn, Y., 2015. Toward the rational design of non-precious transition metal oxides for oxygen electrocatalysis. *Energy & Environmental Science*,*8*(5), pp.1404-1427.

29. Swesi, A.T., Masud, J. and Nath, M., 2016. Nickel selenide as a high-efficiency catalyst for oxygen evolution reaction. *Energy & Environmental Science*, *9*(5), pp.1771-1782.

30. Swesi, A.T.; Masud, J. & Nath, M. Enhancing electrocatalytic activity of bifunctional Ni_3Se_2 for overall water splitting through etching-induced surface nanostructuring. *J. Mater. Res.* , 31, 2888-28961, (2016).

31. Masud, J.; Ioannou, P.C.; Levesanos, N.; Kyritsis, P. & Nath, M. A Molecular Ni-complex Containing Tetrahedral Nickel Selenide Core as Highly Efficient Electrocatalyst for Water Oxidation. *Chem.Sus.Chem*. **9**, 3128-3132 (2016).

32. Swesi, A.T., Masud, J., Liyanage, W.P., Umapathi, S., Bohannan, E., Medvedeva, J. and Nath, M., 2017. Textured $NiSe_2$ Film: Bifunctional Electrocatalyst for Full Water Splitting at Remarkably Low Overpotential with High Energy Efficiency. *Scientific Reports*, *7*(1), p.2401.

33. Pu, Z., Luo, Y., Asiri, A.M. and Sun, X., 2016. Efficient electrochemical water splitting catalyzed by electrodeposited nickel diselenide nanoparticles based film. *ACS applied materials & interfaces*, *8*(7), pp.4718-4723.

34. Wu, X., He, D., Zhang, H., Li, H., Li, Z., Yang, B., Lin, Z., Lei, L. and Zhang, X., 2016. $Ni_{0.85}$ Se as an efficient non-noble bifunctional electrocatalyst for full water splitting. *International Journal of Hydrogen Energy*. *41*(25), pp.10688-10694.

35. Tang, C., Cheng, N., Pu, Z., Xing, W. and Sun, X., 2015. NiSe nanowire film supported on nickel foam: an efficient and stable 3D bifunctional electrode for full water splitting. *Angewandte Chemie*, *127*(32), pp.9483-9487.

36. Sivanantham, A. and Shanmugam, S., 2017. Nickel selenide supported on nickel foam as an efficient and durable non-precious electrocatalyst for the alkaline water electrolysis. *Applied Catalysis B: Environmental*, *203*, pp.485-493.

37. Moloto, N., Moloto, M.J., Coville, N.J. and Ray, S.S., 2009. Optical and structural characterization of nickel selenide nanoparticles synthesized by simple methods. *Journal of Crystal Growth*, *311*(15), pp.3924-3932.

38. Kukunuri, S., Krishnan, M.R. and Sampath, S., 2015. The effect of structural dimensionality on the electrocatalytic properties of the nickel selenide phase. *Physical Chemistry Chemical Physics*, *17*(36), pp.23448-23459.

39. McCrory, C.C., Jung, S., Peters, J.C. and Jaramillo, T.F., 2013. Benchmarking heterogeneous electrocatalysts for the oxygen evolution reaction. *Journal of the American Chemical Society*, *135*(45), pp.16977-16987.

40. Patterson, A.L The Scherrer formula for X-ray particle size determination. *Phys. Rev.* **56**, 978 (1939).

41. Frederick Gronvold and Einar Jacobsen, X-ray and magnetic study of nickel selenide in the range of NiSe and $NiSe_2$, Acta Chemica Scandinavica, 1956,10, 140-1456.

42. Yu, J., Li, Q., Xu, C.Y., Chen, N., Li, Y., Liu, H., Zhen, L., Dravid, V.P. and Wu, J.,2017. $NiSe_2$ pyramids deposited on N-doped graphene encapsulated Ni foam for high-performance water oxidation. *Journal of Materials Chemistry A*, *5*(8), pp.3981-3986.

43. Zhuang, Z., Peng, Q., Zhuang, J., Wang, X. and Li, Y., 2006. Controlled hydrothermal synthesis and structural characterization of a nickel selenide series. *Chemistry–A European Journal*, *12*(1), pp.211-217.

44. Sobhani, A., Davar, F. and Salavati-Niasari, M., 2011. Synthesis and characterization of hexagonal nano-sized nickel selenide by simple hydrothermal method assisted by CTAB. *Applied Surface Science*, *257*(18), pp.7982-7987.

45. Zheng, X., Han, X., Liu, H., Chen, J., Fu, D., Wang, J., Zhong, C., Deng, Y. and Hu, W., 2018. Controllable Synthesis of $Ni_xSe_{(0.5\leq x\leq 1)}$ Nanocrystals for Efficient Rechargeable Zinc–Air Batteries and Water Splitting. *ACS applied materials & interfaces*, *10*(16), pp.13675-13684.

46. Umapathi, S., Masud, J., Swesi, A.T. and Nath, M., 2017. $FeNi_2Se_4$–Reduced Graphene Oxide Nanocomposite: Enhancing Bifunctional Electrocatalytic Activity for Oxygen Evolution and Reduction through Synergistic Effects. *Advanced Sustainable Systems*, *1*(10), p.1700086.

47. GolrokháAmin, B., 2017. $CoNi_2Se_4$ as an efficient bifunctional electrocatalyst for overall water splitting. *Chemical Communications*, *53*(39), pp.5412-5415.

48. Du, Y., Cheng, G. and Luo, W., 2017. Colloidal synthesis of urchin-like Fe doped $NiSe_2$ for efficient oxygen evolution. *Nanoscale*, *9*(20), pp.6821-6825.

49. Boscher, N.D., Carmalt, C.J. and Parkin, I.P., 2006. Atmospheric pressure chemical vapor deposition of WSe_2 thin films on glass—highly hydrophobic sticky surfaces. *Journal of Materials Chemistry*, *16*(1), pp.122-127.

50. Wang, Z., Li, J., Tian, X., Wang, X., Yu, Y., Owusu, K.A., He, L. and Mai, L., 2016. Porous nickel–iron selenide nanosheets as highly efficient electrocatalysts for oxygen evolution reaction. *ACS applied materials & interfaces*, *8*(30), pp.19386-19392.

51. Loeian, M.S., Ziolkowska, D.A., Khosravi, F., Jasinski, J.B. and Panchapakesan, B., 2017. Exfoliated WS 2-Nafion Composite based Electromechanical Actuators. *Scientific reports*, *7*(1), p.14599.

52. Fang, W., Liu, D., Lu, Q., Sun, X. and Asiri, A.M., 2016. Nickel promoted cobalt disulfide nanowire array supported on carbon cloth: an efficient and stable bifunctional electrocatalyst for full water splitting. *Electrochemistry Communications*, *63*, pp.60-64.

53. Gao, M.R., Cao, X., Gao, Q., Xu, Y.F., Zheng, Y.R., Jiang, J. and Yu, S.H., 2014. Nitrogen-doped graphene supported $CoSe_2$ nanobelt composite catalyst for efficient water oxidation. *Acs Nano*, *8*(4), pp.3970-3978.

54. Qiu, Y., Xin, L. and Li, W., 2014. Electrocatalytic oxygen evolution over supported small amorphous Ni–Fe nanoparticles in alkaline electrolyte. *Langmuir*, *30*(26), pp.7893-7901.

55. Kuai, L., Geng, J., Chen, C., Kan, E., Liu, Y., Wang, Q. and Geng, B., 2014. A Reliable Aerosol-Spray-Assisted Approach to Produce and Optimize Amorphous Metal Oxide Catalysts for Electrochemical Water Splitting. *Angewandte Chemie*, *126*(29), pp.7677-7681.

56. Klaus, S., Cai, Y., Louie, M.W., Trotochaud, L. and Bell, A.T., 2015. Effects of Fe electrolyte impurities on $Ni(OH)_2$/NiOOH structure and oxygen evolution activity. *The Journal of Physical Chemistry C*, *119*(13), pp.7243-7254.

57. Feng, L.L., Yu, G., Wu, Y., Li, G.D., Li, H., Sun, Y., Asefa, T., Chen, W. and Zou, X., 2015. High-index faceted Ni_3S_2 nanosheet arrays as highly active and ultrastable electrocatalysts for water splitting. *J. Am. Chem. Soc*, *137*(44), pp.14023-14026.

58. Zhou, W., Wu, X.J., Cao, X., Huang, X., Tan, C., Tian, J., Liu, H., Wang, J. and Zhang, H., 2013. Ni_3S_2 nanorods/Ni foam composite electrode with low overpotential for electrocatalytic oxygen evolution. *Energy & Environmental Science*, *6*(10), pp.2921-2924.

59. Zhu, W., Yue, X., Zhang, W., Yu, S., Zhang, Y., Wang, J. and Wang, J., 2016. Nickel sulfide microsphere film on Ni foam as an efficient bifunctional electrocatalyst for overall water splitting. *Chemical Communications*, *52*(7), pp.1486-1489.

60. Shi, J., Hu, J., Luo, Y., Sun, X. and Asiri, A.M., 2015. Ni 3 Se 2 film as a non-precious metal bifunctional electrocatalyst for efficient water splitting. *Catalysis Science & Technology*, *5*(11), pp.4954-4958.

61. Liu, T., Asiri, A.M. and Sun, X., 2016. Electrodeposited Co-doped $NiSe_2$ nanoparticles film: a good electrocatalyst for efficient water splitting. *Nanoscale*, *8*(7), pp.3911-3915.

62. Xu, X., Song, F. and Hu, X., 2016. A nickel iron diselenide-derived efficient oxygen-evolution catalyst. *Nature communications*, *7* (1), pp.1-7.

63. S. Anantharaj, J. Kennedy, S. Kundu, 2017, Microwave-Initiated Facile Formation of Ni_3Se_4 Nanoassemblies for Enhanced and Stable Water Splitting in Neutral and Alkaline Media. *ACS Appl. Mater. Inter.* 9, pp. 8714-8728.

64. Yu, J., Li, Q., Xu, C.Y., Chen, N., Li, Y., Liu, H., Zhen, L., Dravid, V.P. and Wu, J., 2017. $NiSe_2$ pyramids deposited on N-doped graphene encapsulated Ni foam for high-performance water oxidation. *Journal of Materials Chemistry A*, *5*(8), pp.3981-3986.

65. Xu, R., Wu, R., Shi, Y., Zhang, J. and Zhang, B., 2016. Ni_3Se_2 nanoforest/Ni foam as a hydrophilic, metallic, and self-supported bifunctional electrocatalyst for both H_2 and O_2 generations. *Nano Energy*, *24*, pp.103-110.

66. Xu, K., Ding, H., Jia, K., Lu, X., Chen, P., Zhou, T., Cheng, H., Liu, S., Wu, C. and Xie, Y., 2016. Solution-Liquid-Solid Synthesis of Hexagonal Nickel Selenide Nanowire Arrays with a Nonmetal Catalyst. *Angewandte Chemie International Edition*, *55*(5), pp.1710-1713.

67. Fang, Z., Peng, L., Lv, H., Zhu, Y., Yan, C., Wang, S., Kalyani, P., Wu, X. and Yu, G., 2017. Metallic Transition Metal Selenide Holey Nanosheets for Efficient Oxygen Evolution Electrocatalysis. *ACS nano*. *11*(9), pp.9550-9557.

SECTION

2. CONCLUSION

Hydrogen energy can be served as a main solution for future energy demand due to its chemical energy carrier and the environmental benign processes of hydrogen production and power generation. Water splitting to hydrogen and fuel cells are major two separate technologies in the hydrogen energy field. Also, water splitting process is a sustainable technology for hydrogen production due to its higher efficiency and zero environmental impact. This process has been hampered by the absence of the active, stable electrocatalysts and their inability to deal with the fluctuating conditions. The development of highly efficient materials to the electrocatalytic water splitting process plays a vital role in the energy conversion route. The development of efficient, non-noble metal, inexpensive electrocatalysts are become the key for this main issue. Transition metal chalcogenides have been investigated as highly efficient catalysts due to its excellent conductivity and also have exhibited outstanding activities for OER, HER and ORR. These remarkable inorganic material compositions work as bifunctional and trifunctional electrocatalysts toward the overall water electrolysis process.

In this study mainly consists of designing and development of efficient, excellent catalytic performance materials using inorganic elements which are readily available on the earth and also easily affordable and suitable for this energy application. The key challenges of synthesizing efficient electrocatalysts can be enumerated by emerging several strategies such as chemical modification, structural modification, including

nanostructuring, and preparation of different composite materials. There are four main concepts have been applied in this research work to create the remarkable electrocatalysts. First and foremost, changing the traditional electrocatalysts of oxide materials to the chalcogenide materials. This turn in primarily directed to the development and designing of transition metal based chalcogenides as highly efficient electrocatalysts for water splitting reaction. It provides new direction and opportunities of chalcogenides, specially selenides and tellurides as bifunctional and trifunctional electrocatalysts for energy related application of water electrolysis. This study has mainly considered on transition metals of nickel and cobalt chalcogenides such as selenides and tellurides as highly efficient electrocatalysts for OER, HER and ORR.

Second, synthesizing nano materials of these chalcogenide electrocatalysts such as different nano morphologies also confirmed the synthesizing of an excellent electrocatalytic material toward the water electrolysis process. Catalytic process is a surface phenomenon and nano morphologies of catalytic materials increase the higher surface area of the catalysts which allow to have more interaction between catalytic materials and the electrolytes in the electrolysis. Also synthesizing nanomaterials help to increase the number of active sites of the catalyst. The number of active sites of the catalyst are one major factor that decide the catalytic activity of the material. Higher number of active sites of catalysts will become an excellent electrocatalyst for the water splitting process.

Third, designing and developing different elemental ratios of the same catalytic material such as different ratios of transition metal to chalcogenide, also confirmed the highly efficient electrocatalytic phases toward the water electrolysis process. Fourth,

synthesizing electrocatalysts in different methods confirmed the catalytic activity is an intrinsic property of the inorganic catalyst as well as synthesizing the pure compound of the material and the material production from small scale to larger scale.

Changing chemical composition of oxide to chalcogenides of selenide or telluride as electrocatalysts has a proof that selenide and telluride electrocatalysts materials work as an efficient bifunctional and trifunctional electrocatalysts for OER, HER and ORR in alkaline medium. The low onset potentials, low overpotential at 10 mA cm^{-2} current density, higher stability and higher current density of these electrocatalysts showed the proof of the concept of chalcogenides are highly efficient electrocatalysts for water electrolysis in alkaline medium. Comparatively, telluride based catalysts show remarkable catalytic performance than the selenide based catalyst in the alkaline medium. Ni_3Te_2 has been identified as best bi-functional electrocatalysts towards the OER and HER process in alkaline medium due to its low onset potential of 1.36 V and very low overpotential of 180 mV at 10 $mAcm^{-2}$ current density in OER and low onset potential of -0.149 V and low overpotential of 212 mV at 10 $mAcm^{-2}$ current density in HER respectively.

Also, the transition metal chalcogenides of Ni_3Se_2 and Ni_3Te_2 electrocatalysts surfaces have been studied by creating hypothetical surface models of partially hydroxylated mixed anionic (*Surf(OH)E*) surface and oxide@chalcogenide surface (*Surf-Ox*) to understand the interface evolution of the electrocatalytic process in alkaline medium. *Surf-Ox* models of $NiO_x@Ni_3Se_2$ and $NiO_x@Ni_3Te_2$ were synthesized by electrodeposition of NiO_x layer on Ni_3Se_2 and Ni_3Te_2 electrodeposited films. This in turn provides the *Surf(OH)E* model as the active interface evolution of the electrocatalytic

process in alkaline medium which is also confirmed by the electrochemical measurements and extensive surface analysis techniques of XPS and sXAS. This also confirmed that transition metal based chalcogenide electrocatalysts are definitely stable electrocatalysts for OER in alkaline medium. Transition metal based telluride catalysts have been revealed as revolutionary electrocatalysts due to its excellent catalytic performance and the higher catalytic stability and the durability towards water electrolysis of OER and HER in alkaline medium.

BIBLIOGRAPHY

1. Acar, C. and Dincer, I., 2014. Comparative assessment of hydrogen production methods from renewable and non-renewable sources. *International journal of hydrogen energy*, *39*(1), pp.1-12.

2. Hussein, A.K., 2015. Applications of nanotechnology in renewable energies—A comprehensive overview and understanding. *Renewable and Sustainable Energy Reviews*, *42*, pp.460-476.

3. https://www.eia.gov/totalenergy/data/annual/perspectives.php, October 2020.

4. Marcus, R.J., 1956. Chemical conversion of solar energy. *Science*, *123*(3193), pp.399-405.

5. Chen, J., Yang, D., Song, D., Jiang, J., Ma, A., Hu, M.Z. and Ni, C., 2015. Recent progress in enhancing solar-to-hydrogen efficiency. *Journal of Power Sources*, *280*, pp.649-666.

6. Mazloomi, K. and Gomes, C., Hydrogen as an energy carrier: prospects and challenges. *Renewable and Sustainable Energy Reviews*, 2012. *16*(5), pp.3024-3033.

7. Ball, M. and Wietschel, M., The future of hydrogen–opportunities and challenges. *International journal of hydrogen energy*, 2009. *34*(2), pp.615-627.

8. Veziroglu, A. and Macario, R., 2011. Fuel cell vehicles: State of the art with economic and environmental concerns. *International journal of hydrogen energy*, *36*(1), pp.25-43.

9. Liu, Y., Liu, S., Wang, Y., Zhang, Q., Gu, L., Zhao, S., Xu, D., Li, Y., Bao, J. and Dai, Z., 2018. "Ru modulation effects in the synthesis of unique rod-like Ni@ Ni2P–Ru heterostructures and their remarkable electrocatalytic hydrogen evolution performance."*Journal of the American Chemical Society*, *140*(8), pp.2731-2734.

10. Tiwari, J.N., Lee, W.G., Sultan, S., Yousuf, M., Harzandi, A.M., Vij, V. and Kim, K.S., 2017. "High-affinity-assisted nanoscale alloys as remarkable bifunctional catalyst for alcohol oxidation and oxygen reduction reactions."*ACS nano*, *11*(8), pp.7729-7735.

11. Lewis, N.S., 2007. Toward cost-effective solar energy use. *science*, *315*(5813), pp.798-801.

12. Morton, O., 2006. Solar energy: A new day dawning?: Silicon Valley sunrise. *Nature*, *443*(7107), pp.19-23.

13. Ibrahim, H., Ilinca, A. and Perron, J., 2008. Energy storage systems—Characteristics and comparisons. *Renewable and sustainable energy reviews*, *12*(5), pp.1221-1250.

14. Rand, D.A., 2011. A journey on the electrochemical road to sustainability. *Journal of Solid State Electrochemistry*, *15*(7-8), pp.1579-1622.

15. Gardner, G., 2008. Alternative energy and nanotechnology. *Public Communication of Science and Technology, USA*. Pages 1-11.

16. Burton, T., Sharpe, D., Jenkins, N. and Bossanyi, E., 2001. *Wind energy handbook* (Vol. 2). New York: Wiley.

17. Dalili, N., Edrisy, A. and Carriveau, R., 2009. A review of surface engineering issues critical to wind turbine performance. *Renewable and Sustainable energy reviews*, *13*(2), pp.428-438.

18. Sherif, S.A., Barbir, F. and Veziroglu, T.N., 2005. Wind energy and the hydrogen economy—review of the technology. *Solar energy*, *78*(5), pp.647-660.

19. McKendry, P., 2002. Energy production from biomass (part 1): overview of biomass. *Bioresource technology*, *83*(1), pp.37-46.

20. Demirbas, A., 2007. Progress and recent trends in biofuels. *Progress in energy and combustion science*, *33*(1), pp.1-18.

21. Agarwal, A.K., 2007. Biofuels (alcohols and biodiesel) applications as fuels for internal combustion engines. *Progress in energy and combustion science*, *33*(3), pp.233-271.

22. Naik, S.N., Goud, V.V., Rout, P.K. and Dalai, A.K., 2010. Production of first and second generation biofuels: a comprehensive review. *Renewable and sustainable energy reviews*, *14*(2), pp.578-597.

23. Wang, G., Luo, Y., Deng, J., Kuang, J. and Zhang, Y., 2011. Pretreatment of biomass by torrefaction. *Chinese Science Bulletin*, *56*(14), pp.1442-1448.

24. Winter, C.J., 2009. Hydrogen energy—Abundant, efficient, clean: A debate over the energy-system-of-change. *International journal of hydrogen energy*, *34*(14), pp.S1-S52.

25. Ball, M. and Wietschel, M., 2009. The future of hydrogen–opportunities and challenges. *International journal of hydrogen energy*, *34*(2), pp.615-627.

26. Züttel, A., Remhof, A., Borgschulte, A. and Friedrichs, O., 2010. Hydrogen: the future energy carrier. *Philosophical Transactions of the Royal Society A: Mathematical, Physical and Engineering Sciences*, *368*(1923), pp.3329-3342.

27. Veziroglu, T.N., 2007. 21st Century's energy: Hydrogen energy system. In *Assessment of hydrogen energy for sustainable development* (pp. 9-31). Springer, Dordrecht.

28. https://www.engineering.unsw.edu.au/chemical-engineering/research/our-research-priorities/energy, October 2020.

29. Cipriani, G., Di Dio, V., Genduso, F., La Cascia, D., Liga, R., Miceli, R. and Galluzzo, G.R., 2014. Perspective on hydrogen energy carrier and its automotive applications. *International Journal of Hydrogen Energy*, *39*(16), pp.8482-8494.

30. Fayaz, H., Saidur, R., Razali, N., Anuar, F.S., Saleman, A.R. and Islam, M.R., 2012. An overview of hydrogen as a vehicle fuel. *Renewable and Sustainable Energy Reviews*, *16*(8), pp.5511-5528.

31. https://www.h2sys.fr/en/hydrogen/, October 2020.

32. Van de Loosdrecht, J. and Niemantsverdriet, J.W., 2012. Synthesis gas to hydrogen, methanol, and synthetic fuels. In *Chemical energy storage* (pp. 443-458). Walter de Gruyter GmbH.

33. Rostrup-Nielsen, J. and Christiansen, L.J., 2011. Concepts in syngas preparation. *Catalytic science series. London: Imperial College Press*.

34. Balat, M. and Balat, M., 2009. Political, economic and environmental impacts of biomass-based hydrogen. *International journal of hydrogen energy*, *34*(9), pp.3589-3603.

35. Holladay, J.D., Hu, J., King, D.L. and Wang, Y., 2009. An overview of hydrogen production technologies. *Catalysis today*, *139*(4), pp.244-260.

36. Fabbri, E., Habereder, A., Waltar, K., Kötz, R. and Schmidt, T.J., 2014. Developments and perspectives of oxide-based catalysts for the oxygen evolution reaction. *Catalysis Science & Technology*, *4*(11), pp.3800-3821.

37. Zou, X. and Zhang, Y., 2015. Noble metal-free hydrogen evolution catalysts for water splitting. *Chemical Society Reviews*, *44*(15), pp.5148-5180.

38. Barbir, F., 2005. PEM electrolysis for production of hydrogen from renewable energy sources. *Solar energy*, *78*(5), pp.661-669.

39. Kato, T., Kubota, M., Kobayashi, N. and Suzuoki, Y., 2005. Effective utilization of by-product oxygen from electrolysis hydrogen production. *Energy*, *30*(14), pp.2580-2595.

40. Sapountzi, F.M., Gracia, J.M., Fredriksson, H.O. and Niemantsverdriet, J.H., 2017. Electrocatalysts for the generation of hydrogen, oxygen and synthesis gas. *Progress in Energy and Combustion Science*, *58*, pp.1-35.

41. Vij, Varun, Siraj Sultan, Ahmad M. Harzandi, Abhishek Meena, Jitendra N. Tiwari, Wang-Geun Lee, Taeseung Yoon, and Kwang S. Kim. "Nickel-based electrocatalysts for energy-related applications: oxygen reduction, oxygen evolution, and hydrogen evolution reactions." *Acs Catalysis* 7, no. 10 (2017): 7196-7225.

42. Hong, Wesley T., Marcel Risch, Kelsey A. Stoerzinger, Alexis Grimaud, Jin Suntivich, and Yang Shao-Horn. "Toward the rational design of non-precious transition metal oxides for oxygen electrocatalysis." *Energy & Environmental Science* 8, no. 5 (2015): 1404-1427.

43. Trotochaud, L. and Boettcher, S.W., 2014. Precise oxygen evolution catalysts: Status and opportunities. *Scripta Materialia*, *74*, pp.25-32.

44. Trotochaud, L., Ranney, J.K., Williams, K.N. and Boettcher, S.W., 2012. Solution-cast metal oxide thin film electrocatalysts for oxygen evolution. *Journal of the American Chemical Society*, *134*(41), pp.17253-17261.

45. Whitesides, G.M. and Crabtree, G.W., 2007. Don't forget long-term fundamental research in energy. *science*, *315*(5813), pp.796-798.

46. McCrory, C.C., Jung, S., Peters, J.C. and Jaramillo, T.F., 2013. Benchmarking heterogeneous electrocatalysts for the oxygen evolution reaction. *Journal of the American Chemical Society*, *135*(45), pp.16977-16987.

47. Suntivich, J., May, K.J., Gasteiger, H.A., Goodenough, J.B. and Shao-Horn, Y., 2011. A perovskite oxide optimized for oxygen evolution catalysis from molecular orbital principles. *Science*, *334*(6061), pp.1383-1385.

48. Lee, Seung Woo, Christopher Carlton, Marcel Risch, Yogesh Surendranath, Shuo Chen, Sho Furutsuki, Atsuo Yamada, Daniel G. Nocera, and Yang Shao-Horn. "The nature of lithium battery materials under oxygen evolution reaction conditions." *Journal of the American Chemical Society* 134, no. 41 (2012): 16959-16962.

49. Wang, F., Shifa, T.A., Zhan, X., Huang, Y., Liu, K., Cheng, Z., Jiang, C. and He, J., 2015. Recent advances in transition-metal dichalcogenide based nanomaterials for water splitting. *Nanoscale*, *7*(47), pp.19764-19788.

50. Bockris, J.O., M. & Reddy AKN Modern Eletrochemistry, 1 Ionics. Plenum Press, New York, 1998

51. Koper, M.T., 2011. Thermodynamic theory of multi-electron transfer reactions: Implications for electrocatalysis. *Journal of Electroanalytical Chemistry*, *660*(2), pp.254-260.

52. Li, X., Walsh, F.C. and Pletcher, D., 2011. Nickel based electrocatalysts for oxygen evolution in high current density, alkaline water electrolysers. *Physical Chemistry Chemical Physics*, *13*(3), pp.1162-1167.

53. Faber, M.S. and Jin, S., 2014. Earth-abundant inorganic electrocatalysts and their nanostructures for energy conversion applications. *Energy & Environmental Science*, *7*(11), pp.3519-3542.

54. Rossmeisl, J., Qu, Z.W., Zhu, H., Kroes, G.J. and Nørskov, J.K., 2007. Electrolysis of water on oxide surfaces. *Journal of Electroanalytical Chemistry*, *607*(1-2), pp.83-89.

55. Lee, Youngmin, Jin Suntivich, Kevin J. May, Erin E. Perry, and Yang Shao-Horn. "Synthesis and activities of rutile IrO2 and RuO2 nanoparticles for oxygen evolution in acid and alkaline solutions." *The journal of physical chemistry letters* 3, no. 3 (2012): 399-404.

56. Marshall, A., Børre Børresen, Georg Hagen, Mikhail Tsypkin, and Reidar Tunold. "Hydrogen production by advanced proton exchange membrane (PEM) water electrolysers—Reduced energy consumption by improved electrocatalysis." *Energy* 32, no. 4 (2007): 431-436.

57. Zhang, J., Zhao, Z., Xia, Z. and Dai, L., 2015. A metal-free bifunctional electrocatalyst for oxygen reduction and oxygen evolution reactions. *Nature nanotechnology*, *10*(5), pp.444-452.

58. Seh, Z.W., Kibsgaard, J., Dickens, C.F., Chorkendorff, I.B., Nørskov, J.K. and Jaramillo, T.F., 2017. Combining theory and experiment in electrocatalysis: Insights into materials design. *Science*, *355*(6321).

59. Tiwari, J.N., Nath, K., Kumar, S., Tiwari, R.N., Kemp, K.C., Le, N.H., Youn, D.H., Lee, J.S. and Kim, K.S., 2013. Stable platinum nanoclusters on genomic DNA–graphene oxide with a high oxygen reduction reaction activity. *Nature communications*, *4*(1), pp.1-7.

60. https://en.wikipedia.org/wiki/Abundance_of_elements_in_Earth%27s_crust, October 2020.

61. Trasatti, S., 1984. Electrocatalysis in the anodic evolution of oxygen and chlorine. *Electrochimica Acta*, *29*(11), pp.1503-1512.

62. Trasatti, S., 1991. Physical electrochemistry of ceramic oxides. *Electrochimica acta*, *36*(2), pp.225-241.

63. Betley, T.A., Wu, Q., Van Voorhis, T. and Nocera, D.G., 2008. Electronic design criteria for O− O bond formation via metal− oxo complexes. *Inorganic chemistry*, *47*(6), pp.1849-1861.

64. Liu, F., Concepcion, J.J., Jurss, J.W., Cardolaccia, T., Templeton, J.L. and Meyer, T.J., 2008. Mechanisms of water oxidation from the blue dimer to photosystem II. *Inorganic Chemistry*, *47*(6), pp.1727-1752.

65. Brimblecombe, R., Dismukes, G.C., Swiegers, G.F. and Spiccia, L., 2009. Molecular water-oxidation catalysts for photoelectrochemical cells. *Dalton Transactions*, (43), pp.9374-9384.

66. Hodes, G., Manassen, J. and Cahen, D., 1980. Electrocatalytic electrodes for the polysulfide redox system. *Journal of the Electrochemical Society*, *127*(3), p.544.

67. Miles, M.H., 1975. Evaluation of electrocatalysts for water electrolysis in alkaline solutions. *Journal of Electroanalytical Chemistry and Interfacial Electrochemistry*, *60*(1), pp.89-96.

68. Trasatti, Sergio. "Work function, electronegativity, and electrochemical behaviour of metals: III. Electrolytic hydrogen evolution in acid solutions." *Journal of Electroanalytical Chemistry and Interfacial Electrochemistry* 39, no. 1 (1972): 163-184.

69. Sun, H., Yan, Z., Liu, F., Xu, W., Cheng, F. and Chen, J., 2020. Self-supported transition-metal-based electrocatalysts for hydrogen and oxygen evolution. *Advanced Materials*, *32*(3), p.1806326.

70. Kuhn, A. T., C. J. Mortimer, G. C. Bond, and J. Lindley. "A critical analysis of correlations between the rate of the electrochemical hydrogen evolution reaction and physical properties of the elements." *Journal of Electroanalytical Chemistry and Interfacial Electrochemistry* 34, no. 1 (1972): 1-14.

71. High, J.G., 1999. eld, E. Claude and K. Oguro. *Electrochim. Acta*, *44*, pp.2805-2814.

72. Greeley, J., Nørskov, J.K., Kibler, L.A., El-Aziz, A.M. and Kolb, D.M., 2006. Hydrogen evolution over bimetallic systems: Understanding the trends. *ChemPhysChem*, *7*(5), pp.1032-1035.

73. Jaksic, M.M., 2001. Hypo–hyper-d-electronic interactive nature of interionic synergism in catalysis and electrocatalysis for hydrogen reactions. *International journal of hydrogen energy*, *26*(6), pp.559-578.

74. Greeley, J., Stephens, I.E.L., Bondarenko, A.S., Johansson, T.P., Hansen, H.A., Jaramillo, T.F., Rossmeisl, J., Chorkendorff, I.N.J.K. and Nørskov, J.K., 2009. Alloys of platinum and early transition metals as oxygen reduction electrocatalysts. *Nature chemistry*, *1*(7), pp.552-556.

75. Pletcher, D., 1984. Electrocatalysis: present and future. *Journal of applied electrochemistry*, *14*(4), pp.403-415.

76. Brown, D.E., Mahmood, M.N., Turner, A.K., Hall, S.M. and Fogarty, P.O., 1982. Low overvoltage electrocatalysts for hydrogen evolving electrodes. *International Journal of Hydrogen Energy*, *7*(5), pp.405-410.

77. McKone, J.R., Marinescu, S.C., Brunschwig, B.S., Winkler, J.R. and Gray, H.B., 2014. Earth-abundant hydrogen evolution electrocatalysts. *Chemical Science*, *5*(3), pp.865-878.

78. Navarro-Flores, E., Chong, Z. and Omanovic, S., 2005. Characterization of Ni, NiMo, NiW and NiFe electroactive coatings as electrocatalysts for hydrogen evolution in an acidic medium. *Journal of Molecular Catalysis A: Chemical*, *226*(2), pp.179-197.

79. Brown, D.E., Mahmood, M.N., Man, M.C.M. and Turner, A.K., 1984. Preparation and characterization of low overvoltage transition metal alloy electrocatalysts for hydrogen evolution in alkaline solutions. *Electrochimica Acta*, *29*(11), pp.1551-1556.

80. Conway, B.E. and Bai, L., 1986. H2 evolution kinetics at high activity Ni-Mo-Cd electrocoated cathodes and its relation to potential dependence of sorption of H. *International journal of hydrogen energy*, *11*(8), pp.533-540.

81. Raj, I.A., 1992. Nickel based composite electrolytic surface coatings as electrocatalysts for the cathodes in the energy efficient industrial production of hydrogen from alkaline water electrolytic cells. *International journal of hydrogen energy*, *17*(6), pp.413-421.

82. Wang, C., Sui, Y., Xiao, G., Yang, X., Wei, Y., Zou, G. and Zou, B., 2015. Synthesis of Cu–Ir nanocages with enhanced electrocatalytic activity for the oxygen evolution reaction. *Journal of Materials Chemistry A*, *3*(39), pp.19669-19673.

83. Alia, S.M., Shulda, S., Ngo, C., Pylypenko, S. and Pivovar, B.S., 2018. Iridium-based nanowires as highly active, oxygen evolution reaction electrocatalysts. *ACS Catalysis*, *8*(3), pp.2111-2120.

84. Park, J., Sa, Y.J., Baik, H., Kwon, T., Joo, S.H. and Lee, K., 2017. Iridium-based multimetallic nanoframe@ nanoframe structure: an efficient and robust electrocatalyst toward oxygen evolution reaction. *ACS nano*, *11*(6), pp.5500-5509.

85. Fu, L., Cheng, G. and Luo, W., 2017. Colloidal synthesis of monodisperse trimetallic IrNiFe nanoparticles as highly active bifunctional electrocatalysts for acidic overall water splitting. *Journal of Materials Chemistry A*, *5*(47), pp.24836-24841.

86. Lv, F., Feng, J., Wang, K., Dou, Z., Zhang, W., Zhou, J., Yang, C., Luo, M., Yang, Y., Li, Y. and Gao, P., 2018. Iridium–tungsten alloy nanodendrites as pH-universal water-splitting electrocatalysts. *ACS central science*, *4*(9), pp.1244-1252.

87. Feng, J., Lv, F., Zhang, W., Li, P., Wang, K., Yang, C., Wang, B., Yang, Y., Zhou, J., Lin, F. and Wang, G.C., 2017. Iridium-based multimetallic porous hollow nanocrystals for efficient overall-water-splitting catalysis. *Advanced Materials*, *29*(47), p.1703798.

88. Metal Oxides Catalysis, M.O., 2009. SD Jackson and JSJ Hargreaves. Wiley-VCH, Weinheim.

89. Chen, Z., Higgins, D., Yu, A., Zhang, L. and Zhang, J., 2011. A review on non-precious metal electrocatalysts for PEM fuel cells. *Energy & Environmental Science*, *4*(9), pp.3167-3192.

90. Han, Xiaopeng, Fangyi Cheng, Tianran Zhang, Jingang Yang, Yuxiang Hu, and Jun Chen. "Hydrogenated uniform Pt clusters supported on porous CaMnO3 as a bifunctional electrocatalyst for enhanced oxygen reduction and evolution." *Advanced Materials* 26, no. 13 (2014): 2047-2051.

91. Du, J., Chen, C., Cheng, F. and Chen, J., 2015. Rapid synthesis and efficient electrocatalytic oxygen reduction/evolution reaction of CoMn2O4 nanodots supported on graphene. *Inorganic chemistry*, *54*(11), pp.5467-5474.

92. Li, C., Han, X., Cheng, F., Hu, Y., Chen, C. and Chen, J., 2015. Phase and composition controllable synthesis of cobalt manganese spinel nanoparticles towards efficient oxygen electrocatalysis. *Nature communications*, *6*(1), pp.1-8.

93. Zhao, Q., Yan, Z., Chen, C. and Chen, J., 2017. Spinels: controlled preparation, oxygen reduction/evolution reaction application, and beyond. *Chemical reviews*, *117*(15), pp.10121-10211.

94. Lu, X.F., Gu, L.F., Wang, J.W., Wu, J.X., Liao, P.Q. and Li, G.R., 2017. Bimetal-organic framework derived CoFe2O4/C porous hybrid nanorod arrays as high-performance electrocatalysts for oxygen evolution reaction. *Advanced materials*, *29*(3), p.1604437.

95. Guan, C., Liu, X., Ren, W., Li, X., Cheng, C. and Wang, J., 2017. Rational design of metal-organic framework derived hollow NiCo2O4 arrays for flexible supercapacitor and electrocatalysis. *Advanced Energy Materials*, *7*(12), p.1602391.

96. Liu, J., Zhu, D., Ling, T., Vasileff, A. and Qiao, S.Z., 2017. S-NiFe2O4 ultra-small nanoparticle built nanosheets for efficient water splitting in alkaline and neutral pH. *Nano Energy*, *40*, pp.264-273.

97. Jin, Y., Wang, H., Li, J., Yue, X., Han, Y., Shen, P.K. and Cui, Y., 2016. Porous MoO_2 nanosheets as non-noble bifunctional electrocatalysts for overall water splitting. *Advanced Materials*, *28*(19), pp.3785-3790.

98. Zhao, Y., Chang, C., Teng, F., Zhao, Y., Chen, G., Shi, R., Waterhouse, G.I., Huang, W. and Zhang, T., 2017. Defect-engineered ultrathin δ-MnO_2 nanosheet arrays as bifunctional electrodes for efficient overall water splitting. *Advanced Energy Materials*, *7*(18), p.1700005.

99. Ye, Z., Li, T., Ma, G., Dong, Y. and Zhou, X., 2017. Metal-Ion (Fe, V, Co, and Ni)-doped MnO2 ultrathin nanosheets supported on Carbon fiber paper for the oxygen evolution reaction. *Advanced Functional Materials*, *27*(44), p.1704083.

100. May, K.J., Carlton, C.E., Stoerzinger, K.A., Risch, M., Suntivich, J., Lee, Y.L., Grimaud, A. and Shao-Horn, Y., 2012. Influence of oxygen evolution during water oxidation on the surface of perovskite oxide catalysts. *The journal of physical chemistry letters*, *3*(22), pp.3264-3270.

101. May, K.J., Carlton, C.E., Stoerzinger, K.A., Risch, M., Suntivich, J., Lee, Y.L., Grimaud, A. and Shao-Horn, Y., 2012. Influence of oxygen evolution during water oxidation on the surface of perovskite oxide catalysts. *The journal of physical chemistry letters*, *3*(22), pp.3264-3270.

102. Zhu, Y., Zhou, W., Zhong, Y., Bu, Y., Chen, X., Zhong, Q., Liu, M. and Shao, Z., 2017. A perovskite nanorod as bifunctional electrocatalyst for overall water splitting. *Advanced Energy Materials*, *7*(8), p.1602122.

103. Xu, X., Chen, Y., Zhou, W., Zhu, Z., Su, C., Liu, M. and Shao, Z., 2016. A perovskite electrocatalyst for efficient hydrogen evolution reaction. *Advanced Materials*, *28*(30), pp.6442-6448.

104. Liu, X., Liu, W., Ko, M., Park, M., Kim, M.G., Oh, P., Chae, S., Park, S., Casimir, A., Wu, G. and Cho, J., 2015. Metal (Ni, Co)-metal oxides/graphene nanocomposites as multifunctional electrocatalysts. *Advanced Functional Materials*, *25*(36), pp.5799-5808.

105. Stern, L.A. and Hu, X., 2015. Enhanced oxygen evolution activity by NiOx and Ni $(OH)_2$ nanoparticles. *Faraday discussions*, *176*, pp.363-379.

106. Qiu, Y., Xin, L. and Li, W., 2014. Electrocatalytic oxygen evolution over supported small amorphous Ni–Fe nanoparticles in alkaline electrolyte. *Langmuir*, *30*(26), pp.7893-7901.

107. Subbaraman, R., Tripkovic, D., Chang, K.C., Strmcnik, D., Paulikas, A.P., Hirunsit, P., Chan, M., Greeley, J., Stamenkovic, V. and Markovic, N.M., 2012. Trends in activity for the water electrolyser reactions on 3 d M (Ni, Co, Fe, Mn) hydr (oxy) oxide catalysts. *Nature materials*, *11*(6), pp.550-557.

108. Huang, Y., Song, X., Deng, J., Zha, C., Huang, W., Wu, Y. and Li, Y., 2019. Ultra-dispersed molybdenum phosphide and phosphosulfide nanoparticles on hierarchical carbonaceous scaffolds for hydrogen evolution electrocatalysis. *Applied Catalysis B: Environmental*, *245*, pp.656-661.

109. Stern, L.A., Feng, L., Song, F. and Hu, X., 2015. Ni 2 P as a Janus catalyst for water splitting: the oxygen evolution activity of Ni 2 P nanoparticles. *Energy & Environmental Science*, *8*(8), pp.2347-2351.

110. Read, C.G., Callejas, J.F., Holder, C.F. and Schaak, R.E., 2016. General strategy for the synthesis of transition metal phosphide films for electrocatalytic hydrogen and oxygen evolution. *ACS applied materials & interfaces*, *8*(20), pp.12798-12803.

111. Wang, J., Yue, X., Yang, Y., Sirisomboonchai, S., Wang, P., Ma, X., Abudula, A. and Guan, G., 2020. Earth-abundant transition-metal-based bifunctional catalysts for overall electrochemical water splitting: A review. *Journal of Alloys and Compounds*, *819*, p.153346.

112. Tang, Y.J., Zhu, H.J., Dong, L.Z., Zhang, A.M., Li, S.L., Liu, J. and Lan, Y.Q., 2019. Solid-phase hot-pressing of POMs-ZIFs precursor and derived phosphide for overall water splitting. *Applied Catalysis B: Environmental*, *245*, pp.528-535.

113. Jiao, C., Hassan, M., Bo, X. and Zhou, M., 2018. Co0. 5Ni0. 5P nanoparticles embedded in carbon layers for efficient electrochemical water splitting. *Journal of Alloys and Compounds*, *764*, pp.88-95.

114. Wang, W., Xu, M., Xu, X., Zhou, W. and Shao, Z., 2020. Perovskite Oxide Based Electrodes for High-Performance Photoelectrochemical Water Splitting. *Angewandte Chemie International Edition*, *59*(1), pp.136-152.

115. Huang, Y., Song, X., Deng, J., Zha, C., Huang, W., Wu, Y. and Li, Y., 2019. Ultra-dispersed molybdenum phosphide and phosphosulfide nanoparticles on hierarchical carbonaceous scaffolds for hydrogen evolution electrocatalysis. *Applied Catalysis B: Environmental*, *245*, pp.656-661.

116. Liao, L., Wang, S., Xiao, J.J., Bian, X.J., Zhang, Y.H. and Scanlon, M.D., 2014. X. l. Hu, Y. Tang, BH Liu and HH Girault. *Energy Environ. Sci*, *7*, pp.387-392.

117. Xiao, P., Yan, Y., Ge, X., Liu, Z., Wang, J.Y. and Wang, X., 2014. Investigation of molybdenum carbide nano-rod as an efficient and durable electrocatalyst for hydrogen evolution in acidic and alkaline media. *Applied Catalysis B: Environmental*, *154*, pp.232-237.

118. Chen, W.F., Muckerman, J.T. and Fujita, E., 2013. Recent developments in transition metal carbides and nitrides as hydrogen evolution electrocatalysts. *Chemical communications*, *49*(79), pp.8896-8909.

119. Li, R., Li, X., Yu, D., Li, L., Yang, G., Zhang, K., Ramakrishna, S., Xie, L. and Peng, S., 2019. Ni3ZnC0. 7 nanodots decorating nitrogen-doped carbon nanotube arrays as a self-standing bifunctional electrocatalyst for water splitting. *Carbon*, *148*, pp.496-503.

120. Ham, D.J. and Lee, J.S., 2009. Transition metal carbides and nitrides as electrode materials for low temperature fuel cells. *Energies*, *2*(4), pp.873-899.

121. Chen, Z., Song, Y., Cai, J., Zheng, X., Han, D., Wu, Y., Zang, Y., Niu, S., Liu, Y., Zhu, J. and Liu, X., 2018. Tailoring the d-band centers enables Co4N nanosheets to be highly active for hydrogen evolution catalysis. *Angewandte Chemie*, *130*(18), pp.5170-5174.

122. Xue, S., Zhang, W., Zhang, Q., Du, J., Cheng, H.M. and Ren, W., 2020. Heterostructured Ni–Mo–N nanoparticles decorated on reduced graphene oxide as efficient and robust electrocatalyst for hydrogen evolution reaction. *Carbon*.165, 2020, 122-128.

123. Wu, A., Xie, Y., Ma, H., Tian, C., Gu, Y., Yan, H., Zhang, X., Yang, G. and Fu, H., 2018. Integrating the active OER and HER components as the heterostructures for the efficient overall water splitting. *Nano Energy*, *44*, pp.353-363.

124. Rasmussen, F.A. and Thygesen, K.S., 2015. Computational 2D materials database: electronic structure of transition-metal dichalcogenides and oxides. *The Journal of Physical Chemistry C*, *119*(23), pp.13169-13183.

125. Xu, Y. and Schoonen, M.A., 2000. The absolute energy positions of conduction and valence bands of selected semiconducting minerals. *American Mineralogist*, *85*(3-4), pp.543-556.

126. Swesi, A.T., Masud, J. and Nath, M., 2016. Enhancing electrocatalytic activity of bifunctional Ni3Se2 for overall water splitting through etching-induced surface nanostructuring. *Journal of Materials Research*, *31*(18), p.2888-2896.

127. Kwak, I.H., Im, H.S., Jang, D.M., Kim, Y.W., Park, K., Lim, Y.R., Cha, E.H. and Park, J., 2016. CoSe2 and NiSe2 nanocrystals as superior bifunctional catalysts for electrochemical and photoelectrochemical water splitting. *ACS applied materials & interfaces*, *8*(8), pp.5327-5334.

128. Masud, J., Ioannou, P.C., Levesanos, N., Kyritsis, P. and Nath, M., 2016. A Molecular Ni-complex containing tetrahedral nickel selenide core as highly efficient electrocatalyst for water oxidation. *ChemSusChem*, *9*(22), pp.3128-3132.

129. Xu, X., Song, F. and Hu, X., 2016. A nickel iron diselenide-derived efficient oxygen-evolution catalyst. *Nature communications*, *7*(1), pp.1-7.

130. Swesi, A.T., Masud, J. and Nath, M., 2016. Nickel selenide as a high-efficiency catalyst for oxygen evolution reaction. *Energy & Environmental Science*, *9*(5), pp.1771-1782.

131. De Silva, U., Masud, J., Zhang, N., Hong, Y., Liyanage, W.P., Zaeem, M.A. and Nath, M., 2018. Nickel telluride as a bifunctional electrocatalyst for efficient water splitting in alkaline medium. *Journal of Materials Chemistry A*, *6*(17), pp.7608-7622.

132. Pradhan, S., Das, R., Biswas, S., Das, D.K., Bhar, R., Bandyopadhyay, R. and Pramanik, P., 2017. Chemical synthesis of nanoparticles of nickel telluride and cobalt telluride and its electrochemical applications for determination of uric acid and adenine. *Electrochimica Acta*, *238*, pp.185-193.

133. Gao, Q., Huang, C.Q., Ju, Y.M., Gao, M.R., Liu, J.W., An, D., Cui, C.H., Zheng, Y.R., Li, W.X. and Yu, S.H., 2017. Phase-selective syntheses of cobalt telluride nanofleeces for efficient oxygen evolution catalysts. *Angewandte Chemie*, *129*(27), pp.7877-7881.

134. Wang, K., Ye, Z., Liu, C., Xi, D., Zhou, C., Shi, Z., Xia, H., Liu, G. and Qiao, G., 2016. Morphology-controllable synthesis of cobalt telluride branched nanostructures on carbon fiber paper as electrocatalysts for hydrogen evolution reaction. *ACS Applied Materials & Interfaces*, *8*(5), pp.2910-2916.

135. Levesanos, N., Liyanage, W.P., Ferentinos, E., Raptopoulos, G., Paraskevopoulou, P., Sanakis, Y., Choudhury, A., Stavropoulos, P., Nath, M. and Kyritsis, P., 2016. Investigating the structural, spectroscopic, and electrochemical properties of [Fe {(EPiPr2) 2N} 2](E= S, Se) and the formation of iron selenides by chemical vapor deposition. *European Journal of Inorganic Chemistry*, *2016*(34), pp.5332-5339.

136. Wombwell, C. and Reisner, E., 2015. Synthetic active site model of the [NiFeSe] hydrogenase. *Chemistry (Weinheim an Der Bergstrasse, Germany)*, *21*(22), p.8096.

VITA

Sammu Handi Umanga Iroshini De Silva received her Bachelor of Science (BS) degree in December 2003 from University of Colombo, Sri Lanka and the Graduate degree in chemistry (Chemist) from College of Chemical Sciences, Institute of Chemistry Ceylon, Sri Lanka in January 2006 and the Master of Science (MS) degree in Polymer Technology in March 2010 from University of Moratuwa, Sri Lanka.

She joined Missouri University of Science and Technology to pursue Ph. D. in Chemistry. During the course of her research, she published two journal articles, one co-authored article, submitted three journal articles for publication and presented her research in four national conferences and three regional conferences. During her graduate studies, she worked as graduate research assistant and graduate teaching assistant in the Chemistry department. During her Ph.D. work she received first place award in Graduate Research Showcase poster competition from the Council of Graduate Students in Missouri University of Science and Technology. Also, she was awarded several travel grants for national conferences from the Electrochemical Society, Council of Graduate Students and College of Arts, Sciences and Business at Missouri University of Science and Technology. In May 2021, she received her Ph.D. in Chemistry from Missouri University of Science and Technology.